MICRO ELECTRONIC MECHANICAL DEVICES COLLECTION

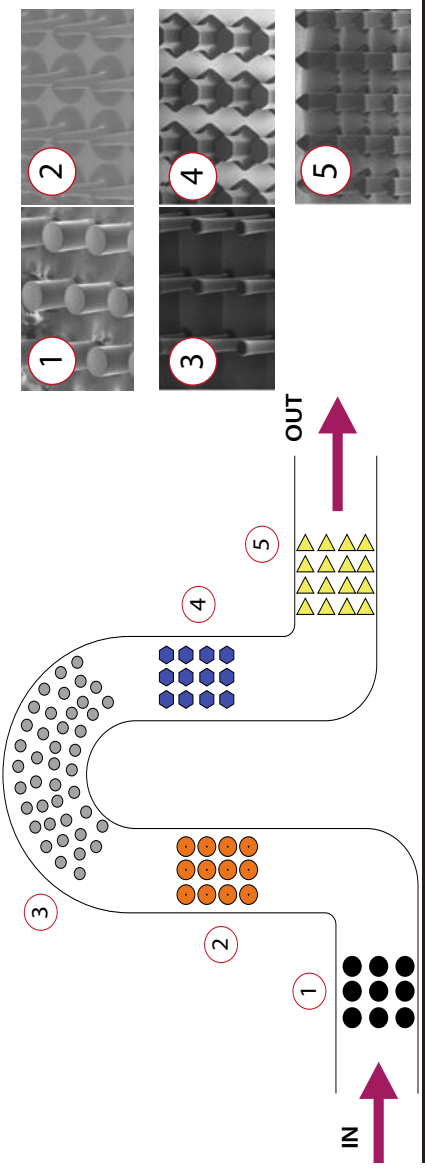

Carbon: The Next Silicon?

Book 2 – Applications

Marc J. Madou
Victor H. Perez-Gonzalez
Bidhan Pramanick

MOMENTUM PRESS
ENGINEERING

CARBON: THE NEXT SILICON?

CARBON: THE NEXT SILICON?

Book 2 – Applications

MARC J. MADOU,
VICTOR H. PEREZ-GONZALEZ, AND
BIDHAN PRAMANICK

MOMENTUM PRESS
ENGINEERING

MOMENTUM PRESS, LLC, NEW YORK

Carbon: The Next Silicon?: Book 2 – Applications

First published by Momentum Press®, LLC
222 East 46th Street, New York, NY 10017
www.momentumpress.net

ISBN-13: 978-1-60650-883-1 (print)
ISBN-13: 978-1-60650-884-8 (e-book)

Momentum Press Micro Electronic Mechanical Devices Collection

Cover and interior design by Exeter Premedia Services Private Ltd., Chennai, India

10 9 8 7 6 5 4 3 2 1

Printed in the United States of America

Abstract

Nuclear Magnetic Resonance (NMR) and Electron Spin Resonance (ESR) spectroscopies are well-known characterization techniques that reveal the molecular details of a sample non-invasively. We not only discuss how NMR can provide useful information on the microstructure of carbon and its surface properties, but also explain how C-MEMS/C-NEMS technology can be explored for building improved NMR microdevices. The manipulation of fluids and particles by dielectrophoresis and the use of carbon electrodes for dielectrophoresis in Lab-on-a-Chip applications is also discussed. The use of these electrodes in sample preparation through electrical polarization of a sample for identification, manipulation and lysis of bioparticles is emphasized. A new generation of neural prosthetics based on glassy carbon micromachined electrode arrays is introduced. The tuning of the electrical, electrochemical and mechanical properties of these patternable electrodes for applications in bio-electrical signal recording and stimulation, and results from in-vivo testing of these glassy carbon microelectrode arrays is reported, demonstrating a quantifiable superior performance compared to metal electrodes. Also the merits of high aspect ratio 3D C-MEMS/C-NEMS electrodes is made abundantly clear. When using carbon Interdigitated Electrode Arrays (IDEAS) the lower limits of detection (LODs) are often equivalent or better that those of the much more complicated and expensive optical fluorescence sensing schemes.

KEYWORDS

Carbon allotropes catalysis electrochemistry surface modification MEMS and NEMS super capacitors energy storage devices CNTs glassy carbon NMR electrospinning redox amplification AC/DC electrokinetics pyrolysis electroanalysis

Contents

List of Figures

List of Tables

About the Contributors

Dr. Marc J. Madou, before joining UCI as the Chancellor's Professor in Mechanical and Aerospace Engineering (MEA), Dr. Madou was Vice President of Advanced Technology at Nanogen in San Diego, California. He specializes in the application of miniaturization technology to chemical and biological problems (BIO-MEMS). He is the author of several books in this burgeoning field he helped pioneer both in Academia and in Industry. He founded several micromachining companies and has been on the board of many more.

Many of his colleagues became well know in their own right in academia and through successful MEMS start-ups. Madou was the founder of the SRI International's Microsensor Department, founder and President of Teknekron Sensor Development Corporation (TSDC), Visiting Miller Professor at UC Berkeley and Endowed Chair at the Ohio State University (Professor in Chemistry and Materials Science and Engineering). The third edition of "Fundamentals of Microfabrication," an introduction to MEMS and NEMS, which has become known as the "bible" of micromachining, was published in July of last year (http://fundamentalsofmicrofabrication.wordpress.com/).

Some of Dr. Madou's current research work involves a compact disc-based fluidic platform and carbon MEMS, the two latter fields were pioneered by Dr. Madou. To find out more about those recent research projects, visit www.biomems.net.

Dr. Victor H. Perez-Gonzalez, received the BS degree in Electronics and Communications Engineering (honors) from *Universidad Autonoma de Nuevo Leon*, Mexico, in 2006; and the MS in Electronics Engineering and PhD in Information Technologies and Communications from *Tecnologico de Monterrey*, Mexico, in 2008 and 2013, respectively. He has held a visiting research position at the University of California Irvine. For the past 2 years he has been a Research Associate at *Tecnologico de Monterrey*,

Mexico. In 2015 he was awarded with the National Researcher Level 1 distinction by the *Sistema Nacional de Investigadores*, Mexico, and became a member of the IEEE *Eta Kappa Nu* Honor Society. His research has been supported by CONACYT and UC-MEXUS.

Dr. Perez-Gonzalez's research interests are focused in the multidisciplinary area of Micro-/Nano- Electro-Mechanical Systems (MEMS/NEMS). From this broad research field, where he has published several papers in international journals and conference proceedings, his efforts are strongly aligned in the development of the sensing or actuating stages of Lab on a Chip devices and their integration with microelectronic elements. For the development of such stages he uses a broad range of materials, including: carbon, metals, electroconductive polymers, PDMS, and glass, among others. His current research projects deal with (1) the application of electrokinetic and mechanical forces for the manipulation, separation, or characterization of particles (e.g., microalgae, proteins, and bacteria) or fluids; (2) the development of highly sensitive amperometric sensors with Carbon-MEMS/NEMS; and (3) the development of novel micro/nano fabrication processes. Research efforts integrate mathematical modeling with experimental work for extending the practical applications of these technologies.

Dr. Bidhan Pramanick, received PhD Degree from Indian Institute of Technology (IIT) Kharagpur, India, in 2012 after completing B. Tech and M. Tech courses in Electronics and Communication Engineering from Kalyani Government Engineering College, India, in 2005 and 2007, respectively. He worked more than 2 years as Assistant Professor in Indian Institute of Space Science and Technology (IIST), an Institute of ISRO (Indian Space Research Organization) family. Dr. Pramanick joined Tecnologico de Monterrey, Mexico as Postdoctoral Research Investigator in January, 2015 in collaboration with University of California Irvine, CA, U.S. He was a recipient of the CSIR SRF Fellowship (India) for his PhD Programme and UGC grant for his Masters Programme.

He has authored or co-authored more than 16 papers in international journals and conference proceedings, two book chapters and one book. He was also one of the editors of two books on C-MEMS. He was a JPO in ISRO-sponsored project and he has successfully developed MEMS-based Microvalve and Micropump for space applications.

His current research interests include Carbon MEMS/NEMS especially Carbon Nanowire based sensors. He is also interested in the area of Micropropulsion and RFMEMS.

Foreword

UC Irvine, Sept 14–16, 2014. Chair: Dr. Marc Madou
Co-Chairs: Dr. Chunlei Wang, Dr. Rodrigo Martinez-Duarte and Mr. Jacob Moebius

Dear reader, two books: Carbon: The Next Silicon? Book 1-Fundamentals and Carbon: The Next Silicon? Book 2-Applications came about as a follow-up to the 1st International Conference on Carbon Micro and Nano Electromechanical Systems (C-MEMS /C-NEMS) held September 14–16, 2014 on the UC Irvine campus (see conference LOGO above). This was an invitation only event with delegates from the US, Italy, Spain, Malaysia, Mexico, Denmark, Germany, Switzerland and India. The group was limited to 60–70 researchers currently working in the field and expected to contribute to breakthroughs in this field and interested in international collaborations. Indeed research funding is weak globally and by leveraging efforts internationally we still have a chance to remain productive scientists regardless of politicians' irresponsibility. The pictures below are from some of the C-MEMS/C-NEMS team at the 2014 conference.

At the conference we had presentations on the latest C-MEMS and C-NEMS results, suggested future directions and discussed what each country is offering in terms of funding for international collaborations and formed several motivated proposal teams. We identified opportunities for students to be part of this international C-MEMS/C-NEMS research

ring and to be able to work in any one laboratory that is part of this ring to faster produce science breakthroughs and in the process become broader-thinking global citizens.

The format of the conference was a new and exciting experiment in itself. Over the last decade we have developed serious doubts about the effectiveness of huge, profit driven conferences so instead we brought together a small group of researchers in an intimate setting and made this an occasion where there was plenty of time to talk and make friends and make plans over drinks and food. Besides the science sessions we had several cultural events, including a class on Ancient Indian History: Aryan Invasion: Myth or Reality? (Prof. A. Ghosh) and a Malay board game: Congkak (Prof. Fatimah Ibrahim). We also had exhibits of paintings and photography and plenty of music [from Persian classical music to sixties rock and roll (UC Irvine Professor Band-Second Law), Russian love ballads (Dr. Lawrence Kulinsky) and Frank Sinatra (Prof. Jan Korvink)] we even had a yoga class (Prof. Regina Ragan) all by and for the invited C-MEMS/C-NEMS researchers. Art and science have a lot in common, in both one must create de-novo, not accept any preconceived notion of what the best science/art might be or where it will lead and in both cases, if good enough, one can transcend even the most miserable of times.

Part of the C-MEMS/C-NEMS team at the 1st C-MEMS International Conference. Sept 14–16, 2014. Location: Lobby CalIT2 on the UC Irvine Campus.

Dr. Swati Sharma (Karlsruhe Institute of Technology, Germany) on C-MEMS and EPR (Left panel). Sharifah Bee Binti O.A Abd Hamid on carbon and nano catalysis (Right panel). At the 1st C-MEMS International Conference. UC Irvine, Sept 14–16, 2014

A mixed-media sketch by Ashutosh Sharma (Indian Institute of Technology Kanpur) (Left panel). A Malay board game called Congkak –I kid you not! (Right panel). At the 1st C-MEMS International Conference. UC Irvine, Sept 14–16, 2014.

Prof. Jan Korvink (Karlsruhe Institute of Technology, Germany) singing Frank Sinatra's I did it my way" at the 1st C-MEMS International Conference. UC Irvine, Sept 14–16, 2014.

Quick Overview of Book 2-Applications

In Chapter 1 of Book 2-Applications, Swati Sharma et al are introducing perhaps a most unexpected application into the C-MEMS/C-NEMS community i.e., Magnetic Resonance (MR).

In this Chapter 1, this team discusses C-MEMS/C-NEMS for Magnetic Resonance Applications. Nuclear Magnetic Resonance (NMR) and Electron Spin Resonance (ESR) spectroscopies are well-known characterization techniques that reveal the molecular details of a sample non-invasively. These authors not only discuss how NMR can provide useful information on the microstructure of carbon and its surface properties, but they also explain how C-MEMS/C-NEMS technology can be explored for building improved NMR microdevices. In Chapter 2 Nicholas Green and Hamza Rouabah, the team that pioneered the use of carbon electrodes for AC electroosmotic flow, are detailing an important C-MEMS/C-NEMS application i.e., the manipulation of fluids and particles by dielectrophoresis. Along the same line Monsur Islam et al are tackling the use of carbon electrodes for dielectrophoresis in Lab-on-a-Chip applications in Chapter 3. They emphasize the use of these electrodes in sample preparation through electrical polarization of a sample for identification, manipulation and lysis of bioparticles. Of this team, Rodrigo Martinez was the first to combine C-MEMS dielectrophoresis with compact disc (CD) based microfluidics. In Chapter 4 Sam Kassegne and his team introduce a new generation of neural prosthetics based on glassy carbon micromachined electrode arrays. He reports on the tuning of the electrical, electrochemical and mechanical properties of these patternable electrodes for applications in bio-electrical signal recording and stimulation. Results from in-vivo testing of these glassy carbon microelectrode arrays is reported, demonstrating a quantifiable superior performance compared to metal electrodes. We did briefly touch upon C-MEMS/C-NEMS supercapacitors

in Chapter 1 of Book 1 but in Chapter 5 of Book 2, Chunlei Wang delves a couple of levels deeper into the topic of C-MEMS/C-NEMS on-chip micro-supercapacitors. In Chapters 6 (Paolo Scopece et al) and 7 (Victor Perez et al) the power of electrochemical analysis with C-MEMS/C-NEMS electrodes is detailed. In Chapter 7 the merits of high aspect ratio 3D C-MEMS/C-NEMS electrodes is made abundantly clear. When using carbon Interdigitated Electrode Arrays (IDEAS) the lower limits of detection (LODs) are often equivalent or better that those of the much more complicated and expensive optical fluorescence sensing schemes.

Acknowledgments

1. Acknowledgments for “C-MEMS/C-NEMS Introduction”: NSF grant. 1449397
2. Acknowledgments for “The Beautiful World of Carbon”: Financial supports from Malaysian Ministry of Higher Education HIR F00032, TRGS TR002B-2014B, and University of Malaya grant UMRG (RP022-2012A) are acknowledged.
3. Acknowledgments for “Synthesis of Nanocarbons and Tuning of Their Properties”: Financial support from the University Malaya UMRG (RP022-2012A), Ministry of Higher Education (MOHE) Transdisciplinary Research Grant Scheme (TR002A-2014B), Ministry of Science Technology and Innovation (MOSTI) Science Fund (SF-020-2014), and University of Malaya Flagship Grant (FL001-14AET) for the Carbon NEMS research are acknowledged.
4. Acknowledgments for “Historical Overview of Carbon Nanowire Fabrication Methods”: The financial support from UC-Mexus grant UCM-104728 and CONACYT Ciencia Basica CB-2014-01-241458.
5. Acknowledgments for “Carbon Nanowire Fabrication: C-MEMS”: Financial support from CONACYT Ciencia Basica CB-2014-01-241458, Ministry of Higher Education (MOHE) Transdisciplinary Research Grant Scheme (TR002A-2014B), Ministry of Science Technology and Innovation (MOSTI) Science Fund (SF-020-2014), and University of Malaya Flagship Grant (FL001-14AET) for the Carbon NEMS research, University Malaya UMRG (RP022-2012A) are acknowledged.
6. Acknowledgments for “C-MEMS based On-Chip Microsupercapacitors”: This article was supported financially by the National Science Foundation (NSF), (Award number 1506640) and NSF ASSIST center seed funding. Richa Agrawal acknowledges

University Graduate School (UGS) at Florida International University for support through a Doctoral Evidence Acquisition (DEA) Fellowship. The previous works summarized in this chapter were funded by the US Defense Advanced Research Projects Agency (DARPA), Young Faculty Award program (Project No. HR0011-08-1-0036), NSF (MRI program CMMI-0821582) and the American Chemical Society Petroleum Research Fund (49301-0N110).

7. Acknowledgments for "Glassy Carbon Microelectrodes for Neural Signal Sensing and Stimulation": The project described was supported by Award Number EEC-1028725 from the National Science Foundation. The content is solely the responsibility of the authors and does not necessarily represent the official views of the National Science Foundation.
8. Acknowledgments for "Advanced Electroanalysis with C-MEMS": Financial support by MIUR-PRIN 2010AXENJ8 and Veneto Region Project RESMIA is acknowledged.
9. Acknowledgments for "Carbon MEMS for Magnetic Resonance": The financial support from the European Research Council through the senior grant 290586 NMCEL.
10. Acknowledgments for "C-MEMS-Based 3D Interdigitated Electrode Arrays for Redox Amplification": The financial support from UC-Mexus grant UCM-104728 and CONACYT Ciencia Basica CB-2014-01-241458.

CHAPTER 1

CARBON MEMS FOR MAGNETIC RESONANCE

Swati Sharma, Neil MacKinnon, Vlad Badilita,
Lorenzo Bordonali, Sebastian Z. Kiss, and Jan G. Korvink

Karlsruhe Institute of Technology, Germany

1.1 BACKGROUND

The ability to form three-dimensional carbon micro- and nanostructures that feature varying molecular morphology holds interesting potential for magnetic resonance (MR) spectroscopy and instrumentation.

The *first* aspect that comes to mind is the ability to unravel the structure of these carbon molecular networks, so as to shed light on the fascinating material properties that are measured experimentally. Nuclear and electronic spin spectroscopies are powerful tools that provide detailed information on the molecular details of carbon. Nuclear magnetic resonance (NMR) spectroscopy is carried out for both ^{1}H and ^{13}C. During ^{13}C NMR, one needs to consider that it is a low-abundance isotope and requires an optimum experimental design for a reliable investigation. *Second*, structured carbon holds high potential for many applications, as the other chapters of this volume conclusively demonstrate. These applications stand to benefit from MR analyses, especially the fairly recent emergence of MR microscopy, which can shed light on chemical kinetics and ionic transport. *Third*, carbon also holds potential as a functional material within MR microsystems. We explore and review these three viewpoints.

We first offer a brief introduction to NMR and electron spin resonance (ESR, also known as electron paramagnetic resonance, EPR).

A plethora of literature is available on these topics, and some excellent general textbooks are recommended to the interested reader [1, 2]. The introduction is followed by a literature review on MR characterization techniques for investigating the underlying microstructure of carbon materials. From this review, one acquires insights on how MR spectroscopy can be useful for determining the hybridization degree of carbon atoms as well as the identity of surface functional groups that strongly influence the electrochemical properties of the material. The subsequent section details how advanced carbon microelectromechanical system (C-MEMS) applications such as battery anodes can benefit from MR spectroscopy, which is capable of providing real-time information on the kinetics and ion transport of such devices. On the basis of our experience in both MR spectroscopy and the manufacture of carbon materials, we envision some new application areas, for example, using carbon structures for the hyperpolarization of hydrogen and for the fabrication of microwave (MW) resonators, with the latter integrating these two new research areas. We hope that the information we provide on MR technology and our suggestions on possible future work will inspire carbon scientists and engineers to use this powerful, noninvasive tool for the characterization of carbon and to explore new ideas on how C-MEMS and carbon nanoelectromechanical system (C-NEMS) technology can be used to build improved MR microdevices.

1.2 INTRODUCTION TO MR

MR encompasses a group of spectroscopic techniques exploiting the quantum mechanical property of spin. Particles that possess spin (we are concerned with nuclei and electrons) also possess spin angular momentum and when placed in an external magnetic field, a splitting of otherwise degenerate energy levels results. While not rigorously correct, one may draw an analogy with the bar magnet of a compass aligning in the direction of the Earth's magnetic field, which is the energetically favorable configuration. Similarly, particles possessing spin angular momentum also have a magnetic moment, which aligns along the direction of an applied magnetic field (typically defined as along the z-direction in Cartesian coordinates). The difference from the classical picture is that quantum mechanics actually describes a superposition of states $|I, m>$ in which the magnetic momentum is aligned with and against the applied field. When a measurement is performed, an alignment in one of these two directions is observed. The energy of each state is given by

$$E = -\gamma \hat{I}_z B_z \tag{1.1}$$

with the spin angular momentum $\hat{I}_z$

$$\hat{I}_z = m\hbar \tag{1.2}$$

The magnitude of the applied magnetic field in the z-direction is B_z (Tesla), $\hat{I}_z$ is the spin angular momentum in the direction of the applied field, and g is the gyromagnetic ratio, a constant for each particle (MHz/Tesla). The spin angular momentum is dependent on the spin quantum number of the particle (I = ½ for ^{1}H, ^{13}C, and electrons), with values of m ranging from –I to +I in increments of 1. Thus for particles with I = ½, the values of m = ± ½, which produces two states. This breaking of degeneracy of the energy levels is known as Zeeman splitting and may be probed by external radiation, which typically falls in the megahertz (MHz; nuclei) to gigahertz (GHz; electrons) range depending on the type of particle and the strength of the external magnetic field.

There are important consequences resulting from the Zeeman splitting, which define MR as a spectroscopic technique. First, the energy differences typically encountered at ambient conditions are comparable to the thermal energy (kT), and thus population differences between the energy states are exceedingly small. In order to obtain a signal, a relatively large sample is required as compared to the alternative spectroscopic techniques (e.g., ultraviolet–visible [UV–Vis] spectroscopy and Raman spectroscopy). There are benefits to the nearly equal population distributions, the first being that relaxation rates from excited states are slow, commonly on the order of seconds for nuclear species and micro- to nanoseconds for electron spins. This permits the probing of spin–spin coupling structures inherent to the system with sophisticated, multipulse experiments, which is simply not possible in the optical spectroscopy domain (although femtosecond [fs] laser pulses have been used for two-dimensional infrared [2D IR] spectroscopy). Second, the linewidth of the detected resonances can be exceptionally narrow (of the order of parts per billion [ppb] on a megahertz scale for nuclear spins), which yields extremely detailed local chemical and structural information.

The local interactions are determined by the local magnetic fields created by neighboring nuclei and electrons. These magnetic fields are typically orders of magnitude smaller than the strength of the external magnetic field, and thus they are often treated as perturbations to the main field. These interactions may be broadly defined as a *chemical shift* and *dipolar*

coupling (many interactions exist but are outside of the scope of this chapter). In terms of Hamiltonians, the nuclear chemical shift is given by

$$\hat{H}_{cs,nucleus} = -\gamma\hbar\hat{I}_z \cdot \sigma \cdot B_z \tag{1.3}$$

which describes an orientation-dependent shift in the resonance frequency of the given spin caused by the presence of local magnetic fields encapsulated in the chemical shift tensor, σ. These local fields are most often caused by the electron density in the neighboring chemical bonds. The electron g-factor is given by

$$g = \frac{h\nu}{\mu_B B_z} \tag{1.4}$$

which is dependent on the applied microwave frequency, ν; Planck's constant, h; the Bohr magneton, μ_B; and the magnetic field strength, B_z. A value significantly different from that of a free electron (g_e = 2.002319) indicates a magnetic interaction with neighboring electrons and nuclei and, therefore, contains chemical structure information. The dipolar coupling Hamiltonian is given by

$$\hat{H}_{dipolar} = -\left(\frac{\mu_o}{4\pi}\right)\frac{\gamma_I\gamma_S\hbar}{r^3}\left(3\cos^2\theta - 1\right)\left[\hat{I}_z\hat{S}_z - \frac{1}{2}\left(\hat{I}_x\hat{S}_x + \hat{I}_y\hat{S}_y\right)\right] \tag{1.5}$$

which describes a shift in the resonance frequency inversely dependent on the distance between two spins (denoted as I and S). The electron spin possesses a hyperfine coupling Hamiltonian, which describes interactions between nuclear and electron spins:

$$\hat{H}_{hyperfine} = \hat{I} \cdot A \cdot \hat{S} \tag{1.6}$$

Without going into detail, the hyperfine coupling is dependent on 'A' describing two interactions including the Fermi contact, dependent on the electron wave function overlap with the nuclear position, and the dipolar interaction, taking a form comparable to Equation 1.6. In general, these interactions are anisotropic and solid samples yield broad spectral lines attributable to the contribution of each orientation to the respective interaction. In the case of solution samples, in which the molecules tumble isotropically, the broadening is reduced to the isotropic chemical shift while the dipolar coupling averages to 0 and high-resolution spectra are obtained. Solids can be made to act as

isotropic samples as well by mechanically rotating the solid sample at an angle of 54.7° relative to the main magnetic field. Under these conditions ($3\cos^2\theta-1$), a term that appears to first order in all anisotropic interactions *magically* goes to zero and thus the technique is referred to magic-angle spinning (MAS).

1.3 CHARACTERIZATION OF PYROLYTIC CARBON USING MR

C-MEMS and C-NEMS structures are fabricated by first patterning the desired geometry into a high carbon-containing polymer and then pyrolyzing the patterned polymer precursor so as to obtain the desired carbon shape. In the case of photopatterning photoresist precursors such as SU-8, the process yields a glasslike carbon (commonly known as glassy carbon or GC) whose microstructure features entangled graphite ribbonlike structures with <5 nm pores [3]. These pores are found to be smaller, or even absent, depending on the nature of the starting material and the fabrication methodology [4–6]. Electronic, electrochemical, and surface properties of GC are strongly intertwined with its microstructure. Thus, for the fabrication of GC-based electronic and electrochemical sensors (see Chapters 4–7) with optimal properties, it is extremely important that one understands the chemical and morphological nature of the GC microstructure at the nano-length scale.

Carbon allotropes and carbon-containing compounds may either feature pure *sp*, sp^2, or sp^3 hybridization or contain a mixture of them. For example, diamond and graphite display pure sp^3- and sp^2-hybridized carbon atoms, respectively, while fullerenes, carbon nanotubes (CNTs), diamond-like carbon, and amorphous carbon possess a mixture of differently hybridized carbon [7]. The microstructure and resulting properties of some of these carbon materials correlate with the ratio of the sp^2- and sp^3-hybridized carbon in the matrix [7].

Common techniques for probing the graphitic content in a carbon material such as GC are Raman spectroscopy, X-ray diffraction (XRD), transmission electron microscopy (TEM), and, in some cases, electrical property measurements. Raman spectroscopy and XRD measurements are noninvasive techniques; however, the information one obtains on carbon's crystallinity from these techniques is an average value of the crystallinity in a large area such as a circular spot with ~100 μm diameter. In case of GC, the *D* and *G* Raman bands and the characteristic 002 planes of graphite in XRD tend to be broad owing to the fact that this material is

a mixture of sp^2- and sp-hybridized carbon atoms, and sp carbons result in a broad Raman peak. It is often difficult to draw any conclusion on carbon's atomic or molecular arrangements from these techniques, and one needs to use supporting characterization techniques such as high-resolution transmission electron microscopy (HR-TEM) imaging and electron diffraction patterning. HR-TEM analysis often requires powdered or focused ion beam milled samples that are only a few nanometers thick, which may not be possible for all C-MEMS patterns. In summary, none of these common techniques can directly provide quantitative information on the type of hybridization of the carbon atoms in a specific area on a given sample.

MR is a noninvasive technique and is highly compatible with C-MEMS patterns that can easily be placed into typical MR sample holders. Several examples of the application of NMR for carbon characterization are described in the literature, including, but not limited to, the characterization of coal [8–10], charcoal [11, 12], graphite or graphite oxide [8, 13–15], graphene [16], diamond [8, 17], nanodiamond [18–21], nanohorns [22], nanotubes [23, 24], and amorphous hydrogenated carbon [25]. In these studies, ^{13}C is the most common probe of the molecular structure, which is often assisted by the presence of ^{1}H in the sample. Several material properties can be addressed using the combination of these two nuclei: the presence and distribution of both domains and paramagnetic centers and the content of carbon that is (i) sp^3 versus sp^2 hybridized, (ii) CH or CH_2 or CH_3 or quaternary, (iii) nonprotonated, (iv) aromatic, and (v) functionalized (C–OH, C–O–C, C=O, etc.). In the case of ESR, a nearly equivalent quantity of literature exists with applications including, but not limited to, coal [26–31], graphite or graphite oxide [32–34], nanodiamond [19, 35, 36], nanohorns [37, 38], and nanotubes [39–41]. The principal spectral parameters that may be determined include the electron g-value (dependent on the chemical environment), the signal line width (dependent on spin–spin couplings, paramagnetic gas exchange, etc.), signal line shape (differentiating localized and conducting electron signals), hyperfine couplings (electron–nucleus interactions), and paramagnetic electron concentrations.

From the perspective of NMR, the first choice to study carbon materials would naturally be solid-state experiments based on ^{13}C and, depending on the details of the material, ^{1}H (see Table 1.1 for the NMR relevant details of these nuclei).

The low natural abundance of ^{13}C requires rather large sample quantities but results in the absence of carbon–carbon couplings, which

Table 1.1. NMR relevant properties of ^{13}C and ^{1}H nuclei

MR sensitive isotope	Natural isotopic abundance (%)	Spin quantum number (I)	Gyromagnetic ratio (MHz/T)	Relative sensitivity	Chemical shift range (ppm)
^{13}C	1.1	1/2	10.7	0.02	250
^{1}H	99.9	1/2	42.7	1	10

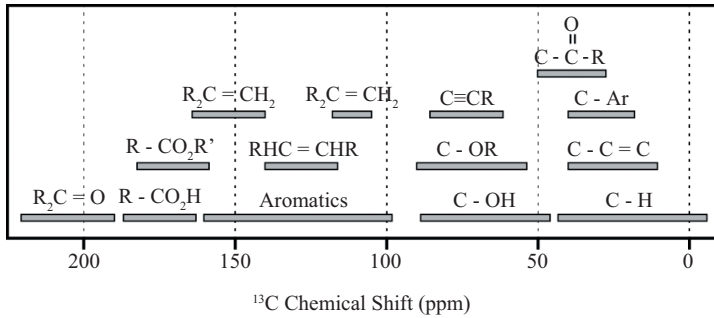

Figure 1.1. Chemical shift range for ^{13}C in NMR spectroscopy.

greatly simplifies the resulting spectrum and analysis. The ^{13}C chemical shift range, that is, the spread over which the resonance frequencies are detected, is 25 times larger than that of ^{1}H (Figure 1.1).

This implies that the resonance frequency response to chemical environment is much more sensitive and indeed ^{13}C NMR can be used to distinguish hybridization states and functionalization (see Figure 1.1). While ^{1}H NMR is also sensitive to the same chemical information, the large natural abundance and gyromagnetic ratio combined with the narrow chemical shift dispersion typically result in spectra with broad resonance line shapes, especially in solid-state NMR, complicating data analysis. The benefit of the presence of ^{1}H in the same sample is the possibility to transfer magnetization from the highly abundant, highly sensitive ^{1}H to the low abundance, insensitive ^{13}C using a technique known as cross polarization magic-angle spinning (CPMAS). This technique has the potential to enhance ^{13}C signals by a factor of 4 (the ratio of the gyromagnetic ratios).

Accessing these material properties required the development of sophisticated NMR experiments capable of exploiting the various nuclear interactions. For a better perspective, graphite was first studied by ^{13}C NMR spectroscopy in 1958, just over a decade after the discovery of NMR [42], and because of the broad spectral lines observed with the first spectrometers, very little structural or chemical information was obtained. Some early studies explicitly aimed at the determination of chemical composition of carbon materials were carried out in the 1970s [8, 43] with the investigation of graphite, coal, and diamond. With the development of MAS [44, 45] and cross polarization (CP) [46–48], unprecedented structural detail could suddenly be accessed. State-of-the-art work (as of 2015) uses a variety of NMR experiments based on careful control of various nuclear interactions to truly approach atomic-level detail

about the molecular structure. MAS is such a ubiquitous technique that, in describing all further experiments, it should be assumed that the sample was spinning.

In the most straightforward case, the ^{13}C spectrum of carbon materials will contain contributions from each carbon species comprising the sample. This spectrum is referred to as the direct polarization (DP) or Bloch decay spectrum because it is produced by exciting all ^{13}C nuclei without bias. From the DP spectrum, hints about chemical composition are revealed, including the presence of sp^3, sp^2, or functionalized carbon (purely based on the differences in chemical shift). Gaining further insight into the chemical structure of the material relies on the ability to edit the DP spectrum for particular features of interest. Features that may be exploited in solid-state NMR for spectral editing include relaxation times (spin–lattice T_1 and spin–spin T_2), number of attached hydrogen atoms, mobility of the functional group (e.g., methyl group rotation), and distance to nonbonded hydrogen. The remainder of this section will briefly examine some of the common NMR experiments that are performed and how their results relate to chemical structure.

The first strategy commonly used is CP. This technique takes advantage of the ^1H nuclei present in the sample and aims to transfer the large ^1H polarization to the less-abundant, less-sensitive ^{13}C nuclei, resulting in ^{13}C signal enhancement. The polarization transfer is permitted only when the Zeeman energy levels of the two nuclei are equal. This is accomplished by applying a spin-lock radiofrequency (RF) pulse simultaneously to both nuclei with the condition that the field strength is the same on both channels. Polarization is then transferred as a function of the contact time, that is, the period in which the spin-lock pulse is applied. One might expect that long contact times will greatly enhance the ^{13}C signal; however, one is also competing with relaxation mechanisms that deplete the total polarization, and thus there is an optimal contact time that maximizes the ^{13}C enhancement. It is important to note that the nuclear interaction Hamiltonian responsible for the polarization transfer is the dipolar coupling between the ^1H and ^{13}C. One example of spectral editing then becomes clear—only ^{13}C nuclei in the proximity of ^1H will be enhanced. The contact time offers another alternative for spectral editing and exploits the strength of the dipolar coupling. By choosing a globally suboptimal, short contact time (SCT), only those ^{13}C nuclei with strongly dipolar coupled ^1H nuclei will be enhanced, often permitting the distinction of bonded versus nonbonded hydrogen.

A second strategy that uses the strength of the dipolar coupling interaction is dipolar dephasing (DD), also referred to as gated decoupling

[49, 50]. This technique requires the selective introduction of the dipolar coupling, which is otherwise suppressed with appropriate decoupling RF pulse sequences. By *turning on* the dipolar coupling for a short period (~40 μs), strongly coupled ^{13}C will lose coherence and, therefore, will not contribute to the detected signal. When combined with DP or CP spectroscopy, the resulting spectrum will be edited to highlight nonprotonated and mobile ^{13}C nuclei.

A third strategy for spectral editing takes advantage of differential relaxation rates of the ^{13}C (or ^{1}H) nuclei. The relaxation mechanisms may be complicated, but it is sufficient to note that different domains within the material may possess different relaxation rates (e.g., aliphatic versus aromatic domains) [25]. By carefully timing the delays in the NMR pulse sequence, it is possible to eliminate contributions from the quickly relaxing population relative to the slowly relaxing population.

A fourth strategy aims to directly map the correlations between the ^{13}C and ^{1}H. These are 2D NMR techniques, which aim to correlate ^{13}C chemical shifts with bonded or neighboring ^{1}H chemical shifts (heteronuclear correlation, HetCor [51]) or ^{1}H linewidths (wideline separation, WISE [52, 53]). These spectra offer insight into chemical shift assignment (via chemical shift correlations), proximity of functional groups [14], and mobility (via ^{1}H line widths).

With a careful choice of the appropriate experiments, it becomes possible to uncover structural details of the carbon material (see Table 1.2). Straightforward application of the techniques described will reveal proximity to ^{1}H, while maintaining the chemical environment information encoded in the chemical shift. Further detail is gained by taking spectral differences of two experiments—for example, CH signals may be obtained by taking the difference between a CP spectrum (all ^{13}C near ^{1}H) and a CP or DD spectrum (^{13}C near ^{1}H but not bonded) [21].

A powerful application involving control of the dipolar coupling is in determining domain structures. There are several cases where this is important: in determining aliphatic domain sizes, in determining fused aromatic domain sizes, and in the determination of nanoparticle surface signals versus core signals. The key to determining aliphatic domain sizes is in the ability to monitor polarization (i.e., signal) loss as it flows through a dipolar-coupled network. One must create *channels* through which polarization is allowed to flow in the form of multiple quantum (MQ) coherences. These coherences are allowed only in the case of multiple spin couplings, and they may be described by an MQ order dictated by the number of coupled spins. Therefore, by monitoring signal intensity as a function of the type of MQ coherence that is accessed, and how long it

Table 1.2. Various NMR experiment designs for carbon material characterization

Experiment	Details revealed	Details concealed	Example refs
DP	All ^{13}C	-	Standard
CP	^{13}C near ^{1}H	^{13}C distant from ^{1}H	Standard
Relaxation Edit	Domain features	-	[25]
MQMAS	Domain features	-	[25]
DP or DD	Mobile and np ^{13}C	Rigid ^{13}C–H groups	[10, 12, 20, 21, 55]
CP or DD	Mobile and np ^{13}C	Rigid ^{13}C–H groups	[10, 12, 13, 20, 21, 25, 55]
SCT-CP	Quaternary and p ^{13}C	^{13}C distant from ^{1}H (>3 bonds)	[12, 13, 20, 55]
SCT-CP or DD	Quaternary and mobile ^{13}C	^{13}C distant from ^{1}H, rigid ^{13}C–H groups	[12, 20, 55]
RFDR	^{13}C–^{13}C correlations	-	[14]
WISE	^{1}H spectral pattern at each resolved ^{13}C	-	[19, 20]
HetCor	^{1}H–^{13}C chemical shift correlation	-	[10, 20]
DEPT (MQ)	^{13}C–H and quaternary	^{13}C–H_2 groups	[20]

(*Continued*)

Table 1.2. Various NMR experiment designs for carbon material characterization (Continued)

Experiment	Details revealed	Details concealed	Example refs
DETP(MQ) or DD	Quaternary ^{13}C	$^{13}C–H_2$ and rigid $^{13}C–H$ groups	[20]
LR-REDOR	Domain features (p versus np)	-	[10, 12, 20, 54, 55]
DIPSHIFT	p ^{13}C and residual np ^{13}C	-	[20]
DIPSHIFT or DD	p ^{13}C	-	[20]
HARDSHIP	Domain and particle size	-	[20]
CSA filtering	sp^3 ^{13}C (alkyl)	sp^2 and sp ^{13}C	[10, 12, 53, 55]

DP, direct polarization; CP, cross polarization; MQMAS, multiple quantum magic angle spinning; DD, dipolar dephasing; SCT, short contact time; RFDR, radio frequency driven recoupling; WISE, wideline separation; HetCor, heteronuclear correlation; DEPT, distortionless enhancement by polarization transfer; LR, long range; DIPSHIFT, dipolar and chemical shift (correlation); HARDSHIP, heteronuclear recoupling with dephasing by strong homonuclear interactions of protons; CSA, chemical shift anisotropy; np, non-protonated; p, protonated.

is allowed to exist (all controlled by the RF pulse sequence), it is possible to determine the number of correlated spins. This experiment was used by Jaeger et al. to probe the nanostructure of amorphous hydrogenated carbon [25]. By including relaxation time editing, the authors were able to reveal the heterogeneous nanostructure of the material, concluding with the existence of small sp^3 CH_2 domains (approximately five CH_2 groups) separated by nonhydrogenated olefinic sp^2 carbons among a statistical distribution of olefinic sp^2 and sp^3 CH groups.

A second technique reliant on the decay of signal as a function of proximity to ^1H has been used to measure the size of fused aromatic domains. The principle of the experiment is based on DD with a modification to include long-range couplings [54]. With short DD times, the long-range couplings permit the observation of ^{13}C signals originating from within fused aromatic systems. As the DD time increases, these signals are destroyed quickly for small domains and persist for longer DD times for large domains. This technique has been used to identify surface versus interior carbons in nanodiamonds [15] and to study fused aromatic systems in coals [10, 12] and charcoal [55].

1.3.1 NMR FOR INVESTIGATING CARBON HYBRIDIZATION

In the case of glasslike carbons as obtained in the C-MEMS process, the NMR analysis can shed light on the extent of graphitization as well as on the presence of H impurities. The sp^2 and sp^3 peaks resulting from the different types of amorphous carbon exhibit slight variations in their chemical shifts, which makes NMR a particularly useful characterization tool. In Table 1.3, the sp^2 and sp^3 NMR peak positions as observed in various carbon film samples are summarized [56]. One can determine the presence of differently hybridized atoms in a carbon material based on the number and the area of the peaks that are present at their respective values in parts per million. It is also reported that NMR can be used as a standard method to calibrate the sp^2-to-sp^3 ratio derived from other methods [57]. An illustration of typical NMR spectrum of various carbon samples is shown in Figure 1.2.

This technique can also be very useful for detecting the presence of H in the given carbon, for example, in carbon materials obtained from low-temperature pyrolysis. The low-temperature pyrolysis materials have fascinating properties and are a research topic for scientists studying the mechanism of the pyrolysis process [64].

The second MR spectroscopic technique, ESR, is dependent on the presence of unpaired electrons in the material. From the perspective of

Table 1.3. sp^2 and sp^3 NMR peak positions of carbon films [56]

Film type	sp^2 Peak position (ppm)	sp^3 Peak position (ppm)	sp^2/sp^3	H (at%)	Reference
Diamond powder	120	36 ± 2	~0/100	-	[17]
Graphite	135	-	100/0	0	[8]
Diamond-like carbon	140	50	1.5–1.7	0.3-0.4	[58]
a-C:H	130	40	0.55, 0.34, 0.19	-	[57]
a-C:H	130	40	1.44	0.35	[25]
a-C:H	130	40	2.35, 1.85, 1.25	0.34, 0.40, 0.42	[59]
a-C:H	140	50	1.63	-	[60]
a-C	130 ± 5	62	14.6	<0.15	[61]
a-C:H	130	40	0.16, 0.25, 1.00, 1.25, 1.63	0.61, 0.58, 0.47, 0.31, 0.35	[62]
a-C:H	140	39	-	-	[63]

a-C:H *and* ***a-C*** *denote amorphous carbon films with and without H, respectively.*

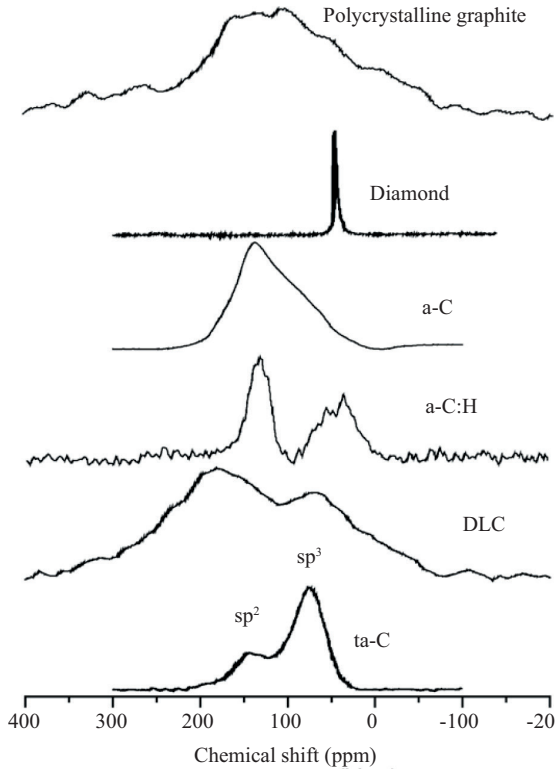

Figure 1.2. NMR spectra for various carbon films [56]: a-C, softer carbon films without hydrogen usually formed at low energy or higher temperature; a-C:H, softer carbon films with hydrogen; DLC, diamondlike carbon; and ta-C, tetrahedral amorphous carbon films with high content of sp^3 bonding and without hydrogen.

carbon materials, an ESR signal typically arises from broken carbon–carbon bonds (dangling bonds) or transition metal impurities. If impurities are excluded, then ESR is a technique that primarily uses the *g*-value to identify the chemical environment of the electron. As summarized by Petrakis et al., characteristic *g*-values are known for aromatic hyrdocarbons of various ring sizes, aliphatic hydrocarbons, oxygen-containing radicals (e.g., quinones and ethers), and nitrogen- or sulfur-containing radicals [29], which by comparison reveal hints as to the environment of the electron in the carbon material. From the linewidth of the ESR signal, details about chemical environment distributions may be inferred. The linewidth is also strongly affected by adsorbed oxygen (a paramagnetic molecule), and thus

investigations into signal linewidth as a function of oxygen partial pressure reveal details such as material porosity. If the material is conductive, then the transition from a symmetric dispersive to an asymmetric dispersive ESR signal may be used to differentiate localized and conduction electrons, respectively. Recent advances in pulsed ESR techniques have allowed even further details to be uncovered, including hyperfine interactions hidden within the broad ESR signal (electron-spin-echo envelope modulation [ESEEM], hyperfine sublevel correlation [HYSCORE] [40]), and direct measurement of nuclear-electron interactions electron nuclear double resonance (ENDOR [36]). In a landmark report, nanodiamond samples with nitrogen defects have been used to detect a single electron spin [65].

1.3.2 NMR FOR CARBON SURFACES

NMR spectroscopy can also serve as an important tool for electrochemists who wish to quantify C=O and C=C functional groups on carbon electrode surfaces. Electrochemical devices such as supercapacitors and battery anodes are some of the most researched application areas of GC and C-MEMS technology. The performance of such electrochemical devices depends on establishing charge-storage processes on high surface area electrodes and is strongly influenced by carbon's surface properties. High-surface-area carbons are known to have complicated kinetics because of the presence of various surface functional groups [66]. These surface groups may contain functionalities such as quinoid, quinhydrone, phenolic, carboxyl, carbonyl, or lactone depending on the fabrication technique used for manufacturing the electrodes. NMR has the unique ability to quantitatively analyze the surface composition of carbon materials and this can be very useful in C-MEMS electrochemical technology.

In a recent report, ^{13}C NMR was used to detect and quantify very small amounts of sp^2-hybridized carbon on the surface of nanodiamond particles of ~5 nm diameter [21]. The authors were also able to determine whether or not the carbon atoms were protonated, that is, if there is any H impurity in detonation nanodiamonds (also known as ultradispersed diamonds). Typical NMR spectra for the nanodiamond material prepared using different heat treatments are shown in Figure 1.3.

In their analysis of the surface functional groups present in detonation nanodiamonds, the authors used MAS and TOSS (total suppression of spinning sidebands) techniques and quantitatively determined the presence of C−H, C−OH, C=O, and C–C groups, which, in this case, accounts for 12 to 14 percent of all carbon. Clearly, in addition to the characterization

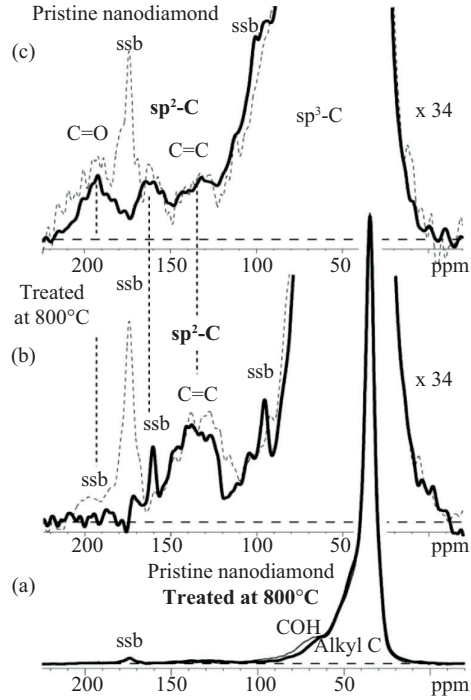

Figure 1.3. Quantitative, direct-polarization ^{13}C NMR spectra of detonation nanodiamond and a heat-treated reference sample. (a) Spectra of pristine nanodiamond (thin line) and the 800°C heat-treated material (thick line), taken at 14 kHz MAS. (b) Spectra after 800°C heat treatment, expanded 34 times vertically, taken at 14 kHz MAS (dashed line) and 6 kHz with TOSS (full line). A broad CC band is clearly visible. (c) Same as (b) for pristine nanodiamond (except higher spinning frequency of 6.5 kHz for TOSS spectrum). ssb, spinning sideband [21].

of carbon's atomic arrangements and hybridization, the potential of NMR for investigating the presence and extent of similar functional groups on the surface of C-MEMS electrodes could be a very interesting area for further research.

1.4 NMR FOR KEY CARBON MEMS APPLICATIONS AND DEVICES

Small foot print batteries and supercapacitors are two types of electrical energy storage devices that have been developed during the past three decades to meet the dramatically increased energy demand in portable electronic devices. Batteries exhibit remarkably high energy densities; however, they suffer from a rather limited cycle life [67]. On the other hand, supercapacitors, also known as electrochemical double-layer capacitors (EDLCs), in spite of a relatively lower energy density, show essentially unlimited cycle lives and very fast charge or discharge rates (also see Volume 2, Chapter 5) [68].

There is a wide range of graphitic carbon materials that meet the requirements of conductivity, porosity, and electrochemical stability for use in supercapacitors: carbon onions [69] and nanohorns [70]; activated, templated, and carbide-derived carbons [71]; and CNTs [72]. Activated carbons are the most widely used materials nowadays in the fabrication of supercapacitors because of their high surface area and high electronic conductivity, along with low cost. The key characteristic to achieve high surface area is the porosity of this class of materials, which is tunable in the synthesis process. Activated carbons are derived from organic precursors such as wood, coconut shells, or coal, and a porous network is created upon activation in the bulk of the carbon particles. The mean pore size is tuned by means of temperature and activation time (longer activation time or higher temperatures lead to larger mean pore size [68]): micropores (<2nm in size), mesopores (2–50nm), and macropores (>50nm). The small pore sizes are typically slightly larger than the solvated electrolyte ions [73]. The storage mechanism in supercapacitors is based on the formation of an electrical double layer at the interface between the solid porous electrode and the liquid electrolyte solution. In order to provide an in-depth understanding of the associated processes taking place during the charge or discharge cycles and to investigate the behavior of ions inside the nanopores, a wide variety of experimental methods and theoretical studies have been used. Changes in the concentration of electrolyte ions inside the pores versus the applied potential have been assessed by small-angle neutron scattering. Ion diffusion inside mesoporous carbon electrodes has been investigated for different charge states by neutron diffraction [74]. Other experimental techniques include in situ electrochemical quartz crystal microbalance methodologies [75] and in situ IR spectroscopy [76]. In parallel with the experimental efforts, a significant amount of theoretical work has been dedicated to the understanding of the

storage mechanism in supercapacitors. The anomalous increase in capacitance in nanoporous supercapacitors has been explained by a mean field theoretical model [77], further extended to take into account the dynamics of charging [78]. Molecular dynamics simulations have also successfully predicted the anomalous enhancement of capacitance experimentally observed in micropores [79–81].

In spite of all the efforts presented earlier, an investigation methodology capable of direct observation and quantitative measurement of the evolution of ion environments in supercapacitors is still needed. MR-based investigation methods have been attracting a lot of attention in the past several years and are more and more used in the study of batteries and supercapacitors. The versatility of NMR as an investigation method comes from the weak coupling between the nuclear spin states and the surrounding environment, making it extremely sensitive to the local environment. NMR is therefore a perfect tool for the study of electrochemical interfaces, in particular for the investigation of supercapacitors and batteries, offering quantitative and element-selective information at the molecular level about the structure and dynamics of the ions in the electrolyte and at the electrode–electrolyte interface.

As NMR spectroscopy enables direct observation of the adsorbed atomic species storing the electrical charge in the carbon-based matrix, the most straightforward and convenient experimental arrangement is ex situ NMR investigation [82, 83]. This usually means that the device, supercapacitor or battery, is disassembled at different charge or discharge states, and an NMR spectrum or image is acquired from the carbon electrode soaked with electrolyte. Ex situ NMR is capitalizing on the opportunity of using MAS spectroscopy, therefore, taking advantage of higher spectral resolution to gain exquisite information about changes in the immediate neighborhood of the intercalating ions. However, ex situ NMR brings along a series of inherent disadvantages such as uncertainties about modifying the charge state of the device by ion desorption during the disassembly procedure as well as the obvious evaporation of the solvent (usually acetonitrile [ACN]), which may trigger changes in binding and even cause electrolyte solidification.

In situ NMR circumvents the physical and chemical changes that occur on disassembling the cells and before actual measurements are being recorded. Taking advantage of NMR being a noninvasive technique, in situ NMR investigation enables real-time monitoring of interactions and distributions of anions and cations separately in the carbon electrodes offering a more realistic picture of the behavior of working devices. The price to be paid is a significant decrease in spectral resolution because of the inherent incompatibility between in situ NMR and MAS.

1.4.1 NMR FOR EDLCs

A large number of C-MEMS-based EDLCs are based on high surface area porous carbons. Solid-state NMR constitutes a powerful means of discrimination for species that have been adsorbed inside the porous carbon matrix. This is especially the case of very small pore sizes with a high trapping efficiency, where liquid-state NMR is not able to provide enough information because of the limited ion mobility. Solid-state NMR has been used to observe and study ex situ the electrolyte organization in nanoporous-activated carbon supercapacitor electrodes [83], as the adsorbed molecules within the graphene layers yield NMR signals that are shifted by approximately −6 ppm relative to the free molecules. In this study, natural abundance ^{13}C MAS NMR was used to investigate the degree of structural disorder of the nanoporous-activated carbon electrodes, the results being confirmed by Raman spectroscopy. Together with ^{13}C spectra, ^{11}B MAS NMR spectra were used to quantify the amounts of electrolyte molecules—ACN and tetraethylammonium tetrafluoroborate (TEA^+ and BF_4^-)—either outside or trapped inside the nanoporous carbon matrix, for uncharged and charged supercapacitors [83]. Moreover, 2D exchange spectra performed on both ^{11}B and natural abundance ^{13}C provide information about the dynamics of the electrolyte species as well as about the chemical exchange between the adsorption sites and the free state of the electrolyte.

In the case of EDLCs, a number of other nuclei found in the organic electrolyte are used to characterize activated carbon electrodes using NMR spectroscopy techniques. A typical example exploits the ^{11}B and ^{19}F species found in the organic electrolyte tetraethylammonium-tetrafluoroborate (Et_4NBF_4). Lee et al. [84] used solid-state ^{11}B NMR to study two different activated carbons used as electrode material in EDLCs: M500 activated carbon and M3000 activated carbon exhibiting medium (500 m^2/g) and high (3,000 m^2/g) surface area, respectively (Figure 1.4). ^{11}B MAS NMR spectra recorded for each of the two types of electrodes allow for the identification of two BF_4 species that differ through the localization of the ions in the matrix of the activated carbons. The MAS spectra for M500 electrodes show that a larger amount of electrolyte is left on the external surface of the activated carbon matrix (A-peaks) compared to the electrolyte solution, which has been adsorbed within the small, pore volume (B-peaks). For the high surface area (M3000) electrodes, ^{11}B MAS spectra show a reversed tendency as more BF_4^- ions are localized inside the large pores compared to what is left at the outer surface. T_1 (spin–lattice relaxation times) have been estimated for both cases using the saturation recovery method [1]. This allows for a common ground to compare

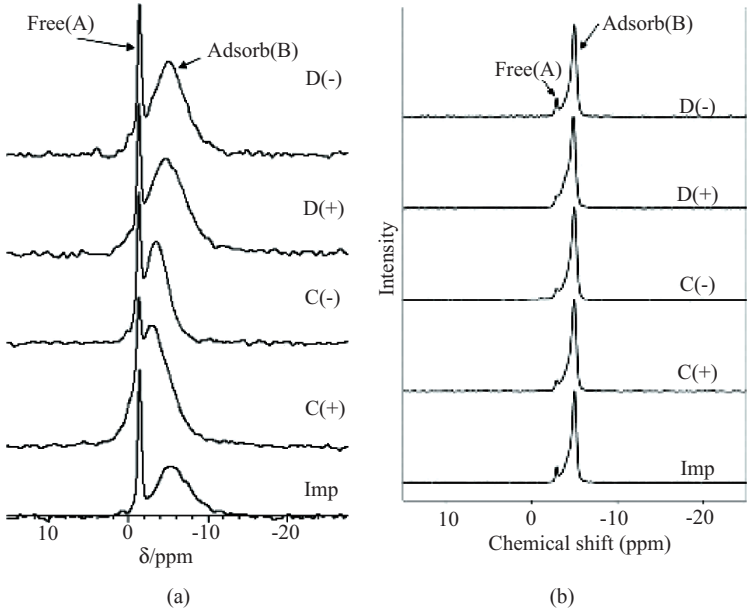

Figure 1.4. (a) ^{11}B MAS NMR spectra of BF_4 in activated carbons with specific surface area of 500 m^2/g for impregnated, charged, and discharged states as presented in [84]; (b) ^{11}B MAS NMR spectra of BF_4 in activated carbons with specific surface area of 3,000 m^2/g for impregnated, charged, and discharged states. The sharp peaks (A) have been assigned to free BF_4 species, and the broad peaks have been assigned to adsorbed BF_4 species. (Legend: Imp = impregnated; C/D +/− = charged/discharged positive/negative polarization)

the mobility of various ionic species within the same activated carbon, as well as between the two samples under consideration.

Along the same line of characterizing the matrix of activated carbons in EDLCs, liquid-state NMR has been performed on the fluorine in atom in the BF_4^- anion [85], exploiting the fact that ^{19}F is a spin ½ nucleus with 100 percent natural abundance, therefore, constituting a precious NMR investigation instrument. However, the characterization is rather limited to the interaction of the BF_4^- with the surface of the activated carbon electrode, as liquid-state NMR cannot capture the information from the ions trapped inside the small pores, which have very limited mobility.

Grey et al. [86] have implemented in situ NMR to investigate the migration of electrolyte ions between the supercapacitor carbon electrodes in real time, as well as their interaction within the porous electrode matrix itself (Figure 1.5). The authors have proposed a special supercapacitor

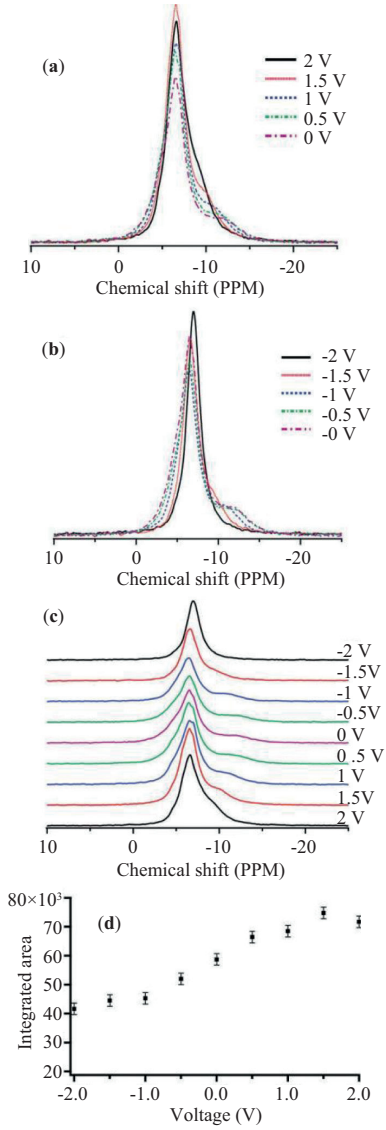

Figure 1.5. ^{11}B static NMR spectra taken in situ from a supercapacitor at various voltages, as presented in [86]: (a) spectra of the positive electrode charged up to 2 V; (b) spectra of the negative electrode charged up to 2 V; (c) chemical shift evolution for each electrode as a function of the applied voltage; and (d) integrated areas for each electrode spectra as a function of the applied voltage.

design with the electrodes spatially shifted with respect to each other, which allows one to separate the resonances associated with each electrode, as only one electrode can be placed inside the NMR coil detector at a time. ^{11}B NMR spectra were acquired in situ as a function of the supercapacitor state of charge as controlled with an external charger, and the dynamics and binding of ions within the supercapacitor were followed this way. NMR experiments have also revealed a significant decrease in the T_1 relaxation times from 2.1 to 0.3 s when the voltage was increased from −2 to 2 V [86], one potential cause for this trend is attributed to an increased interaction between the anions and the carbon matrix at positive potentials.

A follow-up work from the same group uses in situ NMR spectroscopy to gain insight into the charge storage mechanism in EDLCs [87]. This is achieved by NMR spectra collected in real time for direct observation of the changes in the amount of charge storing species (adsorbed species) on the applied voltage and for differentiating various charge storage regimes.

In situ NMR investigation of EDLCs has been recently pushed one step forward when the first magnetic resonance imaging (MRI) results were published [88], yielding spatially resolved chemical information related to the electrolyte ions. Chemical shift information data is acquired fast enough to provide real-time snapshots of the nonequilibrium states of the supercapacitor during electrochemical cycling, thus differentiating the specific charge storage mechanisms during charging and discharging, respectively. ^{1}H NMR information was used to characterize the cation (NEt_4^+), as the ACN solvent used here was deuterated, while ^{11}B NMR information was used to characterize the anion (BF_4^-). Multinuclear imaging on ^{1}H and ^{11}B nuclei allows for capturing information from each type of ions occupying each electrode of the cell during electrochemical cycling.

1.4.2 NMR FOR BATTERIES

As described in Chapter 5, graphite and GC are very suitable electrode materials to study the mechanism of lithium intercalation in lithium-ion batteries. Graphite and GC are preferred over other carbon materials because of their higher volumetric energy density and lower cost. During charging and discharging cycles, lithium ions intercalate into and deintercalate out of the graphitic layers, processes that are associated with significant changes in the electrode volume [89]. Another process profoundly affecting the subsequent battery performance is the formation of passive films on the graphite electrodes because of the decomposition reactions of

the battery electrolyte, especially when using propylene carbonate (PC) [90]. This process is irreversible and diminishes the cycling efficiency of graphite electrodes leading to a large capacity loss in lithium-ion batteries after the first cycle.

Kim et al. [91] have concomitantly used ^{7}Li and ^{13}C NMR together with electrochemical impedance spectroscopy in order to study the intercalation or deintercalation mechanisms of lithium ions into graphite layers as well as the association of the lithium ion with various solvents. Chemical shifts in the ^{7}Li NMR spectra are expected to reveal whether solvent molecules are intercalated together with Li ions inside the electrode graphite lattice. These results are being cross-checked with ^{13}C NMR spectra of charged graphite electrodes in electrolyte solutions that should exhibit signals corresponding to the solvents if these are present in the graphite structure. Kim et al. have shown that using crown ethers, these ethers indeed cointercalate with lithium ions in the graphite structure slowing down the passivation reaction. However, this occurs at the expense of a lower charge-transfer rate in the battery [91].

A well-known issue in lithium-metal [ion] batteries is the formation of metallic lithium dendrites on the lithium-metal anode during the charging process. The strategy that emerged to alleviate this problem was the development of graphite negative electrodes in lithium-ion batteries. The latter come with the compromise that the discharge capacity of a graphite electrode is smaller than the discharge capacity of metallic lithium. The discharge capacity of the graphite electrode can be improved by doping the graphite with boron, taking advantage of the fact that the boron atomic size is comparable to that of carbon; therefore, it does not introduce significant distortion of the carbon lattice. However, the discharge capacity of a graphite electrode doped with boron is a function of the percentage of dissolved boron and the maximum solubility of boron in graphite is only about 2.35 percent even at 2,350°C [92]. It is, therefore, important to precisely characterize the structural states of boron atoms in the carbon lattice, and besides classical methods such as Raman or Auger electron spectroscopy, NMR has the capability to decipher the chemical environments of the boron atoms.

Lee et al. [93] have successfully characterized the structural states of boron in boron-doped graphite obtained by mixing graphite with various percentages (1, 2.5, 5, and 7 wt.%) of boron carbide during the graphitization process by solid-state ^{11}B NMR spectroscopy. The results show that, for low concentrations, all boron atoms are replacing carbon atoms in the graphite lattice. However, excess boron diffuses fast between the graphite planes, it being a light mass atom, eventually forming graphite carbide and

preventing the free movement of the actual charge carriers [93], therefore affecting the ultimate performance of the battery.

While graphite and lithium easily form intercalation compounds [94], this is not the case between graphite and sodium when Na^+ is being electrochemically reduced at a carbon electrode. Gotoh et al. [95] have used MAS and static NMR to analyze the state of the ^{23}Na nucleus inserted in hard carbon electrodes and to compare sodium with lithium intercalation in the carbon matrix. The authors observed a significantly different behavior of sodium spectra compared to ^7Li NMR in hard carbon. At ambient temperature, very different from the lithium, the sodium signal does not shift as a function of sodium content, whereas at low temperature, the lineshapes of MAS and static NMR spectra did not change and the peaks did not exhibit any splitting [95]. Gotoh et al. concluded that the behavior of sodium with respect to hard carbon electrodes is qualitatively different from that of lithium with the exchange of sodium between different carbon matrix sites happening at a slow rate relative to the NMR time scale. At the same time, NMR experiments show that sodium does not form metallic clusters in the closed nanopores of hard carbon [95].

Gerald et al. [96] have demonstrated an NMR platform for the in situ investigation of ^7Li ions in carbon electrode materials. Similar to the case of supercapacitors, in situ battery NMR allows for the observation of ongoing electrochemical processes during battery cycling, as opposed to disassembling the battery after a certain number of charge or discharge cycles. This advantage comes with the drawback of the incompatibility between MAS and in situ NMR spectroscopy, with the associated resolution loss. Gerald et al. developed a device, which integrates an electrochemical cell and an NMR detector, identifying the signatures of several lithium species within the same spectrum: lithium in the electrolyte, intercalated lithium, and inorganic lithium in the solid–electrolyte interphase. With in situ NMR, the evolution of each species during multiple charge or discharge cycles can be followed.

1.5 FUTURE OPPORTUNITIES

1.5.1 CARBON MEMS FOR MR-RELATED RF AND MW APPLICATIONS

In this section, we explore new possible applications of photoresist-derived carbon as a functional material for MR experiments. We are well aware of the fact that some of the concepts presented may not be so readily

applicable to current NMR hardware design, but carbon MEMS is still a very young technology which we believe has great potential to influence in one way or other way even such seemingly disparate disciplines as MR hardware engineering.

The performance of an MR detector relies heavily on the quality of the RF resonances. As shown in Figure 1.6, a standard resonant circuit comprises an inductor (NMR probe) and two capacitors for frequency tuning and impedance matching. The energy inside the system is stored periodically in the form of electric and magnetic fields inside the capacitors and the inductor, respectively. A commonly used figure of merit and measure of the effectiveness of a resonating system to store energy is the quality factor $Q = 2\pi$ (maximum energy stored per cycle)/(average energy loss per cycle).

For RF and MW resonators, losses have at least four causes: dielectric, conduction, radiation, and external losses. In Figure 1.6, the effect of loss on the resonance linewidth and thus the Q-factor is schematically illustrated. For MR detector design, it is highly desirable to efficiently translate a given amount of current into a confined magnetic field that is stimulating the sample. Hence, it is important to try to minimize all potential loss mechanisms that might obscure or degrade the actual MR signal to be detected from the sample. For example, the signal-to-noise ratio (SNR) for metal-based inductive detectors is directly proportional to $R^{-1/2}$ with R being the equivalent ohmic resistance of the electrical conductor [101].

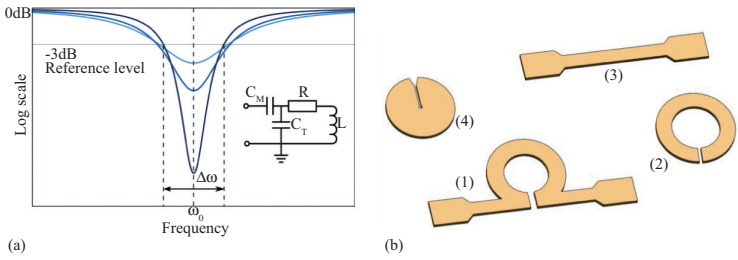

Figure 1.6. (a) Schematic representation of frequency dependence of the reflection coefficient. The quality factor Q can be directly evaluated from the −3 dB bandwidth Δω around the resonance frequency ω_0. Mismatched resonant circuits (matching capacitance C_M) as well as loss (depict by the equivalent resistance R) degrade the resonance performance of the system. (b) Sketch of a variety of planar MW resonators; (1) planar ohm-shaped resonator [97], (2) split-ring resonator [98], (3) half-wavelength resonator [99], and (4) surface loop-gap resonator [100].

Among the emerging but still rather exotic optical and force-based MR detection principles, Faraday induction is by far the most prevalent and is an industry standard. The archetype of inductive detectors is a solenoid made of metal wire. However, a vast variety of surface resonators (spirals [102, 103], microstrip lines [104], slot lines [105], loop gaps [100]) and volume resonator types (Helmholtz pairs [106], bird cage coils, metal cavities [107], or loop-gap resonators [108, 109]) have been used, each motivated by a particular application. Material-wise, metals of high electric conductivity and matched magnetic susceptibility are typically used. For ESR experiments that operate at exceedingly higher frequencies compared to NMR ($f_{ESR} \approx 28$ GHz/T vs. $f_{NMR} \approx 42$ MHz/T), dielectric materials have been used for years as a low loss complement to metal cavity resonators [110]. Upon the advent of high field NMR (>10 T) and MRI (>7 T) experiments, dielectrics became an interesting alternative as a material for high-frequency MR probes [111]. Dielectric materials relevant for MR are essentially electric insulators with relative permittivities ε_r that range from 10 to several hundreds to thousands. Typically, these materials (e.g., ceramics such as barium titanate and zirconium oxides) show a low dielectric loss tangent ($\tan\delta \approx 10^{-5}$) and low temperature coefficients ($\tau \approx 15$ to -15 ppm/K) and are formed into cylindrical or ring-type resonant structures, which effectively act as field concentrators or storage for a narrow range of frequencies. The resonance frequency of a resonator is determined by the permittivity of the material and its near surroundings, as well as its overall physical dimensions. Owing to their potentially high permittivity, the electromagnetic (EM) fields are well confined to the structure, which decreases radiation loss. Even more interesting for miniaturized MEMS-based devices, higher ε_r is also connected to a decreased wavelength inside the material and shrinks the overall resonator size proportional to $1/(\varepsilon_r)^{1/2}$ [112].

The material properties discussed earlier are a function of frequency, which must be known for rational RF or MW engineering decisions. However, there is only limited literature available on the dielectric properties of suitable GC films in the RF or MW regimes. In contrast, composite materials made from carbon-based fillers such as CNTs or carbon black mixed into polymer matrixes are being actively characterized and are established as dielectric electromagnetic interference (EMI) sheets or foam absorbers [113–115]. Apart from free space and transmission line techniques (e.g., planar lines [116] and open ended lines [117]), resonant methods provide a highly accurate and sensitive way to characterize MW material properties at a particular frequency or a discrete set of frequencies. Therefore, the perturbation in the response (phase, magnitude of s-parameters) of a

resonator of known performance is measured on sample loading. The perturbation because of the interaction of the sample under test with the electric field results in a resonant frequency peak shift as well as a decreased loaded Q-factor of the known probing resonator. The loaded Q-factor Q_L is obtained by the measured resonant frequency f and the half power (−3db) bandwidth Δf of the mode resonance: $Q_L = f/\Delta f$. Especially, planar resonators, such as ring [118] or microstripline [119] resonators, seem to be a reasonable choice to investigate carbon MEMS thin films as produced by standard UV lithography. The reliable assessment of the C-MEMS material permittivity as a function of frequency is a crucial requirement for further investigations leading to interesting RF or MW applications.

The specific resistivity of photoresist-derived carbon can vary by orders of magnitude depending on annealing, ranging between that of semimetals and semiconductors [120]. For C-MEMS films to be considered as a suitable RF or MW dielectric, its dielectric losses are most probably too high. On the other hand, its semimetallic character is not reaching the high electric performance standard of metals such as silver or copper. Hence, modifications of the material should aim for one of the two goals, namely, to render it more metal-like (i.e., higher electric conductivity) and to improve its dielectric properties (e.g., reduce conduction loss).

We envision three possible routes to approach this challenge that all take advantage of the tailorability of carbon: (1) tuned process and preparation conditions, (2) the use of fillers, and (3) galvanic metal reinforcement:

1. Park et al. [120] confirmed the remarkable dependence of the electrical conductivity on the carbonization temperature. Park et al. and Singh et al. [120, 121] suggested that a further increase in carbonization temperature (beyond 1,000°C) will also lead to a further increase in conductivity, denser structures, and nucleation of small graphitic nanocrystallites (graphitization completion at 2,700°C). This route seems to be promising; however, besides higher machine complexity, the glass-transition temperature of the utilized substrate will naturally limit at some point the maximal applicable temperature. Other process parameters such as gas pressure and type might influence the physical properties of the achieved structures. The concept of donor or acceptor gasses can be exploited, whereas increased process pressure might enhance the tendency of the material to form graphitic domains.
2. There is an opportunity to tailor the dielectric RF or MW performance of the carbon film matrix by forming mixtures of two materials of different ε_r, Q, and so on. The photoresist precursor

can be readily mixed with dielectric fillers such as calcium titanate ($CaTiO_3$) or barium titanate ($BaTiO_3$) powders, so that the permittivity as well as the dielectric loss can be varied in the given range of start or end values as a function of the mass fraction of the two materials [112]. The carbonization or sintering temperature represents a further parameter with which to adjust the material properties. Interestingly, many technical ceramics exhibit sintering temperatures (starting at approximately 900°C) that are covered by the carbonization process used for photoresist-derived carbon. As the resist becomes successively more opaque as the filler concentration increases, a major issue is the decreased performance of the UV lithography resulting in degraded conformity and resolution of the resist patterns. As shown by Rashidian et al. [122], a feasible alternative to UV lithography for patterning polymer matrixes with high solid filler content is casting the solution into prepatterned forms followed by baking and hard UV or X-ray exposure.

3. Galvanization leaves the carbonized structure itself unchanged but improves its electrical conductivity by reinforcing it with a thin layer of highly conductive metal by means of electroplating. Particularly for higher frequencies (MHz to several GHz), the skin effect is very pronounced with the current density highest near the surface or *skin* of the conductor, and as a consequence, most of the resistive losses occur there. For example, a conductor made from copper features a skin depth of 63 μm at 1 MHz but only 2 μm at 1 GHz. For electrical applications, typically, copper or gold electroplating baths or electroless plating solutions are used to change the surface properties of an object. The metal plating process should be optimized in order to yield smooth metal surfaces as well as high structural conformity by, for example, avoiding nonuniform electroplating current distributions. In a study from Reijerse et al. [123], a CW ESR or ENDOR resonator was manufactured from high density graphite, which was electroplated with 10 to 15 μm gold. For ESR or ENDOR experiments, a high-frequency (typically MW) ESR resonator excites electrons inside a sample, while a second low-frequency signal (typically RF) modulation field is simultaneously applied. In this case, the graphite offers the advantage of being suitable for plating and can be used to geometrically define the MW cavity while offering at the same time a low enough specific resistance to prevent excessive damping of the RF modulation field.

A useful feature of photoresist-derived carbon structures is that numerous units can be reproducibly fabricated on a single substrate or wafer, in parallel and with high precision. Another aspect is the potential to pattern the photoresist not only in 2D but also in 3D. With the advent of 3D laser lithography, which allows direct writing of precise and arbitrary 3D patterns into a photosensitive resin, hollow structures, spirals, ring resonators, or spherical objects can be readily fabricated at microscale dimensions. Given that losses could be overcome or substantially reduced, 3D micro NMR detectors made from photoresist-derived carbon would offer superior sensitivity (e.g., for coil detectors the SNR is proportional to d^{-1} where d is the outer diameter) per unit volume as stronger magnetic fields can be generated.

Similar to polymer composites filled with, for example, carbonaceous particles, photoresist-derived carbon might also play a role in integrated MW absorbing coatings and for developing antielectrostatic measures with increased chemical resistance [124]. This includes, for example, the reduction of backradiation of microstrip resonators or reduced EMI among electrical components and circuits [113]. The work of Kuzhir et al. [115] demonstrated that even nanometrically thin pyrolytic carbon (PyC) films produced via chemical vapor deposition offer reasonably high EM attenuation. The authors proposed that the semitransparent PyC films might emerge as a promising material for manufacturing ultrathin microwave filters and shields.

1.5.2 CARBON FOR SHIMMING

The ability to form a material with tunable magnetic susceptibility has important consequences for MR engineering. Carbon in its many forms displays magnetic susceptibilities varying from -3.5×10^{-7} emu/g for C_{60} all the way to -3×10^{-5} emu/g for graphite perpendicular to the 002 plane, a span of almost two orders of magnitude (see also Table 1.4). In case of pyrolytic carbon, the susceptibility values depend on the nature of the starting material as well as the pyrolysis temperature. One can, therefore, tune the susceptibility of the material to suit the desired application.

Even small susceptibility differences (in ppm) between material layers along the field lines cause variations in magnetic field strengths. As this type of variance is three orders of magnitude larger than that tolerable for the measurement of NMR signals (required resolution: parts-per-billion range), one of the maxims of conventional NMR engineering is the parallel arrangement of materials with respect to the strong B_0 magnetic

Table 1.4. Susceptibility values of carbon allotropes

Carbon allotrope	Susceptibility in [emu/g]	Reference
Diamond	-4.9×10^{-7}	[125]
Graphite parallel to plane	-5×10^{-7}	[125]
Graphite perpendicular to plane	-3×10^{-5}	[125]
C_{60}	3.5×10^{-7}	[125]
C_{70}	-5.9×10^{-7}	[125]
Pyrolytic (glassy) carbon obtained from polyvinylchloride between 1,000°C–2,000°C	Range: 0 to -6.0×10^{-6}	[126]
Pyrolytic (glassy) carbon obtained from polyvinylidene chloride at 3,000°C	-4.7×10^{-6}	[126]

field, thus avoiding susceptibility jumps close to the measurement volume. As susceptibility jumps are undesirable, NMR systems contain multiple shimming magnets that are intended to compensate for such effects. With continued progress in miniaturization and integration, and because designs do not follow necessarily the design rules of traditional macroscopic NMR hardware, shimming becomes much more complicated. One remedy is to perform the so-called structural preshimming through the addition of regions of materials of given susceptibility that help to compensate for these shifts in magnetic field strength in the active region of the NMR detection system.

In essence, the concept is straightforward. Jumps in susceptibilities are the reason for field shifts, that is, the differential jump strength along the field direction for a directed area element. So a surface element d$\mathbf{A}$ with unit normal $\mathbf{n}$ is measured in $(\chi_1 - \chi_2)\cdot dA(\mathbf{B}\cdot\mathbf{n})/|\mathbf{B}|$, and can be considered a *source* term (in the sense that charge is the source for electric fields) for the field shifts that penetrate the surrounding medium. Hence, by distributing additional bounding shapes of materials of particular susceptibility χ_j, we can directly shim a region of interest. In Jia et al. [127], it is shown how this can be achieved through the addition of materials with positive or negative susceptibility using topology optimization—here mainly for an MRI application of interventional surgical devices.

Ryan et al. [128] suggested that a similar shimming effect can be achieved by creating specially shaped air holes surrounding the functional part of a lab-on-a-chip device for an application in NMR, using a Monte-Carlo simulation method. We speculate that resist-derived, patterned, carbon films are an excellent source for structural shimming. As the susceptibility of pyrolytic carbon can be widely varied according to processing conditions, this suggests the ability to tune the degree of passive shimming depending on NMR sample needs.

1.5.3 PYROLYTIC CARBON FOR ON-DEMAND HYPERPOLARIZATION

Hydrogen is widely considered a promising clean energy alternative to fossil fuels. In a hydrogen-centered energy economy, the biggest market would be represented by fuel cells, to generate electricity at high efficiency. Particular efforts are being put into the design and characterization of fuel cells, and NMR is contributing by enabling investigations into the H_2 adsorption characteristics of hydrogen storage materials. However, the energy sector is not the only one that is currently driving general interest of NMR researchers toward hydrogen: The need for on-demand H_2 production, and in particular parahydrogen (pH_2) production, has been growing since the 1990s, thanks to the advances in NMR technology. Specifically, parahydrogen-induced hyperpolarization, or PHIP [129, 130], is a well-known and established technique for NMR signal enhancement in analytical chemistry, medical imaging [131–133], metabolomics [134–137], and gas and fluid analytics [138–140]. NMR detector miniaturization and integration in portable and multipurpose analytical devices would also benefit significantly from a signal-boosting technique such as PHIP.

Parahydrogen is one of the two spin isomers of the H_2 molecule, having an antiparallel nuclear spin configuration; orthohydrogen, the parallel-spin isomer, has a much higher state density than parahydrogen so that, at room temperature and 1 bar pressure, H_2 gas is naturally found as a 3:1 mixture of ortho- and parahydrogen. The relevance of parahydrogen in NMR stems from the availability of NMR signal enhancement techniques (hyperpolarization) that exploit the very large reservoir of spin order represented by pH_2; indeed, PHIP offers enhancement factors of more than 10^5-fold [130].

Parahydrogen production relies on the slow-rate conversion mechanism of the ortho-H_2 fraction at very low temperatures at which the para state is the low lying energy state [141]. Conversion from a triplet ortho

state (S = 1) to the singlet para state (S = 0) is prohibited by the angular momentum conservation principle, thus a catalytic action from an agent, such as an iron oxide substrate or an activated carbon substrate, is usually necessary to enable and boost the conversion. Parahydrogen mixtures as pure as 98 percent pH_2 content can be achieved, for example, by driving the conversion at T < 14K. The need for catalytic o–p conversion in the hydrogen production industry originates from the necessity to deal with the release of heat upon spontaneous o–p H_2 conversion, which is responsible for the evaporation of more than 60 percent of the liquefied H_2.

The established large-scale hydrogen production route is based on fossil fuel and natural gas reforming. Common feedstocks for hydrogen production are methanol, ethanol, and ammonia. Aqueous-phase reforming of biomass and bio-produced H_2 (i.e., fermentative H_2) are two production strategies that are also gaining momentum [142]. Efforts have been put into the miniaturization of hydrogen production and storage devices to achieve a higher energy density in fuel cells or to alleviate the problems associated with storing a large quantity of either liquid or gaseous hydrogen [143].

Carbon-based materials, and potentially C-MEMS, enter the PHIP picture from two aspects: On the one hand, carbon is currently being explored as a catalyst for H_2 production via an electrocatalytic reaction route and as a catalyst-supporting material for aqueous phase reforming reactions. On the other hand, activated forms of carbon are also required as parahydrogen conversion catalysts in pH_2 converters. It is possible to envision a scenario where C-MEMS devices are streamlining both the production and conversion processes at the micro level and could thus meet the on-demand need for H_2 and pH_2 gas, for example, in hyperpolarized NMR. We will now explore the potential of carbon in the context of these two applications.

Traditionally, the development of H_2 microgenerators has stemmed from the need for on-demand H_2 production for fuel cells: The storing of small volumes of hydrogen for small fuel cells (e.g., portable fuel cells) has proved to be very challenging, if not impossible. As an alternative to compressed gas and liquid hydrogen, hydrogen-packed chemicals, such as hydrides, have gained attention as hydrogen storage materials, providing high hydrogen densities at room temperature and ambient pressure.

The feasibility of hydrogen microgenerators has been demonstrated a number of times; here we report on just a few inspiring examples. A good amount of experimentation has been dedicated to the fabrication of methanol reforming hydrogen microgenerators [144]. Gervasio et al. [145] fabricated a room-temperature-operated microfluidic device for heterogeneous catalytic hydrolysis of aqueous alkaline borohydride solution. Kim [146] and

Hoeppner [147] proposed two different microreactors for hydrogen generation from sodium borohydride as a convenient room-temperature solutions to the H_2 production problem. More recently, Zhu et al. [148] proposed an on-demand microfluidic hydrogen generator with self-regulated gas generation, and Um et al. [149] reported on a micro-TPV (microscale-thermophotovoltaic) device integrated with a microreformer for hydrogen (H_2) production by burning and reforming ammonia (NH_3).

Electrocatalytic hydrogen production from water, commonly known as hydrogen evolution reaction (HER), is also an option that still needs to be fully exploited in the context of MEMS. The most commonly used metal catalyst for HER devices is Pd, although the very fact that Pd is a rare earth element has pushed the research toward finding viable alternatives, such as Mo, Ni, Co, and Fe. Although cheaper, transition metals are prone to oxidation and corrosion, two factors that ultimately impact the long-term durability and catalytic effectiveness. Carbon is a recent addition to the list of possible HER catalysts: The high tunability of molecular topology, the large material availability, and the marked chemical resistance render carbon-based materials quite advantageous for metal-free catalytic hydrogen production. In several instances, carbon-based materials have attracted much attention as suitable catalyst support for HER reactions: Structured carbon devices supporting noble metal catalysts have been evaluated for both oxygen reduction reactions (ORR) and HER, leading to promising results (see, e.g., [150] and references therein). FeN_4-containing CNTs have been investigated for electrocatalytic activity [151] and have been found stable toward the ORR in an acidic electrolyte. Li et al. [152] reported an oxygen reduction electrocatalyst based on CNT–graphene complexes showing high catalytic activity, as well as superior stability in comparison to other nonprecious metal catalysts, in both acidic and alkaline solutions. Gong et al. [153] investigated the possibility of using nitrogen-containing CNTs for ORR, reporting an impressive 4.1 mA/cm^2 output current density if compared to platinum–carbon electrodes (1.1 mA/cm^2). Dubey et al. [154] reported a significant rate of electrolytic hydrogen production at anodic voltages as low as 1 V using CNT electrodes as the anode. More recently, Zheng et al. [155, 156] demonstrated a P- and N-doped graphene catalyst for HER, featuring highly efficient electrocatalytic activity because of the promotion of both proton absorption and reduction kinetics.

Microbial electrolysis cells (MEC) are attractive and scalable alternate possibilities for hydrogen production. These bioelectrochemical devices exploit the metabolic action of living microorganisms to produce hydrogen. The appeal of such devices is the very-low-voltage requirement and the possibility to operate at room temperatures.

The operating principle of an MEC is a variant of the microbial fuel cell (MFC). In an MFC, organic matter is oxidized by a bacterial colony (e.g., *Pseudomonas* spp. or *Shewanella* spp.), producing carbon dioxide as a waste product, while releasing protons to the liquid medium and electrons that are collected at the anode. Spontaneous current generation ensues when oxygen is reduced at the cathode. However, under anaerobic conditions, and forcing a small positive voltage across the anode and the cathode (as little as +0.2 V), hydrogen gas is produced at the cathode. Thus an MEC is different from an MFC in that an MEC is equivalent to an electrolytic cell that produces hydrogen (i.e., the system's Gibbs Free energy is positive, $\Delta G > 0$), while an MFC is analogous to a galvanic current generator ($\Delta G < 0$).

Carbon-based materials in the form of carbon cloth, carbon paper, graphite felt, graphite granules, and graphite brushes are ideal for the anode in an MEC, offering a favorable growth substrate for bacteria to thrive on [157]. In this instance, an MEC capable of supporting a bacterial population on carbon-based scaffolds would make for a sustainable hydrogen generator with extremely low energy requirements. We speculate that the easy patternability of carbon-based materials and the low voltage requirements for conventional or microbial electrolysis would make C-MEMS technology very appealing for the design of on-demand hydrogen generators.

We will now briefly discuss the opportunities offered by carbon-based materials to the conversion of ortho-rich to para-rich hydrogen. The main requirements for successful ortho-to-parahydrogen (o–p) conversion are (i) low temperatures and (ii) the presence of a suitable catalyst to trigger the spin flip transition from triplet to singlet nuclear spin state. Thus, a catalytic converter is usually composed of three elements: a refrigerator stage, a conversion chamber, and a gas collection system. In this context, the catalyst is usually a material containing paramagnetic defects, and the spin flip is caused by the hydrogen molecule coming in close proximity to such defects [158].

As for requirement (i), technology for localized in situ cryogenics is already in place, with steady advances each year. Notable mentions from the recent literature are, for example, low-cost microthermoelectric coolers [159], a Stirling microcooler [160], and a Joule–Thomson cryocooler [12], where the cooling fluid itself is hydrogen gas.

Carbon could play a major role as the material to fulfill requirement (ii), namely, as an ortho-to-parahydrogen conversion catalyst. Commonly used conversion catalysts to rapidly convert from ortho- to para-H_2 are iron oxide and hydrous ferric oxide, nickel sulfate and nickel silicate, chromic oxide,

ruthenium metal and ruthenium alloys, and activated charcoal (see Ref. [161] for a review). The conversion chamber is usually designed as a storage space for a large quantity of catalyst and with an inlet and the outlet for H_2 gas and pH_2-rich gas mixtures. The geometry of the chamber is optimized for the largest possible contact surface between H_2 gas and the catalyst.

Although the o–p conversion phenomenon has been intensely investigated and theoretically explained [162], this is not true for most allotropes of carbon that feature paramagnetic properties and as such theoretically viable for o–p conversion. This knowledge gap offers an opportunity for research on a form of carbon that is suited to perform the o–p conversion at high efficiency and easily fabricated in a C-MEMS manner at the same time. Catalytic activity in the case of the o–p conversion is essentially tied to the presence of paramagnetic centers and the rates of H_2 adsorption and desorption; pyrolitic carbon, for instance, could represent a solution to decouple the paramagnetism problem, which is a tunable bulk property of carbon, from H_2 adsorption, which is mostly a surface-related problem and can be solved by cleverly patterning the sacrificial polymer. We thus propose that existing parahydrogen converter designs might be miniaturized by exploiting the potentialities of carbon as an MEMS building material, for example, in the shape of consolidated solutions such as packed-bed microreactors or flow-through cell microreactors.

1.6 CONCLUSIONS

The potential of MR spectroscopy for the characterization of carbon materials and C-MEMS devices has not yet been fully recognized. There are several, but unconnected, scattered studies where MR technology has been implemented to unravel the molecular arrangement and properties of a variety of carbon materials. Here we have summarized a number of such reports to inspire the C-MEMS community for making use of this widespread powerful technology. NMR and ESR are excellent tools for probing carbon's microstructure and its surface and to characterize the performance of a variety of C-MEMS devices.

Additionally, C-MEMS is not yet an established technology for applications in NMR or ESR. Nevertheless, the potential for a number of such applications has been identified, which range from catalysis to shimming, and we foresee concrete applications emerging in the near future. It is especially the ability to prepattern the precursor polymers in a variety of ways, through electrospinning and lithography with subsequent pyrolysis, which presents a real opportunity to combine carbon structures with other system components at the microscale.

Many applications depend on having carbon structures of predefined molecular morphology. Here, especially ESR is an important tool with which to probe the electronic structure of the resultant carbon samples, with the ability to reveal the extent to which the amorphous and polycrystalline material matrix consists of unpaired electrons. On the other hand, NMR can reveal intimate structural details, especially in conjunction with chemical bonds formed with other compounds.

With its stronger sensitivity to protons and other electrochemically active species, NMR microscopy is predestined to become a method of choice with which to spatially analyze and discriminate dynamic molecular processes, to reveal, for example, the degradation mechanisms that confront electrochemical energy storage and energy conversion devices. Through hyphenation with other techniques, such as optical excitation and detection, we expect to see numerous advances that build on the impressive capabilities already available today. We, therefore, expect the trio consisting of carbon in general, C-MEMS as a specific embodiment, and MR both as a method of investigation and targeted application, to be a fruitful combination of techniques in the short to medium term.

REFERENCES

[1] Abragam, A. 1983. *The Principles of Nuclear Magnetism*.

[2] Levitt, M. 2008. *Spin Dynamics: Basics of Nuclear Magnetic Resonance*. 2nd ed. Chichester: John Wiley.

[3] Harris, P.J.F. 1997. "Structure of Non-Graphitising Carbons." *International Materials Reviews* 42, no. 5, p. 206–18. doi: http://dx.doi.org/10.1179/imr.1997.42.5.206

[4] Fitzer, E., W. Schaefer, and S. Yamada. 1969. "The Formation of Glasslike Carbon by Pyrolysis of Polyfurfuryl Alcohol and Phenolic Resin." *Carbon* 7 no. 6, p. 643–48. doi: http://dx.doi.org/10.1016/0008-6223(69)90518-1

[5] Sharma, S., A. Sharma, Y.K. Cho, and M. Madou. 2012."Increased Graphitization in Electrospun Single Suspended Carbon Nanowires Integrated with Carbon-MEMS and Carbon-NEMS Platforms." *ACS Applied Materials & Interfaces*, 4, no. 1, p. 34–39. doi: http://dx.doi.org/10.1021/am2014376

[6] Sharma, S., R. Kamath, and M. Madou. 2014. "Porous Glassy Carbon Formed by Rapid Pyrolysis of Phenol-Formaldehyde Resins and Its Performance as Electrode Material for Electrochemical Double Layer Capacitors." *Journal of Analytical and Applied Pyrolysis* 108, p. 12–18. doi: http://dx.doi.org/10.1016/j.jaap.2014.05.025

[7] Somani, P., and M. Umeno. 2007. "Modern Research and Educational Topics in Microscopy." In *Number 3 of the Microscopy Book Series*, eds. A. Méndez-Vilas, and J. Díaz, 634–42.

[8] Retcofsky, H.L., and R.A. Friedel. 1973. "Carbon-13 Magnetic Resonance in Diamonds, Coals, and Graphite." *The Journal of Physical Chemistry* 77, no. 1, pp. 68–71. doi: http://dx.doi.org/10.1021/j100620a015

[9] Li, W., and Y. Zhu. 2014. "Structural Characteristics of Coal Vitrinite During Pyrolysis." *Energy & Fuels* 28, no. 6, pp. 3645–54. doi: http://dx.doi.org/10.1021/ef500300r

[10] Li, Y., X. Cao, D. Zhu, M.A. Chappell, L.F. Miller, and J. Mao. 2012. "Characterization of Coals and Their Laboratory-Prepared Black Carbon Using Advanced Solid-State 13C Nuclear Magnetic Resonance Spectroscopy." *Fuel Processing Technology* 96, pp. 56–64. doi: http://dx.doi.org/10.1016/j.fuproc.2011.12.014

[11] Rawal, A., C.H. Chia, S.D. Joseph, R. Linser, J.M. Hook, and P. Munroe. 2014. "Microstructural Characterization of White Charcoal." *Journal of Analytical and Applied Pyrolysis* 109, pp. 215–21. doi: http://dx.doi.org/10.1016/j.jaap.2014.06.009

[12] Cao, H.S., H.J. Holland, C.H. Vermeer, S. Vanapalli, P.P.P.M. Lerou, M. Blom, and H.J.M.T Brake. 2013. "Characterization of a Two-Stage 30 K Joule–Thomson Microcooler." *Journal of Micromechanics and Microengineering* 23, no. 6, p. 065022. doi: http://dx.doi.org/10.1088/0960-1317/23/6/065022

[13] Lerf, A., H. He, M. Forster, and J. Klinowski. 1998. "Structure of Graphite Oxide Revisited." *Journal of Physical Chemistry B* 102, no. 23, pp. 4477–82. doi: http://dx.doi.org/10.1021/jp9731821

[14] Cai, W., R.D. Piner, F.J. Stadermann, S. Park, M.A. Shaibat, Y. Ishii, D. Yang, A. Velamakanni, S.J. An, M. Stoller, J. An, D. Chen, and R.S. Ruoff. 2008. "Synthesis and Solid-State NMR Structural Characterization of 13C-Labeled Graphite Oxide." *Science* 321, no. 5897, pp. 1815–17. doi: http://dx.doi.org/10.1126/science.1162369

[15] Gao, W., L.B. Alemany, L. Ci, and P.M. Ajayan. 2009. "New Insights into the Structure and Reduction of Graphite Oxide." *Nature Chemistry* 1, no. 5, pp. 403–08. doi: http://dx.doi.org/10.1038/nchem.281

[16] Si, Y., and E.T. Samulski. 2008. "Synthesis of Water Soluble Graphene." *Nano Letters* 8, no. 6, pp. 1679–82. doi: http://dx.doi.org/10.1021/nl080604h

[17] McNamara, K.M., and K.K. Gleason. 1992. "Selectively 13C-Enriched Diamond Films Studied by Nuclear Magnetic Resonance." *Journal of Applied Physics* 71, no. 6, p. 2884. doi: http://dx.doi.org/10.1063/1.351392

[18] Alam, T.M. 2004. "Solid-State Magic Angle Spinning NMR Spectroscopy Characterization of Particle Size Structural Variations in Synthetic Nanodiamonds." *Materials Chemistry and Physics* 85, no. 2–3, pp. 310–15. doi: http://dx.doi.org/10.1016/j.matchemphys.2004.01.029

[19] Giraudet, J., M. Dubois, K. Guérin, E. Petit, N. Batisse, A. Hamwi, N. Komatsu, P. Pirotte, and F. Masin. 2009. "Solid-State NMR Study of Nanodiamonds Produced by the Detonation Technique." *The Journal of Physical Chemistry C* 113, no. 24, pp. 10371–78. doi: http://dx.doi.org/10.1021/jp901274f

[20] Fang, X., J. Mao, E.M. Levin, and K. Schmidt-Rohr. 2009. "Nonaromatic Core−Shell Structure of Nanodiamond from Solid-State NMR Spectroscopy." *The Journal of the American Chemical Society* 131, no. 4, pp. 1426–35. doi: http://dx.doi.org/10.1021/ja8054063

[21] Cui, J.-F., X.-W. Fang, and K. Schmidt-Rohr. 2014. "Quantification of C=C and C=O Surface Carbons in Detonation Nanodiamond by NMR." *Journal of Physical Chemistry C*, 118, no. 18, pp. 9621–27. doi: http://dx.doi.org/10.1021/jp503053r

[22] Imai, H., P.K. Babu, E. Oldfield, A. Wieckowski, D. Kasuya, T. Azami, Y. Shimakawa, M. Yudasaka, Y. Kubo, and S. Iijima. 2006. "C-13 NMR Spectroscopy of Carbon Nanohorns." *Physical Review B*, 73, no. 12, p. 125405. doi: http://dx.doi.org/10.1103/physrevb.73.125405

[23] Peng, H.Q., L.B. Alemany, J.L. Margrave, and V.N. Khabashesku. 2003. "Sidewall Carboxylic Acid Functionalization of Single-Walled Carbon Nanotubes." *Journal of the American Chemical Society* 125, no. 49, pp. 15174–82. doi: http://dx.doi.org/10.1021/ja037746s

[24] Abou-Hamad, E., Y. Kim, M. Bouhrara, Y. Saih, T. Wågberg, D.E Luzzi, and C. Goze-Bac. 2012. "NMR Strategies to Study the Local Magnetic Properties of Carbon Nanotubes." *Physica B: Condensed Matter* 407, no. 4, pp. 740–42. doi: http://dx.doi.org/10.1016/j.physb.2011.12.012

[25] Jäger, C., J. Gottwald, H.W. Spiess, and R.J. Newport. 1994. "Structural Properties of Amorphous Hydrogenated Carbon. III. NMR Investigations." *Physical Review B* 50, no. 2, pp. 846–52. doi: http://dx.doi.org/10.1103/physrevb.50.846

[26] Uebersfeld, J., A. Etienne, and J. Combrisson. 1954. "Paramagnetic Resonance, a New Property of Coal-Like Materials." *Nature* 174, no. 4430, p. 614. doi: http://dx.doi.org/10.1038/174614a0

[27] Tapley, J.G., D.J.E. Ingram, R. Jackson, R.L. Bond, and A.R. Murnaghan. 1954. "Paramagnetic Resonance in Carbonaceous Solids." *Nature* 174, no. 4434, pp. 797–98. doi: http://dx.doi.org/10.1038/174797a0

[28] Retcofsky, H.L., J.M. Stark, and R.A. Friedel. 1968. "Electron Spin Resonance in American Coals." *Analytical Chemistry*, 40, no. 11, pp. 1699–1704. doi: http://dx.doi.org/10.1021/ac60267a011

[29] Grandy, D.W., and L. Petrakis. 1978. "Electron-Spin Resonance Spectrometric Study of Free-Radicals in Coals." *Analytical Chemistry* 50, no. 2, pp. 303–08. doi: http://dx.doi.org/10.1021/ac50024a034

[30] Green, U., K. Keinan-Adamsky, S. Attia, Z. Aizenshtat, G. Goobes, S. Ruthstein, and H. Cohen. 2014. "Elucidating the Role of Stable Carbon Radicals in the Low Temperature Oxidation of Coals by Coupled EPR–NMR Spectroscopy—A Method to Characterize Surfaces of Porous Carbon Materials." *Physical Chemistry Chemical Physics* 16, no. 20, p. 9364. doi: http://dx.doi.org/10.1039/c4cp00791c

[31] Liu, J., X. Jiang, J. Shen, and H. Zhang. 2014. "Chemical Properties of Superfine Pulverized Coal Particles. Part 1. Electron Paramagnetic Resonance Analysis of Free Radical Characteristics." *Advanced Powder Technology* 25, no. 3, pp. 916–25. doi: http://dx.doi.org/10.1016/j.apt.2014.01.021

[32] Wagoner, G. 1960. "Spin Resonance of Charge Carriers in Graphite." *Physical Review* 118, no. 3, pp. 647–53. doi: http://dx.doi.org/10.1103/physrev.118.647

[33] Kazumata, Y. 1983. "ESR of Pyrolytic Graphite Irradiated by Neutrons at Low Temperature." *Journal of Physics and Chemistry of Solids* 44, no. 11, pp. 1025–31. doi: http://dx.doi.org/10.1016/0022-3697(83)90084-7

[34] Rao, S.S., A. Stesmans, Y. Wang, and Y. Chen. 2012. "Direct ESR Evidence for Magnetic Behavior of Graphite Oxide." *Physica E-Low-Dimensional Systems & Nanostructures* 44, no. 6, pp. 1036–39. doi: http://dx.doi.org/10.1016/j.physe.2011.07.019

[35] Kempiński, W., A.I. Shames, A.M. Panich, A.E. Alexenskii, M.V. Baidakova, A.T. Dideikin, V.Y. Osipov, V.I. Siklitski, E. Osawa, M. Ozawa, and A.Y. Vul. 2002. "Defects and Impurities in Nanodiamonds: EPR, NMR and TEM Study." *Journal of Physics and Chemistry of Solids* 63, no. 11, pp. 1993–2001. doi: http://dx.doi.org/10.1016/s0022-3697(02)00185-3

[36] Yavkin, B.V., V.A. Soltamov, R.A. Babunts, A.N. Anisimov, P.G. Baranov, F.M. Shakhov, S.V. Kidalov, A.Y. Vul, G.V. Mamin, and S.B. Orlinskii. 2014. "Defects in Nanodiamonds: Application of High-Frequency cw and Pulse EPR, ODMR." *Applied Magnetic Resonance* 45, no. 10, pp. 1035–49. doi: http://dx.doi.org/10.1007/s00723-014-0582-y

[37] Garaj, S., L. Thien-Nga, R. Gaal, L. Forró, K. Takahashi, F. Kokai, M. Yudasaka, and S. Iijima. 2000. "Electronic Properties of Carbon Nanohorns Studied by ESR." *Physical Review B* 62, no. 24, pp. 17115–19. doi: http://dx.doi.org/10.1103/physrevb.62.17115

[38] Bandow, S., F. Kokai, K. Takahashi, M. Yudasaka, and S. Iijima. 2001. "Unique Magnetism Observed in Single-Wall Carbon Nanohorns." *Applied Physics A-Materials Science & Processing* 73, no. 3, pp. 281–85. doi: http://dx.doi.org/10.1007/s003390100794

[39] Murphy, R., J.N. Coleman, M. Cadek, B. McCarthy, M. Bent, A. Drury, R.C. Barklie, and W.J. Blau. 2002. "High-Yield, Nondestructive Purification and Quantification Method for Multiwalled Carbon Nanotubes." *Journal of Physical Chemistry B* 106, no. 12, pp. 3087–91. doi: http://dx.doi.org/10.1021/jp0132836

[40] Corzilius, B., K.-P. Dinse, and K. Hata. 2007. "Single-Wall Carbon Nanotubes and Peapods Investigated by EPR." *Physical Chemistry Chemical Physics* 9, no. 46, p. 6063. doi: http://dx.doi.org/10.1039/b707936m

[41] Kim, D., K.W. Lee, E.H. Choi, and C.E. Lee. 2014. "Electron Spin Resonance Study of the La0.8Sr0.2MnO3 Nanoparticle-Decorated Carbon Nanotubes." *Materials Research Bulletin* 59, pp. 142–144. doi: http://dx.doi.org/10.1016/j.materresbull.2014.06.030

[42] Abragam, A., A. Landesman, and J.M. Winter 1958. "Effet Overhauser Dans Les Charbons Et Graphites." *Comptes Rendus Hebdomadaires Des Seances De l Academie Des Sciences* 247, no. 21, pp. 1852–1853. doi: http://www.sudoc.fr/134958438

[43] Friedel, R.A., and H.L. Retcofsky. 1971. "Confirmation of the High Aromaticity of Anthracite by Broadline Carbon-13 Magnetic Resonance Spectrometry." *Analytical Chemistry* 43, no. 3, pp. 485–487. doi: http://dx.doi.org/10.1021/ac60298a044

[44] Andrew, E.R., A. Bradbury, and R.G. Eades. 1958. "Nuclear Magnetic Resonance Spectra from a Crystal Rotated at High Speed." *Nature* 182, no. 4650, p. 1659. doi: http://dx.doi.org/10.1038/1821659a0

[45] Andrew, E.R., A. Bradbury, and R.G. Eades. 1959. "Removal of Dipolar Broadening of Nuclear Magnetic Resonance Spectra of Solids by Specimen Rotation." *Nature* 183, no. 4678, pp. 1802–03. doi: http://dx.doi.org/10.1038/1831802a0

[46] Pines, A., M.G. Gibby, and J.S. Waugh. 1973. "Proton-enhanced NMR of Dilute Spins in Solids." *The Journal of Chemical Physics* 59, no. 2, p. 569. doi: http://dx.doi.org/10.1063/1.1680061

[47] Stejskal, E.O., and J. Schaefer. 1976. "Carbon-13 Nuclear Magnetic Resonance of Polymers Spinning at the Magic Angle." *Journal of the American Chemical Society* 98, no. 4, pp. 1031–32. doi: http://dx.doi.org/10.1021/ja00420a036

[48] Stejskal, E.O., J.S. Waugh, and J. Schaefer. 1977. "Magic-Angle Spinning and Polarization Transfer in Proton-Enhanced NMR." *Journal of Magnetic Resonance (1969)* 28, no. 1, pp. 105–12. doi: http://dx.doi.org/10.1016/0022-2364(77)90260-8

[49] Opella, S.J., and M.H. Frey. 1979. "Selection of Nonprotonated Carbon Resonances in Solid-State Nuclear Magnetic Resonance." *Journal of the American Chemical Society* 101, no. 19, pp. 5854–56. doi: http://dx.doi.org/10.1021/ja00513a079

[50] Grant, D.M., L.B. Alemany, T.D. Alger, and R.J. Pugmire. 1983. "Cross Polarization and Magic Angle Sample Spinning NMR Spectra of Model Organic Compounds. 3. Effect of the Carbon-13-Proton Dipolar Interaction on Cross Polarization and Carbon-Proton Dephasing". *Journal of the American Chemical Society* 105, no. 22, pp. 6697–704. doi: http://dx.doi.org/10.1021/ja00360a025

[51] Maudsley, A.A., L. Moller, and R.R. Ernst. 1977. "Cross-Correlation of Spin-Decoupled NMR Spectra by Heteronuclear Two-Dimensional Spectroscopy." *Journal of Magnetic Resonance (1969)* 28, no. 3, pp. 463–69. doi: http://dx.doi.org/10.1016/0022-2364(77)90288-8

[52] Clauss, J., K. Schmidt-Rohr, and H.W. Spiess. 1992. "Correlation of Structure, Mobility, and Morphological Information in Heterogeneous Polymer materials by Two-Dimensional Wideline-Separation NMR Spectroscopy." *Macromolecules* 25, no. 12, pp. 3273–77. doi: http://dx.doi.org/10.1021/ma00038a037

[53] Mao, J.-D., and K. Schmidt-Rohr. 2004. "Separation of Aromatic-Carbon 13C NMR Signals from di-Oxygenated Alkyl Bands by a Chemical-Shift-Anisotropy Filter." *Solid State Nuclear Magnetic Resonance* 26, no. 1, pp. 36–45. doi: http://dx.doi.org/10.1016/j.ssnmr.2003.09.003

[54] Mao, J.-D., and K. Schmidt-Rohr. 2003. "Recoupled long-Range C–H Dipolar Dephasing in Solid-State NMR, and Its Use for Spectral Selection of Fused Aromatic Rings." *Journal of Magnetic Resonance* 162, no. 1, pp. 217–27. doi: http://dx.doi.org/10.1016/s1090-7807(03)00012-0

[55] Pignatello, J.J., X. Cao, Y. Li, C. Lattao, M.A. Chappell, N. Chen, L.F. Miller, and J. Mao. 2012. "Characterization of Wood Chars Produced at Different Temperatures Using Advanced Solid-State 13C NMR Spectroscopic Techniques." *Energy & Fuels* 26, no. 9, pp. 5983–91. doi: http://dx.doi.org/10.1021/ef300947s

[56] Chu, P.K., and L. Li. 2006. "Characterization of Amorphous and Nanocrystalline Carbon Films." *Materials Chemistry and Physics* 96, no. 2–3, pp. 253–77. doi: http://dx.doi.org/10.1016/j.matchemphys.2005.07.048

[57] Jarman, R.H., G.J. Ray, R.W. Standley, and G.W. Zajac. 1986. "Determination of Bonding in Amorphous Carbon Films: A Quantitative Comparison of Core-Electron Energy-Loss Spectroscopy and 13C Nuclear Magnetic Resonance Spectroscopy." *Applied Physics Letters* 49, no. 17, p. 1065. doi: http://dx.doi.org/10.1063/1.97476

[58] Ham, M. 1990. "Diamond-Like Carbon Films Grown by a Large-Scale Direct Current Plasma Chemical Vapor Deposition Reactor: System Design, Film characteristics, and Applications." *Journal of Vacuum Science & Technology A, Vacuum, Surfaces, and Films* 8, no. 3, p. 2143. doi: http://dx.doi.org/10.1116/1.577030

[59] Donnet, C., J. Fontaine, F. Lefèbvre, A. Grill, V. Patel, and C. Jahnes. 1999. "Solid State [sup 13] C and [sup 1] H Nuclear Magnetic Resonance Investigations of Hydrogenated Amorphous Carbon." *Journal of Applied Physics* 85, no. 6, p. 3264. doi: http://dx.doi.org/10.1063/1.369669

[60] Grill, A., B.S. Meyerson, V.V. Patel, J.A. Reimer, and M.A. Petrich. 1987. "Inhomogeneous Carbon Bonding in Hydrogenated Amorphous Carbon Films." *Journal of Applied Physics* 61, no. 8, p. 2874. doi: http://dx.doi.org/10.1063/1.337883

[61] Pan, H., M. Pruski, B.C. Gerstein, F. Li, and J.S. Lannin. 1991. "Local Coordination of Carbon Atoms in Amorphous Carbon." *Physical Review B* 44, no. 13, pp. 6741–45. doi: http://dx.doi.org/10.1103/physrevb.44.6741

[62] Kaplan, S., F. Jansen, and M. Machonkin. 1985. "Characterization of Amorphous Carbon-Hydrogen Films by Solid-State Nuclear Magnetic Resonance." *Applied Physics Letters* 47, no. 7, p. 750. doi: http://dx.doi.org/10.1063/1.96027

[63] Golzan, M.M., P.B. Lukins, D.R. McKenzie, A.M. Vassallo, and J.V. Hanna. 1995. "NMR Evidence for Strained Carbon Bonding in Tetrahedral Amorphous Carbon." *Chemical Physics* 193, no. 1–2, pp. 167–72. doi: http://dx.doi.org/10.1016/0301-0104(94)00421-6

[64] Sharma, S. 2013. *Microstructural Tuning of Glassy Carbon for Electrical and Electrochemical Sensor applications*. Irvine, CA: University of California.

[65] Grinolds, M.S., S. Hong, P. Maletinsky, L. Luan, M.D. Lukin, R.L. Walsworth, and A. Yacoby. 2013. "Nanoscale Magnetic Imaging of a Single Electron Spin Under Ambient Conditions." *Nature Physics* 9, no. 4, p. 215. doi: http://dx.doi.org/10.1038/nphys2543

[66] Frackowiak, E. 2007. "Carbon Materials for Supercapacitor Application." *Physical Chemistry Chemical Physics* 9, no. 15, p. 1774. doi: http://dx.doi.org/10.1039/b618139m

[67] Tarascon, J.-M., and M. Armand. 2001. "Issues and Challenges Facing Rechargeable Lithium Batteries." *Nature* 414, no. 6861, pp. 359–67. doi: http://dx.doi.org/10.1038/35104644

[68] Simon, P., and Y. Gogotsi. 2008. "Materials for Electrochemical Capacitors." *Natural Materials* 7, no. 11, pp. 845–54. doi: http://dx.doi.org/10.1038/nmat2297

[69] Portet, C., J. Chmiola, Y. Gogotsi, S. Park, and K. Lian. 2008. "Electrochemical Characterizations of Carbon Nanomaterials by the Cavity Microelectrode Technique." *Electrochimica Acta* 53, no. 26, pp. 7675–80. doi: http://dx.doi.org/10.1016/j.electacta.2008.05.019

[70] Yang, C.-M., Y.J. Kim, M. Endo, H. Kanoh, M. Yudasaka, S. Iijima, and K. Kaneko. 2007. "Nanowindow-Regulated Specific Capacitance of Supercapacitor Electrodes of Single-Wall Carbon Nanohorns." *Journal of the American Chemical Society* 129, no. 1, pp. 20–21. doi: http://dx.doi.org/10.1021/ja065501k

[71] Kyotani, T.C.J., and Y. Gogotsi. 2009. "Chapter. 13." In *Carbon Materials for Electrochemical Energy Storage Systems*, eds. F. Beguin, and E. Frackowiak. CRC/Taylor and Francis.

[72] Futaba, D.N., K. Hata, T. Yamada, T. Hiraoka, Y. Hayamizu, Y. Kakudate, O. Tanaike, H. Hatori, M. Yumura, and S. Iijima. 2006. "Shape-Engineerable and Highly Densely Packed Single-Walled Carbon Nanotubes and Their Application as Super-Capacitor Electrodes." *Natural Materials* 5, no. 12, pp. 987–94. doi: http://dx.doi.org/10.1038/nmat1782

[73] Chmiola, J., G. Yushin, Y. Gogotsi, C. Portet, P. Simon, and P.L. Taberna. 2006. "Anomalous Increase in Carbon Capacitance at Pore Sizes Less Than 1 Nanometer." *Science* 313, no. 5794, pp. 1760–63. doi: http://dx.doi.org/10.1126/science.1132195

[74] Sharma, K., H.Z. Bilheux, L.M.H. Walker, S. Voisin, R.T. Mayes, J.O. Kiggans, Jr., S. Yiacoumi, D.W. DePaoli, S. Dai, and C. Tsouris. 2013. "Neutron Imaging of Ion Transport in Mesoporous Carbon Materials." *Physical Chemistry Chemical Physics*15, no. 28, pp. 11740–747. doi: http://dx.doi.org/10.1039/c3cp51310f

[75] Levi, M.D., G. Salitra, N. Levy, D. Aurbach, and J. Maier. 2009. "Application of a Quartz-Crystal Microbalance to Measure Ionic Fluxes in Microporous Carbons for Energy Storage." *Natural Materials* 8, no. 11, pp. 872–75. doi: http://dx.doi.org/10.1038/nmat2559

[76] Richey, F.W., B. Dyatkin, Y. Gogotsi, and Y.A. Elabd. 2013. "Ion Dynamics in Porous Carbon Electrodes in Supercapacitors Using in Situ Infrared Spectroelectrochemistry." *Journal of the American Chemical Society* 135, no. 34, pp. 12818–826. doi: http://dx.doi.org/10.1021/ja406120e

[77] Kondrat, S., and A. Kornyshev. 2011. "Superionic State in Double-Layer Capacitors with Nanoporous Electrodes." *Journal of Physics: Condensed Matter* 23, no. 2, p. 022201. doi: http://dx.doi.org/10.1088/0953-8984/23/2/022201

[78] Kondrat, S., and A. Kornyshev. 2013. "Charging Dynamics and Optimization of Nanoporous Supercapacitors." *The Journal of Physical Chemistry C* 117, no. 24, pp. 12399–406. doi: http://dx.doi.org/10.1021/jp400558y

[79] Feng, G., and P.T. Cummings. 2011. "Supercapacitor Capacitance Exhibits Oscillatory Behavior as a Function of Nanopore Size." *The Journal of Physical Chemistry Letters* 2, no. 22, pp. 2859–64. doi: http://dx.doi.org/10.1021/jz201312e

[80] Feng, G., R. Qiao, J. Huang, B.G. Sumpter, and V. Meunier. 2010. "Ion Distribution in Electrified Micropores and Its Role in the Anomalous Enhancement of Capacitance." *ACS Nano* 4, no. 4, pp. 2382–90. doi: http://dx.doi.org/10.1021/nn100126w

[81] Merlet, C., B. Rotenberg, P.A. Madden, and M. Salanne. 2013. "Computer Simulations of Ionic Liquids at Electrochemical Interfaces." *Physical Chemistry Chemical Physics* 15, no. 38, pp. 15781–792. doi: http://dx.doi.org/10.1039/c3cp52088a

[82] Azaïs, P., L. Duclaux, P. Florian, D. Massiot, M.A. Lillo-Rodenas, A. Linares-Solano, J.P. Peres, C. Jehoulet, and F. Béguin.2007. "Causes of Supercapacitors Ageing in Organic Electrolyte." *Journal of Power Sources* 171, no. 2, pp. 1046–053. doi: http://dx.doi.org/10.1016/j.jpowsour.2007.07.001

[83] Deschamps, M., E. Gilbert, P. Azais, E. Raymundo-Piñero, M.R. Ammar, P. Simon, D. Massiot, and F. Béguin. 2013. "Exploring Electrolyte Organization in Supercapacitor Electrodes with Solid-State NMR." *Nature Materials* 12, no. 4, pp. 351–58. doi: http://dx.doi.org/10.1038/nmat3567

[84] Lee, S.-I., K. Saito, K. Kanehashi, M. Hatakeyama, S. Mitani, S.-H. Yoon, Y. Korai, and I. Mochida. 2006. "11B {NMR} Study of the Anion in Activated Carbons at Various Stages of Charge of {EDLCs} in Organic Electrolyte." *Carbon* 44, no. 12, pp. 2578–586. doi: http://dx.doi.org/10.1016/j.carbon.2006.06.001

[85] Hun Min, K., Y. Takimoto, K. Yamada, T. Simoyama, K. Yamamoto, S. Yonemori, and K. Hiratsuka. 2001. *State Analysis of Electrolyte in Carbon Electrode for Electric Double Layer Capacitor Studied by ^{19}F NMR Spectroscopy*.

[86] Wang, H., T.K-J. Köster, N.M. Trease, J. Segalini, P.L. Taberna, P. Simon, Y. Gogotsi, and C.P. Grey. 2011. "Real-Time NMR Studies of Electrochemical Double-Layer Capacitors." *Journal of the American Chemical Society* 133, no. 48, pp. 19270–273. doi: http://dx.doi.org/10.1021/ja2072115

[87] Wang, H., A.C. Forse, J.M. Griffin, N.M. Trease, L. Trognko, P.L. Taberna, P. Simon, and C.P. Grey. 2013. "In Situ NMR Spectroscopy of Supercapacitors: Insight into the Charge Storage Mechanism." *Journal of the American Chemical Society* 135, no. 50, pp. 18968–980. doi: http://dx.doi.org/10.1021/ja410287s

[88] Ilott, A.J., N.M. Trease, C.P. Grey, and A. Jerschow.2014. "Multinuclear in Situ Magnetic Resonance Imaging of Electrochemical Double-Layer Capacitors." *Nature communications* 5. doi: http://dx.doi.org/10.1038/ncomms5536

[89] Scrosati, B.1992. "Lithium Rocking Chair Batteries: An Old Concept?" *Journal of the Electrochemical Society* 139, no. 10, pp. 2776–781. doi: http://dx.doi.org/10.1149/1.2068978

[90] Shu, Z.X., R.S. McMillan, and J.J. Murray.1993. "Electrochemical Intercalation of Lithium into Graphite." *Journal of the Electrochemical Society* 140, no. 4, pp. 922–27. doi: http://dx.doi.org/10.1149/1.2056228

[91] Kim, Y.-O., and S.-M. Park. 2001. "Intercalation Mechanism of Lithium Ions into Graphite Layers Studied by Nuclear Magnetic Resonance and Impedance Experiments." *Journal of the Electrochemical Society* 148, no. 3, pp. A194–A199. doi: http://dx.doi.org/10.1149/1.1345870.

[92] Lowell, C.E. 1967. "Solid Solution of Boron in Graphite." *Journal of the American Ceramic Society* 50, no. 3, pp. 142–44. doi: http://dx.doi.org/10.1111/j.1151-2916.1967.tb15064.x

[93] Lee, Y., D.Y. Han, D. Lee, A.J. Woo, S.H. Lee, D. Lee, and Y.K. Kim. 2002. "11B NMR of Boron-Doped Graphite as the Negative Electrode of a Lithium Secondary Battery." *Carbon* 40, no. 3, pp. 403–08. doi: http://dx.doi.org/10.1016/s0008-6223(01)00120-8

[94] Enoki, T, M. Suzuki., and M. Endo.2003. "Chapters 3 and 9." In *Graphite Intercalation Compounds and Applications*. Oxford: Oxford.

[95] Gotoh, K., T. Ishikawa, S. Shimadzu, N. Yabuuchi, S. Komaba, K. Takeda, A. Goto, K. Deguchi, S. Ohki, K. Hashi, T. Shimizu, and H. Ishida.2013. "NMR Study for Electrochemically Inserted Na in Hard Carbon Electrode of Sodium Ion Battery." *Journal of Power Sources* 225, pp. 137–140. doi: http://dx.doi.org/10.1016/j.jpowsour.2012.10.025

[96] Gerald II, R.E., J. Sanchez, C.S. Johnson, R.J. Klingler, and J.W. Rathke.2001. In Situ Nuclear Magnetic Resonance Investigations of Lithium Ions in Carbon Electrode Materials Using a Novel Detector. *Journal of Physics: Condensed Matter* 13, no. 36, p. 8269. doi: http://dx.doi.org/10.1088/0953-8984/13/36/304

[97] Narkowicz, R., D. Suter, and R. Stonies. 2005. "Planar Microresonators for EPR Experiments." *Journal of Magnetic Resonance* (1969–1992) 175, no. 2, p. 10–10. doi: http://dx.doi.org/10.1016/j.jmr.2005.04.014

[98] Pendry, J.B., A.J. Holden, D.J. Robbins, and W.J. Stewart. 1999. "Magnetism from Conductors and Enhanced Nonlinear Phenomena." In *IEEE Transactions on Microwave Theory Techniques* 47,no. 11, pp. 2075–084. doi: http://dx.doi.org/10.1109/22.798002

[99] Torrezan, A.C., T.P.M. Alegre, and G. Medeiros-Ribeiro.2009. Microstrip Resonators for Electron Paramagnetic Resonance Experiments. In *Review of Scientific Instruments* 80, no. 7, pp. 075111–075111. doi: http://dx.doi.org/10.1063/1.3186054

[100] Twig, Y., E. Dikarov, and A. Blank. 2013. "Ultra Miniature Resonators for Electron Spin Resonance: Sensitivity Analysis, Design and Construction Methods, and Potential Applications." *Molecular Physics* 111, no. 18–19, pp. 2674–682. http://dx.doi.org/10.1080/00268976.2012.762463

[101] Hoult, D.I., and R. Richards.1976. "The Signal-to-noise Ratio of the Nuclear Magnetic Resonance Experiment." *Journal of Magnetic Resonance* (1969–1992) 24, no. 1,pp. 71–85. doi: http://dx.doi.org/10.1016/0022-2364(76)90233-x.

[102] Massin, C., G. Boero, F. Vincent, J. Abenhaim, P.-A. Besse, R.S. Popovic. 2002. "High-Q Factor RF Planar Microcoils for Micro-Scale NMR Spectroscopy." *Journal of Magnetic Resonance* 97–98, pp. 280–88. doi: http://dx.doi.org/10.1016/s0924-4247(01)00847-0

[103] Eroglu, S., B. Gimi, B. Roman, G. Friedman, and R.L. Magin. 2003. "NMR Spiral Surface Microcoils: Design, Fabrication, and Imaging." *Concepts in Magnetic Resonance Part B: Magnetic Resonance Engineering* 17, no. 1, pp. 1–10. doi: http://dx.doi.org/10.1002/cmr.b.10068

[104] van Bentum, P.J.M., J.W.G. Janssen, A.P.M. Kentgens, J. Bart, and J.G.E. Gardeniers. 2007. "Stripline Probes for Nuclear Magnetic Resonance." *Journal of Magnetic Resonance (1969–1992)* 189, no. 1, pp. 104–13. doi: http://dx.doi.org/10.1016/j.jmr.2007.08.019

[105] Maguire, Y., I.L. Chuang, S. Zhang, and N. Gershenfeld. 2007. "Ultra-Small-Sample Molecular Structure Detection Using Microslot Waveguide Nuclear Spin Resonance." In *Proceedings of the National Academy of Sciences* 104, no. 22, pp. 9198–203. doi: http://dx.doi.org/10.1073/pnas.0703001104

[106] Spengler, N., A. Moazenzadeh, R.C. Meier, V. Badilita, J.G. Korvink, and U. Wallrabe. 2014. "Micro-Fabricated Helmholtz Coil Featuring Disposable Microfluidic Sample Inserts for Applications in Nuclear Magnetic Resonance." *Journal of Micromechanics and Microengineering* 24, no. 3, p. 034004. doi: http://dx.doi.org/10.1088/0960-1317/24/3/034004

[107] Sidabras, J.W., R.R. Mett, W. Froncisz, T.G. Camenisch, J.R. Anderson, and J.S. Hyde. 2007. "Multipurpose EPR Loop-Gap Resonator and Cylindrical TE011 Cavity for Aqueous Samples at 94GHz." *The Review of Scientific Instruments* 78, no. 3, p. 034701. doi: http://dx.doi.org/10.1063/1.2709746

[108] Klein, K., B. Hauer, B. Stoib, M. Trautwein, S. Matich, H. Huebl, O. Astakhov, F. Finger, R. Bittl, M. Stutzmann, and M.S. Brandt. 2013. "The Electrically Detected Magnetic Resonance Microscope: Combining Conductive Atomic Force Microscopy with Electrically Detected Magnetic Resonance." *Review of Scientific Instruments* 84, no. 10, p. 103911. doi: http://dx.doi.org/10.1063/1.4827036

[109] Wood, R.L., W. Froncisz, and J.S. Hyde. 1984. "The Loop-Gap Resonator. II. Controlled Return Flux Three-Loop, Two-Gap Microwave Resonators for ENDOR and ESR spectroscopy." *Journal of Magnetic Resonance (1969-1992)* 58, no. 2, pp. 243–53. doi: http://dx.doi.org/10.1016/0022-2364(84)90214-2

[110] Annino, G., M. Cassettari, I. Longo, and M. Martinelli. 1999. "Dielectric Resonators in ESR: Overview, Comments and Perspectives." *Applied Magnetic Resonance* 16, no. 1, pp. 45–62. doi: http://dx.doi.org/10.1007/bf03161914

[111] Webb, A.G. 2011. "Dielectric Materials in Magnetic Resonance." *Concepts in Magnetic Resonance Part A* 38A, no. 4, pp. 148–84. doi: http://dx.doi.org/10.1002/cmr.a.20219

[112] Mailadil, S.T. 2010. *Dielectric Materials for Wireless Communication,* 688. Elsevier.

[113] Qin, F., and C. Brosseau. 2012. "A Review and Analysis of Microwave Absorption in Polymer Composites Filled with Carbonaceous Particles." *Journal of Applied Physics* 111, no. 6, p. 62012. doi: http://dx.doi.org/10.1063/1.3688435

[114] Bychanok, D., P. Kuzhir, S. Maksimenko, S. Bellucci, and C. Brosseau. 2013. "Characterizing Epoxy Composites Filled with Carbonaceous Nanoparticles from DC to Microwave." *Journal of Applied Physics* 113, no. 12, p. 124103. doi: http://dx.doi.org/10.1063/1.4798296

[115] Kuzhir, P.P., A.G. Paddubskaya, S.A. Maksimenko, A. Celzard, V. Fierro, G. Amaral-Labat, A. Pizzi, J. Macutkevic, G. Valusis, M. Ivanov, J. Banys, and S. Bellucci. 2012. "Highly Porous Conducting Carbon Foams for Electromagnetic Applications." In *International Symposium on Electromagnetic Compatibility*—EMC EUROPE, p. 1–4. doi: http://dx.doi.org/10.1109/emceurope.2012.6396811

[116] Katsounaros, A., M.T. Cole, H.M. Tuncer, W.I. Milne, and Y. Hao. 2013. "Near-Field Characterization of Chemical Vapor Deposition Graphene in the Microwave Regime." *Applied Physics Letters* 102, no. 23, p. 233104. doi: http://dx.doi.org/10.1063/1.4810759

[117] Decrossas, E., M.A.E. Sabbagh, V.F. Hanna, and S.M. El-Ghazaly. 2012. "Rigorous Characterization of Carbon Nanotube Complex Permittivity Over a Broadband of RF Frequencies." *IEEE Transactions on Electromagnetic Compatibility* 54, no. 1, pp. 81–87. doi: http://dx.doi.org/10.1109/temc.2011.2174788

[118] Heinola, J.-M., K.P. Lätti, J.P. Ström, M. Kettunen, and P. Silventoinen. 2004. "A Strip Line Ring Resonator Method for Determination of Dielectric Properties of Printed Circuit Board Material in Function of Frequency." In *IEEE 2004 Annual Report Conference on Electrical Insulation and Dielectric Phenomena. CEIDP'04* IEEE pp. 692–695. doi: http://dx.doi.org/10.1109/ceidp.2004.1364344

[119] Suzuki, H. 2006. "Microwave Measurement of Complex Permittivity by Placing a Microstripline Resonator on the Material Under Test." In *Microwave Conference, 36th European,* IEEE pp. 395–98. doi: http://dx.doi.org/10.1109/eumc.2006.281357

[120] Park, B.Y., L. Taherabadi, C. Wang, J. Zoval, and M.J. Madou. 2005. "Electrical Properties and Shrinkage of Carbonized Photoresist Films and the Implications for Carbon Microelectromechanical Systems Devices in Conductive Media." *Journal of the Electrochemical Society* 152, no. 12, p. J136. doi: http://dx.doi.org/10.1149/1.2116707

[121] Singh, A., J. Jayaram, M. Madou, and S. Akbar. 2002. "Pyrolysis of Negative Photoresists to Fabricate Carbon Structures for Microelectromechanical Systems and Electrochemical Applications." *Journal of the Electrochemical Society* 149, no. 3, p. E78. doi: http://dx.doi.org/10.1149/1.1436085

[122] Rashidian, A., D.M. Klymyshyn, M.T. Aligodarz, M. Boerner, and J. Mohr. 2012. "Microwave Performance of Photoresist-Alumina Microcomposites for Batch Fabrication of Thick Polymer-Based Dielectric Structures." *Journal of Micromechanics and Microengineering* 22, no. 10, p. 105002. doi: http://dx.doi.org/10.1088/0960-1317/22/10/105002

[123] Reijerse, E., F. Lendzian, R. Isaacson, and W. Lubitz. 2012. "A Tunable General Purpose Q-Band Resonator for CW and Pulse EPR/ENDOR Experiments with Large Sample Access and Optical Excitation." *Journal of Magnetic Resonance* 214, pp. 237–43. doi: http://dx.doi.org/10.1016/j.jmr.2011.11.011

[124] Liu, L., L.B. Kong, S. Matitsine, W.Y. Yin, and Y. Chen. 2010. *Microwave Dielectric Properties of Carbon Nanotube Composites*. InTech—Book Chapter.

[125] Heremans, J., C.H. Olk, and D.T. Morelli. 1994. "Magnetic Susceptibility of Carbon Structures." *Physical Review B* 49, no. 21, pp. 15122–25. doi: http://dx.doi.org/10.1103/physrevb.49.15122

[126] Jenkins, G.M. 1976. *Polymeric Carbons—Carbon Fibre, Glass and Char*, 178. Cambridge, New York: Cambridge University Press.

[127] Jia, F., R. Kumar, and J.G. Korvink. 2013. "Optimal Magnetic Susceptibility Matching in 3D." *Magnetic Resonance in Medicine* 69, no. 4, pp. 1146–156. doi: http://dx.doi.org/10.1002/mrm.24323

[128] Ryan, H., A. Smith, and M. Utz. 2014. "Structural Shimming for High-Resolution Nuclear Magnetic Resonance Spectroscopy in Lab-on-a-Chip Devices." *Lab on a Chip* 14, no. 10, pp. 1678–685. doi: http://dx.doi.org/10.1039/c3lc51431e

[129] Bowers, C.R., and D.P. Weitekamp. 1986. "Transformation of Symmetrization Order to Nuclear-Spin Magnetization by Chemical Reaction and Nuclear Magnetic Resonance." *Physical Review Letters* 57, no. 21, p. 2645. doi: http://dx.doi.org/10.1103/physrevlett.57.2645

[130] Natterer, J., and J. Bargon. 1997. "Parahydrogen Induced Polarization." *Progress in Nuclear Magnetic Resonance Spectroscopy* 31, 4, pp. 293–315. doi: http://dx.doi.org/10.1016/s0079-6565(97)00007-1

[131] Graafen, D.M. 2013. *Parahydrogen Induced Polarization on a Clinical MRI System: Polarization Transfer of Two Spin Order* [PhD dissertation]. Universitätsbibliothek Mainz.

[132] Nelson, S.J., J. Kurhanewicz, D.B. Vigneron, P.E.Z. Larson, A.L. Harzstark, M. Ferrone, M. van Criekinge, J.W. Chang, R. Bok, I. Park, G. Reed, L. Carvajal, E.J. Small, P. Munster, V.K. Weinberg, J.H. Ardenkjaer-Larsen, A.P. Chen, R.E. Hurd, L.-I. Odegardstuen, F.J. Robb, J. Tropp, and J.A. Murray. 2013. "Metabolic Imaging of Patients with Prostate Cancer Using Hyperpolarized [1-13C]Pyruvate." *Science Translational Medicine* 5, no. 198, pp. 198ra108–198ra108. doi: http://dx.doi.org/10.1126/scitranslmed.3006070

[133] Zeng, H., J. Xu, J. Gillen, M.T. McMahon, D. Artemov, J.M. Tyburn, J.A.B. Lohman, R.E. Mewis, K.D. Atkinson, G.G.R. Green, S.B. Duckett, and P.C.M. van Zijl. 2013. "Optimization of SABRE for Polarization of The Tuberculosis Drugs Pyrazinamide and Isoniazid." *Journal of Magnetic Resonance* (San Diego, CA: 1997) 237, pp. 73-8. doi: http://dx.doi.org/10.1016/j.jmr.2013.09.012

[134] Gabellieri, C., S. Reynolds, A. Lavie, G.S. Payne, M.O. Leach, and T.R. Eykyn. 2008. "Therapeutic Target Metabolism Observed Using Hyperpolarized 15N Choline." *Journal of the American Chemical Society* 130, no. 14, pp. 4598–99. doi: http://dx.doi.org/10.1021/ja8001293

[135] Bhattacharya, P., E.Y. Chekmenev, W.F. Reynolds, S. Wagner, N. Zacharias, H.R. Chan, R. Bünger, and B.D. Ross. 2011. "Parahydrogen-Induced Polarization (PHIP) Hyperpolarized Mr Receptor Imaging in Vivo: A Pilot Study of 13C Imaging of Atheroma in Mice." *NMR in Biomedicine* 24, no. 8, pp. 1023–28. doi: http://dx.doi.org/10.1002/nbm.1717

[136] Zacharias, N., H. Chan, N. Sailasuta, B.D. Ross, and P. Bhattacharya. 2011. "Real-Time Molecular Imaging of Tricarboxylic Acid Cycle Metabolism in Vivo by Hyperpolarized 1-13C Diethyl Succinate." *Journal of the American Chemical Society* 134, 2, pp. 934–43. doi: http://dx.doi.org/10.1021/ja2040865

[137] Sauer, G., D. Nasu, D. Tietze, T. Gutmann, S. Englert, O. Avrutina, H. Kolmar, and G. Buntkowsky. 2014. "Effective PHIP Labeling of Bioactive Peptides Boosts the Intensity of the NMR Signal." *Angewandte Chemie (International ed. in English)* 53, no. 47, pp. 12941–45. doi: http://dx.doi.org/10.1002/anie.201404668

[138] Telkki, V.-V., V.V. Zhivonitko, S. Ahola, K.V. Kovtunov, J. Jokisaari, and I.V. Koptyug. 2010. "Microfluidic Gas-Flow Imaging Utilizing Parahydrogen-Induced Polarization and Remote-Detection NMR." *Angewandte Chemie International Edition* 49, no. 45, pp. 8363–66. doi: http://dx.doi.org/10.1002/anie.201002685

[139] Zhivonitko, V.V., V.-V. Telkki, and I.V. Koptyug. 2012. "Characterization of Microfluidic Gas Reactors Using Remote-Detection MRI and Parahydrogen-Induced Polarization." *Angewandte Chemie (International ed. in English)* 51, no. 32, pp. 8054–8. doi: http://dx.doi.org/10.1002/anie.201202967

[140] Sharma, R., and L.-S. Bouchard. 2012. "Strongly Hyperpolarized Gas from Parahydrogen by Rational Design of Ligand-Capped Nanoparticles." *Scientific Reports* 2. doi: http://dx.doi.org/10.1038/srep00277

[141] Buntkowsky, G., B. Walaszek, A. Adamczyk, Y. Xu, H.-H. Limbach, and B. Chaudret. 2006. "Mechanism of Nuclear Spin Initiated Para-H2 to Ortho-H2 Conversion." *Physical Chemistry Chemical Physics* 8, no. 16, p. 1929. doi: http://dx.doi.org/10.1039/b601594h

[142] Ni, M., D.Y.C. Leung, and M.K.H. Leung. 2007. "A Review on Reforming Bio-Ethanol for Hydrogen Production." *International Journal of Hydrogen Energy* 32, no. 15, pp. 3238–47. doi: http://dx.doi.org/10.1016/j.ijhydene.2007.04.038

[143] Evans, A., A. Bieberle-Hütter, J.L.M. Rupp, and L.J. Gauckler. 2009. "Review on Microfabricated Micro-Solid Oxide Fuel Cell Membranes." *Journal of Power Sources* 194, no. 1, pp. 119–29. doi; http://dx.doi.org/10.1016/j.jpowsour.2009.03.048

[144] Pattekar, A.V., and M.V. Kothare. 2004. "A Microreactor for Hydrogen Production in Micro Fuel Cell Applications." *Journal of Microelectromechanical Systems* 13, no. 1, pp. 7–18. doi: http://dx.doi.org/10.1109/jmems.2004.823224

[145] Gervasio, D., S. Tasic, and F. Zenhausern. 2005. "Room Temperature Micro-Hydrogen-Generator." *Journal of Power Sources* 149, pp. 15–21. doi: http://dx.doi.org/10.1016/j.jpowsour.2005.01.054

[146] Kim, T. 2009. "Micro Reactor for Hydrogen Generation from Sodium Borohydride." In *PowerMEMS,* 33–36. Washington, DC.

[147] Hoeppner, K., R. Hahn, H. Reichl, M. Esashi, and S. Tanaka. 2009. "Fabrication and Evaluation of a NaBH4 Hydrogen Microreactor Assembled by Triple Stack Glass Bonding." In *PowerMEMS*, 29–32. Washington, DC.

[148] Zhu, L., N. Kroodsma, J. Yeom, J.L. Haan, M.A. Shannon, and D.D. Meng. 2011. "An On-Demand Microfluidic Hydrogen Generator with Self-Regulated Gas Generation and Self-Circulated Reactant Exchange with a Rechargeable Reservoir." *Microfluidics and Nanofluidics* 11, no. 5, pp. 569–78. doi: http://dx.doi.org/10.1007/s10404-011-0822-5

[149] Um, D.H., T.Y. Kim, and O.C. Kwon. 2014. "Power and Hydrogen Production from Ammonia in a Micro-Thermophotovoltaic Device Integrated with a Micro-Reformer." *Energy* 73, pp. 531–42. doi: http://dx.doi.org/10.1016/j.energy.2014.06.053

[150] Kongkanand, A., S. Kuwabata, G. Girishkumar, and P. Kamat. 2006. "Single-Wall Carbon Nanotubes Supported Platinum Nanoparticles with Improved Electrocatalytic Activity for Oxygen Reduction Reaction." *Langmuir* 22, no. 5, pp. 2392–96. doi: http://dx.doi.org/10.1021/la052753a

[151] Yang, J., D.J. Liu, N.N. Kariuki, and L.X. Chen. 2008. "Aligned Carbon Nanotubes with Built-in FeN_4 Active Sites for Electrocatalytic Reduction of Oxygen." *Chemical Communications* 3, pp. 329–31. doi: 10.1039/B713096A

[152] Li, Y., W. Zhou, H. Wang, L. Xie, Y. Liang, F. Wei, J.C. Idrobo, S.J. Pennycook, and H. Dai. 2012. "An Oxygen Reduction Electrocatalyst Based on Carbon Nanotube-Graphene Complexes." *Nature Nanotechnology* 7, no. 6, pp. 394–400. doi: http://dx.doi.org/10.1038/nnano.2012.72

[153] Gong, K., F. Du, Z. Xia, M. Durstock, and L. Dai. 2009. "Nitrogen-Doped Carbon Nanotube Arrays with High Electrocatalytic Activity for Oxygen Reduction." *Science* 323, no. 5915, pp. 760–64. doi: http://dx.doi.org/10.1126/science.1168049

[154] Dubey, P.K., A.S.K. Sinha, S. Talapatra, N. Koratkar, P.M. Ajayan, and O.N. Srivastava. 2010. "Hydrogen Generation by Water Electrolysis Using Carbon Nanotube Anode." *International Journal of Hydrogen Energy* 35, no. 9, pp. 3945–50.doi: http://dx.doi.org/10.1016/j.ijhydene.2010.01.139

[155] Zheng, Y., Y. Jiao, L.H. Li, T. Xing, Y. Chen, M. Jaroniec, and S.Z. Qiao. 2014. "Toward Design of Synergistically Active Carbon-Based Catalysts for Electrocatalytic Hydrogen Evolution." *ACS Nano* 8, no. 5, pp. 5290–96. doi: http://dx.doi.org/10.1021/nn501434a

[156] Zheng, Y., Y. Jiao, Y. Zhu, L.H. Li, Y. Han, Y. Chen, A. Du, M. Jaroniec, and S.Z. Qiao. 2014. "Hydrogen Evolution by a Metal-Free Electrocatalyst." *Nature Communications* 5, p. 3783. doi: http://dx.doi.org/10.1038/ncomms4783

[157] Logan, B.E., D. Call, S. Cheng, H.V.M. Hamelers, T.H.J.A. Sleutels, A.W. Jeremiasse, and R.A. Rozendal. 2008. "Microbial Electrolysis Cells for High Yield Hydrogen Gas Production from Organic Matter." *Environmental Science & Technology* 42, no. 23, pp. 8630–40. doi: http://dx.doi.org/10.1021/es801553z

[158] Palmer, R., and R. Willis. 1987. "Rotational States of Physisorbed Hydrogen on Graphite." *Surface Science* 179, no. 1, pp. 1–5. doi: http://dx.doi.org/10.1016/0039-6028(87)90105-1

[159] Huang, I.-Y., Jr-C. Lin, K.D. She, M.C. Li, J.H. Chen, and J.S. Kuo. 2008. "Development of Low-Cost Micro-Thermoelectric Coolers Utilizing MEMS Technology." *Sensors and Actuators A: Physical* 148, no. 1, pp. 176–85. doi: http://dx.doi.org/10.1016/j.sna.2008.07.017

[160] Guo, D., J. Gao, A.J.H. McGaughey, G.K. Fedder, M. Moran, and S.C. Yao. 2013. "Design and Evaluation of a MEMS-Based Stirling Microcooler." *Journal of Heat Transfer* 135, no. 11, p. 111003. doi: http://dx.doi.org/10.1115/1.4024596

[161] Weitzel, D.H., W.V. Loebenstein, J.W. Draper, and O.E. Park. 1958. "Ortho-Para Catalysis in Liquid-Hydrogen Production." *Journal of Research of the National Bureau of Standards* 60, no. 3, p. 221. doi: http://dx.doi.org/10.6028/jres.060.026

[162] Yucel, S. 1989. "Theory of Ortho-Para Conversion in Hydrogen Adsorbed on Metal and Paramagnetic Surfaces at Low Temperatures." *Physical Review B* 39, no. 5, pp. 3104–15. doi: http://dx.doi.org/10.1103/physrevb.39.3104

CHAPTER 2

FLUID AND PARTICLE MANIPULATION USING C-MEMS

Hamza A. Rouabah and Nicolas G. Green

Department of Electronics and Computer Science, University of Southampton, UK

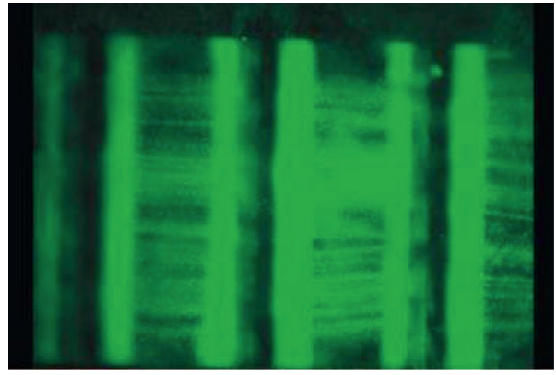

Fluid motion indicated by fluorescent tracer particles and driven by electrical forces over C-MEMs electrodes.

2.1 INTRODUCTION

Microelectromechanical systems (MEMS) are perhaps one of the most important developments that grew out of the semiconductor and microelectronic industries. Usually silicon-based, these multifunctional devices combine and integrate sensing elements, mechanical actuators, and electronic components in single microchips. The applications of this

technology are varied and increasingly ubiquitous. The MEMS market for traditional devices such as accelerometers and gyros continues to grow, while novel devices (such as energy harvesters) have emerged more recently with huge potential for future applications in self-powered and wearable devices. In addition to that, MEMS devices have also found applications in the field of life science and biology. These devices are often referred to as Bio-MEMS and are used as diagnostic tools. MEMS brings improvements to existing biochemical and chemical methods in diagnostics based on

- Ease of fabrication often with standard or only slightly modified IC manufacturing processes;
- Integration with electronics;
- Only small quantities of expensive samples and reagents are required;
- High precision and control of samples; and
- Low fabrication costs, reproducibility, and simple operation.

The potential of Bio-MEMS has drawn the attention of many research institutions to adopt their use and to conduct research and development in this area. BioMEMS applications are geared toward the miniaturization of many of the typical large-scale processes carried out in biochemistry laboratories such as mixing, sorting, sensing, detection, and separation, with the single most important underlying requirement of pumping and handling the minimum possible amount of samples and reagents. This evolution in Bio-MEMS is referred to variously as micro total analysis (μTAS) or lab-on-a-chip (LOC) by researchers, with the ultimate goal to integrate and combine many laboratory functions in a single integrated and automated microchip, which is capable of performing a complete assay from sample collection to read-out [1, 2]. The ability to transport species and handling fluids in microchannels and reservoirs with ease and precision is a central concept in the development of μTAS devices [3–5].

These requirements can be summarized as a need to be able to move fluids around on the microscale and the need to be able to manipulate and separate particles in those fluids. Numerous techniques have been developed for this purpose, with varying degrees of success. Of particular note are pillar-based MEMS microstructures for the separation of nanoparticles and electrode-based systems for particle manipulation using electric fields. Carbon microelectromechanical system (C-MEMS) technology allows for a powerful combination of different physical effects to produce fluid and particle manipulation. In C-MEMS, three-dimensional high-aspect-ratio (HAR) microstructures are easily constructed (in comparison

to conventional metal-based fabrication methods), which can generate complex electric field geometries and induce field-based physical movement. This chapter discusses these two areas of C-MEMS applications.

2.2 SOLID-STATE ELECTRIC-FIELD-DRIVEN PUMPS

A great deal of attention has been focused on micropump research, not only for their use in μTAS systems but also in a large variety of other applications such as aerospace and aircraft engineering, paints and inks, food and beverages, environmental, energy and fuels, and electronics [6]. Micropumps fall into two categories: mechanical and nonmechanical. Mechanical micropumps have typically large dimensions (up to few centimeters) and involve moving parts that reduce their reliability and increase their packaging size, which make these types of micropumps difficult to integrate into microchips. Nonmechanical micropumps are characterized not only by smaller sizes and nonmoving parts but also by steady fluid flows, accuracy, low power consumption, and a long lifetime. Nonmechanical micropumps involve the use of electric fields to move the fluid flow, via several physical principles: electrowetting, electrohydrodynamics, and electroosmosis (EO), each of which has advantages and limitations [7].

2.2.1 GENERATING FLUID FLOW USING AC ELECTROOSMOSIS

One important electric field flow manipulation technique is AC electroosmosis (ACEO), and it is based on the use of sets of interdigitated electrodes to pump fluids at voltages as low as 5 V. In addition to requiring only low applied voltages, these pumps are also easy to fabricate, portable, scalable, and easy to integrate [8]. Typical implementations of this technique rely on planar electrodes patterned at the bottom of fluid channels, usually made from metals such as gold or platinum, in order to produce fluid motion in the channel. As with other electroosmotic pumps, the fact that the fluid driving forces arise from a surface physical phenomenon in a viscously damped environment means that they generally generate low fluid velocities, are not able to withstand significant back-pressures, and have limited lifetime as the metal electrodes undergo chemical reactions.

Improving the performance of this type of micropump requires an increase in the ratio of the driving surface (i.e., the electrode surface area)

to the volume of the fluid being acted upon in the fluidic channel without changing the channel dimensions. An increase in this surface-to-volume ratio can be achieved by the transition from using planar electrodes to three-dimensional (3D) electrodes. The channel then contains vertical electrodes that increase the conductive surface area inside the channel but occupy a still small enough volume such that they do not obstruct fluid flow [9].

An ideal type of 3D structure that meets this requirement is the HAR pillar electrode. Making HAR electrodes using high conductivity metals such as gold or Cu involves the use of expensive and time-consuming electroplating in HAR molds to shape the electrodes. However, making HAR molds of this type is a challenging fabrication process and reproducibility of the process remains an issue [10].

Another aspect of fluid mechanics that is important in the operation of this type of pump (and where 3D structures have a major impact) is the inhibiting effect of viscosity, through which the fluid acts on itself. Where the driving force on the fluid is from the surface of the electrodes, the substrate surface between the electrodes represents a stationary layer that exerts a strong drag on the moving fluid streaming off the electrodes and a corresponding reduction in the overall flow rate. Obviously, 3D pillar electrodes only have gaps between them, with relatively less substrate surface and therefore less drag effect.

In addition, the ACEO flow mechanism is characterized by opposite symmetric rolls generated by the two edges of the electrodes. The two counter-rotating rolls are counterproductive in the sense that a lot of the flow power produced is lost opposing each other. One solution is to use asymmetric electrodes, as described later, where the counter-rotating rolls are on different length scales. Another solution is to use height variation and electrodes with steps in them to offset the rolls in the vertical direction and decouple the fluid rotation and allow them to act in concert to produce a bulk fluid flow [11, 12].

Fabrication of all these types of 3D structures in metals involves multiple lithography processes, with electroplating or deep etching: all slow, expensive, and complicated steps. The final challenge concerns the chemical resistance of metallic electrodes used for the flow generation, an issue best addressed by exploring different materials that can resist or mediate only desirable electrochemical reactions.

Many of the listed challenges can be overcome by adopting C-MEMS technology (see Chapter 1 of Volume 1 of this book on the C-MEMS process in which patterned polymers are converted to conductive carbon electrodes). C-MEMS structures are chemically and electrochemically very stable as evidenced, for example, by the use of C-MEMS electrodes in lithium-ion batteries [13]. The C-MEMS polymer precursor (e.g., SU-8) can be patterned with relative ease using standard photolithography

techniques. Then the entire structure is subjected to pyrolysis to turn the polymer material into carbon. The C-MEMS process is relatively simple and inexpensive in comparison to the fabrication processes for producing HAR metallic structures and constitutes a good candidate for generating fluid flow in LOC applications.

2.2.2 PHYSICS OF ACEO PUMPS

AC signals with frequencies ranging from 100 Hz to 10 kHz and relatively low voltages (<10 V peak to peak) applied to electrodes can generate lateral unidirectional fluid flow if the electrode structure is an asymmetric array of planar microelectrodes, as explained in Figure 2.1 [8, 14–20].

The mechanism for generating unidirectional fluid flow on this type of array is referred to as ACEO in which a nonzero time-averaged electroosmotic slip velocity at the surface of the electrodes is produced. This effect is due to the influence of the nonuniform electric field that is generated between the asymmetric planar electrodes on the EDL induced on the surface of the electrodes. The nonuniform field has a tangential component at the surface that acts on the ions in the EDL, and because, for an AC signal, the direction of the electric field flips and the polarity of the net charge in the EDL also switches, the Coulomb force F_c always points away from the electrode edge and has a nonzero time average over the alternating cycle [15, 16].

In Figure 2.1c, we illustrate the fluid flow that occurs over the asymmetric electrodes [8]. The periodic arrangement of the electrodes produces a nonsymmetric local flow on top of each pair of electrodes, which generates a global flow in the direction of the broken symmetry along the channel, from a rolling motion generated at every electrode edge. This results in two small fluid rolls over the small electrodes, which are similar in size, and because they move in opposite directions, they do not contribute to the overall fluid flow. The fluid rolls over the big electrodes, on the other hand, are highly asymmetric, with the higher velocity occurring at the edge closest to the small electrode, where the electric field is stronger. In addition to being fast, because of the strong electric field generated at the narrow gap, the roll over the edge closest to the narrow gap is significantly larger than that over the farther edge and extends up to the top of the channel. It is, therefore, not balanced and the bulk fluid travels along the channel following the path shown by the solid gray arrow, outwards from the inner edge of the large electrode, then up and over the outer edge and the small electrode, and then down toward the next large electrode as shown schematically. This results in a directional flow along the electrode array, reinforced at every pair of electrodes [8].

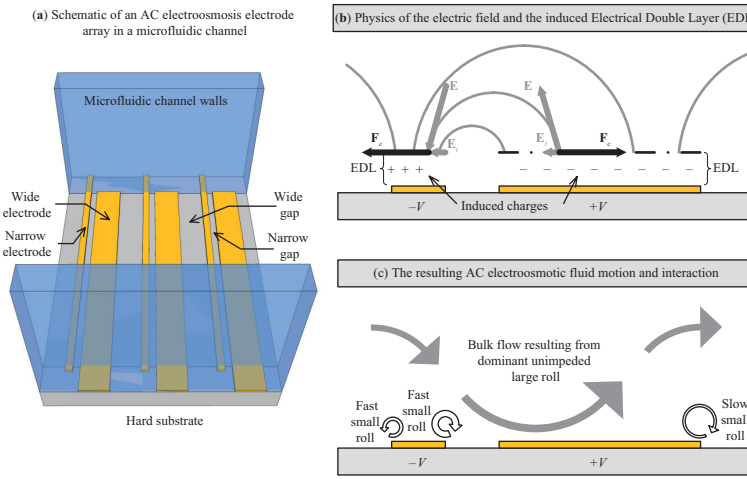

Figure 2.1. (a) Two-dimensional asymmetric planar electrode array used to generate AC electroosmotic pumping, consisting of large and narrow electrodes separated by large and narrow gaps in a periodic manner along a microfluidic channel. (b) The applied AC signal and the ground return are applied alternately to successive electrodes, resulting in induced electrical double layers (EDLs) opposite in sign to the applied potential on each electrode. The electric field simultaneously generated by the applied potential difference, **E**, is nonuniform, curving through the EDLs toward adjacent electrodes and resulting in a tangential field component, $\mathbf{E}_t$. As a result, there is a Coulomb force $\mathbf{F}_c$ acting across the electrode surface and acting on the ions in the layers. The resulting electroosmotic slip velocity across the electrode surface has a nonzero time average because the sign of the charge in the induced EDL is always opposite to the applied potential and the Coulomb force always points away from the electrode edge. (c) The resulting continuous flow arising from the electroosmotic slip on the surface of the electrodes. There are fluid rolls generated over each electrode edge: over the small narrow electrode, the rolls are small and contained near the surface; over the large electrode, one of the rolls is large and fast and the other is small and slow. As a result, the large roll is not balanced by the action of the second and bulk unidirectional flow along the array is produced [8, 15, 16–18].

2.2.3 *FROM 2D ELECTRODES TO 3D ELECTRODES IN ACEO MICROPUMPS*

As stated earlier, ACEO is a surface-driven effect resulting from the interaction between the EDL (induced by an AC electric potential applied to the electrodes) and the electric field generated by the same potential. In order to improve the pumping efficiency inside the fluidic channel, the internal hydrodynamic resistance of the pump should be increased, in order to reduce back

flow through the pump from systemic back pressure. In addition, the surface area of the electrodes should be increased to increase the pumping force.

An increased resistance can be accomplished, for example, by increasing the length of the electrode array. However, the electrical resistance also depends linearly on the length of the electrodes and on the fluid between the electrodes, and therefore, large increases in array length are associated with problems of maintaining a constant electrical potential on electrodes in long arrays. Alternatively, significant improvements in hydrodynamic resistance can be achieved by reducing the channel cross section because the hydrodynamic resistance of a pipe is proportional to the radius or width to the fourth power. Multiple channels in parallel, therefore, have a significantly higher hydrodynamic resistance than a single channel of the same overall cross section, an effect well known in DC electroosmosis, where parallel channels and frits are used [6].

Using these physical principles, a new design was proposed based on C-MEMS technology [21, 22], as shown in Figure 2.2, adapting the existing asymmetric planar electrode array. By incorporating HAR C-MEMS electrodes [22–24], the channel is vertically divided and the asymmetric electrode structure is extended upwards. More driving electrode surface is available for the same channel volume, and the internal resistance is increased, leading to greater pumping flow velocities and pressures. Increasing the surface area of the electrodes increases the power coupled to the fluid movement. By filling the channel volume with conductive pillars, the surface area is increased, but because the channel volume remains the same, this design significantly increases the drive per unit volume.

One key benefit of C-MEMS technology over electroplated metal electrode structures for this application is that electroplating through molds is very difficult when the cross sections of the molding shapes are very different. Indeed, the plating rates in large, broad holes are faster than those in HAR holes. Consequently, highly asymmetric and irregular nonrepeating shapes are difficult to electroplate, something that is not an issue in C-MEMS. C-MEMS pillars and any type of structures are produced by patterning a single layer of photoresist: the feature height is simply a property of the layer thickness. In C-MEMS, yet more complex structures can be produced by multiple-layer C-MEMS designs and they are limited only by lithographic resolution.

An additional important benefit is the nature of the material in C-MEMS technology. Metal electrodes used in microfabrication have a limited stability window compared to the glassy carbon electrodes in C-MEMS. Examples are the electrochemical reaction of gold in chloride salt solutions or the production of pH gradients in solution by platinum electrodes. Although the applied AC potentials used in ACEO are small

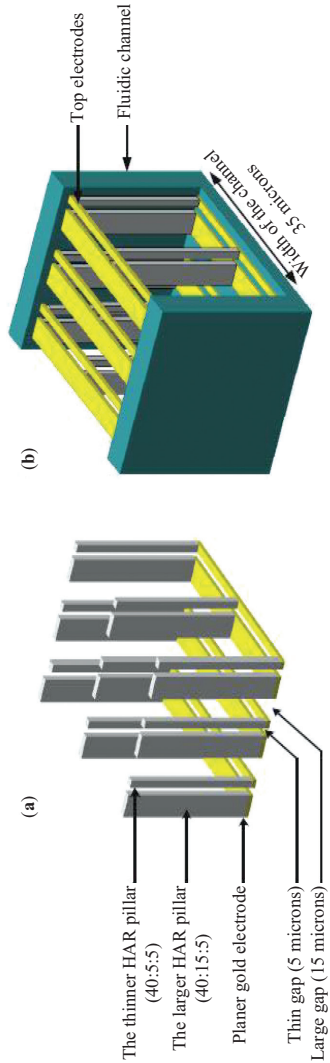

Figure 2.2. An extension of the asymmetric electrode array shows an increase in the electrode surface area from planar to 3D electrodes, but the channel volume remains the same. Enclosed in a channel, electrodes line the walls and top and bottom of the channel and also fill the volume with pillars that all have the same asymmetric configuration.

compared to those used in DCEO, they are still of the order 5 to 10 V_{pp}, which are still high enough to result in reactions. Obviously, as the frequency increases, the smaller time span between the reversal of the potential of the electrodes will reduce the result of these reactions. Nevertheless, typical ACEO frequencies in kilohertz are still low enough for these reactions to be of concern in the ionic medium which most LOC applications require. Although some engineering tweaks have been applied to increase the lifetime of electrodes in an ionic medium, for example, natural oxide layers in titanium-covered gold electrodes give better chemical resistivity than gold; however, the lifetime remains limited [15]. In C-MEMS, polymer 3D structures are converted to conductive glassy carbon electrodes that are chemically resistant, as has been demonstrated successfully even in high-concentration ionic media under applied potentials [25].

2.3 FULLY FUNCTIONAL AC ELECTROOSMOTIC MICROPUMP USING C-MEMS

The fabrication process of the asymmetric HAR pillar electrode array is illustrated in Figure 2.3. The substrate is a silicon wafer with the planar electrodes patterned using standard photolithography. The 3D HAR

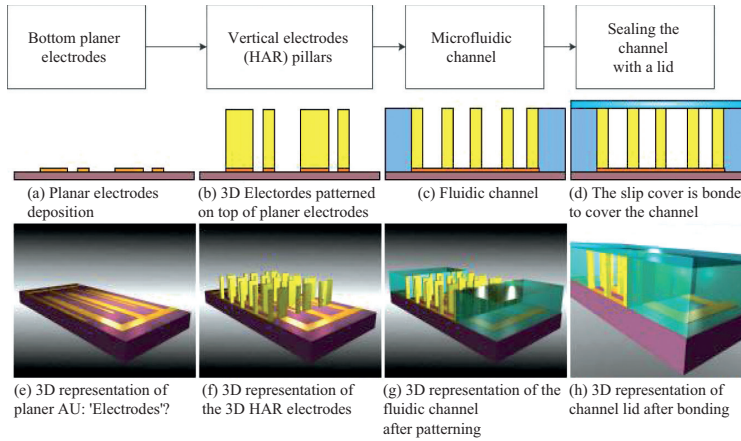

Figure 2.3. The AC electroosmotic micropump fabrication process, constructing an electrically active solid-state device only from SU-8. (a), (e) Asymmetric planar electrodes patterned first on silicon wafer. (b), (f) 3D HAR electrodes are built on the top of the planar array. (c), (g) The electrodes are encapsulated with a fluidic channel. (d), (h) the device is sealed with a transparent lid.

electrodes were then patterned using contact aligners and carefully controlled lithography, followed by pyrolysis as described in Chapter 1 of Volume 1 of this book. The microfluidic device was then constructed around the array by patterning another layer of SU-8 to form the channels and sealed by adding a lid.

As the process requires the use of five layers (including the substrate) and coating multilayers of photoresist on top of each other, numerous problems can arise during the fabrication process, which are worth highlighting along with the solutions.

2.3.1 ACCURATE CONTROL OF LITHOGRAPHY PARAMETERS

Making 3D structures that have a small footprint size along with a HAR is a particularly challenging application for UV photolithography. The tangential field component, which is the source of the force generating the fluid flow, is maximized in planar electrodes because of the sharp corners of the coplanar electrodes. Any rounding of the electrodes when extended to the 3D pillar structures reduces sharp corners and thus reduces the force on the fluid. It is important, therefore, to preserve the shape of the HAR electrodes during the lithography process as the sharp edges of the electrodes can be easily removed because of the T-topping effect (see Figure 2.4a) [9].

The lithography process is further complicated because of the narrow and deep gaps between the electrodes, which can range between 10 and 20 μm with an aspect ratio of 10:1. Comparison of the two images in Figure 2.4 demonstrates the requirement for very accurate control of exposure and development times in determining the final shape of the structures.

2.3.2 THE STICTION EFFECT

A particularly severe problem affecting the current C-MEMS design is the stiction effect. Stiction takes place during the development stage in the lithography process and is due to the capillary forces between the SU-8 walls, as the developer rises in the narrow gaps between pillars and the solvent starts to evaporate. As this occurs, the less stiff narrow pillars bend toward the sturdier ones, resulting in the tops of adjacent pillars coming into contact, as shown in Figure 2.4b. Residual viscous SU-8 on the pillars then ensures that the pillars remain stuck firmly despite shrinking of the structures during the pyrolysis process [26].

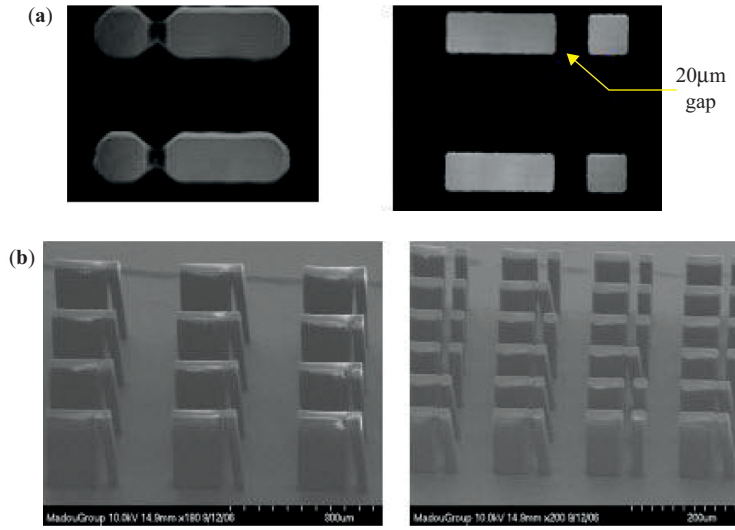

Figure 2.4. Issues occurring during fabrication of HAR pillars. (a) Looking from above, scanning electron microscopy (SEM) images showing a comparison between 150 µm high HAR pillars before and after an optimization process. The picture on the left shows HAR pillars before optimization, where the corners of the pillars are not sharp and the gaps between the large and small pillars are not clear. After optimization of the photolithography parameters, a good resolution, sharp angles, 20 µm clear gaps, and vertical walls of the pillars were achieved (picture on the right). (b) The stiction effect: pairs of large and small electrodes stuck together due to the strong capillary action in the narrow gap during solvent or developer evaporation or removal (picture on the left). This effect is strongly dependent on solvent concentration or composition and temperature, which in some cases produce an erratic stiction (picture on the right).

As C-MEMS are electrical structures in the micropumping application, adjacent electrodes have opposite polarity, and this stiction effect, therefore, results in short circuits. Even intermittent erratic contact of pillars (Figure 2.4b) will result in pairs of electrodes being short circuited and unusable for ACEO pumping because of the lack of field generated between them. The stiction effect for SU-8 is controllably reduced and eliminated by replacing the developer with isopropanol and methanol [9].

2.3.3 RESIDUAL ELECTRICAL RESISTANCE BETWEEN ELECTRODES

A uniform array of 3D HAR electrodes can in most cases be achieved in the C-MEMS process; however, in some cases, after the pyrolysis stage,

the electrical resistance measured between two opposite electrodes may vary from megaohms to kiloohms. This varying series electrical resistance, which is separable and notably greater than the internal electrical resistance of the carbon electrodes, is due to residual SU-8 left after the different patterning stages that forms incomplete, invisibly thin conductive layers after pyrolysis. These traces of photoresist are very difficult to remove during the development stage in the photolithography process, because of its strong adsorption on the oxide layer of the wafer. The resulting thin carbon layers between the electrodes can be eliminated using an oxygen plasma etch [9]. While this step is then necessary, it has the negative effect of roughening the surface of the electrodes, which may reduce fluid velocity.

2.3.4 THE COMPLETE C-MEMS MICROPUMP

In Figure 2.5, we show the final ACEO pump channel, filled with HAR 3D electrodes and planar electrodes. The electrodes can easily be integrated with other layers of photoresist without any adhesion or nonuniformity problems.

The final device following pyrolysis shows significant reduction in pillar size and a change in shape but retains the asymmetric form. The beauty and power of using C-MEMS fabrication processes making use only of the SU-8 photoresist is that the complete ACEO pump can be made from a single material (SU-8).

Experimental measurements on the C-MEMS ACEO micropump using both micro- and nanoparticles as tracer particles in different conditions (aqueous medium composition, signal frequency, voltage) demonstrate typical ACEO behavior. The graph in Figure 2.6 are from the measurements of the movement of 8-μm diameter latex beads over planar carbon electrodes in 1 mM aqueous KCl solution with the beads acting as tracer particles for the flow [9]. An AC signal of 16 V peak to peak (V_{pp}) was applied to the electrodes over a range of frequencies. A steady fluid flow was observed between 4 and 60 kHz, with a maximum velocity of 32 μm/s around 8 kHz (this maximum frequency depends on the exact sizes and proportions of the electrodes).

2.4 AN ALTERNATIVE METHOD FOR INCREASING PUMPING EFFICIENCY: SHAPED 3D PLANAR ELECTRODES

An interesting alternative method for increasing the flow rate generated by induced electrical effects such as ACEO is to elevate the driving electrode

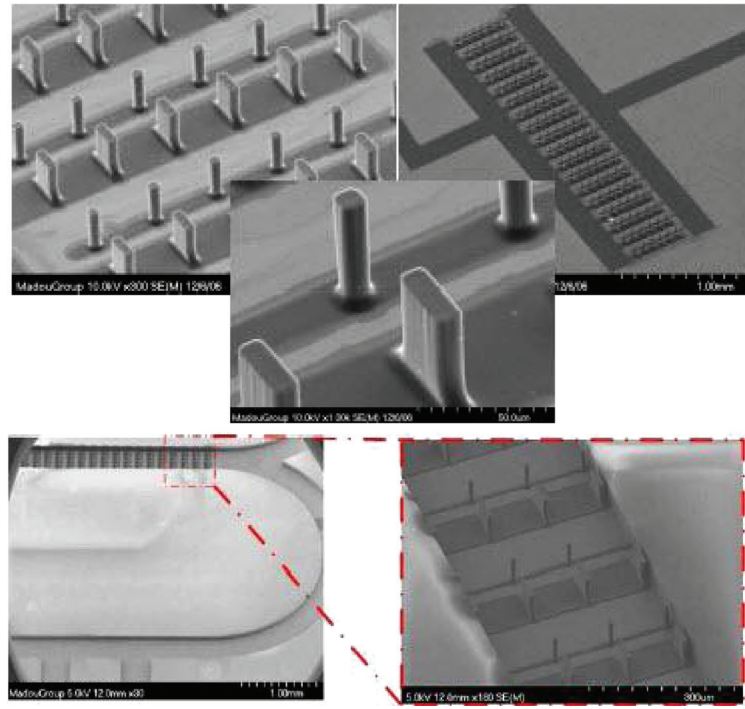

Figure 2.5. Completed electrode array, combining planar electrodes and HAR conductive pillars on top. Following all stages of the C-MEMS processing, a good uniformity, resolution, and verticality were achieved. The shrinkage in the electrode structures that occurs during the pyrolysis stage results in a distinctive shape for the asymmetric structure. The two lower SEM images show the complete 3D ACEO micropump, including planar electrodes, HAR conductive pillars, and fluidic channel. As a result, the whole device was made only from SU-8 photoresist [9].

surface above the silicon substrate between the electrodes. This means that the fluid motion driven by the electroosmotic slip leaves the electrode surface tangentially and is relatively free to travel horizontally, because the retarding viscous drag effect produced by the nonslip surface between the electrodes is at a lower elevation. In addition to different elevations of the electrodes, the profile of the individual electrodes can also move the different fluid rolls to different heights. An example of the latter is illustrated in Figure 2.7: If the section of the wide electrode responsible for generating the large roll is raised up by a height commensurate with the size of the other three rolls, then the bulk flow arising from the large roll is more free to move. As a second-order modification to the design, if

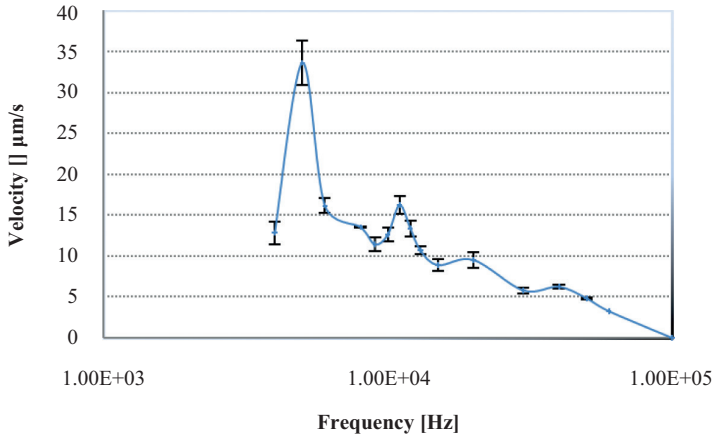

Figure 2.6. Fluid flow velocity measurements versus the variation in frequency in a channel with asymmetric planar carbon electrodes with 20 and 100 µm gaps. A fixed applied voltage of 16 V_{pp} and 8-µm diameter latex tracer particles were used.

the narrow electrode also has a step raising the edge at the wide gap, then the outer small roll here will act in concert with the main driving electrode.

As for pillar electrodes, 3D C-MEMS structures can be constructed in these kinds of shapes easily by means of successive layers of SU-8 and appropriate masks. The use of raised electrodes improved ACEO pumping inside the channel as shown in Figure 2.8. Using a combination of raised planar electrodes and 3D HAR conductive pillars for the generation of electroosmotic flow demonstrated a significant improvement in bulk flow generation.

2.5 ADDITIONAL FLOW EFFECTS INDUCED BY NONUNIFORM AC ELECTRIC FIELDS

For a real-world sample, the motion of particles on top of the electrodes is not necessarily just caused by ACEO. Other field-induced effects can take place on top of the electrodes occurring concurrently with the fluid motion at different frequencies, as shown in Figure 2.9.

The electrolysis of water by the applied electrical potential leads to the formation of bubbles, which can be seen over a range of frequencies. Some of the additional motion of particles in these arrays is no doubt because of the electric-field-related forces on the particles—specifically

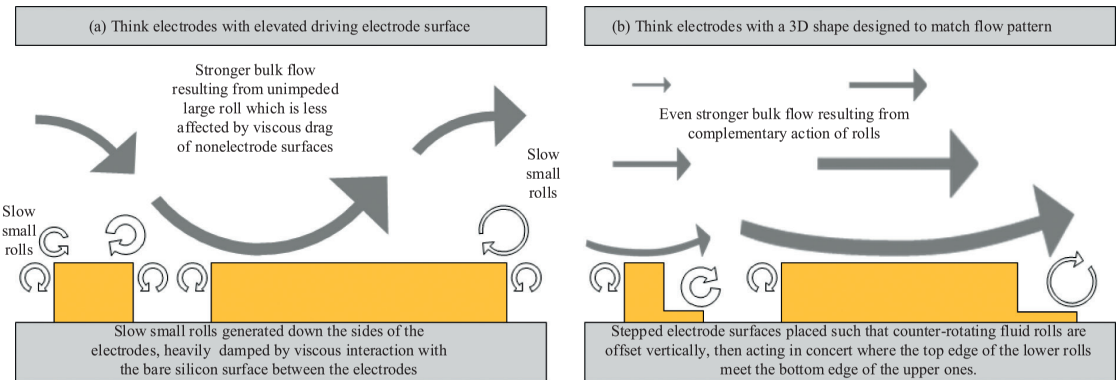

Figure 2.7. Illustration of the effect of changing the cross-sectional profile of the electrodes on the motion and interaction of the different components of the generated fluid flow by (a) increasing the thickness of the electrodes and (b) increasing the thickness of only part of the electrodes and producing a stepped profile.

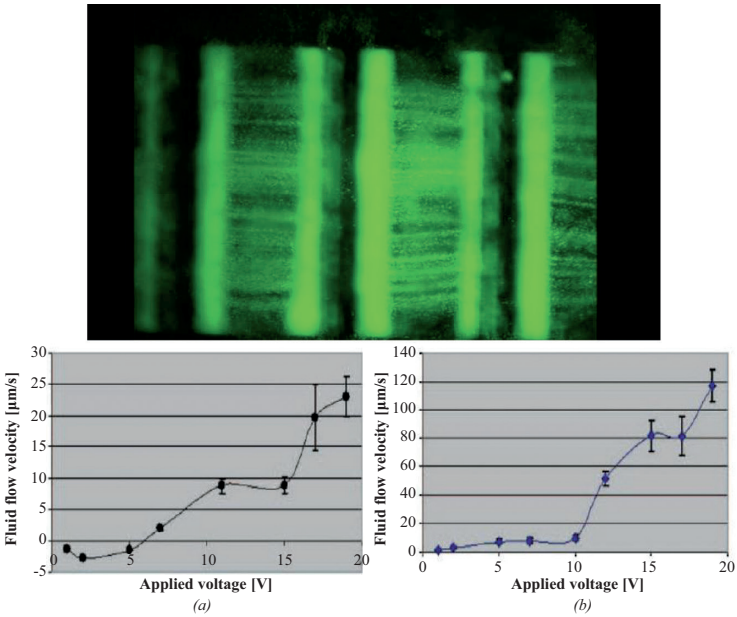

Figure 2.8. (a) Fluid flow motion generated by C-MEMS electrodes tracked using 500-nm diameter fluorescent particles suspended in 0.1 mM phosphate buffered saline. A steady and uniform fluid flow stream can be clearly seen on top of the electrodes inside a 500-µm wide fluidic channel. Comparison of fluid flow velocity with applied voltage for (b) raised carbon planar electrodes and (c) the same array with HAR pillar electrodes [9]. For the 2D device, a slight reverse pumping was noticed at low voltages. The planar array had dimensions as follows: gap 60 µm; electrode 60 µm; gap 20 µm; electrode 20 µm; with the 3D array having 50-µm high pillars spaced at 74 µm along the electrode (across the channel). Experiments were carried out at a fixed frequency of 1 kHz and a voltage varying between 1 V_{pp} and 19 V_{pp}.

dielectrophoresis (DEP), which we discuss in the next section. However, there is a second field-induced fluid effect of particular note, which is related to the thermal heating arising from the application of electrical signals to resistive materials.

2.5.1 THE ELECTROTHERMAL EFFECT

Owing to the small scale of the electrodes, the application of relatively low voltages can produce very strong electric fields. As a result of this and the fact that fluid samples can have a moderately high conductivity, the electrically generated heat in the fluid can be significant around the

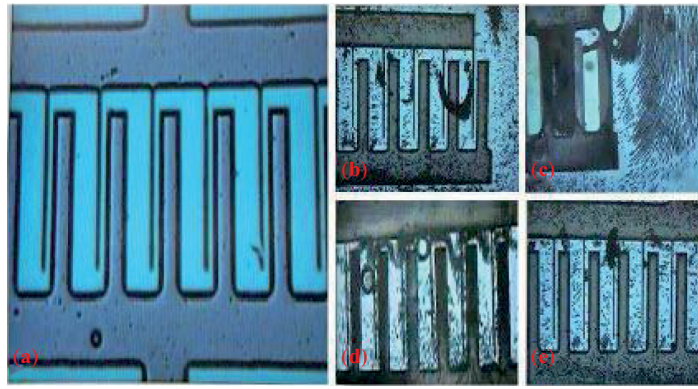

Figure 2.9. Fluid flow test using 8-μm diameter latex beads on asymmetric electrodes with 100-μm wide electrodes or gaps and 20 μm for the narrow electrodes or gaps. (a) Empty planar electrodes (before the injection of latex beads). (b) Mass transportation of latex beads on the top of the electrodes under the action of ACEO including electrode end effects. (c) The generation of bubbles and collection of beads at the exit of the array. (d) Collection of beads at the ends of the large electrodes. (e) Trapping of beads between the ends of the narrow electrodes and the start of the wide ones.

electrodes [14, 20]. The power generated per unit volume (W) is proportional to the conductivity of the medium s_m and the square of the magnitude of the electric field (**E**), which is expressed as

$$W = \sigma_m |\mathbf{E}|^2 . \tag{2.1}$$

The dissipated power density can be highly nonuniform because of the nonuniform fields produced by the electrodes, with maxima at electrode edges. This heat diffuses away from the location of the electrode array, resulting in the formation of temperature gradients in the fluid and corresponding gradients in viscosity, density, permittivity, and conductivity of the fluid. These gradients can give rise to fluid flow in two ways, natural convection and electrothermal fluid flow, although this generally will occur only for high-conductivity aqueous electrolytes.

In C-MEMS applications, the resistance of the carbon electrodes can also have a significant effect. Carbon electrodes have a relatively low electrical conductivity, which results in some potential drop in the electrodes and power dissipation. This also gives rise to thermal gradients in the fluid independently of its conductivity and produces electrothermal fluid flow [26].

2.6 DIELECTROPHORETIC PARTICLE MANIPULATION IN C-MEMS

In addition to the induced electrical forces on the fluid, there are electrical forces on particles contained within the fluid. For a large number of medical or LOC applications, the samples contain particles that are the objects of interest, for example, biological cells, bacteria, viruses, and protein molecules. A key requirement in these application areas, therefore, is the development of methods that can manipulate or separate such particles for further study. A simple but highly useful example would be a technique that can concentrate a low-concentration sample of particles into a highly concentrated blob, as with centrifuges used in every biochemistry laboratory.

Manipulation of particles using electrical forces such as electrophoresis or DEP is especially of interest, the former being used already for more than 200 years, not so much because of the selectivity of the process but primarily because of the noncontact nature of the method. Field-driven effects with solid-state devices (unlike filter concentrators) do not require physical contact, which may damage biological particles such as cells. One of the advantages of DEP over electrophoresis is that it can use low-voltage signals between electrodes at AC frequencies high enough to avoid electrochemical reactions. This is due to the fact that the dielectrophoretic effect is local to the electrodes, a disadvantage compared to electrophoresis that is generated throughout the volume of the fluid. As in the previous example of ACEO pumps, C-MEMS electrodes can be constructed in 3D to fill fluid channels and to extend the influence of DEP effect throughout the fluid volume.

2.6.1 PRINCIPLES OF DIELECTROPHORESIS

DEP is the movement arising from the interaction between a spatially nonuniform electric field and a polarizable particle. In summary, the governing equation for the time-averaged DEP force $\langle \mathbf{F}_{\mathrm{DEP}} \rangle$ on a homogeneous particle of volume υ is given by

$$\mathbf{F}_{DEP} = \upsilon Re\{\tilde{\alpha}\}\nabla|\mathbf{E}|^2 . \tag{2.2}$$

where $\nabla|\mathbf{E}|^2$ is the gradient of the square of the electric field magnitude and $Re\{\tilde{\alpha}\}$ is the real part of the effective polarizability of the particle [27]. The effective polarizability is a complex, frequency-dependent term.

Polarizability depends on several factors, primarily shape terms and electrical terms: specifically, the permittivity and conductivity of both the particle and the fluid it is suspended in. The frequency dependency means that the effective polarizability (real part) has a signature spectrum for a particle type and can be either positive or negative. Negative DEP occurs when particles are repelled from high-field regions, down the gradient typically found at the edges of electrodes. In contrast, positive DEP describes the motion of cells toward high-electric-field regions, with the gradient $\nabla|\mathbf{E}|^2$. Switching between these two behaviors for a particle is typically just a matter of changing the frequency of the applied signal generating the electric field, but it also depends on the composition of the fluid and switching can be done by altering its conductivity. For biological particles, where suspending fluids require a high concentration of salt and, therefore, have a high conductivity, negative DEP is generally all that can be generated but this ensures that cells are kept away from high field regions, which can induce cell damage.

The DEP force scales favorably with reductions in system scale so it can be adapted to micrometer and submicrometer particles with similarly scaled electrodes. Microfluidic devices have been fabricated with microelectrodes for the manipulation of single particles as they flow through the device, and in particular, negative DEP has been widely used to create barriers and for two-dimensional confinement of particles into focused streams [10, 27].

2.6.2 C-MEMS ELECTRODES FOR DIELECTROPHORESIS

One of the demonstrated applications of C-MEMS technology as electrodes is for use in dielectrophoretic devices. In Figure 2.10, we show a typical fabrication process for the production of pillar electrodes used for DEP [28, 29] as a series of SEM images. Again, SU-8 is used throughout as the precursor resist for pyrolysis as well as for the inclusion of insulating layers and to construct microfluidic channels around the electrodes. The lower substrate material was silicon with a thin insulating layer of thermally grown silicon dioxide. The bottom surface of the channel was planarized, in this case by a 1.4 μm layer of SU-8, to isolate the lead structures and to prevent particle adhesion.

As stated previously, because of the $\nabla|\mathbf{E}|^2$ term in the dielectrophoretic force, the force is strongest where the gradients in the field strength are the greatest: logically where the field strength itself is greatest, making it local to the electrodes themselves. With C-MEMS electrodes

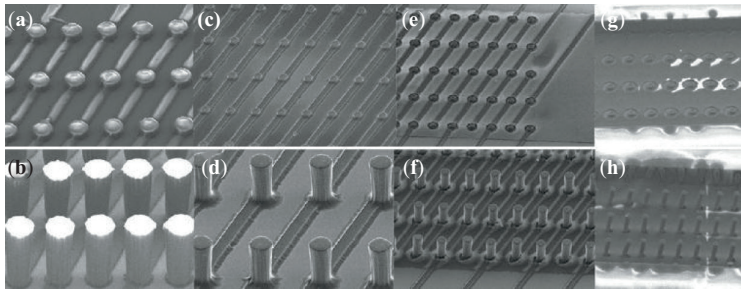

Figure 2.10. SEM images of the C-MEMS fabrication process for dielectrophoretic electrodes with planar electrode structures on the top row and 3D pillar electrodes on the bottom. For reference, the horizontal spacing of the electrodes was 45 and 110 μm in the vertical one. The SU-8 structures were fabricated in a two-step photolithography sequence (a, b) and were then pyrolyzed to final carbon electrodes and connecting leads (c, d). Connecting leads were protected and isolated with a layer of SU-8 (e, f), with the device sealed into an SU-8 fluidic channel (g, h).

Source: Taken from Martinez-Duarte et al. [29].

constructed in 3D to fill fluid channels, this extends the influence of DEP throughout the volume. This is shown clearly in Figure 2.11, which shows the term $|\mathbf{E}|^2$ for the array described earlier and demonstrates this principle. For the planar structure, the value of $|\mathbf{E}|^2$ falls off rapidly with height and, therefore, so would be the dielectrophoretic force. For the pillar structure, the field values and the dielectrophoretic force are uniform with height.

2.6.3 APPLICATIONS OF DIELECTROPHORESIS IN C-MEMS ELECTRODES

Positive DEP, negative DEP, or a combination of both can be induced on different particle types for several applications related to their movement. As DEP is a noncontact effect that can be removed from the system simply by switching the signal off, particles can be filtered from a fluid flow by repulsion, which simultaneously concentrates and retains them for release later. For example, using a single frequency, different particle types can be moved in different directions with one experiencing positive DEP and the other negative DEP. Particles can also be focused to a point in free space by using negative DEP to repel them from a surrounding set of electrodes.

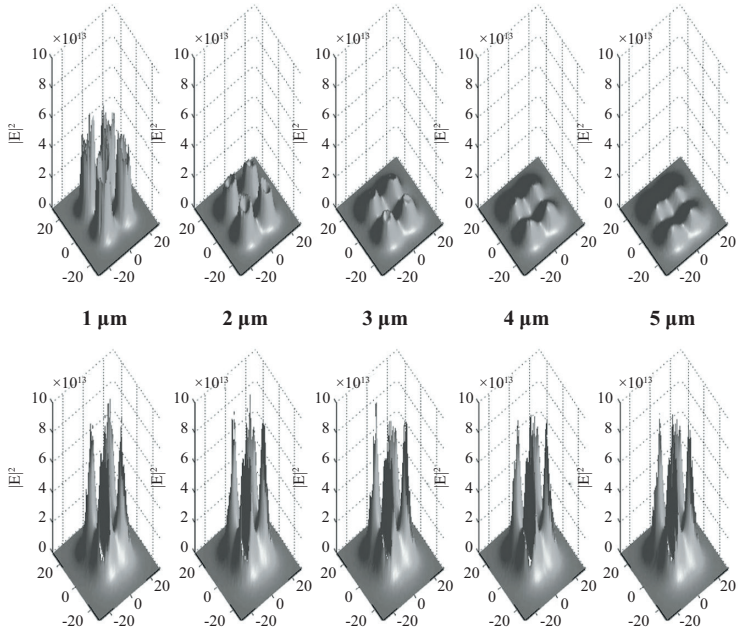

Figure 2.11. 3D surface plots depicting the magnitude of $|\mathbf{E}|^2$ in various horizontal cross sections at different heights above the channel floor for planar electrodes (top) and pillar electrodes of the same size and cross section. The dielectrophoretic force is proportional to the gradient of this term, making these landscape plots pseudo-gravity models of what a particle undergoing DEP would do. For negative DEP, the particles would "roll down" the slopes to the lowest points, and for positive DEP, the particles would "climb up" the slopes to the highest points. What is clear from these plots is that for the pillar electrodes, there is little change in value with height, whereas there is a rapid decrease for the planar electrodes.

Source: Image taken from Park and Madou [28].

C-MEMS devices similar to those in Figure 2.10 have been used to demonstrate a range of DEP applications [28–32]. Figure 2.12 shows comparative results of using 3D versus planar electrodes to perform a retention or filtering operation on yeast cells over a range of flow rates. The benefit of the C-MEMS pillar structures for improving device performance are clearly indicated in this result.

Figure 2.13 shows streaming of cells from the ends of the pillar array having used positive DEP to pull the cells into the vicinity of the pillars. Focusing into streams in this manner is important in terms of a flow through concentrating method, either with the streams pulled off

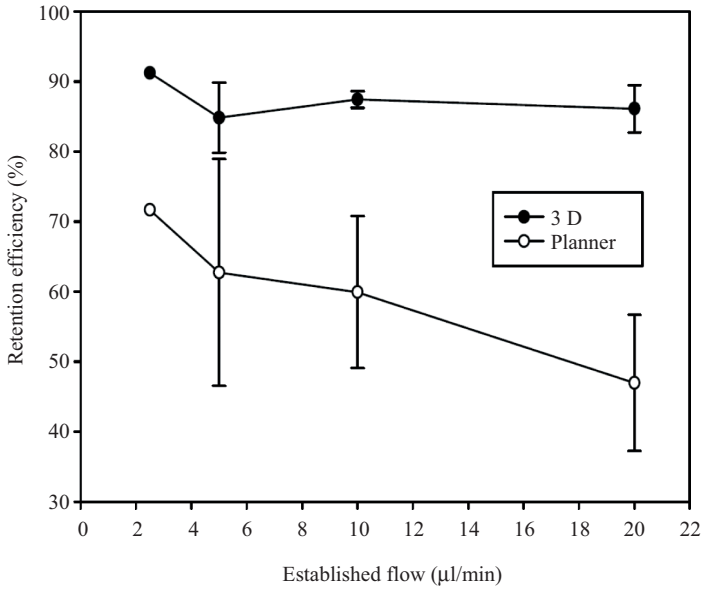

Figure 2.12. Retention efficiency in yeast cell samples as flow rate increases for both planar and volumetric electrodes. The sample conductivity was 51 mS/m and a 10 MHz, 10 Vpp sinusoidal signal was applied between the electrodes to perform DEP trapping of viable yeast cells. The numbers of viable and nonviable yeast cells at the output was determined by direct observation for the same signal and increasing flow rate for a fixed sample volume of 50 µl.

Source: Taken from Martinez-Duarte et al. [29].

for sample extraction or simply to have a specific sensing location with a high signal-to-noise ratio. DEP retention and concentration have also been demonstrated for latex spheres [28], a particle type commonly used as a substrate in chemistry and biochemistry, and for the bacteria *Escherichia coli* [31], one of the many bacteria of interest in the development of water treatment and sensing systems.

2.7 SUMMARY

Microfluidic devices have a wide range of applications in medical, biochemical, and environmental areas. Similarly, electric-field-based solid-state devices have a great deal of potential for LOC devices, owing to their simplicity of operation and the ability to conduct noncontact

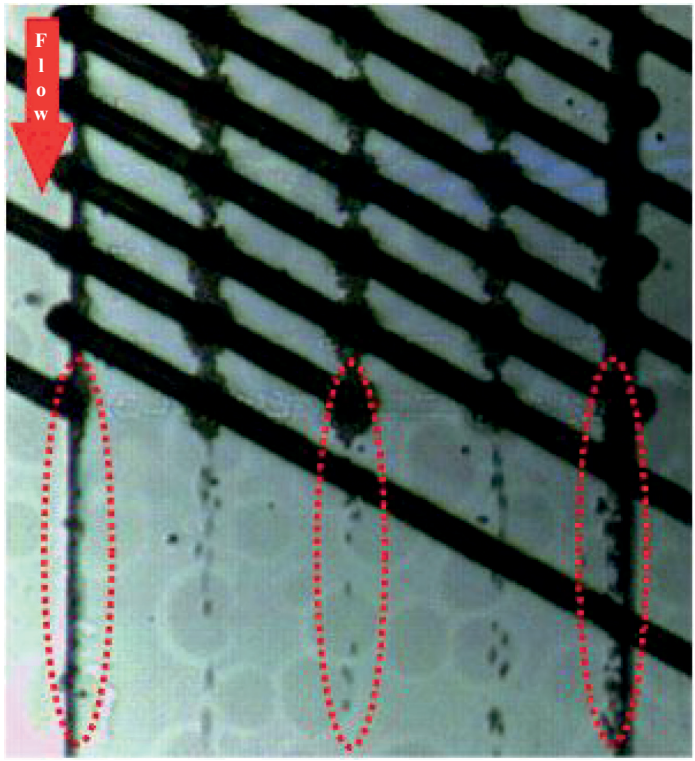

Figure 2.13. Cells focused into streamlines (red ellipses) using positive DEP.

Source: Taken from Martinez-Duarte, Renaud, and Madou [31].

manipulation. C-MEMS technology is uniquely able to produce devices with high pumping power and operational efficiency, both for particle applications (such as active filtering and separation) and for simultaneous movement and pumping of fluids.

REFERENCES

[1] Manz, A., N. Graber, and H.M. Widmer. 1990. "Miniaturized Total Chemical Analysis Systems: A Novel Concept for Chemical Sensing." *Sensors and Actuators B: Chemical* 1, no. 1, pp. 244–48. doi: http://dx.doi.org/10.1016/0925-4005(90)80209-I

[2] Neužil, P., C.D.M. Campos, C.C. Wong, J.B.W. Soon, J. Reboud, and A. Manz. 2014. "From Chip-in-a-Lab to Lab-on-a-Chip: Towards a Single Handheld Electronic System for Multiple Application-Specific Lab-on-a-Chip (ASLOC)." *Lab on a Chip* 14, pp. 2168–76. doi: http://dx.doi.org/10.1039/C4LC00310A

[3] Reyes, D.R., D. Iossifidis, P.A. Auroux, and A. Manz. 2002. "Micro Total Analysis Systems. 1. Introduction, Theory, and Technology." *Analytical Chemistry* 74, no. 12, pp. 2623–36. doi: http://dx.doi.org/10.1021/ac0202435

[4] Hardt, S., and F. Schonfeld. 2007. *Microfluidic Technologies for Miniaturized Analysis Systems*. New York: Springer.

[5] Carrascosa, L.G., M. Moreno, M. Alvarez, and L.M. Lechuga. 2006. "Nanomechanical Biosensors: A New Sensing Tool." *Trends in Analytical Chemistry* 25, no. 3, pp. 196–206. doi: http://dx.doi.org/10.1016/j.trac.2005.09.006

[6] Laser, D.J., and J.G. Santiago. 2004. "A Review of Micropumps." *Journal of Micromechanics and Microengineering* 14, no. 6, pp. 35–64. doi: http://dx.doi.org/10.1088/0960-1317/14/6/R01

[7] Woias, P. 2005. "Micropumps—Past, Progress and Future Prospects." *Sensors and Actuators B: Chemical* 105, no. 1, pp. 28–38. doi: http://dx.doi.org/10.1016/j.snb.2004.02.033

[8] Ramos, A., A. Gonzalez, A. Castellanos, N.G. Green, and H. Morgan. 2003. "Pumping of Liquids with AC Voltages Applied to Asymmetric Pairs of Microelectrodes." *Physical Review E*, 67, no. 5: 056302–1. doi: http://dx.doi.org/10.1103/PhysRevE.67.056302

[9] Rouabah, H.A., B.Y. Park, R.B. Zaouk, H. Morgan, M.J. Madou, and N.G. Green. 2011. "Design and Fabrication of an Ac-Electro-Osmosis Micropump with 3D High-Aspect-Ratio Electrodes Using Only SU-8." *Journal of Micromechanics and Microengineering* 21, no. 3: 035018. doi: http://dx.doi.org/10.1088/0960-1317/21/3/035018

[10] Voldman, J., M.L. Gray, M. Toner, and M.A. Schmidt. 2002. "A Microfabrication-Based Dynamic Array Cytometer" *Analytical Chemistry* 74, no. 16, pp. 3984–90. doi: http://dx.doi.org/10.1021/ac0256235

[11] Bazant, M.Z., and B. Yuxing. 2006. "Theoretical Prediction of Fast 3d AC Electro-Osmotic Pumps." *Lab on a Chip* 6, no. 11, pp. 1455–61. doi: http://dx.doi.org/10.1039/B608092H

[12] Squires, T.M., and M.Z. Bazant. 2006. "Breaking Symmetries in Induced-Charge Electroosmosis and Electrophoresis." *Journal of Fluid Mechanics* 560, pp. 65–101. doi: http://dx.doi.org/10.1017/S0022112006000371

[13] Sharma, S., A. Khalajhedayati, T.J. Rupert, and M.J. Madou. 2014. "SU8 Derived Glassy Carbon for Lithium Ion Batteries." *ECS Transactions* 61, no. 7, pp. 75–84. doi: 10.1149/06107.0075ecst 2014

[14] Ramos, A., H. Morgan, N.G. Green, and A. Castellanos. 1999. "AC Electrokinetics: A Review of Forces in Microelectrode Structures." *Journal of Physics D: Applied Physics* 31, no. 18, pp. 2338–53. doi: http://dx.doi.org/10.1088/0022-3727/31/18/021

[15] Ramos, A., H. Morgan, N.G. Green, and A. Castellanos. 1999. "AC Electric-Field-Induced Fluid Flow in Microelectrodes." *Journal of Colloid and Interface Science* 217, no. 2, pp. 420–22. doi: http://dx.doi.org/10.1006/jcis.1999.6346

[16] Green, N.G., A. Ramos, A. González, H. Morgan, and A. Castellanos. 2000. "Fluid Flow Induced by Nonuniform ac Electric Fields in Electrolytes on Microelectrodes. I. Experimental Measurements." *Physical Review E* 61, no. 4, pp. 4011–18. doi: http://dx.doi.org/10.1103/PhysRevE.61.4011

[17] González, A., A. Ramos, N.G. Green, A. Castellanos, and H. Morgan. 2000. "Fluid Flow Induced by Nonuniform ac Electric Fields in Electrolytes on Microelectrodes. II. A Linear Double-Layer Analysis." *Physical Review E*, 61, no. 4, pp. 4019–28. doi: http://dx.doi.org/10.1103/PhysRevE.61.4019

[18] Green, N.G., A. Ramos, A. González, H. Morgan, and A. Castellanos. 2000. "Fluid Flow Induced by Nonuniform ac Electric Fields in Electrolytes on Microelectrodes. III. Observation of Streamlines and Numerical Simulation." *Physical Review E*, 66, no. 2: 026305. doi: http://dx.doi.org/10.1103/PhysRevE.66.026305

[19] Garcia-Sanchez, P., A. Ramos, N.G. Green, and H. Morgan. 2006. "Experiments on AC Electrokinetic Pumping of Liquids Using Arrays of Microelectrodes." *IEEE Transactions on Dielectrics and Electrical Insulation* 13, no. 3, pp. 670–77. doi: http://dx.doi.org/10.1109/TDEI.2006.1657983

[20] Castellanos, A., A. Ramos, A. González, N.G. Green, and H. Morgan. 2003. "Electrohydrodynamics and Dielectrophoresis in Microsystems: Scaling Laws." *Journal of Physics D: Applied Physics* 36, no. 20, pp. 2584–97. doi: http://dx.doi.org/10.1088/0022-3727/36/20/023

[21] Ranganathan, S., R. McCreery, S.M. Majji, and M. Madou. 2000. "Photoresist-Derived Carbon for Microelectromechanical Systems and Electrochemical Applications." *Journal of the Electrochemical Society* 147, no. 1, pp. 277–82. doi: http://dx.doi.org/10.1149/1.1393188

[22] Wang, C.L., G.Y. Jia, L.H. Taherabadi, and M.J. Madou. 2005. "A Novel Method for the Fabrication of High-Aspect Ratio C-MEMS Structures." *Journal of Microelectromechanical Systems* 14, no. 2, pp. 348–58. doi: http://dx.doi.org/10.1109/jmems.2004.839312

[23] Madou, M.J. 2011. *Manufacturing Techniques for Microfabrication and Nanotechnology*. Boca Raton, FL: CRC Press.

[24] Madou, M.J. 2011. *From MEMS to Bio-MEMS and Bio-NEMS: Manufacturing Techniques and Applications*. Boca Raton, FL: CRC Press.

[25] Hsia, B., M.S. Kim, M. Vincent, C. Carraro, and R. Maboudian. 2013. "Photoresist-Derived Porous Carbon for On-Chip Micro-Supercapacitors." *Carbon* 57, pp. 395–400. doi: http://dx.doi.org/10.1016/j.carbon.2013.01.089

[26] Park, B.Y., L. Taherabadi, C. Wang, J. Zoval, and M.J. Madou. 2005. "Electrical Properties and Shrinkage of Carbonized Photoresist Films and the Implications for Carbon Microelectromechanical Systems Devices in Conductive Media." *Journal of the Electrochemical Society* 152, no. 12, pp. 136–43. doi: http://dx.doi.org/10.1149/1.2116707

[27] Morgan, H., and N.G. Green. 2003. *AC Electrokinetics: Colloids and Nanoparticles*. Baldock, Hertfordshire, UK: Research Studies Press.

[28] Park, B.Y., and M.J. Madou. 2005. "3-D Electrode Designs for Flow-Through Dielectrophoretic Systems." *Electrophoresis* 26, no. 19, pp. 3745–57. doi: http://dx.doi.org/10.1002/elps.200500138

[29] Martinez-Duarte, R., H.A. Rouabah, N.G. Green, M. Madou, and H. Morgan. 2007. *Proceedings of the Eleventh International Conference on Miniaturized Systems for Chemistry and Life Sciences MicroTAS*, pp. 826–28.

[30] Martinez-Duarte, R., R.A. Gorkin, K. Abi-Samrab, and M.J. Madou. 2010. "The Integration of 3D Carbon-Electrode Dielectrophoresis on a CD-Like Centrifugal Microfluidic Platform." *Lab on a Chip* 10, no. 8, pp. 1030–43. doi: http://dx.doi.org/10.1039/b925456k

[31] del Carmen Jaramillo, M., E. Torrents, R. Martınez-Duarte, M.J. Madou, and A. Juarez. 2010. "On-Line Separation of Bacterial Cells by Carbon-Electrode Dielectrophoresis." *Electrophoresis* 31, no. 17, pp. 2921–28. doi: http://dx.doi.org/10.1002/elps.201000082

[32] Martinez-Duarte, R., P. Renaud, and M.J. Madou. 2011. "A Novel Approach to Dielectrophoresis Using Carbon Electrodes." *Electrophoresis* 32, pp. 2385–92. doi: http://dx.doi.org/10.1002/elps.201100059

CHAPTER 3

Carbon MEMS for Selected Lab-on-a-Chip Applications

Monsur Islam, Rucha Natu, and Rodrigo Martinez-Duarte*

Clemson University, USA

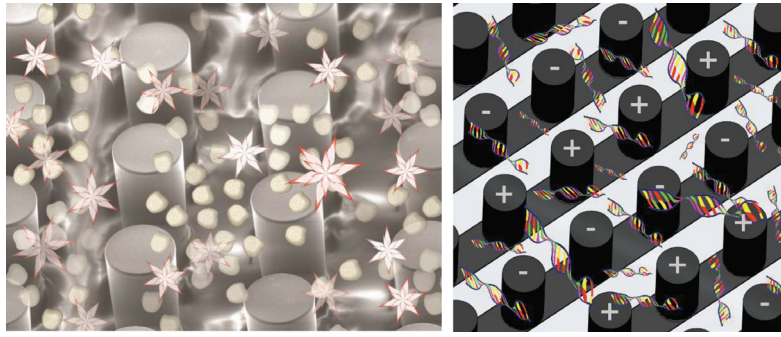

3.1 INTRODUCTION

Lab-on-a-chip, or LOC, is a term describing the integration of laboratory processing steps into a monolithic device. These processes would include sample pretreatment, purification, sorting, amplification, and signal detection. Advantages of LOC devices include rapid analysis and the fact that an LOC device eliminates the need for skilled personnel to perform a clinical assay. The need for low sample volume can also be an advantage of LOC devices in some applications, *say for relatively high-concentration*

* Corresponding author: Prof. Rodrigo Martinez-Duarte, Department of Mechanical Engineering, Clemson University, USA. E-mail: rodrigm@clemson.edu

DNA analysis. However, sample volumes in the order of milliliters may be required in other applications, such as blood analysis to detect the pathogen causing sepsis. The concept of LOC has generated significant interest worldwide; the promise of *shrinking* a whole traditional laboratory into a single device is indeed enticing for a large number of reasons. Different technical challenges have so far prevented the implementation of a full LOC, and references to a chip-in-the-lab instead have emerged recently [1]. In particular, sample pretreatment remains a significant and often overlooked challenge. It is still a daunting task to process raw, clinically relevant samples using a single device. Nevertheless, commercial LOC devices that target at least one type of sample preparation are now available and are successfully used in clinical settings, for example, i-STAT by Abbott Point of Care Inc., Piccolo® xpress from Abaxis Inc, LabChip®90 by Caliper Life Sciences, and Vena8 Endothelial+™ by Cellix.

In this chapter, we present selected LOC capabilities enabled by the carbon microelectromechanical systems (C-MEMS) fabrication technique. Carbon electrodes in microfluidic networks allow for many exciting possibilities. Here we focus on their use in dielectrophoresis-enabled particle manipulation and in electrical lysis. Biosensing and electroosmotic flow are few other capabilities of carbon electrodes and are addressed in other chapters in this book.

Dielectrophoresis (DEP) refers to the motion induced on polarizable particles when under the influence of a spatially nonuniform electric field, **E**. The magnitude of the DEP force depends on the strength of the E^2 gradient, the dimensions of the particle, and the difference between the polarization properties of the media and the targeted particles. Such force is zero if there is no gradient or the polarizability of the media is equal to that of the particle. DEP is advantageous over other particle separation techniques such as flow cytometry or fluorescence-activated cell sorting (FACS) and magnetophoresis or magnetic-activated cell sorting (MACS®) because discrimination between different particles is based solely on their intrinsic physical properties, such as surface structure and internal compartmentalization, and not on external tags like antibody-linked fluorophores or magnetic nanoparticles. Such physical properties determine the particle's dielectric properties and give it a characteristic dielectric phenotype. DEP has been demonstrated in a variety of applications, ranging from the manipulation of cells and bacteria to the separation of proteins and other molecules.

As described earlier, an E^2 gradient is necessary to induce a DEP force on the targeted particle(s). Different methods to establish such gradient exist, and all involve some sort of electrodes, either in direct contact with the media containing the particle or capacitively coupled to it. Our group previously published an extensive review of the

different fabrication techniques readily available to develop DEP-based microfluidic devices [2]. Here, we will focus on the use of 3D carbon electrodes in close contact with the sample volume. First, we delve into carbon-electrode dielectrophoresis (carbonDEP) and then explore the use of the same electrodes for cell lysis. The use of carbon electrodes yields some key benefits that make their use in LOC an attractive alternative to other electrode materials. For example, carbon has a much wider electrochemical stability window than metals commonly used in the field, such as gold and platinum, and therefore affords higher applied voltages and higher field magnitudes in a given solution without electrolyzing it [3]. The electrical conductivity of glass-like carbon [4] is lower than that of metals, but suitable electric fields for DEP and lysis can be generated by polarizing carbon electrodes with voltages in the range of tens of volts (AC). The use of carbon electrodes yields other advantages such as excellent biocompatibility [5], remarkable chemical inertness in almost all solvents or electrolytes [6, 7], and excellent mechanical properties [8].

The use of 3D structures that cover the entire height of a flow channel is presented here as an enabling improvement toward practical LOC applications. The use of such structures greatly improves throughput and efficiency of DEP and lysis devices by reducing the mean distance of any particle to the closest electrode surface, where the E^2 gradient is usually the strongest. This is in contrast to the performance achieved when using more traditional 2D (planar) electrodes positioned at the bottom of a flow channel. In the latter case, many targeted particles remain in the bulk volume of the channel and are far from the electrode surfaces.

This chapter details the fabrication and use of carbon electrodes to enable DEP and lysis in LOC devices. It starts with a brief overview of the fundamentals behind DEP and electrical lysis. The next section is then devoted to the details of the fabrication of carbon electrodes. A brief overview of how carbonDEP has been used for enrichment and purification of yeast cells, *Mycobacterium smegmatis,* and λ-DNA then follows. The chapter closes with a section on how carbon electrodes are used for high-throughput electrical lysis.

3.2 BACKGROUND

3.2.1 DIELECTROPHORESIS

The DEP force on a spherical particle is given by Equation 3.1. Although this equation varies with the shape of the particle [9], for a spherical particle, the DEP force varies with particle size r, magnitude and direction

of ∇E_{rms}^2, permittivity of the media ε_m, and the magnitude of the real part of the Clausius–Mossotti factor or f_{CM}. This factor, detailed in Equation 3.2, describes the difference in polarizability between the targeted particle and its surrounding media (ε_p* being the complex permittivity of the particle, and ε_m* the complex permittivity of the medium). Complex permittivity is given by Equation 3.3, with permittivity ε and conductivity σ of the particle or the medium and the frequency f of the applied electric field. j represents the imaginary number $\sqrt{-1}$.

$$\vec{F}_{DEP} = 2\varepsilon_m r^3 \,\mathrm{Re}\left[f_{CM}\right]\nabla E_{rms}^2 \tag{3.1}$$

$$\mathrm{Re}\left[f_{cm}\right] = \frac{\left(\varepsilon_p^* - \varepsilon_m^*\right)}{\left(\varepsilon_p^* + 2\varepsilon_m^*\right)} \tag{3.2}$$

$$\varepsilon^* = \varepsilon - \frac{j\sigma}{2\pi f} \tag{3.3}$$

Besides contributing to the scale of the DEP force, the Clausius–Mossotti factor solely determines the direction of the particle movement. A positive sign of Re[f_{CM}] means that the particle movement is toward the strongest field and is known as positive DEP or pDEP. A negative value of Re[f_{CM}] indicates negative DEP or nDEP, meaning particles move to the regions of weakest electric field. The reader may find further details on the theory behind DEP in the works by other authors [9, 10]. In practical terms, pDEP is achieved when the particle is more polarizable than the media at a given field frequency; nDEP is obtained in the opposite case. Examination of Equation 3.3 clarifies the importance of the field frequency on the complex permittivity. The same particle may be influenced by a pDEP force at one frequency but by an nDEP force at another frequency, even though the suspending media remains the same. It is that exact behavior we exploit to implement a particle separation protocol later in this chapter. A number of different particles can be trapped and released at different times by just changing the frequency of the field. Other experimental parameters of interest include properties of the media, such as conductivity, pH, viscosity η, and osmolality; frequency (including DC) and magnitude of the polarizing signal; and in flow through experiments, the velocity v of the fluid that determines the Stokes drag force ($F_{DRAG} = 6\pi\eta r v$) acting on the particle.

3.2.2 ELECTRICAL LYSIS

Every cell is enclosed by a plasma membrane. Some cells like bacteria and plant cells also feature a cell wall. A plasma membrane is a lipid bilayer structure, 4 to 10 nm thick with a large collection of proteins embedded in it. Transport of ions through the membrane is highly regulated by transmembrane channel proteins, for example, the sodium–potassium exchange pump, and under normal circumstances, the membrane itself can be regarded as highly nonconducting. For example, the membrane conductivity of yeast cells has been calculated to be 2.5×10^{-7} S·m^{-1} [11]. Cell lysis is a common and important sample preparation step in fields such as metabolomics, genomics, and proteomics, where it is mainly used to extract intracellular components for further analysis. Although the rupture of the cell membrane can be performed in a variety of different ways including chemical [12], electrical [13], mechanical [14], and optical [15], our interest is in electrical cell lysis. A good review of the different lysis techniques is given by Kim et al. [16]. The application of large direct currents (DC) or low-frequency AC electric fields to a cell induces a large potential drop across the plasma membrane that can cause dielectric breakdown, membrane rupture, and a significant increase in membrane conductivity. The length of the electric field pulse is also important, longer times lead to a more rapid cell death. Under specific circumstances, membrane breakdown may also be referred to as electroporation or electropermeabilization. Although cell lysis is commonly used for extraction, it can also be optimized to introduce different agents such as DNA, enzymes, and antibodies into the cell or to create new hybrids by electrofusion [17].

The transmembrane potential V_m is given by Equation 3.4. Experimental parameters of importance include the electric field magnitude E, frequency f, particle radius r, and the conductivity σ of both the particle cytoplasm and the suspending media. α is the angle between the field lines and a normal from the center of the particle to a point of interest on the membrane. It has been shown that membrane breakdown occurs when the potential across the membrane is above the threshold value, specific to the kind of cell but usually between 0.4 and 1 V [18]. For example, the maximum potential for neurons is only 0.4 V [19]. The membrane potential V_m of a spherical particle under an AC electric field can be calculated as [18]

$$V_m = \frac{1.5E\, r \cos\alpha}{\sqrt{(1+2\pi\, f\, \tau)^2}} \tag{3.4}$$

where the time constant τ of the membrane is given by

$$\tau = rC_{mem}\left(\frac{1}{\sigma_{cyto}} + \frac{1}{2\sigma_{media}}\right) \tag{3.5}$$

where C_{mem} is the capacitance of the membrane, σ_{cyto} the conductivity of the cytoplasm, and σ_{media} the conductivity of the suspending media. Equation 3.4 assumes that the membrane conductivity can be neglected and the membrane thickness is much smaller than the cell radius and that the induced membrane potential is sufficiently high to neglect the resting membrane potential (the relatively static membrane potential of quiescent cells) [19]. In general, suspending media with high electric conductivity as well as high strong electric fields with low frequency are desired to maximize cell lysis.

3.3 FABRICATION

In a nutshell, the fabrication process of carbon electrodes starts with a two-step photopatterning of a carbon precursor on a suitable substrate and is followed by high-temperature treatment of this precursor geometry in an inert atmosphere. The entire process to make carbon electrodes for LOC devices is illustrated in Figure 3.1. SU-8 has been used extensively by these and other authors as the carbon precursor. SU-8 is a negative epoxy-based photoresist and is commercially available from Gersteltec Sarl or MicroChem Corporation. The material carbonizes and densifies upon heat treatment at 900°C, and thus viable substrates for fabrication include refractory materials such as silicon, silicon oxide, sapphire, and fused silica. However, a substrate may not be necessary for some applications, and free-standing carbon microparts can be achieved as well [20, 21]. If optical transparency

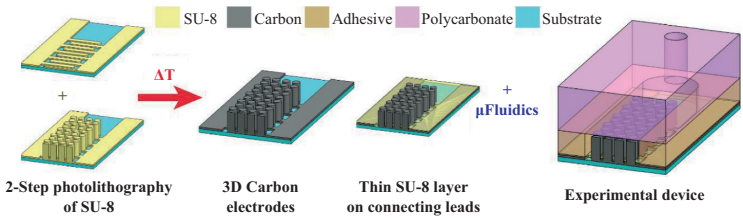

Figure 3.1. Fabrication process of carbon electrodes showing cross sections at different steps. Choice of substrate includes fused silica and silicon. See further details in the text.

is required, fused silica is a good choice for substrate material, given its thermal, mechanical, and optical properties, as well as its relatively affordable price. Indeed, a transparent substrate often improves the versatility of a devices and makes them more amenable for integration with other components. For example, the use of fused silica facilitates the rapid, continuous determination of cell concentration in a microchannel embedded in it using techniques such as spectrophotometry. A transparent substrate also enables the use of an inverted microscope for experimental visualization. The fabrication process varies depending on the substrate used, mainly due to the differences in the thermal expansion coefficients [20] and reflective properties of different materials [20, 22, 23]. For example, the processing of SU-8 on fused silica requires lower exposure doses than those used to initiate cross-linking of an SU-8 layer of similar thickness deposited on a silicon substrate because of the higher reflectivity of fused silica [23]. Furthermore, it is crucial to implement a hard bake at 190°C after the development of SU-8 structures on fused silica. This hard bake improves the adhesion of the polymer structure to the substrate and prevents the SU-8 from peeling off during carbonization [23]

Carbonization of the photopatterned SU-8 structures is performed at 900°C with a heating ramp of 5 to 10°C/min in an inert atmosphere, typically nitrogen, to convert the SU-8 structures into 3D carbon electrodes. Near-isometric shrinkage occurs during carbonization as detailed by Martinez-Duarte, Renaud, and Madou [23]. After carbonization, a thin SU-8 layer, ~2 μm, is patterned around the carbon electrodes to planarize the surface around the base of the electrodes and insulate the connecting leads. Carbon electrode arrays of different geometries, optimizing shapes and dimensions of individual electrode, as well as the spacing between electrodes, have been used for different LOC applications [23–31]. An advantage of the C-MEMS process when using SU-8 is the fact that changes in geometry can easily be implemented by changing the photolithography mask.

The microfluidic channel for the 3D carbon electrodes is fabricated separately from the carbon electrodes. The microchannel is cut from a pressure-sensitive adhesive (PSA) layer using a cutter plotter and is aligned to channel inlet and outlets drilled into a polycarbonate top. The thickness of the PSA is chosen according to the height of the 3D carbon electrodes. For example, a 100-μm-thick PSA film is used for 90-μm-high electrodes. Manual alignment between the substrate with the carbon electrodes and the microfluidic channel is performed to position the electrode array within the channel. Finally, the device is sealed using a rolling laminator. The complete fabrication process has been detailed by Martinez-Duarte, Renaud, and Madou [23].

3.4 SELECTED LOC APPLICATIONS

In this section, we first detail recent applications of carbonDEP as an active filter for the trapping and purification of selected particles. All these applications are based on a similar experimental protocol featuring three main steps: (1) trap targeted particles on the electrode array using pDEP; (2) hold the trapped particles on the electrodes while a washing solution is flowed through the channel; and (3) depolarize the electrodes to release the targeted particles for collection at the exit of the channel. This general protocol allows for the enrichment and purification of a selected particle population from a given sample. Three DEP-enabled active filter applications are introduced: (a) elimination of natural contaminants to increase sensitivity of polymerase chain reaction (PCR)-based protocols, (b) enrichment of bacterial persisters from an antibiotic-treated sample; and (c) trapping of lambda DNA. A final application we present is about the use of 3D carbon electrodes for electrical cell lysis. The reader is referred to many more publications regarding the use of carbon electrodes for DEP [23, 24, 26, 28–31], including the integration of carbonDEP with centrifugal microfluidics toward an automatic sample preparation platform [30].

3.4.1 ELIMINATION OF NATURAL CONTAMINANTS TO INCREASE THE SENSITIVITY OF PCR-BASED PROTOCOLS

Both PCR and real-time PCR are nowadays the methods of choice for the rapid molecular analysis of an extensive number of samples. Several PCR protocols have been optimized to increase sensitivity, but some samples are still challenging to analyze because of the presence of polymerase inhibitors. Common inhibitors include bile salts in feces, heavy metals and humic substances in soil, collagen in food samples, heme in blood, phenolic compounds, and proteinases in milk [32–34]. Unfortunately, these are just a few examples in a rather long list. In many instances, protocols for DNA extraction from complex environmental samples cannot completely prevent coextraction of PCR-inhibiting compounds [35], and approaches to overcome PCR failure owing to inhibitors are constantly being developed. Reported strategies to overcome PCR inhibition include sample-washing steps, density gradient centrifugation, gel electrophoresis, column chromatography, and even the use of additives such as bovine serum albumin [36, 37]. However, these methods tend to be cumbersome,

time consuming, and often expensive. In spite of the wide variety of approaches reported, interference of certain inhibitors with PCR is still a major concern when analyzing several types of samples.

3D carbonDEP is presented here as a viable alternative to prepare samples before PCR processing. This work is the result of an interdisciplinary collaboration between the authors and a group at the Institute of Bioengineering of Catalonia lead by Prof. Antonio Juarez. The aim was to demonstrate the practical use of DEP as a laboratory-based sample preparation tool that can significantly improve the sensitivity of PCR analysis, not only with cells cultured in conventional growth media but with natural samples as well. The full details of these experiments have been published elsewhere [25]. The samples used in such work all featured *Saccharomyces cerevisiae* cells, grown following standard protocols, but resuspended in different media: (1) Sabouraud broth (known for not interfering with PCR analysis), (2) fermented grape must, and (3) media spiked with different amounts of humic acids. Here we focus on the results obtained when the sample was spiked with humic acids, the most prevalent PCR inhibitors in soils and natural surface waters [32, 38]. First, the limit of detection (LOD) of yeast cells in samples with different concentrations of humic acids was determined using only PCR. This was then compared to the LOD of yeast cells in similar samples that had been prepared using carbonDEP enrichment and purification. The goal was to demonstrate that the sensitivity to *S. cerevisiae* cells achievable by PCR in a sample containing humic acids could be increased by trapping, washing, and resuspending yeast cells in a PCR-inhibitor-free media, that is, Sabouraud broth, using 3D carbonDEP.

If present in the sample, humic acids appear to be able to form complexes with the extracted DNA. Such complexes are not easily separable and can thus easily mask the presence of targeted DNA. The importance of this work was the removal of humic acids from a sample, an important step that could enable PCR detection of targeted organisms in an environmental sample. The first step was to assess the minimal concentration of humic acids that inhibits PCR detection of yeast cells. To this end, an overnight culture of *S. cerevisiae* cells in Sabouraud broth was split into fractions and supplemented with humic acids in a concentration range from 1 to 100 μg/ml. Samples were then analyzed using PCR to detect *S. cerevisiae* cells. The maximal concentration of humic acids that still allowed for the detection of yeast cells was 10 μg/ml as shown in Figure 3.2a. In order to verify the capability of the carbonDEP chip to remove humic acids from a sample and increase the sensitivity of the PCR protocol as used before, an overnight culture of *S. cerevisiae* in Sabouraud broth was first diluted

with deionized water and then fractioned into seven 1 ml samples. Humic acids were added to each of them in a concentration ranging from 10 to 100 µg/ml. Two hundred microliters of each of these seven samples were independently subjected to a DEP-based sample preparation protocol where such fractions were flowed at 20 µl/min through a polarized electrode array, at 5 MHz and 10 V_{pp}, to trap viable yeast cells. The trapped cells were then washed with clean Sabouraud media for 30 minutes and finally released for retrieval at the channel exit by turning the field off. The first eluate, 9.8 µl, that was retrieved after the electrodes were turned off was mixed with 0.2 µl of 1M NaOH and analyzed using PCR to detect yeast cells. The results obtained for each of the seven samples are shown in Figure 3.2b. Humic acid concentrations up to 75 µg/ml can be removed by implementing a carbonDEP-based enrichment and purification step before PCR analysis. Therefore, high-throughput 3D carbonDEP chips can be used as pre-PCR sample processing strategy to purify a population of microorganisms and significantly improve the detection sensitivity of

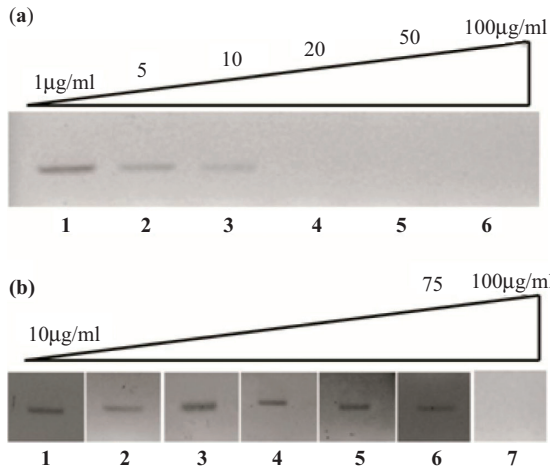

Figure 3.2. PCR results demonstrating (a) the inability of traditional PCR analysis to detect yeast cells when the concentration of humic acids is above 10 µg/ml and (b) significant improvement obtained when using a carbonDEP-based sample preparation module before PCR analysis: humic acids concentrations of up to 75 µg/ml are effectively removed from the sample to enable yeast detection.

Source: Reprinted from [25] with permission from Elsevier.

PCR. In less than 30 minutes, precise numbers of cells could be extracted from a sample volume of 200 µl, washed, and eluted in reduced volumes that are appropriate for PCR analysis. Humic acids, important PCR inhibitors, were readily washed out.

3.4.2 ENRICHMENT OF BACTERIAL PERSISTERS FROM AN ANTIBIOTIC-TREATED SAMPLE

Bacterial persistence [39] has been observed in many different bacterial species exposed to different classes of antimicrobials. Bacterial persistence is a clinically important problem, as it is thought to be responsible for treatment failures, posttherapy relapses, and lengthy treatment regimens in diseases such as leprosy and tuberculosis. Despite this, there have not been many studies to characterize these persisters or to understand the mechanism of persistence. There are several reasons behind this. First, the fraction of persister cells is often very small (10^{-3} to 10^{-6} or lower), which complicates their analysis within mixed populations comprising persister (minority) and nonpersister (majority) subpopulations. Second, the persister phenotype is not mediated through genetic changes and therefore is nonheritable. Instead, the phenotype is transient, usually lasting only as long as the drug remains in the environment. This makes it difficult to purify or isolate the tolerant subpopulations for further analysis. Third, because the persister fraction is usually a small fraction of the total population, analysis of this subpopulation is often confounded by contaminating signals from the majority nonpersister dead cells or cell debris. Besides making it difficult to treat infections, the persistence phenomenon may also increase the probability of emergence of genetic resistance, thus contributing to the short lifespan of antibiotics after they reach the market. Therefore, there is a pressing need for new experimental tools to address the phenomenon of bacterial persistence. A better characterization of the persister subpopulation could enable the design of new drugs that target the persister population and help in reducing the duration of treatment of recalcitrant infections [40, 41]. Purification would facilitate the characterization of these subpopulations using conventional ‘omics-based approaches [42, 43]. While FACS is the most common enrichment technique and provides high-throughput fractionation of cell populations, this technique requires cells to be differentially labeled, which could potentially change the phenotype of the organism.

3D carbonDEP was used for the isolation and purification of bacterial cells remaining viable after a 24-hour treatment with isoniazid (INH), a frontline antituberculosis drug. *M. smegmatis* was used in this work as a

model organism to investigate the mechanisms of dormancy or drug–cell interactions in mycobacterial infections, such as tuberculosis. In a proof-of-concept study enabled by collaboration between the Institute of Microtechnology and the Global Health Institute in EPFL in Switzerland, the label-free isolation and enrichment of viable bacterial cells, deemed persisters, was demonstrated [24]. DEP-based enrichment of intact *M. smegmatis* cells from a mixed input population of INH-treated cells comprising about 90 percent intact cells and 10 percent damaged cells was achieved. After following an experimental protocol similar to the one presented earlier, the intact cell population was enriched from 90 percent to up to 99 percent purity and recovered from the carbonDEP chip as shown in Figure 3.3. The X-axis denotes the sequential fractions recovered from the chip. Trapping from the original sample (control) happens in fractions 1 to 4 and washing in fractions 5 to 9. The purified population is retrieved in fractions 10 to 15. Therefore, DEP-based purification of persister cells could become a useful tool to provide an idealized sample to 'omics-based analysis and shed more light into the mechanisms of persistence under INH exposure. Furthermore, most of the 'omics-based approaches for downstream characterization of purified bacterial populations require a sample containing at least 10^5 to 10^6 targeted cells. As can be seen in Figure 3.3, the established DEP protocol allowed for the recovery of up to 3×10^4 intact cells, with up to 99 percent purity, per assay. Using this setup, serial assays could provide the user with enough material to perform downstream analysis.

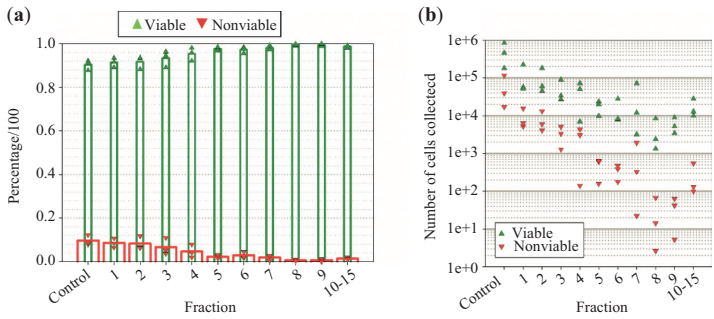

Figure 3.3. (a) The normalized percentage of intact and damaged cells for each sample fraction. The control fraction refers to the original sample, flowed through the chip without polarizing the electrode array, (b) Intact and damaged cell counts of the sequential fractions recovered during the carbon DEP assay. The control fraction refers to the original sample, flowed through the chip without polarizing the electrode array.

Source: Reproduced from Elitas et al. [24] with permission from the Royal Society of Chemistry.

3.4.3 TRAPPING OF LAMBDA DNA

The DEP behavior of DNA under the influence of an electric field gradient within a carbon electrode array has also been studied. Details of this work can be found in a collaborative work with Prof. Alexandra Ros and Dr. Fernanda Camacho-Alanis at Arizona State University [28]. Carbon electrode geometries similar to those used in the previous two applications were used to trap YOYO-labeled λ-DNA. The goal of this work was to demonstrate the capability of carbonDEP to trap biomolecules. This last consideration is important toward the development of a carbonDEP-based sample preparation module capable of (1) purifying a targeted bioparticle population; (2) conducting electrical lysis on such population; and (3) concentrating DNA and other internal organelles extracted during lysis (detailed next).

Figure 3.4a shows the experimentally observed DNA concentration around carbon electrodes upon application of an AC field. DNA concentration by pDEP was observed at frequencies between 10 and 50 kHz. A frequency of 10 kHz provides the most rapid and strongest concentration of DNA around the carbon electrodes. An experimental protocol similar to that afore-described was then implemented for the concentration and retrieval of λ-DNA. Figure 3.4b shows a characteristic elution profile for a

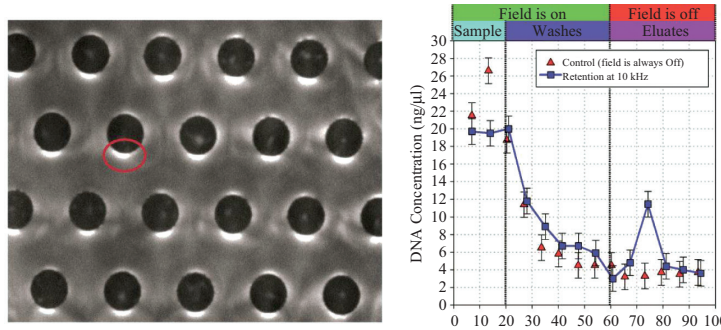

(**a**) (**b**)

Figure 3.4. (a) Fluorescence microscopy images showing DNA concentrated (red ellipse) on the surface of the electrodes by pDEP (AC signal featuring frequency of 10 kHz and magnitude 16 V_{pp}). (b) Characteristic elution profile for a λ-DNA solution with and without the application of a DEP force. Note the characteristic peak obtained at a volume of 80 µl, right after the pDEP force is turned off and the previously trapped DNA is released.

Source: Reproduced from Martinez-Duarte et al. [28] with permission from Wiley Company.

635-nM DNA solution with and without the application of an electric field. The electrode array was polarized using a sinusoidal signal with a frequency of 10 kHz and magnitude of 16 V_{pp}. The flow rate in the channel was 2 µl/min. As in the case of the previous two applications, the elution profiles are divided into three phases: (1) *sample*, where the DNA is extracted from the solution and excess volume collected at the outlet; (2) *washes*, when pure buffer is flushed through the channel; and (3) *eluates*, indicating the potential polarizing the electrodes has been turned off causing the release of the targeted particle. Figure 3.4b demonstrates that DNA is retained in the carbon-electrode device and that only after the potential was set to zero, a peak of higher DNA concentration is eluted. Such peak can clearly be distinguished from the flat baseline in the control experiment.

3.4.4 CELL LYSIS

The throughput achieved using on-chip electrical lysis is typically not enough to provide a sufficient amount of intracellular compounds to perform multiple downstream analyses such as capillary electrophoresis or PCR. Common values reported in the literature are around 1 µl/min [44–46]. Recently, a throughput of up to 333 µl/min was reported by Shahini and colleagues using nanotube-coated 2D electrodes. While their approach certainly increases the electric field gradient across the sample, it also complicates device fabrication and increases the cost of the device [47]. Lu et al. reported electroporation lysis using 3D cylindrical electrodes. Experimentally, the lysis efficiency when working with 3D electrodes is higher than that of planar designs, which results in a higher lysing percentage (30 percent) compared with 2D electrodes (8 percent) [48].

Here we summarize the use of 3D carbon electrodes to improve further the throughput of on-chip electrical cell lysis. Details of this work are published elsewhere [31]. Devices similar to those used for carbonDEP, that is, an electrode array contained in a microfluidic channel, are used for lysis. However, the polarizing voltage for lysis can be up to 130 V_{pp}. The use of frequencies in the few kilohertz is highly recommended. Lysis throughput of yeast cells can be as high as 600 µl/min at high cell density (10^8 cells/ml) at a 90 percent efficiency. Cell density in the sample, often not mentioned in the state-of-the-art literature, is very important as the use of dense samples allows for the extraction of much more material and enables the use of less-sensitive, less-expensive analysis techniques to detect low analyte concentration per cell. The system was evaluated with yeast cells and mammalian cells, and its efficiency when extracting intracellular components from mammalian cells was shown to be comparable to that of chemical lysis.

The efficiency of lysis to extract intracellular compounds was evaluated using mammalian cells. These cells do not require as high electrical fields as yeast cells to be lysed because they lack a cell wall, are bigger, and reach breakdown at lower transmembrane potentials [49], as can be deduced from Equation 3.4. The efficiency during extraction of intracellular compounds at flow rates up to 300 µl/min when using an AC signal with a magnitude of 44 V_{pp} and a frequency of 10 kHz is shown in Figure 3.5. The measured amount of luminescence is divided by the number of cells placed in the luminescence meter to provide an estimation of the luciferase extraction efficiency in arbitrary units. The use of flow rates up to 300 µl/min gives an extraction efficiency of around 0.15, which is close to the 0.17 (dashed grey line) obtained when performing a 10-minute chemical lysis of similar cells. The use of electrical lysis over chemical processes is advantageous because it does not add reagents that could interfere with downstream analysis. At low volumes, in the hundreds of microliters, the tested carbon electrodes could be up to 10 times faster than chemical lysis at extracting similar quantities of intracellular material from the sample volume. An electrical lysis module can either act as a stand-alone device to lyse cells and feed the lysate to other independent instruments or be integrated in a LOC. For example, in the context of bioreactors used in the pharmaceutical industry, an online device incorporating a sample preparation module similar to that presented here could allow for a near real-time

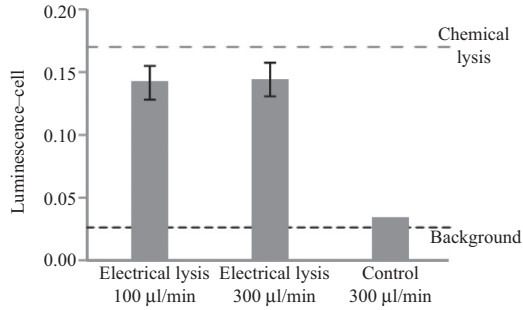

Figure 3.5. Luminescence divided by the number of cells illustrating the luciferase extracted from mammalian cells during lysis. The control experiment was performed without polarizing the electrode array. The top dashed line corresponds to the chemical lysis, whereas the bottom dashed line is the background signal for living cells.

Source: Reproduced from Mernier et al. [31].

and completely automated monitoring of the cell batch for better optimization of the production process. An LOC could be interfaced to the bioreactor to draw a sample of hundreds of microliters, prepare it in a couple of minutes and continuously feed enough material for multiple, and possibly parallel, downstream analyses.

3.5 PERSPECTIVE ON A C-MEMS LOC

A large number of steps can be included in an LOC device. Here we briefly detailed the use of carbon electrodes for particle manipulation using DEP and cell lysis. Our group is currently working on complementing these two functions with an analysis stage toward a sample-to-answer LOC targeting the rapid processing of sample volumes of few hundreds of microliters. We envision a number of electrically independent electrode arrays tailored to perform a specific function. For example, electrically independent arrays may feature different geometries and gaps between them as illustrated in Figure 3.6. The fluidics could be straight, curved, or take on any other shape. The operational principle is as follows. Particles within a certain size range are extracted from the flow, and their population is enriched and purified. These particles are then resuspended in the media that facilitates membrane rupture, either transiently as in electroporation or permanently as in lysis. Once intracellular components are released, a downstream array

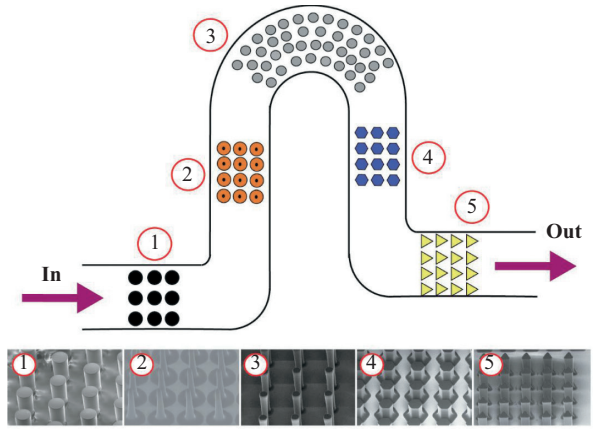

Figure 3.6. Schematic of a multistage carbonDEP device. A number of electrode arrays are embedded in a channel. Each array can be of different geometry and electrically independent.

is optimized to enrich and purify biomolecules in media that will benefit the next analysis stage. The last stage will feature carbon-based biosensors, using antibodies, aptamers, or bacteriophages to provide high specificity to the target. Potential advantages of the proposed system are high throughput, enabled by large microfluidics and 3D electrodes; efficiency; and relative low cost. C-MEMS allows for the relatively straightforward and inexpensive fabrication of 3D carbon geometries. Preliminary results by our group and collaborators include a two-stage carbonDEP device used to separate viable and nonviable cells in separate arrays [27] and a miniaturized function generator featuring multiple channels [50]. The importance of miniaturized power electronics cannot be overstated in LOC applications. The desired result is a disposable LOC and a driving platform that is relatively inexpensive to enable its use at the point of care. Besides economics, an important advantage of the proposed system is the fact that delays between sample extraction, lysis, and cytosol analysis are minimized because of the inclusion of all stages in a single device. This is critical because extracted compounds degrade with time. Furthermore, dead volume would be effectively minimized, preventing false negatives in the assay.

REFERENCES

[1] Ríos, A., M. Zougagh, and M. Avila. 2012. "Miniaturization Through Lab-on-a-Chip: Utopia or Reality for Routine Laboratories? A Review." *Analytica Chimica Acta* 740, pp. 1–11. doi: http://dx.doi.org/10.1016/j.aca.2012.06.024

[2] Martinez-Duarte, R. 2012. "Microfabrication Technologies in Dielectrophoresis Applications—A Review." *Electrophoresis* 33, no. 21, pp. 3110–32. doi: http://dx.doi.org/10.1002/elps.201200242

[3] Wang, C., G. Jia, L.H. Taherabadi, and M.J. Madou. 2005. "A Novel Method for the Fabrication of High-Aspect ratio C-MEMS Structures." *Journal of Microelectromechanical System* 14, no. 2, pp. 348–58. doi: http://dx.doi.org/10.1109/jmems.2004.839312

[4] Ranganathan, S., R. McCreery, S.M. Majji, and M. Madou. 2000. "Photoresist-Derived Carbon for Microelectromechanical Systems and Electrochemical Applications." *Journal of the Electrochemical Society* 147, no. 1, p. 277. doi: http://dx.doi.org/10.1149/1.1393188

[5] Teixidor, G.T., R.A. Gorkin, P.P. Tripathi, G.S. Bisht, M. Kulkarni, T.K. Maiti, T.K. Battacharyya, J.R. Subramaniam, A. Sharma, B.Y. Park, and M. Madou. 2008. "Carbon Microelectromechanical Systems as a Substratum for Cell Growth. "*Biomedical Materials* 3, no. 3, p. 034116. doi: http://dx.doi.org/10.1088/1748-6041/3/3/034116

[6] Yamada, S., and H. Sato. 1962. "Some Physical Properties of Glassy Carbon." *Nature* 193, no. 4812, pp. 261–62. doi: http://dx.doi.org/10.1038/193261b0

[7] Cowlard, F.C., and J.C. Lewis, 1967. "Vitreous carbon—A New Form of Carbon." *Journals of Material Science* 2, no. 6, 507–12. doi: http://dx.doi.org/10.1007/bf00752216

[8] Pesin, L.A. 2002. "Structure and Properties of Glass-Like Carbon." *Journal of Materials Science* 37, no. 1, pp. 1–28. doi: http://dx.doi.org/10.1023/a:1013100920130

[9] Jones, T.B. 2003. "Basic Theory of Dielectrophoresis and Electrorotation." *IEEE Engineering Medicine Biology Magazine* 22, no. 6, pp. 33–42. doi: http://dx.doi.org/10.1109/memb.2003.1304999

[10] Pethig, R. 2010. "Review Article-Dielectrophoresis: Status of the Theory, Technology, and Applications." *Biomicrofluidics* 4, pp. 1–35. doi: http://dx.doi.org/10.1063/1.3456626

[11] Markx, G.H., Y. Huang, X. Zhou, and R. Pethig. 1994. "Dielectrophoretic Characterization and Separation of Micro-Organisms." *Microbiology* 140, no. 3, pp. 585–91. doi: http://dx.doi.org/10.1099/00221287-140-3-585

[12] Irimia, D., R.G. Tompkins, and M. Toner. 2004. "Single-Cell Chemical Lysis in Picoliter-Scale Closed Volumes Using a Microfabricated Device." *Analytical Chemistry.* 76, no. 20, pp. 6137–43. doi: http://dx.doi.org/10.1021/ac0497508

[13] Han, F., Y. Wang, C.E. Sims, M. Bachman, R. Chang, G.P. Li, and N.L. Allbritton. 2003. "Fast Electrical Lysis of Cells for Capillary Electrophoresis." *Analytical Chemistry* 75, no. 15, pp. 3688–96. doi: http://dx.doi.org/10.1021/ac0341970

[14] Di Carlo, D., K.-H. Jeong, and L.P. Lee. 2003. "Reagentless Mechanical Cell Lysis By Nanoscale Barbs in Microchannels for Sample Preparation." *Lab on a Chip* 3, no. 4, pp. 287–91. doi: http://dx.doi.org/10.1039/b305162e

[15] Rau, K.R., A. Guerra, A. Vogel, and V. Venugopalan. 2004. "Investigation of Laser-Induced Cell Lysis Using Time-Resolved Imaging." *Applied Physics Letters* 84, no. 15, p. 2940. doi: http://dx.doi.org/10.1063/1.1705728

[16] Kim, J., M. Johnson, P. Hill, and B.K. Gale. 2009. "Microfluidic Sample Preparation: Cell Lysis and Nucleic acid Purification." *Integrative Biology (Camb)* 1, no. 10, pp. 574–86. doi: http://dx.doi.org/10.1039/b905844c

[17] Neumann, E., A.E. Sowers, and C.A. Jordan. 1989. *Electroporation and Electrofusion in Cell Biology*. New York: Plenum Publishing Corporation.

[18] Zimmermann, U., and G.A. Neil. 1996. *Electromanipulation of cells*. Boca Raton, FL: CRC Press.

[19] Heida, T., J.B.M. Wagenaar, W.L.C. Rutten, and E. Marani. 2002. "Investigating Membrane Breakdown of Neuronal Cells Exposed to Nonuniform Electric Fields by Finite-Element Modeling and Experiments." *IEEE Transactions Biomedical Engineering* 49, no. 10, pp. 1195–203. doi: http://dx.doi.org/10.1109/tbme.2002.803503

[20] Martinez-Duarte, R., M.J. Madou, G. Kumar, and J. Schroers. 2009. "A Novel Method for Amorphous Metal Micromolding Using Carbon MEMS." In *Transducers 2009—2009 International Solid-State Sensors, Actuators and Microsystems Conference,* Vol. 2, pp. 188–91. Denver, CO: IEEE. doi: http://dx.doi.org/10.1109/sensor.2009.5285533

[21] Martinez-Duarte, R. 2009. *Fabrication of Carbon Micro Molds*. Irvine, CA: University of California.

[22] Martinez-Duarte, R. 2010. *Label-Free Cell Sorting Using Carbon-Electrode Dielectrophoresis and Centrifugal Microfluidics*. Irvine, CA: University of California.

[23] Martinez-Duarte, R., P. Renaud, and M.J. Madou. 2011. "A Novel Approach to Dielectrophoresis Using Carbon Electrodes." *Electrophoresis* 32, pp. 2385–92. doi: http://dx.doi.org/10.1002/elps.201100059

[24] Elitas, M.R., Martinez-Duarte, N. Dhar, J.D. McKinney, and P. Renaud. 2014. "Dielectrophoresis-Based Purification of Antibiotic-Treated Bacterial Subpopulations." *Lab Chip* 14, no. 11, 1850–57. doi: http://dx.doi.org/10.1039/c4lc00109e

[25] Jaramillo, M.D.C., R. Martínez-Duarte, M. Hüttener, P. Renaud, E. Torrents, and A. Juárez. 2013. "Increasing PCR Sensitivity by Removal of Polymerase Inhibitors in Environmental Samples by Using Dielectrophoresis." *Biosensors and Bioelectronics* 43, pp. 297–303. doi: http://dx.doi.org/10.1016/j.bios.2012.12.049

[26] Jaramillo, M.D.C., E. Torrents, R. Martínez-Duarte, M.J. Madou, and A. Juárez. 2010. "On-Line Separation of Bacterial Cells by Carbon-Electrode Dielectrophoresis." *Electrophoresis* 31, no. 17, pp. 2921–28. doi: http://dx.doi.org/10.1002/elps.201000082

[27] Martinez-Duarte, R., J. Andrade-Roman, S.O. Martinez, and M. Madou. 2008. "A High Throughput Multi-Stage, Multi-Frequency Filter and Separation Device Based on Carbon Dielectrophoresis." *NSTI-Nanotech* 3, pp. 316–19. ISBN 978-1-4200-8505-1.

[28] Martinez-Duarte, R., F. Camacho-Alanis, P. Renaud, and A. Ros. 2013. "Dielectrophoresis of Lambda-DNA Using 3D Carbon Electrodes." *Electrophoresis* 34, no. 7, pp. 1113–22. doi: http://dx.doi.org/10.1002/elps.201200447

[29] Martinez-Duarte, R., S. Cito, E. Collado-Arredondo, S.O. Martinez, and M.J. Madou. 2008. "Fluido-Dynamic and Electromagnetic Characterization of 3D Carbon Dielectrophoresis with Finite Element Analysis." *Sensors Transducers Journal* 3, pp. 25–36.

[30] Martinez-Duarte, R., R.A. Gorkin, K. Abi-Samra, and M.J. Madou. 2010. "The Integration of 3D Carbon-Electrode Dielectrophoresis on a CD-Like Centrifugal Microfluidic Platform." *Lab on a Chip* 10, no. 8, pp. 1030–43. doi: http://dx.doi.org/10.1039/b925456k

[31] Mernier, G., R. Martinez-Duarte, R. Lehal, F. Radtke, and P. Renaud. 2012. "Very High Throughput Electrical Cell Lysis and Extraction of Intracellular Compounds Using 3D Carbon Electrodes in Lab-on-a-Chip Devices." *Micromachines 3*, no. 4, pp. 574–81. doi: http://dx.doi.org/10.3390/mi3030574

[32] Schriewer, A., A. Wehlmann, and S. Wuertz. 2011. "Improving qPCR Efficiency in Environmental Samples by Selective Removal of Humic acids WITH DAX-8." *Journals of Microbiological Methods* 85, no. 1, pp. 16–21. doi: http://dx.doi.org/10.1016/j.mimet.2010.12.027

[33] Alaeddini, R. 2012. "Forensic Implications of PCR Inhibition—A Review." *Forensic Science International Genetics* 6, no. 3, pp. 297–305. doi: http://dx.doi.org/10.1016/j.fsigen.2011.08.006

[34] Pontiroli, A., E.R. Travis, F.P. Sweeney, D. Porter, W.H. Gaze, S. Mason, V. Hibberd, J. Holden, O. Courtenay, and E.M.H. Wellington. 2011."Pathogen Quantitation in Complex Matrices: a Multi-Operator Comparison of DNA Extraction Methods with a Novel Assessment of PCR Inhibition." *PLoS One* 6, no. 3, p. e17916. doi: http://dx.doi.org/10.1371/journal.pone.0017916

[35] Van Doorn, R., M.M. Klerks, M.P.E. van Gent-Pelzer, A.G.C.L. Speksnijder, G.A. Kowalchuk, and C.D. Schoen. 2009. "Accurate Quantification of Microorganisms in PCR-Inhibiting Environmental DNA Extracts by a Novel Internal Amplification Control Approach Using Biotrove OpenArrays." *Applied and Environmental Microbiology* 75, no. 22, pp. 7253–60. doi: http://dx.doi.org/10.1128/aem.00796-09

[36] Radstrom, P., R. Knutsson, P. Wolffs, M. Dehlenborg, C. Lofstrom, K. Sachse, and J. Frey. 2003. "PCR Detection of Microbial Pathogens." *Methods in Molecular Biology* 216, pp. 31–50.

[37] Rock, C., A. Alum, and M. Abbaszadegan. 2010. "PCR Inhibitor Levels in Concentrates of Biosolid Samples Predicted by a New Method Based on Excitation-Emission Matrix Spectroscopy." *Applied Environmental Microbioogy* 76, no. 24, pp. 8102–09. doi: http://dx.doi.org/10.1128/aem.02339-09

[38] Sagova-Mareckova, M., L. Cermak, J. Novotna, K. Plhackova, J. Forstova, and J. Kopecky. 2008. "Innovative Methods for Soil DNA Purification Tested in Soils with Widely Differing Characteristics." *Applied Environmental Microbiology* 74, no. 9, pp. 2902–07. doi: http://dx.doi.org/10.1128/aem.02161-07

[39] Bigger, J. 1944. "Treatment of Staphylococcal Infections with Penicillin by Intermittent Sterilisation." *Lancet* 244, no. 6320, pp. 497–500.doi: http://dx.doi.org/10.1016/s0140-6736(00)74210-3

[40] Fauvart, M., V.N. De Groote, and J. Michiels. 2011. "Role of Persister Cells in Chronic Infections: Clinical Relevance and Perspectives on Anti-Persister Therapies." *Journal of Medical Microbiology* 60, no. 6, pp. 699–709. doi: http://dx.doi.org/10.1099/jmm.0.030932-0

[41] Dhar, N., and J.D. McKinney. 2007. "Microbial Phenotypic Heterogeneity and Antibiotic Tolerance." *Current Opinion Microbiology* 10, no. 1, pp. 30–38. doi: http://dx.doi.org/10.1016/j.mib.2006.12.007

[42] Altelaar, A.F.M., J. Munoz, and A.J.R. Heck. 2013. "Next-Generation Proteomics: Towards an Integrative View of Proteome Dynamics." *Nature Reviews Genetics* 14, no. 1, pp. 35–48. doi: http://dx.doi.org/10.1038/nrg3356

[43] Stower, H. 2013. "Diluting the Immune Response with Decoys." *Nature Reviews Genetics* 14, no. 9, p. 596. doi: http://dx.doi.org/10.1038/nrg3565

[44] Lee, D.W., and Y.-H. Cho. 2007. "A Continuous Electrical Cell Lysis Device Using a Low DC Voltage for a Cell Transport and Rupture." *Sensors and Actuators B Chemical* 124, no. 1, pp. 84–89.doi: http://dx.doi.org/10.1016/j.snb.2006.11.054

[45] Wang, H.-Y., A.K. Bhunia, and C. Lu. 2006. "A Microfluidic Flow-Through Device for High Throughput Electrical Lysis of Bacterial Cells Based on Continuous dc Voltage." *Biosensors Bioelectronics* 22, no. 5, pp. 582–88. doi: http://dx.doi.org/10.1016/j.bios.2006.01.032

[46] Lu, H., M. A. Schmidt, and K.F. Jensen. 2005. "A Microfluidic Electroporation Device for Cell Lysis." *Lab on a Chip* 5, no. 1, pp. 23–29. doi: http://dx.doi.org/10.1039/b406205a

[47] Shahini, M., and J.T.W. Yeow. 2011. "Carbon Nanotubes for Voltage Reduction and Throughput Enhancement of Electrical Cell Lysis on a Lab-on-a-Chip." *Nanotechnology* 22, no. 32, p. 325705. doi: http://dx.doi.org/10.1088/0957-4484/22/32/325705

[48] Lu, K.-Y., A.M. Wo, Y.-J. Lo, K.-C. Chen, C.-M. Lin, and C.-R. Yang. 2006. "Three Dimensional Electrode Array for Cell Lysis via Electroporation." *Biosensors Bioelectronics* 22, no. 4, pp. 568–74. doi: http://dx.doi.org/10.1016/j.bios.2006.08.009

[49] Shirakashi, R., C.M. Köstner, K.J. Müller, M. Kürschner, U. Zimmermann, and V.L. Sukhorukov. 2002. "Intracellular Delivery of Trehalose into Mammalian Cells by Electropermeabilization." *Journal of Membrane Biology* 189, no. 1, pp. 45–54. doi: http://dx.doi.org/10.1007/s00232-002-1003-y

[50] Gomez-Quiñones, J., H. Moncada-Hernandez, O. Rossetto, R. Martinez-Duarte, B.H. Lapizco-Encinas, M. Madou, and S.O. Martinez-Chapa. 2011. "An Application Specific Multi-Channel Stimulator for Electrokinetically-Driven Microfluidic Devices." In *New Circuits and Systems Conference (NEWCAS)*, pp. 350–53. doi: http://dx.doi.org/10.1109/newcas.2011.5981242

CHAPTER 4

GLASSY CARBON MICROELECTRODES FOR NEURAL SIGNAL SENSING AND STIMULATION

Sam Kassegne,* Maria Vomero, Pieter van Niekerk,
and Mieko Hirabayashi

MEMS Research Lab, Department of Mechanical Engineering, San Diego State University, 5500 Campanile Drive, San Diego, CA 92182, USA.

4.1 INTRODUCTION

Carbon is finding increasing interest in the micro- and nanofabrication research community as a material of choice, where its good conductivity, electrochemical stability in ionic solutions, excellent response to chemical treatments for surface property modifications, and biocompatibility make it an ideal choice for electrochemical applications [1–3]. With the added dimension of new research and clinical efforts in interfacing electronics with the human body for recording as well as stimulation, to address numerous health conditions, carbon—as an engineering material—is poised to garner even more interest from the research and industry

* Address correspondence to Sam Kassegne, Professor of Mechanical Engineering, MEMS Research Lab, Department of Mechanical Engineering, College of Engineering, San Diego State University, 5500 Campanile Drive, CA 92182-1323. E-mail: kassegne@mail.sdsu.edu • Tel: (619) 594-1815.

communities. Of particular interest is glassy carbon (GC), one of the forms of carbon that has excellent performance in a wide range of environmental conditions such as large pH variations, ionic concentration variations, and temperature changes. Further, the ability to derive GC from pyrolysis of polymer precursors that are amenable to patterning through lithography process has made this material an ideal choice for a growing number of applications such as electrodes, biofuels, and batteries [4–9].

As research interest in interfacing microelectrodes with tissues for applications ranging from signal sensing and stimulation of neural signals in brain–computer interface for sensorimotor control to chronic pain management and deep brain stimulation increases, electrode materials with superior long-term performance are finding renewed importance [10–16]. Specifically, over the past several years, there has been significant research concentration on progress in neural signal sensing and stimulation using a variety of electrode architectures (from single neuron recording [17, 18] to complex networks of neurons in large cortical and sensory areas in brains using multiple electrodes [19–21]). Current efforts in recording over a larger area of the brain are further driving innovations in architecture of electrode devices, including the mechanism of implantation deployment of the probes themselves.

For such probes, it is clear that not only the architectures of the electrode structures but also material properties are of considerable importance. Therefore, with this in mind, research has concentrated on conventional and well-known materials that exhibit biocompatibility. As further progress in robust long-term clinical application of bioprobes is pursued, fundamental challenges in their long-term high-fidelity performance in recording electrical and electrochemical signals from implantable probes need to be addressed [22]. For example, long-term implanted bioprobes such as neural prosthetic electrodes face a dynamically changing harsh and corrosive biological environment where, for instance, pH and ionic concentration fluctuate and physical arrangement of blood vessels, neurons, and glial cells shift [23–24]. On the other hand, from the tissue point of view, long-term implantable electrodes pose mechanical and electrochemical strains that affect the structure and health of cells of interest. As neurons are surrounded and supported by glial cells, the introduction of a foreign material or device, such as a neuromuscular electrical stimulator of sorts, has the potential of being rejected [23]. In general, the more invasive the device, the more severe is the reaction from the glial cells. Therefore, the minimization and elimination of these chronic detrimental interactions between electrodes and tissue is a major research focus. For this, the major barriers that need to be overcome are

the mismatch in mechanical stiffness, hardness, electrical impedance, and electrochemical behavior of the electrodes with that of tissue, which cause damages and risks associated with long-term tissue responses to implanted electrodes [23].

Overcoming these barriers, therefore, is a major research interest in the field of neural probes. As starter, from a materials point of view, such barriers could be addressed by modifying the mechanical and electrochemical properties of the electrodes themselves. Along this line, new classes of electrode materials that are amenable to material property tailorability as well as easy fabrication such as through lithographic patterning have been long sought. As recent research has shown, GC, which is derived from the pyrolysis of negative-tone photoresist polymers, fits these requirements well [9]. These GC electrodes have been shown to have excellent conductivity, corrosion resistance, electrochemical stability in ionic solutions, and excellent response to chemical treatments for surface property modifications [25–27]. In addition, it has been shown that GC electrode offers the ability to tailor its mechanical, electrical, and electrochemical properties by varying pyrolysis conditions such as maximum temperature, duration of pyrolysis, and ramp rate [9, 28]. Using these unique properties of GC, microelectrode structures suitable for neural probe arrays with (i) tailorable mechanical stiffness that is more compliant than microwires and silicon shanks, offering a much better stiffness matching with tissues; (ii) tailorable hardness for a better hardness matching with soft tissues; and (iii) tailorable electrical and electrochemical characteristics for better impedance and electrochemistry matching with neurons and tissues have been introduced [9]. This has been accompanied by validation of the electrodes as neural probes through in vivo animal model tests.

This potential for a wider use of GC electrodes is, however, hampered by difficulties such as (i) incompatibility of the high-temperature pyrolysis process with the complementary metal-oxide semiconductor (CMOS) process, (ii) incompatibility of GC bump pads with soldering to metal wires, and (iii) thermal mismatch between resin and silicon substrate that produces warping of traces. Further, these electrodes have almost universally been fabricated on rigid silicon and quartz wafers—and hence severely limiting their wide applications—mainly because of the high-temperature process of pyrolysis that is integral to the fabrication. Therefore, this necessitates the introduction of a new hybrid architecture where the electrodes are made of patternable GC, the traces and bump pads are microfabricated from metals, and then the whole structure is mounted on a flexible substrate such as polyimide. This technology is demonstrated through the microfabrication of a novel biocompatible

GC-based array of microelectrodes on a flexible substrate for applications in neural sensing and simulations, particularly for μECoG (microelectrocorticography) systems. This use of GC electrodes made through microelectromechanical system (MEMS) fabrication (hence, glassy carbon microelectrodes [GC-MEMS]) integrated with flexible substrates for any complete in vivo signal reading and stimulation system supported by animal model test is the first reported case of patternable carbon in neural probe applications.

4.2 BACKGROUND IN NEURAL PROBES

Research in neural probes dates as far back as 1939 [29]. The first functioning neural prosthetic was a cochlear implant that was developed to restore hearing [30]. Over the years, neuroprosthetics developed rapidly into various fields such as interfacing to the heart [31], restoring motor function [32], and bridging spinal cord injury [33]. Initial research efforts in neural probes used glass tubes filled with electrolytes, where the glass acted as a biocompatible insulator [34]. Later developments involved single and arrayed metal wire electrodes that were manually assembled in an array format [35–36]. With MEMS technology, however, microfabrication of arrays of micrometer-sized electrodes of a variety of shapes using silicon, metal, and insulating substrate materials such as polyimide have been made possible, spawning newer generation of neural electrodes [37–40]. As a result, MEMS-based microelectrodes for neural recording and stimulation have, in general, enabled miniaturized and low-power high-density multisite arrays capable of interrogating a wider area. Owing to the ease of manufacturing and structural flexibility that they offer, there has also been an increase in interest in polymer-based microelectrodes, particularly for electrocorticography (ECoG) applications [41–46]. Tsang et al. had reported a flexible multisite array of several electrodes for insect flight biasing using neural simulation [46]. Rubehn et al. reported a 252-channel epicortical ECoG electrode array made of platinum electrodes on polyimide foil substrate [42]. Their array had independently addressable electrodes and is among the largest electrode array reported so far. A stretchable electrode array for noninvasive wearable applications was developed by Ma et al., who used polydimethylsiloxane substrate along with metal electrodes. However, their array was limited to electromyography and electroencephalography with no reported application in neural probing at the cortex or brain [43].

4.3 FABRICATION PROCESS AND PACKAGING

The GC microelectrodes are fabricated using standard negative photolithographic techniques for silicon wafers followed by pyrolysis in a furnace as described in detail in Chapter 1 of Volume 1 of this book and elsewhere [47–48]. The metal traces and bump pads are patterned through the metal lift-off process. In summary, the microfabrication process for the GC electrodes mounted on flexible substrates is shown in Figure 4.1 [9]. It starts with deposition of SU-8 negative tone resist on an oxidized silicon substrate followed by lithography for patterning the microelectrode array. Subsequent to lithography, pyrolysis is carried out in a closed ceramic tube furnace in vacuum or a forming gas atmosphere through gradual heating to about 1,000°C followed by cooling to room temperature [27]. The pyrolysis process is followed by spin coating the first layer of polyimide, patterning it, and then curing it. Subsequently, negative resist is spun and patterened to form a sacrificial layer for the metal traces and bump pads. Then, an adhesion layer of chromium is sputtered, followed by a layer of gold. The negative resist sacrificial layer is then removed in acetone. Then, an insulation layer of polyimide is spin coated, patterned, and cured followed by oxygen plasma etching. Subsequently, the thin-film devices are released using buffered aqueous hydrogen fluoride solution, and the devices are soaked in deionized water, cleaned, and dried. For comparison purposes, during characterization, a similar microelectrode structure with metal (gold) electrodes is microfabricated. The process is essentially the same, except negative lithography and pyrolysis steps are replaced by a simple one-step metal deposition. Figure 4.2a and 4.2b shows scanning electron microscope (SEM) pictures of GC electrodes after pyrolysis and after depositing insulation layer, respectively, whereas Figure 4.2c and 4.2d show the bright-field microscope image of the released hybrid

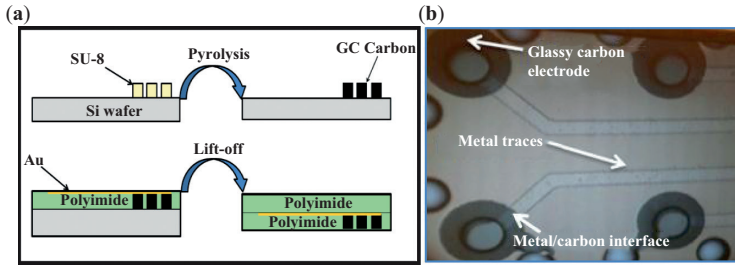

Figure 4.1. (a) Lithography and pyrolysis process for fabricating GC electrodes from a negative tone photoresist. (b) Final hybrid structure with GC electrodes and metal traces.

metal and GC electrode probe structure. The microelectrode structure is then connected to a Hirose 40-pin connector and glued to a printed circuit board (PCB) as shown in Figure 4.3b. The connectors are zero insertion force connectors and are low profile with no need for soldering or gluing on the device side. The flexible, printed, and hybrid packaging described here integrates the unique properties of GC with a convenient neural signal recording or stimulation system.

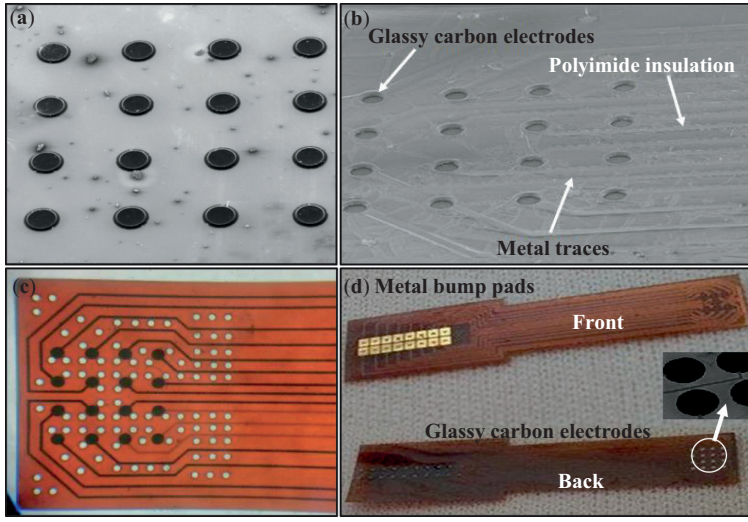

Figure 4.2. Hybrid metal and glassy carbon electrode probes. (a) SEM image of GC electrodes after pyrolysis, (b) SEM image of GC-MEMS electrodes after pyrolysis and depositing insulation layer, (c) bright-field microscope image of final microelectrode array, (d) front and back images of microelectrodes.

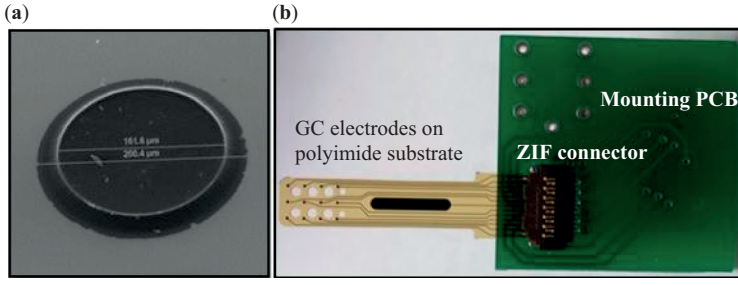

Figure 4.3. Details of a hybrid metal and glassy carbon electrode probes. (a) Microelectrode structure after pyrolysis, (b) complete µECoG device with carbon electrodes connected to Hirose 40-pin connector and glued to PCB for stability.

4.4 ELECTRODE CHARACTERIZATIONS

The suitability of GC (GC-MEMS) electrodes to neural signal reading and stimulation is determined through a variety of rigorous in vitro characterizations consisting of measuring mechanical properties (modulus and hardness), electrical impedance, electrochemical activity, determining microstructures, and in vivo testing of implanted electrodes in an animal model.

4.4.1 MECHANICAL CHARACTERIZATION

Mechanical properties (modulus and hardness) of GC materials (in the form of pillar electrodes with 20 and 700 mm height and 700 mm diameter) are measured using a nanoindentation system that consists of xy-stage for positioning specimen and a z-axis linear motion stage [9]. Load is applied until the indenter stops moving for at least five seconds. A calibrated microscope is used to measure the diamond-shaped indentation marks. Modulus and hardness are then calculated from the load–deflection relationship. The results on variation of Young's modulus and hardness with pyrolysis temperature are summarized in Figure 4.4, where it is shown that the modulus seems to vary from a minimum of ~30 GPa to a maximum of 55 GPa and the hardness from 2.6 to 7 GPa. As expected, the GC-MEMS pillars pyrolyzed to only a maximum of 600°C have the lowest values of modulus and hardness. However, for most ramping rates, except for two hours where there is no drop, the modulus values peak at

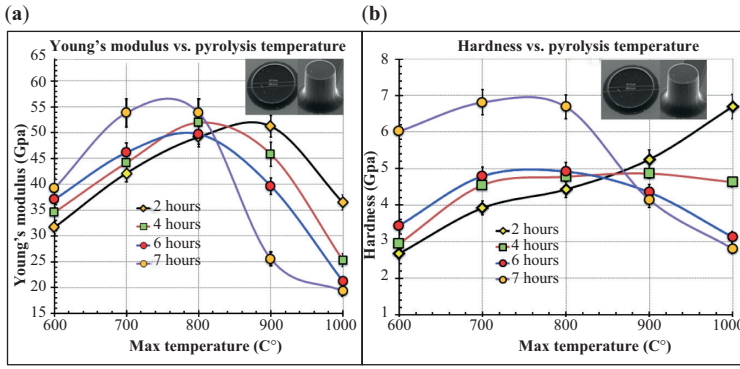

Figure 4.4. (a) Young's modulus for a variety of pyrolysis temperatures and (b) hardness of electrodes for a variety of pyrolysis temperatures. Insets show both types of pillars tested.

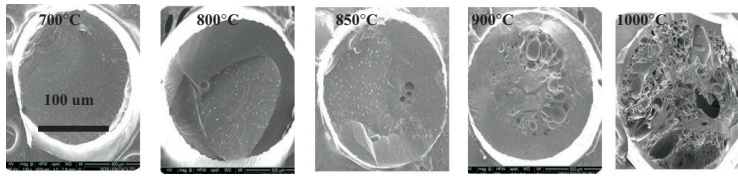

Figure 4.5. SEM images of cross section of glassy carbon pillars pyrolyzed at different temperatures, 700°C, 800°C, 850°C, 900°C, and 1,000°C. At high pyrolysis temperatures, significant pores are observed. The flow rate is kept constant for all temperatures.

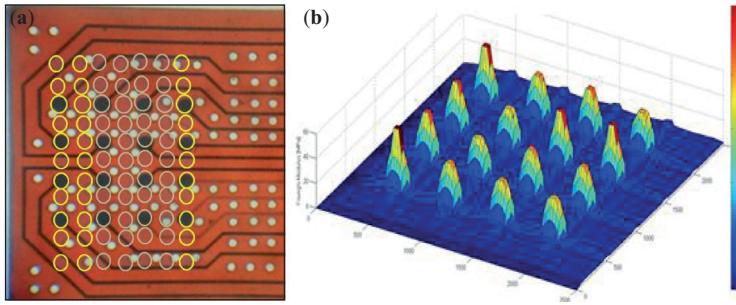

Figure 4.6. Mapping of Young's modulus of hybrid microelectrode array. (a) Testing location on the electrode sets, (b) mapping of Young's Modulus on electrode set. This demonstrates that the modulus of GC electrodes is not substantially different from those of the polyimide substrate itself.

700°C to 800°C and then drop to values as low as 20 GPa. Similar trend is seen in hardness as well. As supported by the SEM image in Figure 4.5, this is caused by the coalescing of pores resulting from escaping hydrogen and other gases. Young's modulus for unpyrolyzed negative resist (SU-8) is found to be 2 GPa and is similar to what is reported in the literature [49]. Figure 4.6 shows a mapping of the variation of the measured modulus across the complete hybrid electrode-set structure with GC electrodes and polyimide substrate.

4.4.2 ELECTRICAL CHARACTERIZATION

AC impedance analysis is carried out by contacting each individual pillar microelectrode and performing galvanostatic impedance measurement in a frequency range from 1 MHz to 1 Hz and an amplitude of 3 mA. The

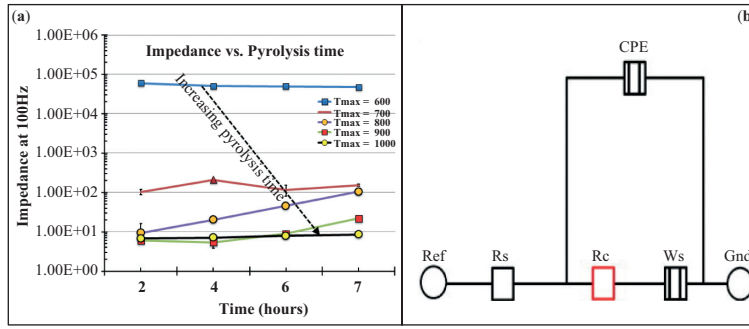

Figure 4.7. (a) Impedance for a variety of pyrolysis temperatures of electrodes at 100 Hz, (b) equivalent modified Randle circuit for the in vitro electrochemical measurement system. Rs = solution resistance, Rc = charge transfer resistance (diameter of first semicircle), Ws = Warburg coefficient, CPE = constant phase element at $\omega = 1$.

results on impedance modulation are summarized in Figure 4.7, which clearly show a decrease in impedance with pyrolysis temperature, from a high impedance of ~100 kΩ (at 100 Hz) at 600°C to as low as 10 Ω (at 100 Hz) for pyrolysis temperature of 1,000°C. The biggest drop in impedance is typically observed between 600°C and 700°C of maximum pyrolysis temperature. For GC traces (as opposed to pillars), similar impedance changes with pyrolysis temperature are observed, demonstrating the same pattern of impedance dependency on temperature for a variety of geometries.

4.4.3 ELECTROCHEMICAL CHARACTERIZATION AND CORROSION TESTS

Electrochemical impedance spectroscopy and voltage transient tests are carried out in a phosphate buffered saline (PBS) solution (0.13M NaCl, 0.022M $NaH_2PO_4 \cdot H_2O$, 0.081M $Na_2HPO_4 \cdot 7H_2O$ at pH ~7.3) for electrochemical characterizations. All in vitro measurements are made in a three-electrode cell using a large-area Pt counter electrode, Ag–AgCl reference electrode, and GC working electrode. Extensive sets of experiments are performed to determine key parameters such as CIC (charge injection capacity) and Rc (charge transfer resistance). These parameters, which quantitatively determine the electrokinetics at the surface of electrodes, are defined in an equivalent modified Randle circuit for the electrochemical system shown in Figure 4.7b [9]. The equivalent circuit consists

of solution resistance (Rs), double layer Rc, Warburg coefficient (Ws), and a constant phase element (CPE). The CPE represents an imperfect capacitor that simulates the effects of the double-layer interaction between the solution and the surface of the GC microelectrodes. CIC, the amount of charge that can move from the electrode to the solution without causing an irreversible chemical reaction (for GC, the water stability window is roughly +1 V/−1 V), is measured through a voltage transient test, with 1-ms wide rectangular, biphasic, symmetric current pulse [22]. The results on charge transfer kinetics are summarized in Figure 4.8, which shows CIC for a variety of pyrolysis temperatures. At a maximum pyrolysis temperature of 1,000°C, a CIC of 1 mC/cm^2 is obtained. This is substantially higher than the CIC values reported for conventional probe materials, such as Pt (0.3 mC/cm^2) and Ta_2O_5 (0.5 mC/cm^2) [22].

The effect of plasma treatment (100 W for 60 secs.) on CIC for a variety of pyrolysis temperatures is also summarized in Figure 4.8b, where it is shown that plasma etching increases CIC, at least for a short term. However, as shown in the figure, the effect of oxygen plasma etching was temporary; the reason being that some of the reactive species created by plasma etching oxidize quite easily in open atmosphere [25]. Nonetheless, the surface roughness caused by plasma etching could account for the slight remaining long-term increase in CIC that was observed; an increase of roughness increases the ability of the material to inject charges to the solution in the reversible range [22]. Finally, corrosion test through soaking in 300 mM H_2O_2 and PBS solution for 21 days was carried out. H_2O_2 is

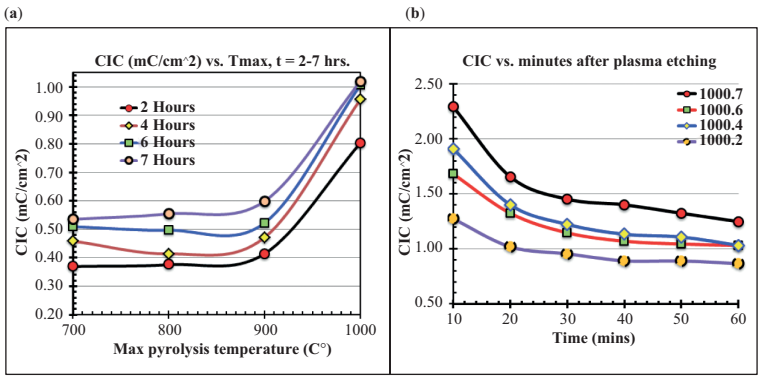

Figure 4.8. (a) CIC for a variety of pyrolysis temperatures, (b) Transient of CIC after plasma treatment for a variety of pyrolysis temperatures (100 W for 60 secs.) showing a temporary effect.

typically released by cells as inflammatory response to electrodes, its concentration being in few millimolar range [50]. The concentration used here is quiet high and is intended to demonstrate the robustness of GC electrodes in corrosive environment. The SEM images as well as FTIR (Fourier transform infrared spectroscopy) results summarized in Figure 4.9 demonstrate no significant corrosion after three weeks of continuous exposure to this buffer, particularly for electrodes pyrolyzed at 1,000°C. Pyrolysis at 700°C seems to have some level of corrosion by-products such as phenyl group, C–O and C=O groups, when exposed to high concentration of peroxide. In comparison, tungsten and platinum electrodes exhibit substantial corrosion even at 30 mM H_2O_2 [51].

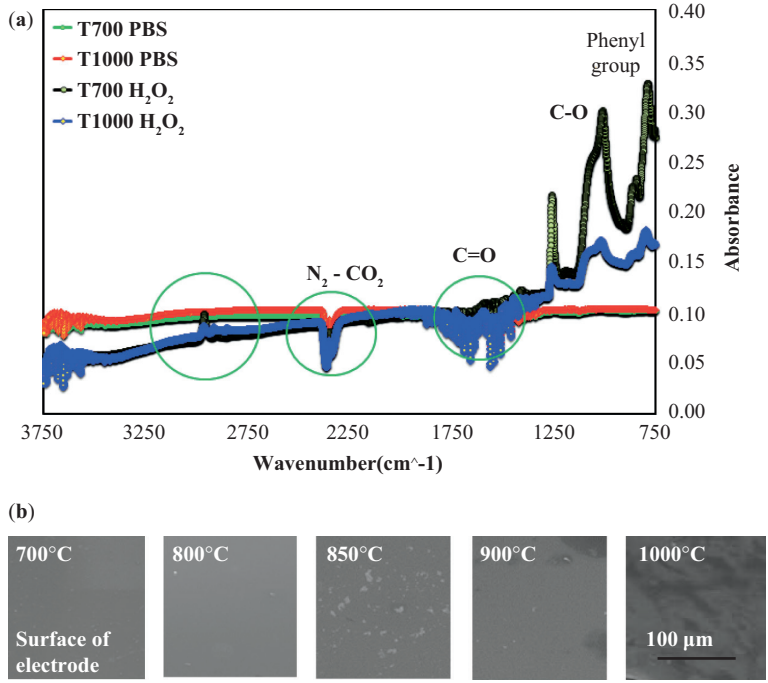

Figure 4.9. Corrosion test in GC-MEMS electrodes involving 21 days of immersion in 300 mM H_2O_2 and PBS. (a) FTIR image shows that for pyrolysis temperature of 1,000°C (both in PBS and H_2O_2), the amount of corrosion by-products such as C–O and C=O structures and phenyl groups is substantially low as compared to electrodes pyrolyzed at 700°C. Note that 300 mM H_2O_2 is almost 10 times the concentration typically seen in inflammatory responses. (b) SEM images of surfaces of electrodes after corrosion test.

4.4.4 RAT IN VIVO STIMULATION AND RECORDING (μECOG)

Following the protocol approved by the Institutional Review Board , in vivo tests involving an anesthetized rat implanted with μECoG array with GC-MEMS microelectrodes was carried out. The μECoG array has 4 × 4 GC-MEMS microelectrode array of 20 μm height and 200 μm diameter, fabricated using the same conditions as presented in Section 4.3. In summary, as shown in Figure 4.10, an incision was made and a small part of the subject's skull removed followed by careful cutting and peeling of the dura mater on top of the brain exposing a 2 mm × 4 mm window to the motor cortex of the brain. The μECoG array was then connected through a Hirose connector to a recording amplifier and then inserted underneath the dura, on top of the left hemisphere of the brain, in the region of the motor cortex. For benchmarking purposes, a similar array was fabricated using metal microelectrodes. As the subject was anesthetized and the recordings are acute, brain activity was fairly low and the recorded signal was not highly modulated (as expected); but beta activity (power in the ~15 to 30 Hz band) was recorded indicating continuing cortical synchronization as can be seen in Figure 4.11. Oscillations in ECoG signals represent synchronization of cortical activity in a local area. Changes in beta band oscillations are related to motor activity. Stimulation results were also obtained, where clear, isolated movements in the nose, whiskers, right forelimb, and right shoulder were elicited by stimuli between 400 and 700 μA delivered to different electrodes on the 16 electrode array, indicating the ability of selective stimulation of the devices (Figure 4.10). In general, the GC arrays were able to provide higher signal power in this low-frequency region than the gold arrays. The large signal-to-noise ratio (SNR) in the beta activity recordings of both the gold and the gold–carbon hybrid

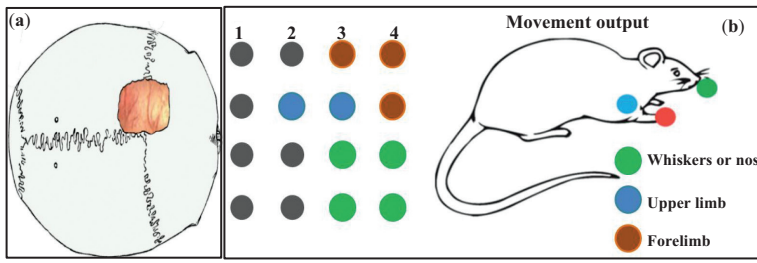

Figure 4.10. (a) Location of implantation of both Au or Pt and Au or C μECoG devices at motor cortex of rat model. (b) Electrode map and locations of elicited movements in anesthetized rat model.

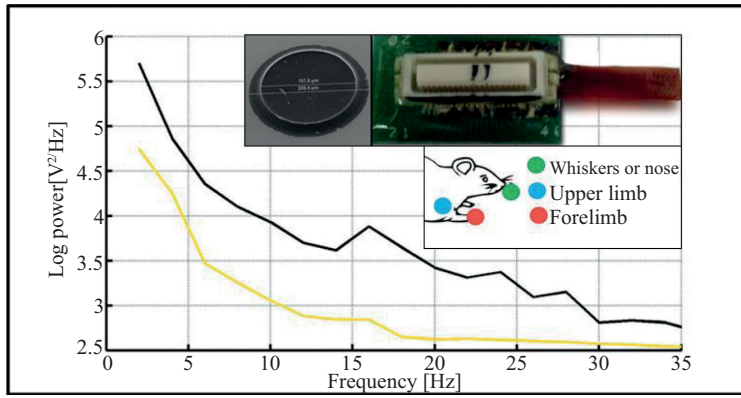

Figure 4.11. Comparison of power spectra recordings by metal and GC-MEMS microelectrodes on anesthetized rat. Beta activity at 15 to 30 Hz band that is captured better by GC-MEMS electrode is clearly visible. The μECoG array shown in the inset had 4 × 4 GC-MEMS microelectrodes of 20 μm height and 200 μm diameter and was placed underneath the dura in the motor cortex region. Locations where movements were elicited through stimulation are also shown.

devices here indicate good connections and low impedance, as well as a strong capability to record biological signals. Further, larger and broader SNR was observed in the GC arrays with a corresponding bump in the power spectra.

4.4.4.1 STIMULATION FOR EVOKED MUSCULAR MOVEMENTS

In addition, Figure 4.12 shows another set of results from electrical stimulation of the median nerve in the forearm of the anesthetized rat, at stimuli between 400 and 700 μA and current large enough to evoke a movement. In electrodes over the forelimb area of sensorimotor cortex on the opposite side of the brain, large evoked responses were seen. Figure 4.12 shows differential recordings (between two electrodes, i.e., electrodes one and two and electrodes three and four) at two electrode sites; the earlier peaks are direct responses of sensory pathways to the stimulus, whereas the later peaks are sensory responses to the movement that was elicited by the stimulation. The power spectrum of these data sets shows peaks in the delta and theta bands, again typical of an anesthetized rat; the higher frequency bands, which are of more interest in a behaving animal, are fairly quiet in this scenario.

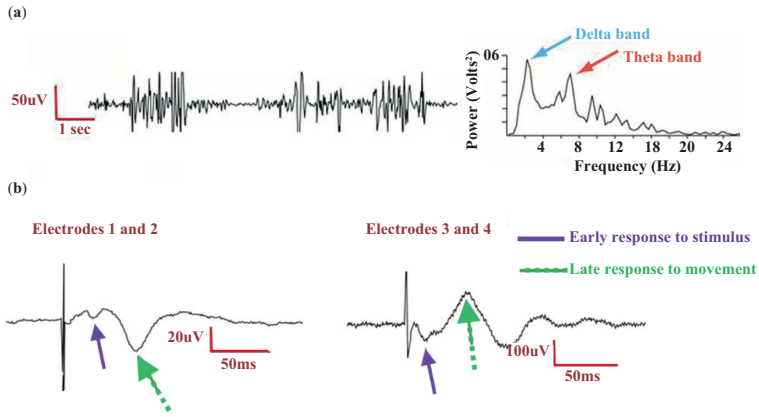

Figure 4.12. (a) Raw ECoG recording and power spectra between two electrodes (i.e., differential recording) with wide bandpass showing oscillations typical for an anesthetized rat. (b) Differential recordings (i.e., between two electrodes) at two sites of evoked potentials when the median nerve in the forearm of the anesthetized rat is stimulated. The earlier peaks are direct responses of sensory pathways to the stimulus; the later peaks are probably sensory responses to the movement that was elicited by the stimulation.

4.5 DISCUSSION

The success of GC as a material of choice for neural signal reading and stimulation depends, largely, on its electrochemical properties and its ability to be tunable in its key relevant properties. Here a detailed discussion of possible factors that drive this tunability is warranted. The mechanism of tunability of GC-MEMS electrodes is better understood by closely looking at the characteristics of the ensuing material as the patterned resists are pyrolyzed. The possible chemical structural shape of GC has been described as *ribbonlike geometry of entangled carbon sheets* through high-resolution transmission electron microscopy, where it is suggested that GC contains sp^2-hybridized carbons with six-membered rings as well as five- and seven-membered rings [52]. As suggested by the Raman spectroscopy (not shown here), the pyrolysis of polymer precursors at different maximum temperatures gives rise to GCs with different packing of this *entangled* and dispersed carbon sheets [9, 52]. Subsequently, therefore, the distribution and shape of these ensuing ribbons of carbon sheets is the key determinant of the electrical and mechanical properties of glassy carbon material. In addition, the key structural changes that happen in the carbonization stage of

pyrolysis (500°C to 1,200°C), where H_2 attached to carbon (C) is cleaved off and removed and aromatic networks become connected, determine the material characteristics of the ensuing GC. Intuitively, therefore, it appears that a compact packing in well-defined direction could give rise to higher modulus. Also, a compact packing of conductive carbon sheets will result in lower impedance. These effects, then, support the observation that varying the pyrolysis temperature and ramping rates, give rise to different packing and distribution of ribbons of carbon sheets, thereby accounting for the tunability reported here. In addition, the introduction of pores at higher pyrolysis temperatures, as gases such as hydrogen escape during carbonization, contributes to a rearrangement of the packing of these carbon sheets.

AC impedance, on the other hand, seems to follow a monotonic decrease with increasing pyrolysis temperature for a variety of geometries. Along the same line, electrochemical characterizations show interesting and monotonically increasing trends where higher pyrolysis temperature clearly results in higher CIC, low R_c, and increased faradaic reactions at the electrode–electrolyte interface, and hence faster electrokinetics. In addition, what is, perhaps, most important aspect here is the interplay between each parameter and an investigation on whether each of these parameters can be modified independent of each other. In general, the correlation between the mechanical, electrical, and electrochemical parameters seems linear, with exceptions observed in some temperature ranges. While the optimum conditions for most of the parameters seem to be around 1,000°C, the modulus and hardness, however, peak at a moderately lower temperature range of 700°C to 800°C for most pyrolysis ramping rates (with the exception of two hours. The impedance and Raman spectroscopy measurements seem to provide a more distinct and narrower range (600°C to 700°C) on the transition from mainly resistive behavior to conductive regime [9]. This is well corroborated by the tightening of the difference between D-band and G-band of Raman spectroscopy at 700°C, where conductive regime starts). The reduction in modulus at higher pyrolysis temperatures because of pores inside the pillars is not entirely unwelcome; it, in fact, may be desirable as stiffness is better matched at these levels. As the optimum electrical and electrochemical properties occur at around 1,000°C, the ability to further decrease the modulus (still keeping the outer surface of electrodes intact) at this temperature further establishes this temperature range as favorable from all aspects.

Finally, the validation of GC-MEMS microelectrodes through in vivo tests offers strong supporting evidence with regard to the matching

of microelectrode properties with those of tissue properties, particularly with regard to impedance matching. As shown in Figure 4.11, beta activity (power in the ~15 to 30 Hz band) was recorded using GC-MEMS μECoG array. The oscillations in ECoG signals represent synchronization of cortical activity in a local area, whereas beta bursts (~15 to 30 Hz band) are typically thought of as a measure of cortical synchronization in an area. Further, changes in beta band oscillations are related to motor activity. As shown in Figure 4.11, GC-MEMS arrays were able to provide higher signal power (in V^2/Hz) in the recorded low-frequency region than the gold arrays, indicating a higher and broader SNR. This is due to better impedance matching, where GC-MEMS electrodes had impedance of ~1 to 10 kΩ as opposed to metals with 10 Ω impedance.

4.6 CONCLUSIONS

This chapter summarizes research progress in a novel microelectrode structure consisting of GC-MEMS patterned using traditional MEMS processes coupled with traces and bump pads made of metals and mounted on a flexible and stretchable polyimide substrate. This unique architecture combines the unique electrical and electrochemical properties of GC-MEMS with metals and, with its flexible substrate mounting, offers a new platform for electrical sensing and actuating probes. Further, GC-MEMS electrodes have higher electrokinetics at their surface enabled by higher CIC as compared to conventional metal probes, making GC a highly competitive neural probe material. More importantly, acute in vivo tests in a rat demonstrate better impedance matching that results in capturing of low-frequency beta activity neural responses accompanied with higher and broader signal and higher CIC that enables less stimulation current for eliciting motor activity.

REFERENCES

[1] Wang, Y., L. Pham, G.P.S. de Vasconcellos, and M.J. Madou. 2010. "Fabrication and Characterization of Micro PEM Fuel Cells Using Pyrolyzed Carbon Current Collector Plates." *Journal of Power Sources* 195, no. 15, pp. 4796–03. doi: http://dx.doi.org/10.1016/j.jpowsour.2010.02.050

[2] Lin, P., B. Park, and M. Madou. 2008. "Development and Characterization of a Miniature PEM Fuel Cell Stack with Carbon Bipolar Plates." *Journal of Power Sources* 176, no. 1, pp. 207–14. doi: http://dx.doi.org/10.1016/j.jpowsour.2007.10.079

[3] Kassegne, S., K. Moon, P. Martín-Ramos, M. Majzoub, G. Ozturk, K. Desai, M. Parikh, B. Nguyen, A. Khosla, and P. Chamorro-Posada. 2012. "Organic MEMS/NEMS-Based High-Efficiency 3D ITO-Less Flexible Photovoltaic Cells." *JMM (Journal of Micromechanics and Microengineering)* 22, no. 11, p. 115015. doi: http://dx.doi.org/10.1088/0960-1317/22/11/115015

[4] Martinez-Duarte, R., P. Renaud, and M.J. Madou. July 2011. "A Novel Approach to Dielectrophoresis Using Carbon Electrodes." *Electrophoresis* 32, no. 17, pp. 2385–92. doi: http://dx.doi.org/10.1002/elps.201100059

[5] Martinez-Duarte, R., R.A. Gorkin Iii, K. Abi-Samra, and M.J. Madou. 2010. "The Integration of 3D Carbon-Electrode Dielectrophoresis on a CD-Like Centrifugal Microfluidic Platform." *Lab on a Chip* 10, no. 8, pp. 1030–43. doi: http://dx.doi.org/10.1039/b925456k

[6] Hirabayashi, M., B. Mehta, B. Nguyen, and S. Kassegne. 2014. "DNA Immobilization on High Aspect Ratio Glassy Carbon (GC-MEMS) Microelectrodes for Bionanoelectronics Applications." *Journal of Microsystem Technologies*, pp. 1–7. doi: http://dx.doi.org/10.1007/s00542-014-2332-3

[7] Vahidi, N.W., M. Hirabayashi, B. Mehta, M. Rayatparvar, D. Wibowo, V. Ramesh, J. Chi, J. Calish, M. Tabares, A. Khosla, J. Mokili, and, S. Kassegne. 2014. "Bionanoelectronics Platform with DNA Molecular Wires Attached to High Aspect-Ratio 3D Metal Microelectrodes." *ECS Journal of Solid State Science and Technology* 3, no. 3, pp. Q29–36. doi: http://dx.doi.org/10.1149/2.001403jss

[8] Ranganathan, S., R. McCreey, S.M. Majji, and M. Madou. 2000. "Photoresist-Derived Carbon for Microelectromechanical Systems and Electrochemical Applications." *Journals of Electrochemical Society* 147, no. 1, pp. 277–82. doi: http://dx.doi.org/10.1149/1.1393188

[9] Kassegne, S., M. Vomero, R. Gavuglio, M. Hirabayashi, E. Özyilmaz, S. Nguyen, J. Rodriguez, E. Özyilmaz, P. van Niekerk, and A. Khosla. 2015. "Electrical Impedance, Electrochemistry, Mechanical Stiffness, and Hardness Tunability in Glassy Carbon MEMS μECoG Electrodes." *Journal of Microelectronics Engineering* 133, pp. 36–44. doi: http://dx.doi.org/10.1016/j.mee.2014.11.013

[10] Suzuki, I., M. Fukuda, K. Shirakawa, H. Jiko, and M. Gotoh. 2013. "Carbon Nanotube Multi-Electrode Array Chips for Noninvasive Real-Time Measurement of Dopamine, Action Potentials, and Postsynaptic Potentials." *Biosensors and Bioelectronics* 49, pp. 270–75. doi: http://dx.doi.org/10.1016/j.bios.2013.05.023

[11] Zachek, M.K., A. Hermans, R.M. Wightman, and G.S. McCarty. 2008. "Electrochemical Dopamine Detection: Comparing Gold and Carbon Fiber Microelectrodes Using Background Subtracted Fast Scan Cyclic Voltammetry." *Journal of Electroanalytical Chemistry* 614, no. 1, pp. 113–20. doi: http://dx.doi.org/10.1016/j.jelechem.2007.11.007

[12] Cho, S.H., H.M. Lu, L. Cauller, M. Romero-Ortega, J.B. Lee, and G.A. Hughes. 2008. "Biocompatible SU-8-Based Microprobes for Recording Neural Spike Signals from Regenerated Peripheral Nerve Fibers." *Sensors Journal IEEE* 8, no. 11, pp. 1830–36. doi: http://dx.doi.org/10.1109/jsen.2008.2006261

[13] Guyton, D.L., and F.T. Hambrecht. 1974. "Theory and Design of Capacitor Electrodes for Chronic Stimulation." *Medical Biological Engineering* 12, no. 5, pp. 613–20. doi: http://dx.doi.org/10.1007/bf02477223

[14] Vitale, F., S.R. Summerson, B. Aazhang, C. Kemere, and M. Pasquali. 2015. "Neural Stimulation and Recording with Bidirectional, Soft Carbon Nanotube Fiber Microelectrodes." *ACS Nano* 9, no. 4, pp. 4465–74. doi: http://dx.doi.org/10.1021/acsnano.5b01060

[15] Nicolelis, M.A.L., and S. Ribeiro. 2002. *"*Multiellectrode Recordings: The Next Step*." Current Opinion Neurobiology* 12*,* no. 5, pp. 602–06. doi: http://dx.doi.org/10.1016/s0959-4388(02)00374-4

[16] Negi, S., R. Bhandari, and R. Solzbacher. 2012. "A Novel Technique for Increasing Charge Injection Capacity of Neural Electrodes for Efficacious and Safe Neural Stimulation." In *34th Annual International Conference of the IEEE EMBS*, San Diego, CA: IEEE. doi: http://dx.doi.org/10.1109/embc.2012.6347151

[17] Hubel, D.H., and T.N. Wiesel. 1977. "Ferrier Lecture: Functional Architecture of Macaque Monkey Visual Cortex." In *Proceeding of the Royal Society London B* 198, no. 1130, pp. 1–59. doi: http://dx.doi.org/10.1098/rspb.1977.0085

[18] McLaughlin, D., R. Shapley, M. Shelley, and D.J. Wielaard. 2000. *"*A Neuronal Network Model of Macaque Primary Visual Cortex (V1): Orientation Selectivity and Dynamics in the Input Layer 4Calpha." In *Proceeding of the National Academy Sciences* 97, no. 14, pp. 8087–92. doi: http://dx.doi.org/10.1073/pnas.110135097

[19] Normann, R.A., D.J. Warren, J. Ammermuller, E. Fernandez, and S. Guillory. 2001. "High-Resolution Spatio-Temporal Mapping of Visual Pathways Using Multi-Electrode Arrays." *Vision Research* 41, no. 10–11, pp. 1261–75. doi: http://dx.doi.org/10.1016/s0042-6989(00)00273-x

[20] Bonini, L., M. Maranesi, A. Livi, S. Bruni, L. Fogassi, T. Holzhammer, O. Paul, and P. Ruther. 2014. "Application of Floating Silicon-Based Linear Multielectrode Arrays for Acute Recording of Single Neuron Activity in Awake Behaving Monkeys." *Biomed Tech (Berl)* 59, no. 4, pp. 273–81. doi: http://dx.doi.org/10.1515/bmt-2012-0099

[21] Hoffman, K.L., and B.L. McNaughton. 2002. "Coordinated Reactivation of Distributed Memory Traces in Primate Neocortex." *Science* 297, no. 5589, pp. 2070–73. doi: http://dx.doi.org/10.1126/science.1073538

[22] Cogan, S.F. 2008. "Neural Stimulation and Recording Electrodes." *Annual Review of Biomedical Engineering* 10, no. 1, pp. 275–309. doi: http://dx.doi.org/10.1146/annurev.bioeng.10.061807.160518

[23] Polikov, V.S., P.A. Tresco, and W.M. Reichert. October 15, 2005. *"*Response of Brain Tissue to Chronically Implanted Neural Electrodes." *Journal of Neuroscience Methods* 148, no. 1, pp. 1–18. doi: http://dx.doi.org/10.1016/j.jneumeth.2005.08.015

[24] Biran, R., D.C. Martin, and P.A. Tresco. 2005. "Neuronal Cell Loss Accompanies the Brain Tissue Response to Chronically Implanted Silicon Microelectrode Arrays." *Experimental Neurology* 195, no. 1, pp. 115–26. doi: http://dx.doi.org/10.1016/j.expneurol.2005.04.020

[25] Hirabayashi, M., B. Mehta, N.W. Vahidi, A. Khosla, and S. Kassegne. 2013. "Functionalization and Characterization of Pyrolyzed Polymer Based Carbon Microstructures for Bionanoelectronics Platforms." *Journal of Micromechanics and Microengineering* 23, no. 11, p. 115001. doi: http://dx.doi.org/10.1088/0960-1317/23/11/115001

[26] Park, B.Y., L. Taherabadi, C. Wang, J. Zoval, and M.J. Madou. 2005. "Electrical Properties and Shrinkage of Carbonized Photoresist Films and the Implications for Carbon Microelectromechanical Systems Devices in Conductive Media." *Journal of the Electrochemical Society* 152, no. 12, pp. J136–43. doi: http://dx.doi.org/10.1149/1.2116707

[27] Wang, C., G. Jia, L.H. Taherabadi, and M. Madou. 2005. "A Novel Method for the Fabrication of High-Aspect Ratio C-MEMS Structures." *Journal of Microelectromechanical Systems* 14, no. 2, pp. 348–58. doi: http://dx.doi.org/10.1109/jmems.2004.839312

[28] Sharma, S., A. Sharma, Y.-K. Cho, and M. Madou. 2012. "Increased Graphitization in Electrospun Single Suspended Carbon Nanowires Integrated with Carbon-MEMS and Carbon-NEMS Platforms." *ACS Applied Materials & Interfaces* 4, no. 1, pp. 34–39. doi: http://dx.doi.org/10.1021/am2014376

[29] Hodgkin, A.L., and A.F. Huxley. 1939. "Action Potentials Recorded from Inside a Nerve Fibre." *Nature* 144, no. 3651, pp. 710–11. doi: http://dx.doi.org/10.1038/144710a0

[30] Fayad, J.N., S.R. Otto, R.V. Shannon, and D.E. Brackmann. 2008. "Cochlear and Brainstem Auditory Prostheses 'Neural Interface for Hearing Restoration: Cochlear and Brain Stem Implants'." *Proceedings of the IEEE* 96, no. 7, pp. 1085–95. doi: http://dx.doi.org/10.1109/JPROC.2008.922577

[31] Record, C.O., P. Sleight, A.J. Gunning, J.M. Kenworthy-Browne, and M. Richings. 1971. "Treatment of Chronic Heart Block with the Lucas Induction Coil Pacemaker." *British Heart Journal* 33, no. 6, pp. 938–42. doi: http://dx.doi.org/10.1136/hrt.33.6.938

[32] Jackson, A., and J.B. Zimmermann. 2012. "Neural Interfaces for the Brain and Spinal Cord-Restoring Motor Function." *Nature Reviews Neurology* 8, no. 12, pp. 690–99. doi: http://dx.doi.org/10.1038/nrneurol.2012.219

[33] David, S., and A.J. Aguayo. November 20, 1981. "Axonal Elongation into Peripheral Nervous System "Bridges" after Central Nervous System Injury in Adult Rats." *Science* 214, no. 4523, pp. 931–33. doi: http://dx.doi.org/10.1126/science.6171034

[34] Rae, J.L., and R.A. Levis. 1992. "Glass Technology for Patch Clamp Electrodes." *Methods in Enzymology* 207, pp. 66–92. doi: http://dx.doi.org/10.1016/0076-6879(92)07005-9

[35] Scherberger, H., I. Fineman, S. Musallam, D.J. Dubowitz, K.A. Bernheim, B. Pesaran, B.D. Corneil, B. Gilliken, and R.A. Andersen. 2003. "Magnetic Resonance Image-Guided Implantation of Chronic Recording Electrodes in the Macaque Intraparietal Sulcus." *Journal of Neuroscience Methods* 130, no. 1, pp. 1–8. doi: http://dx.doi.org/10.1016/s0165-0270(03)00190-0

[36] Tsytsarev, V., M. Taketani, F. Schottler, S. Tanaka, and M. Hara. 2006. "A New Planar Multielectrode Array: Recording from a Rat Auditory Cortex." *Journal of Neural Engineering* 3, no. 4, pp. 293–98. doi: http://dx.doi.org/10.1088/1741-2560/3/4/006

[37] Wise, K.D., J.B. Angell, and A. Starr. 1970. *"*An Integrated-Circuit Approach to Extracellular Microelectrodes*." IEEE Transactions on Biomedical Engineering* BME-17, no. 3, pp. 238–47. doi: http://dx.doi.org/10.1109/tbme.1970.4502738

[38] Wise, K.D., and K. Najafi. 1991. *"*Microfabrication Techniques for Integrated Sensors and Microsystems*." Science* 254, no. 5036, pp. 1335–42. doi: http://dx.doi.org/10.1126/science.1962192

[39] Banks, D., D.J. Ewins, W. Balachandran, and P.R. Richards. 1996. "Microengineered Interfaces with the Nervous System." *IEEE Colloquium on Medical Application of Microengineering* 4, pp. 1–4. doi: http://dx.doi.org/10.1049/ic:19960085

[40] Urban, G.A., O. Prohaska, and F. Olcaytug. 2006. "Chapter 1 (Early BioMEMS Multi-Sensor Neuroprobes)" In *BioMEMS*, 1–13. Chicago, IL: Springer.

[41] Tsang, W.M., A.L. Stone, Z.N. Aldworth, J.G. Hildebrand, T.L. Daniel, A.I. Akinwande, and J. Voldman. 2010. "Flexible Split-Ring Electrode for Insect Flight Biasing Using Multisite Neural Stimulation." *IEEE Transactions on Biomedical Engineering* 57, no. 7, pp. 1757–64. doi: http://dx.doi.org/10.1109/tbme.2010.2041778

[42] Rubehn, B., C. Bosman, R. Oostenveld, P. Fries, and T. Stieglitz. 2009. "A MEMS-Based Flexible Multichannel ECoG-Electrode Array." *Journal of Neural Engineering* 6, no. 3, p. 036003. doi: http://dx.doi.org/10.1088/1741-2560/6/3/036003

[43] Ma, R., D.H. Kim, M. McCormick, T. Coleman, and J. Rogers. 2010. "A Stretchable Electrode Array for Non-Invasive, Skin-Mounted Measurement of Electrocardiography (ECG), Electromyography (EMG) and Electroencephalography (EEG)*."* In *Engineering in Medicine and Biology Society (EMBC), 2010 Annual International Conference of the IEEE*, pp. 6405–08. Buenos Aires: IEEE. doi: http://dx.doi.org/10.1109/iembs.2010.5627315

[44] Henle, C., J. Fischer, W. Meier, J. Rickert, M. Schuettler, and T. Stieglitz. 2011. *Biomed. Tech* 56.

[45] Mercanzini, A., K. Cheung, D.L. Buhl, M. Boers, A. Maillard, and P. Colin. 2008. "Demonstration of Cortical Recording Using Novel Flexible Polymer Neural Probes." *Sensors and Actuators A: Physical* 143, no. 1, pp. 90–96. doi: http://dx.doi.org/10.1016/j.sna.2007.07.027

[46] Nyberg, T., A. Shimada, K. Torimitsu, and J. Neurosci. 2007. *Methods* 160, no. 1, pp. 16–25.
[47] Wang, C., L. Taherabadi, G. Jia, S.K. Kassegne, J. Zoval, and M.J. Madou. 2004. "CarbonMEMS Architectures for 3D Microbatteries*."* In *Proceedings of the SPIE*, Vol. 5455, pp. 295–302. Strasbourg, France.
[48] Kassegne, S.K., B. Wondimu, B. Majzoub, and J. Shin. 2008. "High-Efficiency Microarray of 3-D Carbon MEMS Electrodes for Pathogen Detection Systems." In *Proceeding of the SPIE*, vol. 7266, p. 726615. San Diego, CA.
[49] Schueller, O.J.A., S.T. Brittain, C. Marzolin, and G.M. Whitesides. 1997. "Fabrication and Characterization of Glassy Carbon MEMS."*Chemistry of Materials* 9, no. 6 pp. 1399–406. doi: http://dx.doi.org/10.1021/cm960639v
[50] Leach, J.B., A.K.H. Achyuta, and S.K. Murthy. 2009. "Bridging the Divide Between Neuroprosthetic Design, Tissue Engineering and Neurobiology." *Frontiers in Neuroengineering* 2. doi: http://dx.doi.org/10.3389/neuro.16.018.2009
[51] Patrick, E., M.E. Orazem, J.C. Sanchez, and T. Nishida. 2011. "Corrosion of Tungsten Microelectrodes Used in Neural Recording Applications." *Journal of Neuroscience Methods* 198, no. 2, pp. 158–71. doi: http://dx.doi.org/10.1016/j.jneumeth.2011.03.012
[52] Sharma, S., and M.J. Madou. 2012. "Micro and Nano Patterning of Carbon Electrodes for BioMEMS." *Bioinspired Biomimetic Nanobiomaterials* 1, no. 4, pp. 252–65 (ISSN: 2045–9858, E-ISSN: 2045–9866). doi: http://dx.doi.org/10.1680/bbn.12.00010

TERMINOLOGY

1. **ECoG** (Electrocorticography). An invasive technique of sensing electrical signals from the cerebral cortex of the brain using electrodes placed on the surface of the brain.
2. **EEG** (Electroencephalography). A noninvasive technique of sensing electrical signals from the brain using electrodes placed on the scalp.
3. **EMG** (Electromyography). A noninvasive technique of sensing electrical signals produced by skeletal muscles.
4. **Dura mater**. A thick and dense inelastic membrane that lines the interior of the skull.
5. **CIC** (charge injection capacity). The amount of charge that can be delivered by the electrode to the solution without causing an irreversible chemical reaction. It is measured using voltage transients and is a function of the electrode–electrolyte interface and the geometry of the electrode.
6. **Glial cells**. These are non-neuronal cells that do not participate directly in synaptic interactions and electrical signaling. However,

they help define synaptic contacts and maintain the signaling abilities of neurons.

7. **Cortex**. The outer layer of the cerebrum that is composed of folds of neurons and axons and is responsible for activities such as learning, muscle activity, memory, and consciousness.
8. **Evoked action potential**. An electrical signal recorded from the central nervous system following stimulation.
9. **Beta activity**. A pattern of brain signal activity linked to motor behavior with frequency range from 15 to about 30 Hz.
10. **Theta band**. A pattern of brain signal activity with frequency range from 4 to 7 Hz.
11. **Delta band**. A pattern of brain signal activity with frequency range from 0.5 to 3.5 Hz.

CHAPTER 5

C-MEMS-Based on-Chip Microsupercapacitors

Richa Agrawal and Chunlei Wang

Florida International University, United States

5.1 INTRODUCTION

With the ever-changing advanced technology, reliable energy storage has become rather a prerequisite. Given the myriad of applications ranging from microelectronics to electric vehicles to large-scale stationary applications, the required electrochemical energy storage systems have become very device specific. With the recent boom in the development of miniaturized electronic systems such as wireless sensors, implantable devices, and smart cards, the demand for miniaturized power sources is at an all-time high. Miniaturized energy storage systems including microbatteries, micro fuel cells, and micro energy harvesters are anticipated to be the next-generation energy sources for such systems. However, quite akin to their larger variants, microbatteries and micro fuel cells suffer from low power densities and poor cycle lives, while energy harvesters, on the other hand, require an energy storage device in tandem to store their excess energy. Electrochemical capacitors (ECs) are known for their exceptional power capability along with outstanding cycling life. Such capacitors in their miniaturized form can both complement and replace microbatteries depending on the energy and power requirements.

Carbon microelectromechanical systems (C-MEMS) is a popular microfabrication technique that involves the pyrolysis of a patterned photoresist into carbonaceous structures and has been used for a variety of applications including lithium-ion batteries, fuel cells, ECs, electrochemical

sensors, and biosensors. The preparation of pyrolyzed carbon from organic polymeric photoresists was limited to two-dimensional architectures until 2004, when Wang and Madou at the University of California, Irvine [1] were able to fabricate microstructures with aspect ratios greater than 10. Since then, a wide variety of complex architectures have been fabricated using C-MEMS that include high-aspect-ratio pillars, suspended bridges, plates, and networks [2, 3]. The advantages of using photoresists as the precursor material for carbon are manifold: (i) photoresists can be patterned by photolithography techniques and, therefore, are capable of producing much finer features than silk screening of carbon inks [4]; (ii) photoresists are very controlled materials that form accurate and reproducible carbon electrodes with flexibility in the complexity of geometry and also three-dimensional topographies; (iii) differences in processing parameters such as temperatures and curing conditions result in varied electrical and mechanical properties; and (iv) the material properties are consistent within a given temperature range. Furthermore, the resultant carbon structures from the C-MEMS can be integrated with additive nanomaterials such as carbon nanotubes (CNTs) and graphene in order to enhance the electrochemical, mechanical, and electrical properties.

5.2 BASIC CONCEPTS

5.2.1 ELECTROCHEMICAL CAPACITORS

ECs, also colloquially referred to as *supercapacitors* or *ultracapacitors*, are a class of energy storage devices that essentially bridge the gap between conventional electrolytic capacitors and secondary batteries [5]. Hereafter, the words ECs, supercapacitors, and ultracapacitors will be used interchangeably. ECs are characterized by very high specific power, long cycle life, and modest specific energy. Figure 5.1 depicts the special positioning of ECs in the specific energy–power plot, also known as the Ragone plot.

5.2.1.1 Fundamentals of a Capacitor

A typical capacitor can be understood as a passive circuit component that stores charge in an electrostatic manner, where the energy is stored in an electrostatic field. A parallel plate capacitor consists of two parallel plates separated by a dielectric [5]. Upon the application of an external electric potential, opposite charges accumulate on the plates, generating an

electric field. The capacitance (C) of a capacitor is given as the ratio of the charge on each electrode (Q) to the potential difference between them (V):

$$C = \frac{Q}{V} = \frac{\varepsilon_0 \varepsilon_r A}{d} \tag{5.1}$$

where ε_0 is the electric permittivity of free space, ε_r is the relative permittivity, A is the area of the electrodes, and d is the distance between the electrodes. It can be seen that the capacitance is an inverse function of the distance between the electrodes, and therefore, the smaller the distance between the electrodes, the larger will be the capacitance of the device.

The most important electrochemical characteristics of any energy storage device are the energy density and power density, which can both be expressed per unit mass, per unit area, or per unit volume. Energy and power densities when normalized per unit mass are also referred to as specific energy and specific power and gravimetric energy and power densities. For a capacitor, the energy is given as

$$E = \frac{1}{2} CV^2 \tag{5.2}$$

Power, in general, is defined as the rate of delivering energy per unit time. The maximum power of a capacitor, however, is limited by the internal resistance of the system, also known as the equivalent series resistance (ESR). The maximum power that a capacitor can deliver is given as

$$P_{\max} = \frac{V^2}{4ESR} \tag{5.3}$$

It is evident that the maximum power is an inverse function of the ESR. The ESR can be measured as the iR drop in the charge-discharge curves of the capacitor. Equation 5.3, however, is the maximum power, which is usually greater than the actual power delivered by the system [5].

5.2.1.2 Charge Storage Mechanisms in Electrochemical Capacitors

Charge is stored at the electrode–electrolyte interface in ECs. Depending on the charge storage mechanism, ECs are subdivided into (i) electrochemical double-layer capacitors (EDLCs) and (ii) pseudocapacitors. A third

category of ECs known as the *hybrid electrochemical capacitor* essentially combines both the EDLCs and pseudocapacitors [5]. It should be noted that the term hybrid EC is quite generic and can refer to an EC electrode used in tandem with secondary batteries or even fuel cells. EDLCs, quite similar to electrolytic capacitors, store energy in an electrostatic manner. Charge is stored at the electrode–electrolyte interface, and the capacitance is governed by the thickness of the *double layer* also known as the Helmholtz double layer and hence the name. Upon the application of an external potential, charges accumulate at the electrode surface; the charge buildup leads to diffusion of opposite charges across the separator (membrane that separates the electrodes of an electrochemical capacitor), leading to the formation of a *double layer* on each electrode. The presence of the small double layer in addition to the high-surface electrodes enables EDLCs to possess higher energy densities than electrolytic capacitors. As the charge storage process in EDLCs is primarily electrostatic, these capacitors theoretically possess virtually endless cycle lives. However, because, in practice, the cycle life is a result of various factors such as electrode stability in the electrolyte and electrode material adhesion onto the substrate, the cycle life of such devices is typically limited to 10^5 to 10^6 cycles. Popular EDLC materials include carbon structures such as activated carbon, carbon aerogels, carbon nanostructures including a host of morphologies such as CNTs [6], onionlike carbons [7], carbon nanofibers [8], and graphene [5].

Pseudocapacitors, on the other hand, also sometimes referred to as redox capacitors or faradaic capacitors, store charge in a *faradaic* manner. In other words, the capacitance in this kind of capacitors arises from the transfer of charge between the electrode and electrolyte. Despite the redox charge storage nature of these capacitors, the charge transfer is highly reversible and ultrafast, lending them capacitive charging–discharging characteristics. Owing to the faradaic charge storage mechanism of these capacitors, the energy stored is larger than their EDLC counterparts; however, pseudocapacitors suffer from a shorter life span because of the redox mechanisms. A detailed explanation of the underlying mechanism is the subject of other works [9, 10]. The most commonly used pseudocapacitive materials include metal oxides (mostly ruthenium oxide, manganese oxide, and nickel hydroxide) and conducting polymers including polyaniline, polypyrrole (PPY), polythiophene, and their derivatives [5].

5.2.1.3 Microsupercapacitors

Miniaturized ECs, also known as microsupercapacitors, have gained much attention in recent years. Such capacitors have been used in a host

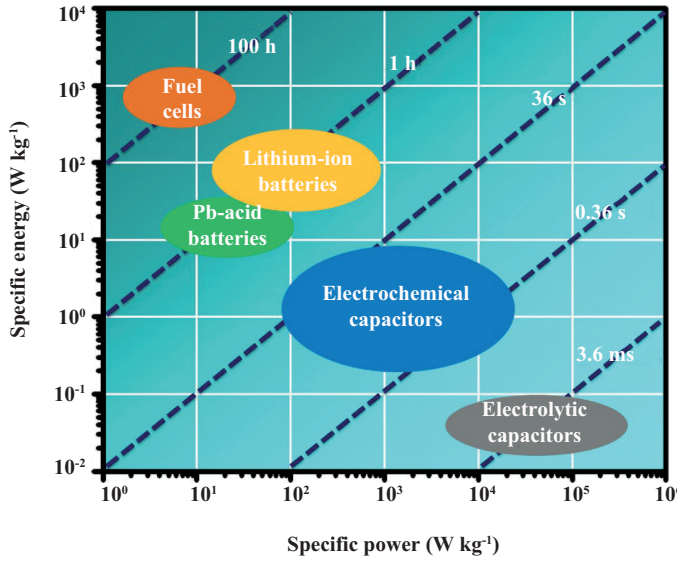

Figure 5.1. The Ragone plot for different energy storage devices. Note that electrochemical capacitors *bridge* the gap between lithium-ion batteries and electrolytic capacitors, with intermediate time constants.

of applications such as in implantable biomedical devices, in environmental sensors, in MEMS, and also in personal electronics that require power in the order of microwatts [5, 11]. Similar to their macrocounterparts, microsupercapacitors can be connected in series or parallel in order to meet the energy and power requirements for a given application. In general, the total footprint area of the microsupercapacitor is in the millimeter or centimeter range. Such capacitors typically consist of either thin film electrodes with thicknesses generally less than 10 μm or 2D or 3D microelectrode arrays. For supercapacitors in the *macro* regime, the energy and power densities are expressed in gravimetric terms, that is, per unit mass; however, for supercapacitors in the *micro*scale, mass is almost negligible, and therefore, the electrochemical performance of a microsupercapacitor is given with respect to its footprint area and energy and power are expressed in terms of *areal density* [5, 12]. The initial microsupercapacitors had the same architecture as planar 2D conventional supercapacitors—comprising two electrodes and a separator soaked in an electrolyte. However, a more recent design consisting of *interdigitated* electrodes offers several advantages over the conventional 2D design, for instance, (i) with the electrodes in the same plane fabrication is easier

and (ii) the smaller distance between the electrodes improves the electron transport and kinetics and thus enhances the overall electrochemical performance of the device.

5.3 FABRICATION PROCESS

5.3.1 CARBON MICROELECTROMECHANICAL SYSTEMS

Carbon microelectromechanical systems, also referred to as carbon-MEMS or C-MEMS, is a term used for a set of fabrication methods used to convert patterned photosensitive polymers to glassy carbonaceous materials using pyrolysis. The typical C-MEMS fabrication process has been illustrated in Figure 5.2. A more detailed description of the C-MEMS techniques is the subject of other works [1–3]. Briefly, first, a SU-8 photoresist is spin coated onto a silicon oxide wafer using a photoresist spinner. Subsequently, the photoresist is soft baked in order to promote adhesion to

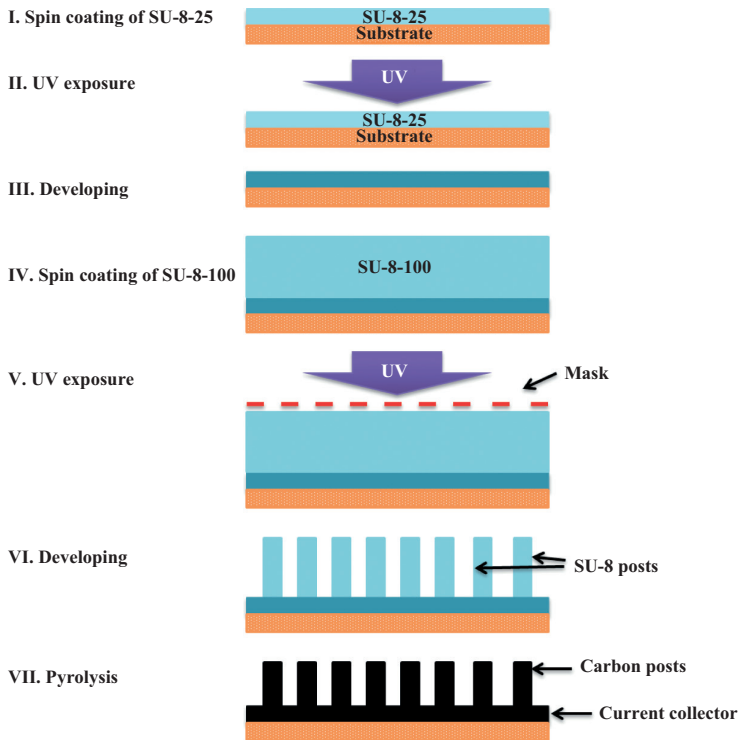

Figure 5.2. Process flow of C-MEMS technology.

the substrate. Next, it is patterned via exposure to UV light through a photomask. After the patterning process, a postexposure bake is carried out. The exposed samples are then developed using SU-8 developer in order to wash away the unexposed photoresist, followed by rinsing and drying. The carbonization process is then carried out in an alumina tube furnace with a constant flow of 500 sccm of forming gas (5% H_2 + 95% N_2). Finally, three-dimensional carbon micropillars are obtained by heating the polymer micropillars from room temperature to 350°C at a ramp of 5°C/min with 40-minute hold time followed by a ramp to 1,000°C at 5°C/min for 60 mins. before cooling down to room temperature.

5.3.2 ELECTROSTATIC SPRAY DEPOSITION

Electrostatic spray deposition (ESD) is a versatile technique that has been used for the successful integration of nanostructures such as CNTs, graphene, and different metal oxides onto C-MEMS architectures. In the ESD process, a precursor solution is atomized into an aerosol by the application of a high electric potential between the spray nozzle and the preheated substrate [13, 14]. The droplets produced using ESD are highly charged; this prevents coagulation and promotes self-dispersion. The quality of the deposited film is a function of several parameters including flow rate, temperature of the substrate, applied potential, nozzle geometry, and the composition of the precursor solution [4, 14]. ESD is particularly attractive owing to the high deposition rate, good uniformity, and the ability to deposit a variety of functional materials as compared to other deposition techniques such as atomic layer deposition, electrodeposition, and spin coating [4]. Figure 5.3 illustrates a schematic of the ESD process [15].

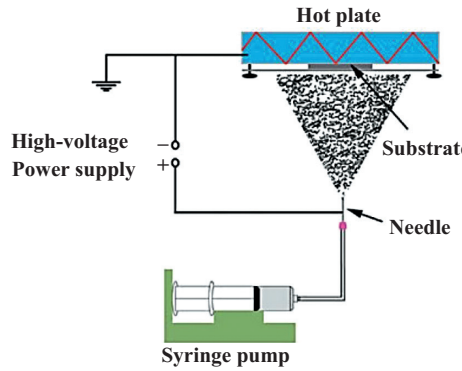

Figure 5.3. Schematic of ESD [15].

5.4 C-MEMS-BASED MICROSUPERCAPACITORS

5.4.1 ELECTROCHEMICALLY ACTIVATED C-MEMS-BASED MICROSUPERCAPACITORS

In this study, interdigitated microelectrode arrays for microsupercapacitors were fabricated using C-MEMS [16]. In order to enhance the capacitive performance, electrochemical activation was carried out. In Figure 5.4a and b, we show the morphology of the SU-8 structures and the pyrolyzed C-MEMS structures, respectively. Upon carbonization, the diameters of the posts ranged between 53 and 68 μm, while the average height of the posts was ~130 μm.

Briefly, the activation processes were carried out by connecting the two electrodes of the C-MEMS microsupercapacitor using a silver wire. The silver wire and the contact pads were then covered with epoxy resin

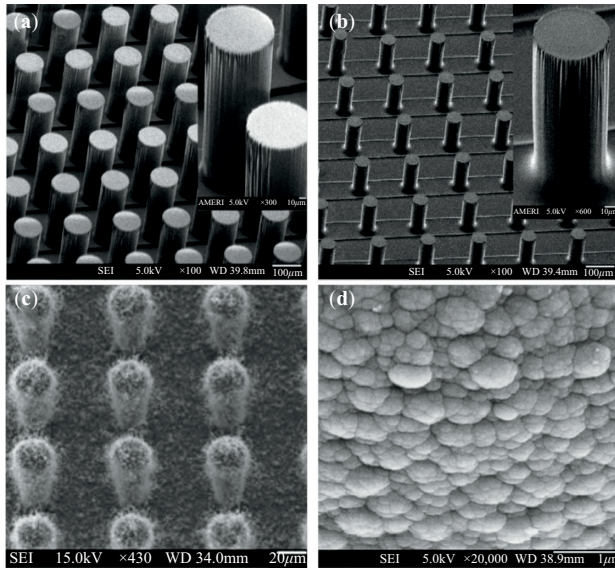

Figure 5.4. (a) Scanning electron microscope (SEM) images of typical SU-8 structures generated using C-MEMS processes [16]; (b) pyrolyzed C-MEMS structures [16]; (c) C-MEMS-based three-dimensional posts incorporated with CNTs [19]; (d) high-magnification image of the carbon post displaying the structure of the PPY film [20].

in order to prevent them from electrolyte exposure. Electrochemical activation was performed using a three-electrode setup in a 0.5 H_2SO_4 electrolyte by applying a potential of 1.9 V [vs. Ag or AgCl] for 30 mins. The electrodes were subsequently negatively polarized at −0.3 V [vs. Ag or AgCl] for 10 mins. In Figure 5.5c, we display the cyclic voltammograms recorded at 100 mVs^{-1} for both the nonactivated C-MEMS electrodes and the electrodes activated for 30 mins. The area under the CV curve of the activated sample is much larger than that of the nonactivated sample, which clearly indicates a larger capacitance for the activated sample. The geometric capacitance of the 30-minute activated sample was 75 mF cm^{-2} as compared to the very low capacitance of 0.07 mF cm^{-2} of the nonactivated C-MEMS sample, when measured at 5 mVs^{-1}. Moreover, for the cyclability tests conducted for the 30-minute activated electrodes, only a 12.3 percent capacitance fade was noted after 1,000 cycles. In Figure 5.5d, we display the charge–discharge curves of the 30-minute activated C-MEMS electrodes for different current densities between a potential of 0 and 1 V [vs. Ag or AgCl]. The charge–discharge curves are typical of a capacitor with nearly triangular curves and small iR drops. Slight deviation from ideal capacitor behavior is attributed to the introduction of pseudocapacitance from the redox-active surface functional groups. As expected, the iR drop increases with higher current densities.

The superior electrochemical characteristics of the activated samples over that of nonactivated samples can be ascribed to (i) the introduction of oxygen-containing functional groups from the activation process, which not only enhances the wettability of the electrode surface but also adds additional pseudocapacitance; and (ii) the increase in the surface area by the electrochemical treatment, because the treatment oxidizes the carbon surface and opens up closed pores; finally, another possible reason for the performance enhancement could be the irreversible intercalation of electrolyte ions during the polarization process; ions are intercalated into the carbon structures during the first polarization cycle and provide larger capacitance for the successive cycles [17].

5.4.2 CARBON-NANOTUBES-INTEGRATED C-MEMS-BASED MICROSUPERCAPACITORS

CNTs are one-dimensional carbon allotropes with a cylindrical structure, which also can be thought of as rolled up graphene sheets. Owing to their extraordinary mechanical strength (~1 TPa), electrical and thermal

conductivities, CNTs have been widely used both in its pristine form and in composites for the improvement in mechanical [18] and electrochemical properties of a wide range of materials. In this study [19], CNTs were integrated onto C-MEMS architectures using chemical vapor deposition (CVD). First, the iron catalyst particles were conformally coated onto the C-MEMS electrodes using ESD and then the CNTs were synthesized on them using catalytic CVD. It was seen that for a deposition time of 90 mins. of the catalyst particles, the resulting CNTs were the most homogenous. In Figure 5.4c, we show a micrograph of CNT-covered C-MEMS posts resulting from a catalyst deposition time of 90 mins. Figure 5.5a shows the CV curves of the pristine C-MEMS structures and the ones loaded with CNTs for different deposition times. It can be seen that the CV curves are rectangular for the potential range of −0.1 to 0.9 V [vs. Ag or AgCl], which is indicative of ideal capacitive behavior. As opposed to the measly capacitance of 1.6 Fg^{-1} exhibited by the bare C-MEMS electrodes, the CNT or C-MEMS composites with catalyst deposited for 90 mins. exhibit a capacitance of 33 Fg^{-1} (8.3 Fcm^{-2} footprint), which is more than 20 times larger. The CNT or C-MEMS composites were further treated with oxygen plasma in order to induce oxygen-containing functional groups. Postplasma treatment, the specific capacitance of the composites was doubled to about 61 Fg^{-1} for the first cycle. However, the increase in the capacitance came at the expense of cycling; only 71 percent of the capacitance was retained after 1,000 cycles as opposed to 97.3 percent retention in the CNT or C-MEMS structures without oxygen treatment.

5.4.3 C-MEMS AND POLYPYRROLE-BASED MICROSUPERCAPACITORS

In this work, microsupercapacitors with 3D symmetric interdigitated electrodes (i.e., both electrodes are identical) were first fabricated using C-MEMS and then PPy films were conformally coated onto those C-MEMS structures [20]. As mentioned earlier, PPy is a pseudocapacitive material and has superior capacitance as compared to EDLC materials. For electropolymerization of PPy films, first, the C-MEMS electrodes were connected as the working electrodes in a three-electrode setup, with an Ag or AgCl electrode as the reference electrode and a platinum wire as the counter electrode. The polymerization process was then carried out using an electrolyte solution containing 0.1M pyrrole monomer and 0.5M $LiClO_4$ supporting salt at a constant current density of 1 $mAcm^{-2}$ for 5 to

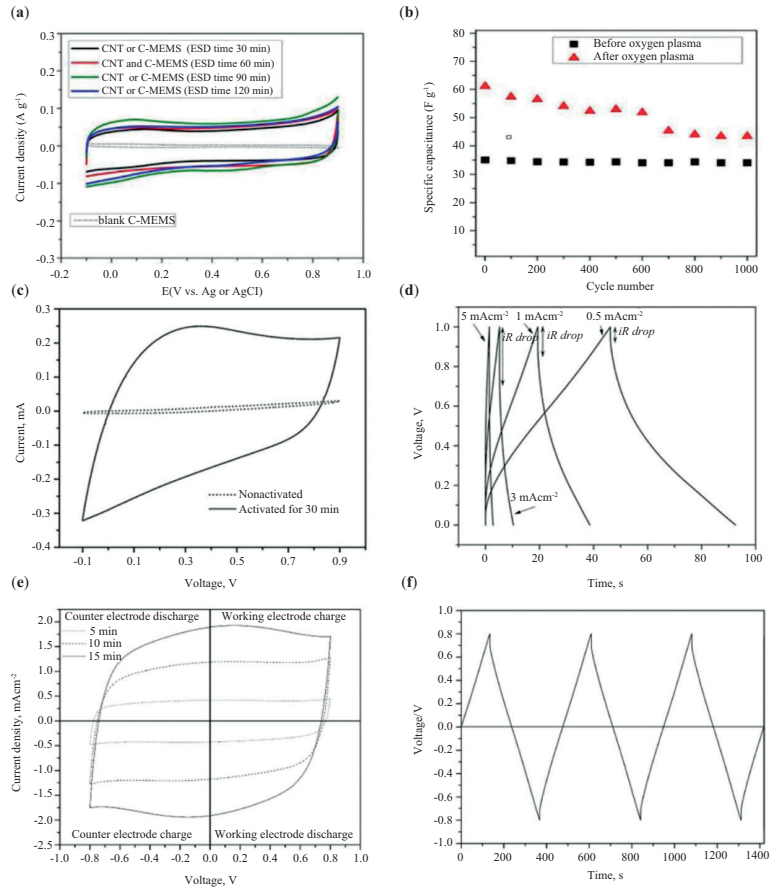

Figure 5.5. (a) CV curves of the bare C-MEMS electrodes (dashed lines) and CNT or C-MEMS composites for different deposition times at a scan rate of 2 mVs^{-1} in 1M Na_2SO_4 electrolyte [19]; (b) charge–discharge cycle stability of the pre- and postoxygen plasma-treated C-MEMS electrodes from cycle 1 to the cycle 1,000 [19]; (c) CVs of nonactivated and 30-minute activated samples at a scan rate of 100 mVs^{-1} [16]; (d) charge–discharge curves for activated C-MEMS samples for different current densities [16]; (e) CVs of symmetric PPy and C-MEMS microsupercapacitors with different polymerization times [20]; (f) galvanostatic charge–discharge profile of a PPy and C-MEMS symmetric microsupercapacitor [20].

15 mins. In Figure 5.4d, we show an SEM image of the resulting PPy films; the morphology is granular raspberrylike, which is typical of perchlorate-doped PPy [20].

In Figure 5.5e, we show the CV curves of a symmetric microsupercapacitor scanned between potentials of −0.8 to 0.8 V [vs. Ag or AgCl]. The CV curves are rectangular, indicative of capacitive behavior. The symmetric microsupercapacitor polymerized for 15 mins. exhibited an average specific capacitance of 78.35 ± 5.67 mF cm^{-2} at a scan rate of 20 mVs^{-1}, which is only slightly lower than half of the capacitance of the PPy and C-MEMS single electrodes from the three electrode tests (81.03 ± 6.20 mF cm^{-2}). In Figure 5.5f, we show the galvanostatic charge–discharge curves of the symmetric PPy and C-MEMS microsupercapacitor. The nearly triangular curves are indicative of ideal capacitive behavior. In addition, the single PPy and C-MEMS electrodes exhibited a specific power of 1.62 ± 0.12 mW cm^{-2} at a scan rate of 20 mVs^{-1}. In Table 5.1, we summarize the performance of different C-MEMS platforms along with other materials for microsupercapacitors. It can be seen that C-MEMS-based supercapacitors have comparable or even better performance than the other systems in terms of specific capacitance.

5.5 CONCLUSIONS

The results from our research indicate that C-MEMS-based structures are promising platforms for microsupercapacitors. Although bare C-MEMS are glassy carbon substrates, they can be further integrated with nanostructures such as CNTs and conducting polymers such as PPY to enhance their electrochemical performance. Furthermore, C-MEMS structures can be activated electrochemically in order to impart oxygen-containing functional groups that lend pseudocapacitive effects to the C-MEMS electrodes and enhance the overall electrochemical performance. We anticipate that further improvement in the performance of microsupercapacitors can be achieved through the optimization of the microelectrode design, the composition of the electrode materials, and the ESD conditions. For instance, the distance between the interdigitated electrodes can be shortened for more facile electronic transport and faster kinetics; nanostructures with excellent electrochemical properties can be coated onto C-MEMS, and ESD parameters can be optimized in order to obtain superior adhesion with the C-MEMS substrates.

Table 5.1. A comparison between different C-MEMS platforms for microsupercapacitors along with other reported microsupercapacitors

Material	Potential window	Gravimetric specific capacitance (Fg^{-1})	Geometric specific capacitance	Specific power*	Capacitive retention	Ref.
Electro-chemically activated C-MEMS	−0.1 to 0.9 V	33 (30-minute activation)	75 $mFcm^{-2}$	------	87.7% after 1,000 cycles	16
CNT or C-MEMS	−0.1 to 0.9 V	33	8.3 F cm^{-2}	------	97.3% of the initial capacitance retained for the untreated sample after 1,000 cycles 71% of the capacitance retained for the oxygen-plasma-treated sample	19
PPy or C-MEMS	0 to 0.8V	237.27 ± 18.19 (15 min polymerization time)	Single electrode 162.07 ± 12.40 mF cm^{-2} at 20 mV s^{-1}	1.62 ± 0.12 mW cm^{-2} at 20 mV s^{-1}	56% of the initial value after 1,000 cycles	20
AC with SU-8 separator	−1 to 1 V	------	160 $mFcm^{-2}$ at 10mVs^{-1}	31.25 $mWcm^{-2}$ at 100 mVs^{-1}	------	21
CoO or CNT	0 to 1.2 V	------	8 F/cm^3 at 1.25 A/cm^3	------	85.2% after 1,700 cycles	22

REFERENCES

[1] Wang, C., L. Taherabadi, G. Jia, M. Madou, Y. Yeh, and B. Dunn. 2015. "C-MEMS for the Manufacture of 3D Microbatteries." *Electrochemical and Solid State Letters* 7, no. 11, pp. A435–38.

[2] Wang, C., and M. Madou. 2005. "From MEMS to NEMS with Carbon." *Biosensors and Bioelectronics* 20, no. 10, pp. 218–2187. doi: http://dx.doi.org/10.1016/j.bios.2004.09.034

[3] Wang, C., G. Jia, L. Taherabadi, and M. Madou. 2005. "A Novel Method for the Fabrication of High-Aspect Ratio C-MEMS Structures." *Journal of Microelectromechanical Systems* 14, no. 2, pp. 348–58. doi: http://dx.doi.org/10.1109/jmems.2004.839312

[4] Song, Y., R. Agrawal, Y. Hao, C. Chen, and C. Wang. 2014. "C-MEMS Based Microsupercapacitors and Microsensors." *ECS Transactions* 61, no. 7, pp. 55–64. doi: http://dx.doi.org/10.1149/06107.0055ecst

[5] Agrawal, R., C. Chen, Y. Hao, Y. Song, and C. Wang. 2015. "Graphene for Supercapacitors." In *Graphene based Energy Devices*, ed. A. Rashid bin Mohd Yusoff, 171–214. Weinheim, Germany: Wiley-VCH Verlag GmbH & Co. KGaA. doi: http://dx.doi.org/10.1002/9783527690312.ch6

[6] Xie, D., Q. Jiang, G. Fu, Y. Ding, X. Kang, W. Cao, and Y. Zhao. 2011. "Preparation of Cotton-Shaped CNT/PANI Composite and Its Electrochemical Performances." *Rare Metals* 30, no. 1, pp. 94–97. doi: http://dx.doi.org/10.1007/s12598-011-0246-0

[7] Pech, D., M. Brunet, H. Durou, P. Huang, V. Mochalin, Y. Gogotsi, P.L. Taberna, and P. Simon. 2010. "Ultrahigh-Power Micrometre-Sized Supercapacitors Based on Onion-Like Carbon." *Nature Nanotechnology* 5, no. 9, pp. 651–54. doi: http://dx.doi.org/10.1038/nnano.2010.162

[8] Chen, C., R. Agrawal, Y. Hao, and C. Wang. 2013. "Activated Carbon Nanofibers as High Capacity Anodes for Lithium-Ion Batteries." *ECS Journal of Solid State Science and Technology* 2, no. 10, pp. M3074–77. doi: http://dx.doi.org/10.1149/2.011310jss

[9] Conway B.E. 1999. *Electrochemical Supercapacitors: Scientific Fundamentals and Technological Applications*. New York, NY: Kluwer Academic/Plenum Publishes.

[10] Beguin, F., and E. Frackowiak, eds. 2013. *Supercapacitors: Materials, Systems, and Applications*. Weinheim, Germany: Wiley-VCH Verlag GmbH & Co. KGaA.

[11] Kim, H., M.Y. Cho, M.H. Kim, K.Y. Park, H. Gwon, Y. Lee, K.C. Roh, and K. Kang. 2013. "A Novel High-Energy Hybrid Supercapacitor with an Anatase TiO 2-Reduced Graphene Oxide Anode and an Activated Carbon Cathode." *Advance Energy Materials* 3, no. 11, pp. 1500–06. doi: http://dx.doi.org/10.1002/aenm.201300467

[12] Arthur, T.S., D.J. Bates, N. Cirigliano, D.C. Johnson, P. Malati, J.M. Mosby, E. Perre, M.T. Rawls, A.L. Prieto, and B. Dunn. 2011. "Three-Dimensional

Electrodes and Battery Architectures." *MRS Bulletin* 36, no. 7, pp. 523–31. doi: http://dx.doi.org/10.1557/mrs.2011.156

[13] Dhanabalan, A., X. Li, R. Agrawal, C. Chen, and C. Wang. 2013. "Fabrication and Characterization of SnO_2/Graphene Composites as High Capacity Anodes for Li-Ion Batteries." *Nanomaterials* 3, no. 4, pp. 606–14. doi: http://dx.doi.org/10.3390/nano3040606

[14] Chen, C., R. Agrawal, T.K. Kim, X. Li, W. Chen, Y. Yu, M. Beidaghi, V. Penmatsa, and C. Wang. 2014. "Nanostructured Electrodes via Electrostatic Spray Deposition for Energy Storage System." *ECS Transactions* 61, no. 27 pp. 155–63. doi: http://dx.doi.org/10.1149/06127.0155ecst

[15] Beidaghi, M., Z. Wang, L. Gu, and C. Wang. 2012. "Electrostatic Spray Deposition of Graphene Nanoplatelets for High-Power Thin-Film Supercapacitor Electrodes." *Journal of Solid State Electrochemistry*16, no. 10, pp. 3341–48. doi: http://dx.doi.org/10.1007/s10008-012-1777-5

[16] Beidaghi, M., W. Chen, and C. Wang. 2011. "Electrochemically Activated Carbon Micro-Electrode Arrays for Electrochemical Micro-Capacitors." *Journal of Power Sources* 196, no. 4, pp. 2403–09. doi: http://dx.doi.org/10.1016/j.jpowsour.2010.09.050

[17] Ruch, P.W., M. Hahn, D. Cericola, A. Menzel, R. Kötz, and A. Wokaun. 2010. "A Dilatometric and Small-angle X-ray Scattering Study of the Electrochemical Activation of Mesophase Pitch-Derived Carbon in Non-Aqueous Electrolyte Solution." *Carbon* 48, no. 7, pp. 1880–88. doi: 10.1016/j.carbon.2010.01.032

[18] Agrawal, R., A. Nieto, H. Chen, M. Mora, and A. Agarwal. 2013. "Nanoscale Damping Characteristics of Boron Nitride Nanotubes and Carbon Nanotubes Reinforced Polymer Composites." *ACS Applied Materials and Interfaces* 5, no. 22, pp. 12052−57. doi: http://dx.doi.org/10.1021/am4038678

[19] Chen, W., M. Beidaghi, V. Penmatsa, K. Bechtold, L. Kumari, W.Z. Li, and C. Wang. 2010. "Integration of Carbon Nanotubes to C-MEMS for On-chip Supercapacitors." *IEEE Transactions on Nanotechnology* 9, no. 6, pp. 734–40. doi: http://dx.doi.org/10.1109/tnano.2010.2049500

[20] Beidaghi, M., and C. Wang. 2011. "Micro-Supercapacitors Based on Three Dimensional Interdigital Polypyrrole/C-MEMS Electrodes." *Electrochimica Acta* 56, no. 25, pp. 9508–14. doi: http://dx.doi.org/10.1016/j.electacta.2011.08.054

[21] Xing, H., X. Wang, C. Shen, and S. Li. 2012. "Fabrication and Tests of a Three-Dimensional Microsupercapacitor Using SU-8 Photoresist as the Separator." *Micro & Nano Letters* 7, no. 12, pp. 1166–69. doi: http://dx.doi.org/10.1049/mnl.2012.0563

[22] Zhu, Y.G., Y. Wang, Y. Shi, J.I. Wong, and H.Y. Yang. 2014. "CoO Nanoflowers Woven by CNT Network for High Energy Density Flexible Micro-Supercapacitor." *Nano Energy* 3, pp. 46–54. doi: http://dx.doi.org/10.1016/j.nanoen.2013.10.006

CHAPTER 6

ADVANCED ELECTROANALYSIS WITH C-MEMS

Paolo Scopece[1], Ligia M. Moretto[2], and Paolo Ugo[2]

[1]*Veneto Nanotech, Marghera-Venice Italy*
[2]*University Ca' Foscari of Venice, Italy*

6.1 CHARACTERISTICS OF PYROLYZED PHOTORESIST CARBON ELECTRODES

Among a large variety of electrode materials used for electroanalytical purposes (including noble metals pyrolytic graphite, carbon paste, and others), glassy carbon (GC) established itself as the gold standard material for electrochemists owing to its chemical inertness, wide electrochemical potential window, low electrical resistivity, low surface roughness, and, consequently, low background signal [1–3]. Interestingly, as described in Chapter 1 of Volume 1 of this book, GC is the prevailing allotropic form of carbon typically obtained when performing controlled pyrolysis of spin-coated films of suitable photoresists. GC *macro-objects* (with dimensions in the millimeter and centimeter range) are obtained even at an industrial scale by firing phenol–formaldehyde resin precursors in an inert atmosphere, using pyrolysis, a process discovered half a century ago [4]. These macro-objects are typically available and commercialized in the shape of crucibles, rods, and plates [4]. Indeed, the final GC macro-object substantially retains the shape premodeled in the polymer precursor. To obtain GC, care must be taken to perform the carbonization process by very slow heating in an inert atmosphere, up to a final temperature of 1,000°C to 1,200°C. After pyrolysis, in order to obtain GC electrodes appropriate for successful electrochemical use, a final surface pretreatment is required to

bring the GC surface to a mirrorlike finish. This is accomplished by careful polishing with graded alumina powder. Additional activation steps via electrochemical, chemical, thermal, or laser treatment have been experimented with and were shown to further enhance the already excellent electrochemical performances of GC electrodes [5, 6]. Several review articles and chapters have been devoted to describe the physicochemical and electrochemical properties of GC electrodes [2, 3, 5, 6]. However, classical GC electrode materials suffer from limitations that can be summarized as follows: (i) even though cheaper than precious metals, GC is rather expensive with a price ranging from several tens of U.S. dollars (USD) for a raw GC rod to several hundreds of USD for a ready to use GC working electrode; (ii) the size of classical GC objects is never lower than the millimeter range; (iii) the range of shapes available is limited to rods, plates, disks, and other shapes derived from those.

The previous points clarify why preparing for the first time GC electrodes from the pyrolysis of patterned photoresists [7] raised great interest in the electrochemistry community. Indeed, this process allows one to overcome the listed limitations so that one can obtain cheap, electrochemically efficient GC electrodes (down to the micrometer or even nanometer dimension), patterned in different shapes by photolithography.

Along this line, the Madou group and later the McCreery group [7, 8] developed novel voltammetric electrodes obtained from pyrolyzed photoresist films (PPF). In these early reports, positive photoresists, mainly based on novolak resins, were used as precursors. The obtained pyrolyzed photoresist carbon electrodes (PPCEs) showed excellent electrochemical properties with an interfacial behavior similar to that of bulk GC electrodes, but with some special features. It was found that for the fabrication of electrochemically efficient PPCEs, the higher the pyrolysis temperature the better is the reversibility in the voltammetric behavior of redox probes such as $[Ru(NH_3)_6]^{2+/3+}$ [8]. This is illustrated by the comparison of the cyclic voltammograms (CVs) shown in Figure 6.1. These data put in evidence the decrease in peak potential separation (ΔE_p) when increasing the pyrolysis temperature, indicating that the electrode pyrolyzed at 1,100°C presents a ΔE_p value of 70 mV, that is close to the 60 mV value theoretically expected for a one-electron reversible reduction.

With respect to the behavior of different redox probes on PPCE, Ranganathan and McCreery [9] came to the conclusion that for redox probes that undergo simple outer-sphere electron transfer (ET), the resistance-corrected ET kinetics at a PPCE compares with that of bulk GC electrodes. On the other hand, for redox systems that require some catalytic interaction with the electrode surface to speed-up the ET process, PPCEs are somehow less reactive than polished or heat-treated glassy

carbon (HTGC) bulk electrodes. This is, for instance, the case with oxygen reduction or dopamine oxidation (see Figure 6.2). For the latter case, the voltammetric pattern recorded with the HTGC presents a smaller ΔE_p

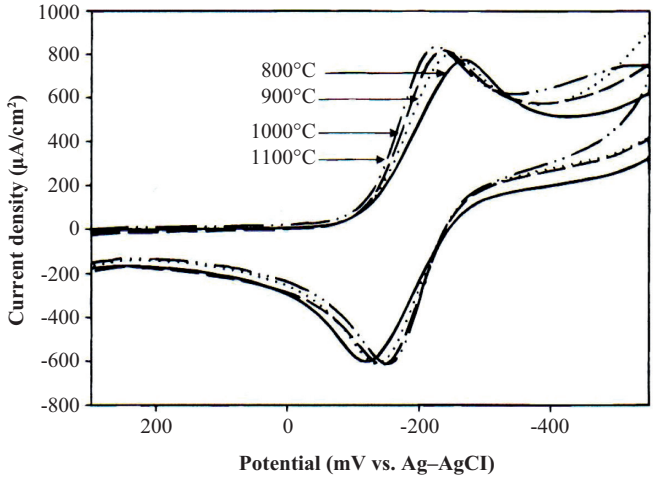

Figure 6.1. Cyclic voltammograms of 1 mM $[Ru(NH_3)_6]^{3+/2+}$ in 1 M KCl on carbon films pyrolyzed at the indicated temperatures. Scan rate: 200 mV s^{-1}.

Source: Reproduced by permission from Ranganathan et al. [8].

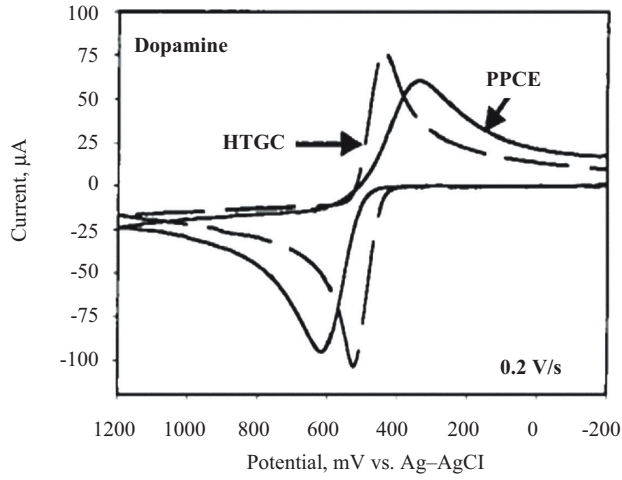

Figure 6.2. Voltammetry of dopamine on PPCE and HTGC.

Source: Reprinted with permission from Ranganathan and McCreery [9].

and higher peak current than that recorded with the PPCE. Dopamine oxidation involves indeed reactant adsorption onto the electrode surface and the ET kinetics is slower if such adsorption is hindered. The surface of the PPCE interacts more weakly with dopamine than the HTGC, decreasing the catalytic effect of the carbon surface [9]. On the contrary, PPCE and bulk GC electrodes behave comparably for outer-sphere redox systems (see, e.g., the earlier $[Ru(NH_3)_6]^{2+/3+}$ case).

Careful physicochemical characterization of PPCEs by Raman spectroscopy, X-ray diffraction (XRD), atomic force microscopy (AFM), X-ray photoelectron spectroscopy (XPS), scanning electron microscopy (SEM), and transmission electron microscopy (TEM) analyses provides important clues about the observed electrochemical behavior [7–9]. Raman spectroscopy, XRD, and electron microscopy data confirmed the glassy nature of the pyrolyzed films [7]. AFM analyses revealed an exceptional surface smoothness of the pyrolyzed C films, better than that of bulk GC and approaching that of atomically smooth basal plane highly oriented pyrolytic graphite [9]. XPS analyses revealed O–C surface ratios lower than that for bulk GC [9]. The extremely low roughness of the PPCE surface is reflected in its low capacitance and weak adsorption properties, while the low surface oxygen content and low percentage of basal plane graphite explain the decreased interfacial electrocatalytic activity of PPCEs with respect to polished or heat-activated GC electrodes. A critical parameter to be taken into account is the electrical resistance of PPCE. The resistivity of PPCEs is slightly higher than that of high-quality bulk GC (5.7×10^{-3} Ω cm vs $4.0 - 4.5 \times 10^{-3}$ Ω cm, respectively). It must be taken into account though that the production of very thin PPCEs on insulating substrates such as Si_3N_4 or SiO_2 can cause a significant increase in the effective electrode resistance because, in thin films the resistance is inversely proportional to the thickness. This increased resistance must be taken into account when using PPCEs for the evaluation of ET kinetics constants [9]. A proof that this ohmic resistance depends only on the PPCE thickness comes from the observation that this parameter becomes negligible when the PPCE is grown onto a conductive substrate such as bulk GC itself [9]. In this case, electrons can move in the conduction band of the underlying conductive substrate so that the thickness of the pyrolyzed film is no more the key parameter controlling the overall rate of electron flow.

Similar electrochemical and physical PPCE properties were obtained using epoxy-based negative photoresist precursors (e.g., SU-8) instead of positive ones [10, 11]. For SU-8 films pyrolyzed at 900°C, the electrode resistance was strongly dependent on the film thickness (see Figure 6.3) reaching a minimum for a film thickness ≥4 μm [11].

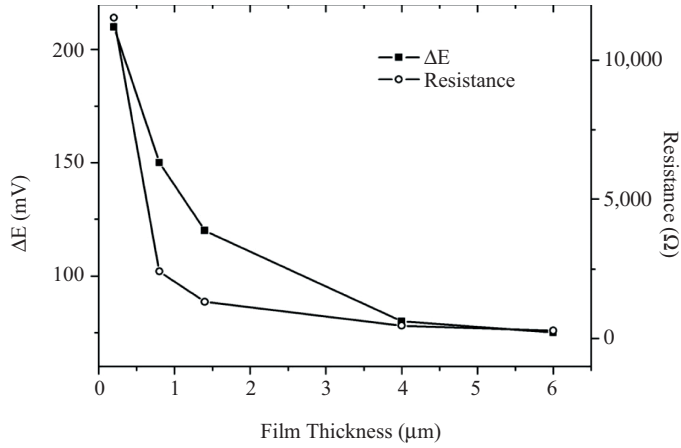

Figure 6.3. Anodic and cathodic peaks potential difference (ΔE) of $[Fe(CN)_6]^{3-/4-}$ in 0.1 M KCl at 25 mV s^{-1} and ohmic resistance for different film thicknesses, keeping other dimensions constant.

Source: Reprinted with permission from Mardegan et al. [11].

An electrochemical characteristic that makes C materials very attractive for electroanalysis is the wide electrochemical potential window that is accessible. Indeed, the number of electroactive analytes that can be detected becomes larger, the wider is the accessible potential window [12, 13]. In Figure 6.4a, we illustrate that the potential window accessible with PPCEs prepared from the negative photoresist SU-8 extends over a 2.2 V span in aqueous electrolytes [11]. The cathodic limit of this accessible region in aqueous solutions is related to the potential at which the hydrogen evolution reaction occurs in the electrolyte under study.

As shown in Figure 6.4b, for a PPCE, the cathodic limit depends on the pH of the supporting electrolyte, shifting toward more negative potential values with increasing pH. A way to extend the cathodic limit of the accessible potential window is to use electrolytes based on aprotic solvents. Data in Figure 6.5 demonstrates that the potential window accessible with a PPCE can be extended to more than 3.2 V when using 0.1 M tetrabuthyl ammonium tetrafluoroborate ($TBABF_4$) in dimethylsulfoxide (DMSO) as nonaqueous electrolyte [14]. The use of an aprotic solvent also has the advantage of extending the number of detectable analytes to redox species that are not soluble in water but are soluble in organic solvents. By measuring the capacitance of a PPCE from a CV run in pure supporting electrolyte (see Figure 6.5) [12], it was found that this parameter for the pyrolyzed photoresist is significantly smaller than that of a polished GC.

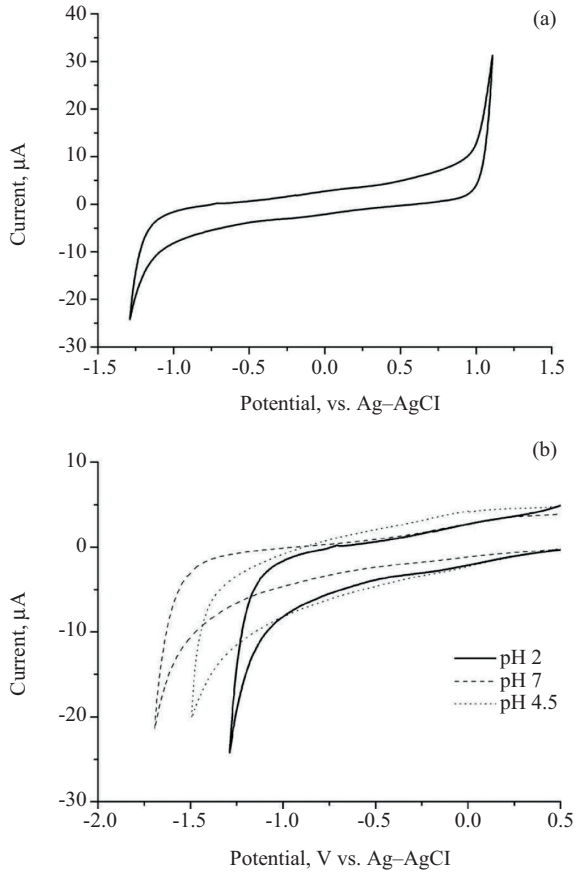

Figure 6.4. (a) Background cyclic voltammogram recorded with a PPCE at 25 mV s^{-1} in 10^{-2} M HCl, pH 2.2; (b) in 10^{-2} M phosphate buffer, pH 7.0 (dashed line), 10^{-2} M acetate buffer, pH 4.5 (dotted line), 10^{-2} M HCl, pH 2.2 (solid line).

Source: Reprinted with permission from Mardegan et al. [11].

As the capacitive current is linearly dependent on the real electrode area exposed to the electrolyte, this datum confirms the exceptional surface smoothness of PPCEs, with ratios between electroactive and geometrical surfaces approaching 1 [14].

All the preceding results indicate that pyrolyzed photoresist carbon prepared from both positive and negative photoresist is an excellent candidate material for the development of advanced electroanalytical sensors. In addition to possessing electrochemical properties comparable to GC,

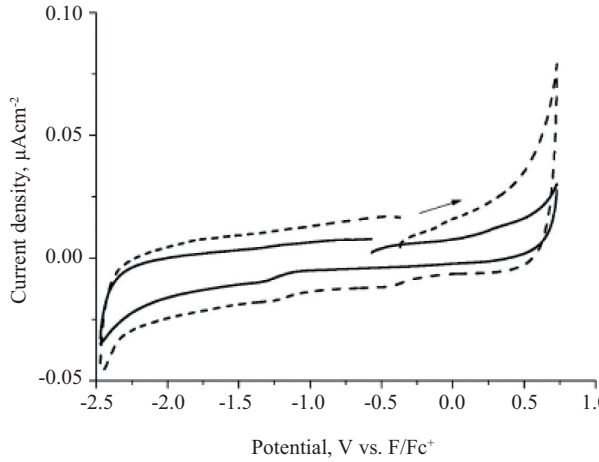

Figure 6.5. Cyclic voltammograms recorded in DMSO, 0.1 M $TBABF_4$ at PPCE (full line) and GCE (dashed line). Scan rate is 100 mV s^{-1}.

Source: Reprinted with permission from Silvestrini et al. [14].

PPCEs come with some unique additional features such as near-atomic flatness and patternability by photolitography. The latter is a desirable feature for developing complex electrode microarchitectures suitable for preparing tailor-made electroanalytical devices and sensors. Chapter 7 of this book deals specifically with the microfabrication and characterization of interdigitated electrode arrays (IDEAs) based on PPCEs. IDEAs exploit the very small gap that can be patterned between two working electrodes to achieve exceptional amplification of voltammetric signals via highly efficient electrochemical redox cycling of the analyte between the interdigitated microelectrodes [15, 16].

Here it is worth mentioning that other interesting electrode geometries can be obtained by photopatterning PPCEs, enabling other novel electroanalytical applications. McCarty, Wightman, and coworkers, for example, fabricated PPCE microelectrode arrays (MEAs) [17] in which the photopatternability of PPCEs was used to produce arrays of individually addressed microelectrodes. Multiple fast-scan CV waveforms were applied to the different PPCEs present on a single substrate. The ability of independently controlling the potential at separate electrodes on the same array allowed to optimize the sensitivity and selectivity for different analytes. By this way, one can perform the simultaneous, decoupled detection of, for example, dopamine and oxygen during neurobiological events [17].

Susan Lunte and coworkers exploited photolithography on pyrolizable photoresists to fabricate a microchip for capillary electrophoresis where the PPCE constitutes an advanced dual-electrode detector [18]. In this chapter, these and other examples of photopatterned PPCEs will be reviewed and discussed in relation to their application for the advanced electroanalysis of inorganic and organic pollutants, as well as electroactive molecules of interest in bioanalytical studies.

6.2 TRACE METAL IONS ANALYSIS WITH PYROLYZED PHOTORESIST CARBON ELECTRODES

Voltammetric analysis of trace metals is one of the main application fields of electroanalysis. The power and scope of voltammetric techniques have been greatly enhanced during the past decades owing to the introduction of novel electrode materials, such as silver, gold, iridium, platinum, several metal alloys like silver–bismuth dental amalgam, and different compositions of carbon paste electrodes, as well as new coating procedures and stripping techniques.

Stripping voltammetry is widely used to detect metal ions at trace concentration levels (in less than micromolar levels). Stripping voltammetry constitutes a group of extremely sensitive electrochemical methods with remarkable sensitivity because of the combination of an effective preconcentration step with advanced measurement techniques that are able to produce an extremely favorable signal-to-background ratio. As the trace metals are preconcentrated onto the electrode by a factor of 100 or 1,000, detection limits (DL) are lowered by two or three orders of magnitude compared to solution-phase voltammetric measurements [13]. Different stripping methods can be distinguished depending on the nature of the deposition and measurement step; the most used in trace metal ions analysis are represented by anodic stripping voltammetry (ASV), cathodic stripping voltammetry (CSV), and adsorptive stripping voltammetry (AdSV). In ASV, the preconcentration of the analyte is performed by the faradaic reduction of the metal ion, which is accumulated, typically under the form of an Hg amalgam, on the electrode surface and detected via an anodic stripping voltammetric scan. In CSV, the analyte is accumulated on the electrode as an insoluble salt generated by chemical or faradaic reaction with the electrode material (typically Hg, Ag, or Au) and stripped via a cathodic scan. In AdSV, a complex of the metal ion of interest is accumulated by adsorption on the electrode surface and detected as an active species, typically with a cathodic scan.

Historically, all the aforementioned techniques required the use of mercury as the electrode material that can be under the form of a mercury film electrode or hanging mercury drop electrode. Indeed, mercury offers the widest cathodic limit for the accessible potential window because it is the metallic material with the highest overpotential for the hydrogen evolution reaction. Moreover, the high adsorptive capability of mercury makes it suitable for AdSV analyses. In recent years, because of the increasing concern on the widespread use of toxic mercury as electrode material, several alternative materials have been examined such as gold, silver, iridium, various alloys, and amalgams, as well as different forms of carbon [19–21], but none of them approached the attractive electroanalytical behavior of mercury.

At the beginning of 2000, bismuth film electrodes (BiFEs) were introduced by Wang, Hocevar, Ogorevc, and others as an efficient replacement for mercury [22]. BiFEs exhibit a cathodic limit of the operational potential window similar to that of mercury, with even superior performance in the presence of dissolved oxygen. Owing to nontoxic character and excellent electroanalytical performances, BiFEs have been exploited for various electroanalytical applications, even at the nanoscale, producing Bi film nanoelectrodes [23]. Several applications were performed on GC-modified BiFEs [24–27], so that, when PPCEs became available, an obvious evolution of these research endeavors was the preparation, characterization, and electroanalytical application of bismuth-modified pyrolyzed photoresist carbon electrodes (Bi-PPCEs).

Mardegan and coworkers [11] prepared PPCEs from the epoxy-based photoresist SU-8, assembling the electrodes as shown in Figure 6.6. In situ surface modification of PPCE with bismuth was performed via electrodeposition of a Bi(III) solution conducted in the presence of the analytes of interest. The so-obtained Bi-PPCEs increase the overpotential for hydrogen evolution in the cathodic range, thus enabling simultaneous ASV detection of Cd(II) and Pb(II) in the range between 5 and 30 μg L^{-1} for both analytes. Typical results are shown in Figure 6.7.

Analyses performed using a relatively short preconcentration time of 300 s, furnished DLs of 0.8 μg L^{-1} for Pb(II) and 0.7 μg L^{-1} for Cd(II), which compares well with those obtained on commercially available GC substrates [28, 29].

Continuing this line of research, Bi-PPCEs were applied to the AdCSV analysis and redox speciation of trace level of chromium [30]. Among hazardous metal ions, chromium(VI) is one of the most harmful inorganic pollutants because of its high toxicity and cancerogenicity. Nonetheless, Cr(VI) is widely used in several industrial processes such as metal plating,

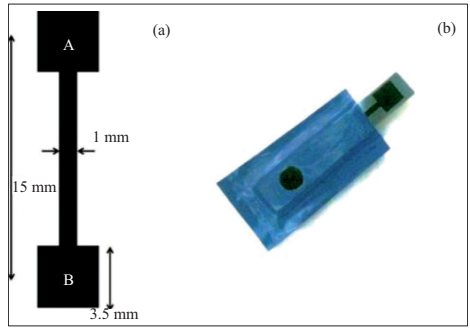

Figure 6.6. Scheme of the PPC and electrode assembly.

Source: Reprinted with permission from ref Mardegan et al. [11, 30].

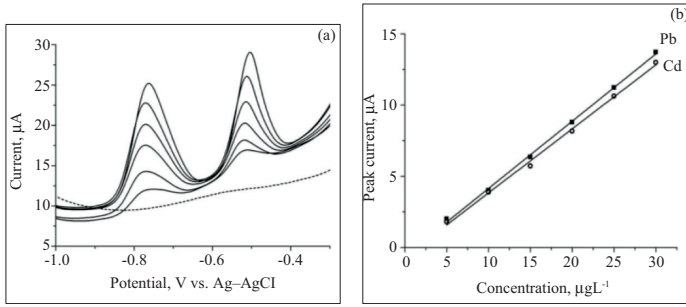

Figure 6.7. (a) SW-ASV recorded at the in situ prepared Bi-PPCE in 0.1 M acetate buffer (pH 4.5), 10 mg L^{-1} Bi(III) in the absence (dotted line) and the presence of increasing concentrations of Pb(II) and Cd(II), from 5 to 30 µg L^{-1} (full lines). Deposition at −1.1 V for 300 s. Square wave voltammetry parameters: frequency 20 Hz, amplitude 50 mV, potential step of 5 mV. (b) Corresponding calibration plots.

Source: Reprinted with permission from Mardegan et al. [11].

leather tanning, and paint making. The analysis of Cr(VI) and the ability to differentiate Cr(VI) from Cr(III) (much less toxic) constitute an issue of general concern. Pyrocatechol violet (PCV) is used as an efficient complexing agent for the AdCSV determination of Cr(VI) [31–33]. The mechanism of the complexation reaction with PCV involves the oxidation of the ligand by Cr(VI), producing Cr(III) and PCV oxidized (PCVox); this is followed

by complexation of Cr(III) by PCVox, which is finally adsorbed on the electrode surface by the application of a potential between −0.2 and 0 V (see Figure 6.8).

It is worth mentioning that unoxidized PCV can also bind Cr(III), but the resulting complex is not electroactive. This behavior ensures that the observed electrochemical signal is exclusively owing to Cr(VI) [34]. The adsorptive cathodic stripping signal is enhanced by the presence of nitrate ions that reoxidize Cr(II) ions produced in the electrochemical reduction of the complex (see Figure 6.9).

Mardegan et al. developed a method for Cr(VI) analysis and speciation based on the application of the PCV method to Bi-PPCEs [30]. Typical results are shown in Figure 6.10. A linear calibration plot was obtained using an accumulation time of 60 s, achieving a DL of 0.1 μg L^{-1}, which is comparable or even lower than that obtained with other electroanalytical methods [33, 35, 36]. The method was successfully applied to the determination of the total inorganic Cr in waste water samples.

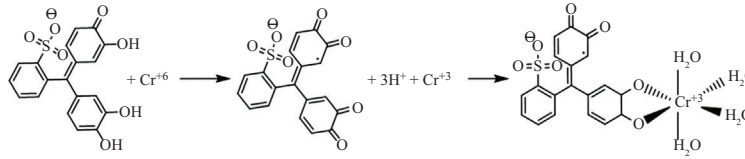

Figure 6.8. Cr(III)-PCVox is electroactive and adsorbed on the electrode surface.

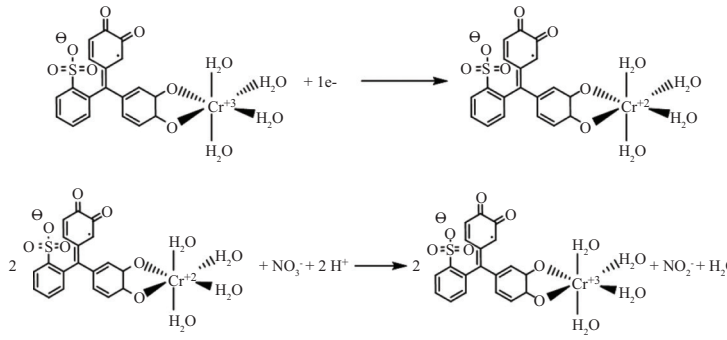

Figure 6.9. Cathodic reaction of Cr(III)–PCVox that is reduced to Cr(II)–PCVox. In the presence of NO_3^-, a catalytic cycle is active.

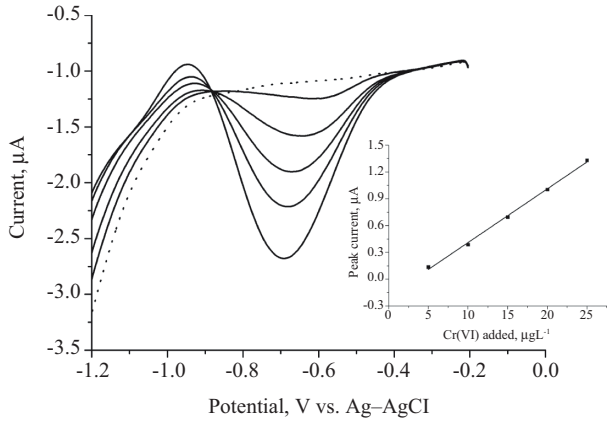

Figure 6.10. AdCSVs at the ex-situ prepared Bi-PPCE in the solution of 5 µg L^{-1} of Cr(III) for increasing concentrations of Cr(VI) in the range of 5 to 25 µg L^{-1}, in acetate buffer solution 0.01 mol L^{-1} (pH 6) containing 0.1 mol L^{-1} $NaNO_3$ and 0.5 mmol L^{-1} PCV. Inset: Corresponding calibration plot.

Source: Reprinted with permission from Mardegan et al. [30].

Rehacek et al. studied pyrolysis of various photoresists on alumina substrates and characterized their electrical, microstructural, and electrochemical properties. The so-obtained PPCEs were successfully applied for the determination of heavy metals (Pb, Cd, and Zn) in aqueous solution by square wave ASV on in-situ-formed bismuth film electrodes (Bi-PPCEs). These authors studied the effect of the presence of an additional Nafion coating, which improves the detection capabilities of the PPCE by exploiting the well-known cation-exchanging preconcentration capability of this ionomer [37]. After the optimization of the Nafion-coated PPCE preparation, the analytical performance of the Nafion coated or not coated Bi-PPCEs were compared (see Figure 6.11).

It was found that the analytical sensitivities for Pb(II) and Cd(II) were two times higher compared with non-coated Bi-PPCEs. In the best case, the DLs were estimated as 3×10^{-9}, 6×10^{-9}, and 2.4×10^{-8} mol L^{-1} for Pb(II), Cd(II), and Zn(II), respectively. Recently, the same Nafion-coated BiFEs NC-Bi-PPCEs have been applied for the analytical determination of Pb, Cd, and Zn in real samples of tap and river water [38].

Sánchez-Molas and coworkers recently proposed a new route to define the surface of PPCEs exposed to the electrolyte solution by using a passivation layer deposited by chemical vapor deposition (CVD) and

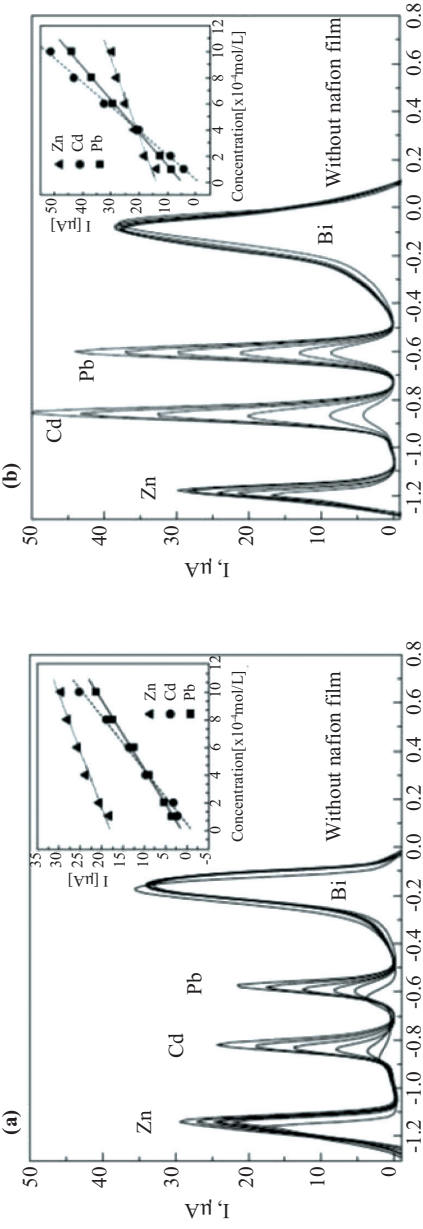

Figure 6.11. (a) Square wave stripping voltammograms (E_{step} = 10 mV, E_{pulse} = 50 mV and frequency 50 Hz). Dependence of current responses of bare Bi-PPCE on concentration of target metals in 0.1 mol L^{-1} acetate buffer (pH 4.5); preconcentration at −1.3 V for 180 s; concentration of Bi(III): 1×10^{-6} mol L^{-1}; calibration plots inside. (b) Square wave stripping voltammograms (E_{step} = 10 mV, E_{pulse} = 50 mV and frequency 50 Hz). Dependence of current responses of Nafion-coated BiFE on concentration of target metals in 0.1 mol L^{-1} acetate buffer (pH 4.5); preconcentration at −1.3 V for 180 s; concentration of Bi(III): 2×10^{-6} mol L^{-1}; calibration plots inside.

Source: Reprinted with permission from Rehacek et al. [37].

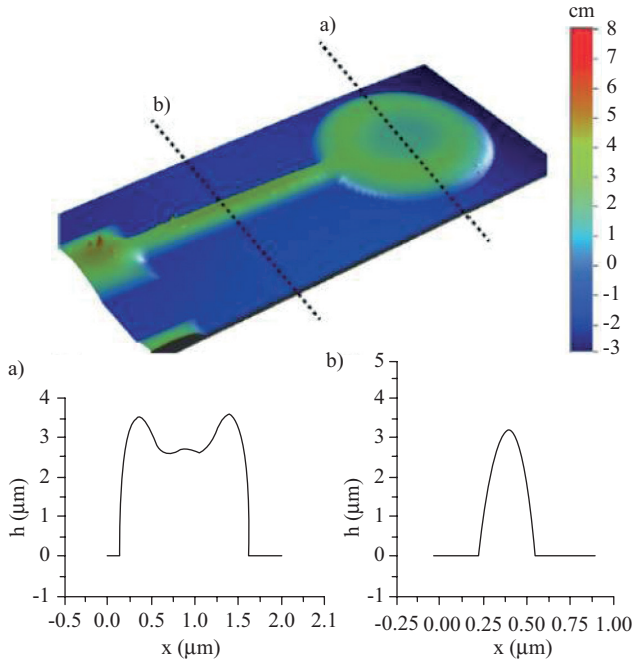

Figure 6.12. Confocal microscopy image of the PPCE structure used in the microfabrication of disk electrodes. The dotted lines indicate the areas where the profilometric data displayed in subfigures (a) and (b) were collected. (a) The wavy profile and round edges are the result of resist flow during pyrolysis.

Source: Reprinted with permission from Sánchez-Molas et al. [39].

its opening by deep reactive ion etching. To improve the adhesion of the passivation layer, the PPCE is treated with a mild ammonia plasma and silanized immediately before CVD [39]. A confocal microscopy image of the so-obtained PPCE structure is shown in Figure 6.12 together with the profilometric data of an electrode structure after pyrolysis. The resulting disk electrodes are 1.5 mm in diameter and connected to a 0.8 mm × 3 mm contact pad by a 0.5-mm-wide and 3-mm-long conducting track. The figure shows how resist flow during pyrolysis results in the rounding of the structure edges.

These electrodes were applied to the determination of Hg in aqueous solution at pH 1.5, using anodic stripping and square wave voltammetry. With a deposition time of 30 min, the authors achieved a DL of 2.35 ± 0.25 µg L^{-1}, with a linear range extended from 2 to 15 µg L^{-1}.

6.3 ELECTROANALYSIS OF ORGANIC ANALYTES WITH PYROLYZED PHOTORESIST CARBON ELECTRODES

6.3.1 DIRECT ELECTROANALYSIS OF ORGANICS

The application of PPCEs for the direct determination of organic compounds was exploited by Mardegan et al. [40]. To improve the sensitivity and for lowering the DL of o-toluidine in aqueous solution, the authors proposed the modification of pyrolyzed photoresist carbon electrodes with carbon nanotubes (PPCE–CNTs). The particular PPCE design allows for the use of a new carbon nanotube deposition method based on spray coating, improving the deposition reproducibility, homogeneity, and uniformity compared with the drop casting procedure. In Figure 6.13, we show a schematic of the nebulizer used to deposit consecutive layers of CNT on the PPCE surface [40]. This deposition technique is based on a two-step approach: CNTs are first dispersed in an aqueous medium, avoiding the use of toxic dimethylformamide (DMF), and then deposited onto the PPCE surface by spray coating. The electrode surface is heated at a temperature higher than the boiling point of water, allowing efficient and controlled drying. By changing the number of spray deposition scans, different extents of modification with CNTs are obtained, and the electrochemical behavior can be optimized for specific analytical purposes.

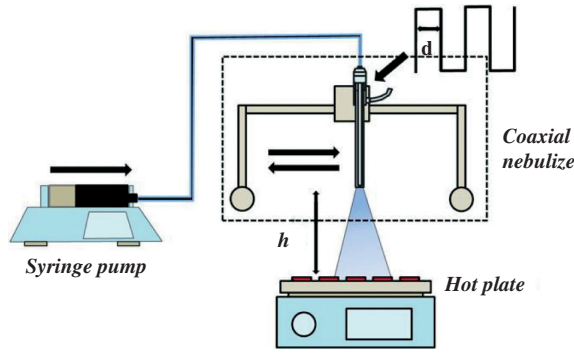

Figure 6.13. Scheme of the spray-coater system with coaxial nebulizer.

Source: Reprinted with permission from Mardegan et al. [40].

The PPCE–CNTs were characterized by CV and electrochemical impedance spectroscopy (EIS). The o-toluidine electroanalytical determination was carried out by linear sweep voltammetry. A linear range between 0.5 and 5 ppm with a DL of 0.089 ppm were obtained.

Application of PPCE in aprotic solvents was presented for the first time by Silvestrini et al. [14] who studied the electrochemistry of bilirubin (BR) in DMSO containing 0.1 M $TBABF_4$ as the supporting electrolyte. It is known that unconjugated BR is poorly soluble in water, and many studies in the literature address its electrochemical behavior in solvents such as DMF and DMSO. However, there is no agreement on the oxidation mechanism or even on the number of electrons involved in the oxidation steps, because different authors report different results [41–43]. The application of PPCE to the study of the electrochemical behavior of BR was aimed at clarifying the BR oxidation mechanism. In particular, it was demonstrated that the oxidation of BR to biliverdin (BV) involves the formation of a relatively stable intermediate whose fate depends on the timescale of the experiment.

A very interesting aspect of this work is the possibility of studying the reactions between the superoxide anion [$O_2^{\bullet-}$] and BR. In living systems, $O_2^{\bullet-}$ arises from oxygen-consuming reactions and its concentration is tightly regulated by a number of enzymatic and nonenzymatic reactions, including reactions with BR [44]. In this study, the superoxide radical anion was electrogenerated at the PPCE by the one-electron electrochemical reduction of dissolved oxygen, which is relatively stable in aprotic media. Data shown in Figure 6.14 indicate that electrogenerated $O_2^{\bullet-}$ quickly reacts with BR, this reaction reflecting on an electrocatalytic increase of the oxygen reduction peak. This is an important evidence supporting the radical scavenging capability of BR. From a mechanistic viewpoint, it can be noted that the reduction of O_2 to $O_2^{\bullet-}$ on the PPCE is slightly less reversible than that on bulk GC, probably because of the lower amount of quinone groups on the PPCE surface that catalyze oxygen reduction. This is probably related to the fact that the pyrolysis of SU-8 is performed in an inert N_2 atmosphere [8].

6.3.2 IN VIVO AND FLOW ANALYSIS

For performing bioanalytical studies both *in vivo* and *in vitro*, various electrochemical detection schemes have been proposed. In particular, for following *in vivo* fast processes such as the release of neurotransmitters (a phenomenon that occurs within a 200 ms timescale), a technique

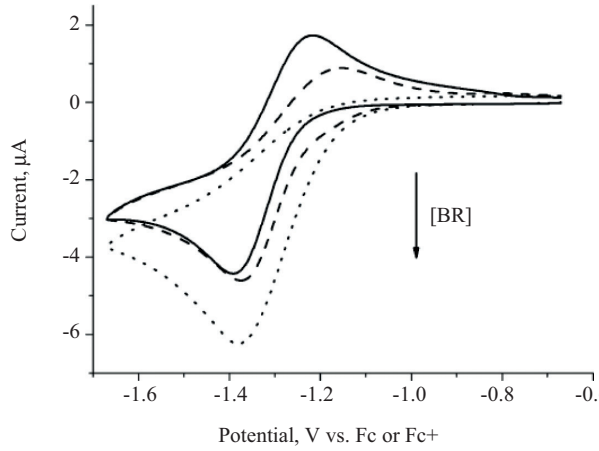

Figure 6.14. Cyclic voltammograms for the one-electron reduction of O_2 recorded in 0.1 M $TBABF_4$, DMSO at a PPCE in the presence of atmospheric oxygen at different BR concentrations, namely, 0 (full line), 0.8 (dashed line), and 4 mM (dotted line). Scan rate 50 mV s^{-1}.

Source: Reprinted with permission from Silvestrini et al. [14].

named fast scan cyclic voltammetry (FSCV) has been implemented by Mark Wightman and coworkers [17, 45–47]. The application of FSCV at arrays of individually addressed microelectrodes (MEAs) allows one to detect simultaneously the release of different neurotransmitters from different neuroanatomical areas. To this aim, arrays of PPCEs have been developed [17]. With respect to arrays of metal microelectrodes, arrays of micro-PPCEs present several advantages that can be summarized as higher resistance to biofouling, wider operative potential window, and lower manufacturing cost. Special care was taken in the fabrication of the PPCE microarrays in order to produce sensitive and selective electrochemical sensors able to detect different analytes simultaneously and independently. The arrays were made of a pyrolyzed positive tone photoresist, insulated by a negative photoresist, adopting photolithographic techniques. Figure 6.15 presents an SEM image and a drawing of the carbon MEA.

The electrochemical response of these arrays compares with that of polyacrylonitrile carbon fiber microelectrodes that have been used for many years to quantitatively determine concentrations of neurotransmitters *in vivo* by FSCV [17]. This study has shown the ability of the PPCEs of the array to work in synchrony without crosstalk, allowing the simultaneous decoupled detection of dopamine and oxygen.

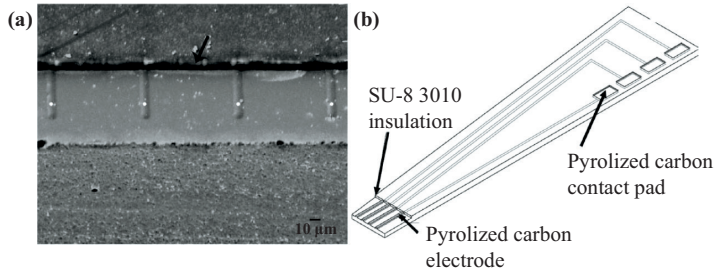

Figure 6.15. PPF microelectrode array. (a) SEM image taken of the PPCE microelectrode array after dicing. Each of the four electrodes is 10 µm wide and 50 µm long. The white dots indicate the four electrodes, while the arrow indicates the insulation layer. (b) Drawing of the device (not scaled).

Source: Reproduced with permission Zachek et al. [17].

In a following work, Wightman et al. [6] proposed a method to renew on site the surface of the PPCEs of the array. The method is based on the use of a voltammetric waveform that extends up to an anodic potential of 1.4 V versus Ag–AgCl, using a scan rate of 400 V s^{-1}. At such a positive potential, the oxidative etching of carbon occurs, therefore renewing the electrode surface before the next measurement. As catecholamines strongly adsorb onto the carbon surface, such a periodical renewal of the electrode surface reflects in significant improvements in the sensitivity and reproducibility of catechols determination.

The excellent performances of carbon electrodes are finding wide application also in the field of electrochemical detectors for capillary electrophoresis (CE-EC). Microchip-based CE-EC have been developed using carbon fibers or carbon paste fixed in a poly(dimethyl siloxane) (PDMS) channel [48, 49], screen-printed thick-film electrodes [50, 51], or conventional carbon fiber microdisk electrodes aligned at the outlet of the channel [52, 53]. A disadvantage of using carbon in microchips is that traditional carbon forms cannot be patterned by photolithography. The use of PPCE for electrochemical detection in microchips has been, therefore, proposed in the literature to overcome this limit [54, 55]. Larsen et al. [55] showed how PPCEs can be used for the CE-EC detection of the potassium-induced release of neurotransmitters from large groups of neuronal cells. The effect of using two different photoresist (AZ 4330 and AZ 5214) for the fabrication of PPCEs was investigated.

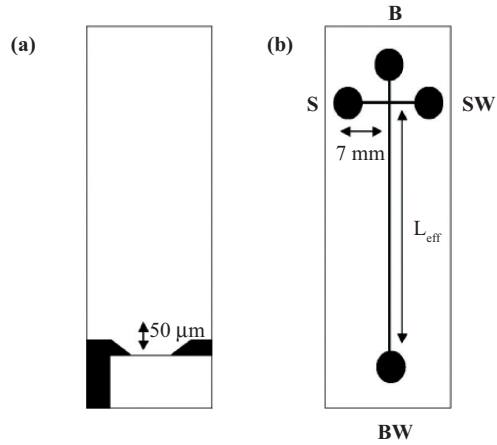

Figure 6.16. Electrode geometry and microchip layout. (a) Illustration of PPCE geometry. The electrode is 50 µm wide at the center working area. (b) Channel dimensions: 20 µm wide, 7 µm deep, 7 mm from each sample (S), sample waste (SW), and buffer (B) wells to the injection T, effective separation length (L_{eff}) varied.

Source: Reproduced with permission from Hebert et al. [54].

The application of PPCEs in a microchip capillary electrophoresis device for the separation and the determination of neurotransmitters was proposed by Hebert et al. [54]. A high sensitivity was achieved by applying sinusoidal voltammetric detection reaching a DL (S/N = 3) of 100 nM for dopamine. The electrode geometry and microchip layout are illustrated in Figure 6.16.

As evidenced by the data in Figure 6.17, the proposed procedure was suitable for the separation of the dopamine signal from that of excess ascorbic acid. The effectiveness of the device was further confirmed by the separation of the signals of four different neurotransmitters, as shown in Figure 6.18.

The lithographically fabricated electrodes allow for the design of truly integrated CE-EC microchips. Effective decoupling of the electrochemical and electrophoresis fields allows the planar electrodes to be placed in the separation channel, still retaining a stable background level, even when high fields are applied. On-chip CE with sinusoidal voltammetry detection at PPCEs can be envisioned as a tool to explore a wide variety of analytical problems.

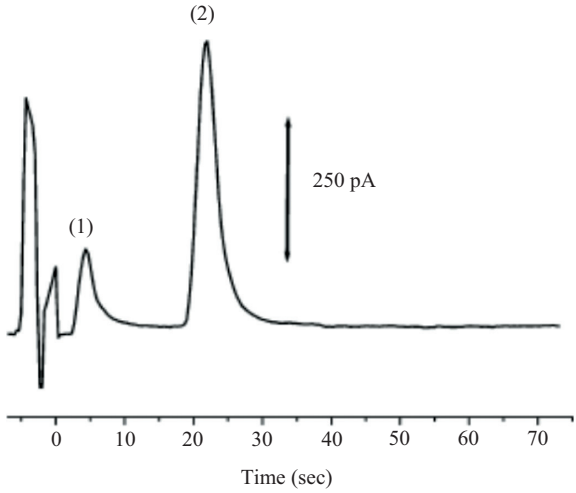

Figure 6.17. Rapid separation of 5 µM dopamine (1) and 250 µM ascorbic acid (2), first harmonic (3 Hz) time course. Electrophoresis buffer 25 mM phosphate, 2 mM NaCl (pH 7.4); separation voltage, +750 V (440 V cm^{-1}) with +405 V pull-back voltage; injection, +1 kV for 3 s. Effective separation length of channel is 1 cm. SV detection was accomplished by applying a 3-Hz sine wave from −50 to 550 mV (vs. Ag–AgCl).

Source: Reproduced with permission from Hebert et al. [54].

Fischer et al. [56] studied the analytical performances of the integrated CE-EC for analyzing catecholamines. The influence of the electrode alignment on the analytical performance was studied in detail. Figure 6.19, shows three different designs of the electrodes, end-channel, off-channel, and in-channel alignments, investigated using dopamine, norepinephrine, and catechol as test analytes. Experiments using an in-channel electrode alignment significantly reduced the amount of band broadening observed with other electrode alignment schemes. Compared with end- and off-channel alignments, this led to a decrease in peak skew and peak tailing with increased resolution and theoretical plates number.

Lunte et al. exploited the improvement of the selective detection of compounds that present chemically reversible redox reactions obtained using two electrodes in series, to develop PPCEs for microchip capillary electrophoresis with dual-electrode electrochemical detection [18]. In this detection scheme, a different potential is applied to each electrode; for example, at the first electrode (generator), the analyte is oxidized, and

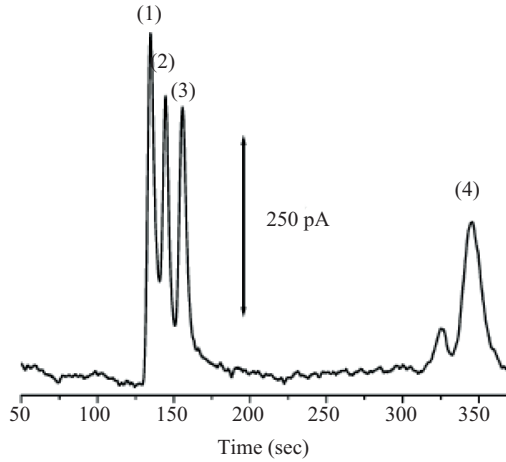

Figure 6.18. Separation of 10 μM dopamine (1), 25 μM epinephrine (2), 25 μM isoproterenol (3), and 100 μM L-dopa (4) at the first harmonic (3 Hz). Electrophoresis buffer 50 mM MES, 20 mM phosphate, 2 mM KCl (pH 5.3); separation voltage, +1 kV (180 V cm^{-1}) with +470 V pull-back voltage; injection, +2 kV for 2 s. Effective separation length of channel is 4.8 cm. SV detection was accomplished by applying a 3-Hz sine wave from −100 to 400 mV (vs. Ag–AgCl).

Source: Reproduced with permission from Hebert et al. [54].

at the second one (detector), the generated oxidized species is revealed by reduction. Dual-electrode detection offers the enhanced selectivity required to separate the signals of analytes displaying different electrochemical reversibility. For instance, it was shown that dual-electrode detection allows one to separate the signal of catechol from that of 5-hydroxyindole-3-acetic acid: both compounds are indeed oxidized at the first electrode, but catechol alone shows a significant response at the second electrode; in fact only the latter displays a reversible electrochemical behavior [18]. One of the difficulties in performing dual-electrode detection is positioning the two electrodes in close proximity to one another. The deposition of metal electrodes is fairly straightforward and metal-based dual-electrode systems have been reported [57]. On the contrary, when using traditional carbon forms, carbon-based dual-electrode detectors are much more difficult to fabricate. This limit was overcome

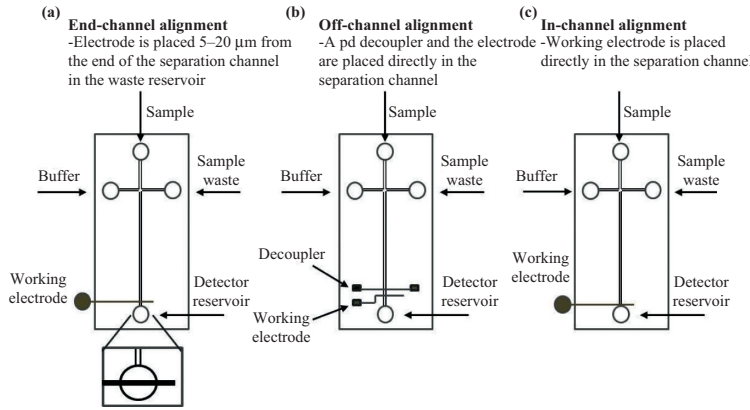

Figure 6.19. Schematic diagram of different electrode alignments for microchip electrophoresis with EC detection: (a) end-channel electrode alignment, (b) off-channel electrode alignment, and (c) in-channel electrode alignment. In-channel alignment is possible only when using an electrically isolated potentiostat.

Source: with permission from Fischer et al. [56].

by Lunte and coworkers [18, 56] who demonstrated that it is possible to fabricate very efficient PPCE-based dual-electrodes for CE-EC by photolithography and following controlled pyrolysis of the resist.

Furthermore, the photolithographic fabrication of the PPCEs allows the creation of a truly integrated separation and detection system. A scheme illustrating the photolithographic procedure for the fabrication of the electrodes and the microchip is shown in Figure 6.20.

6.4 CONCLUSIONS AND PROSPECTS

This chapter gives only a flavor of the great potential for PPCEs in applied fields such as environmental control, food safety, biomedical studies, and advanced molecular diagnostics devices. Novel electroanalytical detection schemes can be imagined as a future path for highly efficient electrochemical sensors obtained by photopatterning and pyrolyzing miniaturized GC electrodes. Recent studies show that the already excellent detection capabilities of PPCEs can be improved further by modifying their surface with other advanced C-based materials such as CNTs [40] or graphene [58] even generating defined 3D nanostructures

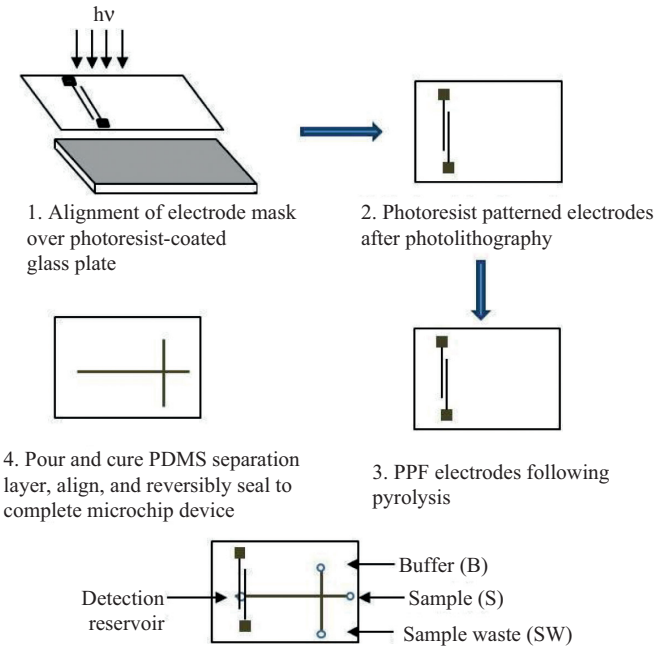

Figure 6.20. Schematic of the photolithographic fabrication procedure used for the PPCEs (images not to scale). 1: alignment of electrode mask over photoresist-covered glass plate; 2: photoresist patterned electrodes after photolithography; 3: PPCE following pyrolysis; 4: pour and cure PDMS separation layer, align, and reversibly seal to complete microchip device.

Source: with permission from Fischer et al. [18].

by the controlled deposition of these materials on the surface of PPCEs [59]. This will allow one to prepare tailor-patterned electrodes, with a highly specific electroactive surface and special electrocatalytic properties suitable for the development of highly miniaturized and highly efficient electrode systems. Moreover, the recently demonstrated possibility of preparing optically transparent carbon electrodes made by pyrolyzed photoresist [60] is opening the way to extend the previous advantages to fields where optical and electrochemical detection methods are combined, such as in spectroelectrochemical analyses and electrochemically induced luminescence. Research in the field of PPCE-based electroanalytical devices is only in its infancy and there are plenty of exciting new possibilities to be explored.

REFERENCES

[1] Kinoshita, K. 1988. *Carbon: Electrochemical and Physicochemical Properties*. New York, NY: Wiley.

[2] McCreery, R.L., and K.K. Cline. 1996. "Carbon Electrodes." In *Laboratory Techniques in Electroanalytical Chemistry,* eds. P.T. Kissinger and W.R. Heineman, 293–332. New York, NY: Marcel Dekker, Inc.

[3] Van der Linden, W.E., and J.W. Dieker. 1980. "Glassy Carbon as Electrode Material in Electro-Analytical Chemistry." *Analytica Chimica Acta* 119, no. 1, pp. 1–24. doi: http://dx.doi.org/10.1016/s0003-2670(00)00025-8

[4] Lewis, J.C., B. Redfern, and F.C. Cowlard. 1963. "Vitreous Carbon as a Crucible Material for Semiconductors." *Solid-State Electronics* 6, no. 3, pp. 251–IN4. doi: http://dx.doi.org/10.1016/0038-1101(63)90081-9

[5] McCreery, R.L. 2008. "Advanced Carbon Electrode Materials for Molecular Electrochemistry." *Chemical Reviews* 108, no. 7, pp. 2646–87. doi: http://dx.doi.org/10.1021/cr068076m

[6] Takmakov, P., M.K. Zachek, R.B. Keithley, P.L. Walsh, C. Donley, G.S. McCarty, and R.M. Wightman. 2010. "Carbon Microelectrodes with a Renewable Surface." *Analytical Chemistry* 82, no. 5, pp. 2020–28. doi: http://dx.doi.org/10.1021/ac902753x

[7] Kim, J., X. Song, K. Kinoshita, M. Madou, and R. White. 1998. "Electrochemical Studies of Carbon Films from Pyrolyzed Photoresist." *Journal of the Electrochemical Society* 145, no. 7, pp. 2314–19. doi: http://dx.doi.org/10.1149/1.1838636

[8] Ranganathan, S., R. McCreery, S.M. Majji, and M. Madou. 2000. "Photoresist-Derived Carbon for Microelectromechanical Systems and Electrochemical Applications." *Journal of the Electrochemical Society* 147, no. 1, pp. 277–82. doi: http://dx.doi.org/10.1149/1.1393188

[9] Ranganathan, S., and R.L. McCreery. 2001. "Electroanalytical Performance of Carbon Films with Near-Atomic Flatness." *Analytical Chemistry* 73, no. 5, pp. 893–900. doi: http://dx.doi.org/10.1021/ac0007534

[10] Wang, C., L. Taherabadi, G. Jia, M. Madou, Y. Yeh, and B. Dunn. 2004. "C-MEMS for the Manufacture of 3D Microbatteries." *Electrochemical and Solid-State Letters* 7, no. 11, pp. A435–38. doi: http://dx.doi.org/10.1149/1.1798151

[11] Mardegan, A., R. Kamath, S. Sharma, P. Scopece, P. Ugo, and M. Madou. 2013. "Optimization of Carbon Electrodes Derived from Epoxy-Based Photoresist." *Journal of the Electrochemical Society* 160, no. 8, pp. B132–37. doi: http://dx.doi.org/10.1149/2.107308jes

[12] Bard, A.J., and L.R. Faulkner. 2001. *Electrochemical Methods: Fundamentals and Applications*. New York, NY: Wiley.

[13] Wang, J. 2000. *Analytical Electrochemistry*. New York, NY: Wiley-VCH.

[14] Silvestrini, M., A. Mardegan, R. Kamath, M. Madou, L.M. Moretto, S. Passamonti, P. Scopece, and P. Ugo. 2014. "Pyrolyzed Photoresist Carbon Electrodes in Aprotic Solvent: Bilirubin Electrochemistry and

Interaction with Electrogenerated Superoxide." *Electrochimica Acta* 147, pp. 401–07. doi: http://dx.doi.org/10.1016/j.electacta.2014.09.046

[15] Heo, J.I., D.S. Shim, G.T. Teixidor, S. Oh, M.J. Madou, and H. Shin. 2011. "Carbon Interdigitated Array Nanoelectrodes for Electrochemical Applications." *Journal of the Electrochemical Society* 158, no. 3, p. J76. doi: http://dx.doi.org/10.1149/1.3531952

[16] Kamath, R.R., and M.J. Madou. 2014. "Three-Dimensional Carbon Interdigitated Electrode Arrays for Redox-Amplification." *Analytical Chemistry* 86, no. 6, pp. 2963–71. doi: http://dx.doi.org/10.1021/ac4033356

[17] Zachek, M.K., P. Takmakov, B. Moody, R.M. Wightman, and G.S. McCarty. 2009. "Simultaneous Decoupled Detection of Dopamine and Oxygen Using Pyrolyzed Carbon Microarrays and Fast-Scan Cyclic Voltammetry." *Analytical Chemistry* 81, no. 15, pp. 6258–65. doi: http://dx.doi.org/10.1021/ac900790m

[18] Fischer, D.J., W.R. Vandaveer, R.J. Grigsby, and S.M. Lunte. 2005. "Pyrolyzed Photoresist Carbon Electrodes for Microchip Electrophoresis with Dual-Electrode Amperometric Detection." *Electroanalysis* 17, no. 13, pp. 1153–59. doi: http://dx.doi.org/10.1002/elan.200503239

[19] Nolan, M.A., and S.P. Kounaves. 1999. "Microfabricated Array of Iridium Microdisks as a Substrate for Direct Determination of Cu 2+ or Hg 2+ Using Square-Wave Anodic Stripping Voltammetry." *Analytical Chemistry* 71, no. 16, pp. 3567–73. doi: http://dx.doi.org/10.1021/ac990126i

[20] Mikkelsen, Ø., S.M. Skogvold, K.H. Schrøder, M.I. Gjerde, and T.A. Aarhaug. 2003. "Evaluations of Solid Electrodes for Use in Voltammetric Monitoring of Heavy Metals in Samples from Metallurgical Nickel Industry." *Analytical Bioanalytical Chemistry* 377, no. 2, pp. 322–26. doi: http://dx.doi.org/10.1007/s00216-003-2102-z

[21] Švancara, I., M. Matoušek, E. Sikora, K. Schachl, K. Kalcher, and K. Vytřas. 1997. "Carbon Paste Electrodes Plated with a Gold Film for the Voltammetric Determination of Mercury(II)." *Electroanalysis* 9, no. 11, pp. 827–33.doi: http://dx.doi.org/10.1002/elan.1140091105

[22] Wang, J., J. Lu, S.B. Hocevar, P.A.M. Farias, and B. Ogorevc. 2000. "Bismuth-Coated Carbon Electrodes for Anodic Stripping Voltammetry." *Analytical Chemistry* 72, no. 14, pp. 3218–22. doi: http://dx.doi.org/10.1021/ac000108x

[23] Mardegan, A., S. Dal Borgo, P. Scopece, L.M. Moretto, S.B. Hočevar, and P. Ugo. 2012. "Bismuth Modified Gold Nanoelectrode Ensemble for Stripping Voltammetric Determination of Lead." *Electrochemistry Communications* 24, pp. 28–31. doi: http://dx.doi.org/10.1016/j.elecom.2012.08.012

[24] Królicka, A. 2002. "Bismuth-Film-Plated Carbon Paste Electrodes." *Electrochemistry Communications* 4, no. 2, pp. 193–96.doi: http://dx.doi.org/10.1016/s1388-2481(01)00301-0

[25] Hutton, E.A., S.B. Hočevar, B. Ogorevc, and M.R. Smyth. 2003. "Bismuth Film Electrode for Simultaneous Adsorptive Stripping Analysis of Trace Cobalt and Nickel Using Constant Current Chronopotentiometric and Voltammetric Protocol." *Electrochemistry Communications* 5, no. 9, pp. 765–69. doi: http://dx.doi.org/10.1016/s1388-2481(03)00177-2

[26] Hutton, E.A., S.B. Hočevar, L. Mauko, and B. Ogorevc. 2006. "Bismuth Film Electrode for Anodic Stripping Voltammetric Determination of Tin." *Analytica Chimica Acta* 580, no. 2, pp. 244–50. doi: http://dx.doi.org/10.1016/j.aca.2006.07.075

[27] Królicka, A., and A. Bobrowski. 2004. "Bismuth Film Electrode for Adsorptive Stripping Voltammetry—Electrochemical and Microscopic Study." *Electrochemistry Communications* 6, no. 2, pp. 99–104. doi: http://dx.doi.org/10.1016/j.elecom.2003.10.025

[28] Economou, A. 2005. "Bismuth-Film Electrodes: Recent Developments and Potentialities for Electroanalysis." *TrAC Trends in Analytical Chemistry* 24, no. 4, pp. 334–40. doi: http://dx.doi.org/10.1016/j.trac.2004.11.006

[29] Arduini, F., J.Q. Calvo, G. Palleschi, D. Moscone, and A. Amine. 2010. "Bismuth-Modified Electrodes for Lead Detection." *TrAC Trends in Analytical Chemistry* 29, no. 11, pp. 1295–304. doi: http://dx.doi.org/10.1016/j.trac.2010.08.003

[30] Mardegan, A., M. Cettolin, R. Kamath, V. Vascotto, A.M. Stortini, P. Ugo, P. Scopece, M. Madou, and L.M. Moretto. 2015. "Speciation of Trace Levels of Chromium with Bismuth Modified Pyrolyzed Photoresist Carbon Electrodes." *Electroanalysis* 27, no. 1, pp. 128–34. doi: http://dx.doi.org/10.1002/elan.201400392

[31] Vukomanovic, D.V., G.W. Vanloon, K. Nakatsu, and D.E. Zoutman. 1997. "Determination of Chromium (VI) and (III) by Adsorptive Stripping Voltammetry with Pyrocatechol Violet." *Microchemical Journal* 57, no. 1, pp. 86–95. doi: http://dx.doi.org/10.1006/mchj.1997.1495

[32] Domínguez, O., and M. Julia Arcos. 2002. "Simultaneous Determination of Chromium(VI) and Chromium(III) at Trace Levels by Adsorptive Stripping Voltammetry." *Analytica Chimica Acta* 470, no. 2, pp. 241–52. doi: http://dx.doi.org/10.1016/s0003-2670(02)00757-2

[33] Pifferi, V., F. Spadavecchia, G. Cappelletti, E.A. Paoli, C.L. Bianchi, and L. Falciola. 2013. "Electrodeposited Nano-Titania Films for Photocatalytic Cr(VI) Reduction." *Catalysis Today* 209, pp. 8–12. doi: http://dx.doi.org/10.1016/j.cattod.2012.08.031

[34] Vargas, M.C., O.D. Renedo, and M.J. Arcos Martinez. 2003. "Simultaneous Determination of Chromium(VI) and Aluminum(III) by Adsorptive Stripping Voltammetry with Pyrocatechol Violet." *Helvetica Chimica Acta* 86, no. 7, pp. 2434–40. doi: http://dx.doi.org/10.1002/hlca.200390196

[35] Chatzitheodorou, E., A. Economou, and A. Voulgaropoulos. 2004. "Trace Determination of Chromium by Square-Wave Adsorptive Stripping Voltammetry on Bismuth Film Electrodes." *Electroanalysis* 16, no. 21, pp. 1745–54. doi: http://dx.doi.org/10.1002/elan.200403051

[36] Jorge, E.O., M.M. Rocha, I.T.E. Fonseca, and M.M.M. Neto. 2010. "Studies on the Stripping Voltammetric Determination and Speciation of Chromium at a Rotating-Disc Bismuth Film Electrode." *Talanta* 81, no. 1–2, pp. 556–64. doi: http://dx.doi.org/10.1016/j.talanta.2009.12.043

[37] Rehacek, V., I. Hotovy, M. Vojs, T. Kups, and L. Spiess. 2012. "Nafion-Coated Bismuth Film Electrodes on Pyrolyzed Photoresist/Alumina Supports for Analysis of Trace Heavy Metals." *Electrochimica Acta* 63, pp. 192–96. doi: http://dx.doi.org/10.1016/j.electacta.2011.12.075

[38] Rehacek, V., I. Hotovy, and M. Vojs. 2014. "Bismuth Film Voltammetric Sensor on Pyrolyzed Photoresist/Alumina Support for Determination of Heavy Metals." *Electroanalysis* 26, no. 5, pp. 898–903. doi: http://dx.doi.org/10.1002/elan.201400020

[39] Sánchez-Molas, D., J. Cases-Utrera, P. Godignon, and F. Javier del Campo. 2013. "Mercury Detection at Microfabricated Pyrolyzed Photoresist Film (PPF) Disk Electrodes." *Sensors and Actuators B: Chemical* 186, pp. 293–99. doi: http://dx.doi.org/10.1016/j.snb.2013.06.017

[40] Mardegan, A., V. Pifferi, E. Pontoglio, L. Falciola, P. Scopece, and L.M. Moretto. 2014. "Sprayed Carbon Nanotubes on Pyrolysed Photoresist Carbon Electrodes: Application to o-Toluidine Determination." *Electrochemistry Communications* 48, pp. 13–16. doi: http://dx.doi.org/10.1016/j.elecom.2014.08.004

[41] Slifstein, C., and M. Ariel. 1973. "The Electrochemistry of Bilirubin in Dimethylsulfoxide." *Journal of Electroanalytical Chemistry and Interfacial Electrochemistry* 48, no. 3, pp. 447–63. doi: http://dx.doi.org/10.1016/s0022-0728(73)80377-8

[42] Moussa, F., G. Kanoute, C. Herrenknecht, P. Levillain, and F. Trivin. 1988. "Electrochemical Oxidation of Bilirubin and Biliverdin in Dimethyl Sulfoxide." *Analytical Chemistry* 60, no. 11, pp. 1179–85. doi: http://dx.doi.org/10.1021/ac00162a017

[43] Ribo, J.M., J.-A. Ferrera, J. Claret, and K. Grubmayr. 1992. "Reactivity of Pyrrole Pigments." *Bioelectrochemistry Bioenergetics* 29, no. 1, pp. 1–17. doi: http://dx.doi.org/10.1016/0302-4598(92)80049-m

[44] Liochev, S.I. 2013. "Reactive Oxygen Species and the Free Radical Theory of Aging." *Free Radical Biology and Medicine* 60, pp. 1–4. doi: http://dx.doi.org/10.1016/j.freeradbiomed.2013.02.011

[45] Heien, M.L.A.V., P.E.M. Phillips, G.D. Stuber, A.T. Seipel, and R.M. Wightman. 2003. "Overoxidation of Carbon-Fiber Microelectrodes Enhances Dopamine Adsorption and Increases Sensitivity." *Analyst* 128, no. 12, pp. 1413–19. doi: http://dx.doi.org/10.1039/b307024g

[46] Robinson, D.L., P.E.M. Phillips, E.A. Budygin, B.J. Trafton, P.A. Garris, and R.M. Wightman. 2001. "Sub-Second Changes in Accumbal Dopamine During Sexual Behavior in Male Rats." *NeuroReport: For Rapid Communication of Neuroscience Research* 12, no. 11, pp. 2549–52. doi: http://dx.doi.org/10.1097/00001756-200108080-00051

[47] Zachek, M.K., A. Hermans, R.M. Wightman, and G.S. McCarty. 2008. "Electrochemical Dopamine Detection: Comparing Gold and Carbon Fiber Microelectrodes Using Background Subtracted Fast Scan Cyclic voltammetry." *Journal of Electroanalytical Chemistry* 614, no. 1–2, pp. 113–20. doi: http://dx.doi.org/10.1016/j.jelechem.2007.11.007

[48] Gawron, A.J., R.S. Martin, and S.M. Lunte. 2001. "Fabrication and Evaluation of a Carbon-Based Dual-Electrode Detector for Poly(Dimethylsiloxane) Electrophoresis Chips." *Electrophoresis* 22, no. 2, pp. 242–48. doi: http://dx.doi.org/10.1002/1522-2683(200101)22:2%3C242::aid-elps242%3E3.0.co;2-w

[49] Martin, R.S., K.L. Ratzlaff, B.H. Huynh, and S.M. Lunte. 2002. "In-Channel Electrochemical Detection for Microchip Capillary Electrophoresis Using an Electrically Isolated Potentiostat." *Analytical Chemistry* 74, no. 5, pp. 1136–43. doi: http://dx.doi.org/10.1021/ac011087p

[50] Wang, J., M.P. Chatrathi, and B.M. Tian. 2001. "Microseparation Chips for Performing Multienzymatic Dehydrogenase/Oxidase Assays: Simultaneous Electrochemical Measurement of Ethanol and Glucose." *Analytical Chemistry* 73, no. 6, pp. 1296–300. doi: http://dx.doi.org/10.1021/ac001205t

[51] Wang, J., A.P. Chatrathi, A. Ibanez, and A. Escarpa. 2002. "Micromachined Separation Chips with Post-Column Enzymatic Reactions of "Class" Enzymes and End-Column Electrochemical Detection: Assays of Amino Acids." *Electroanalysis* 14, no. 6, pp. 400–04. doi: http://dx.doi.org/10.1002/1521-4109(200203)14:6%3C400::aid-elan400%3E3.0.co;2-w

[52] Backofen, U., F.M. Matysik, and C.E. Lunte. 2002. "A Chip-Based Electrophoresis System with Electrochemical Detection and Hydrodynamic Injection." *Analytical Chemistry* 74, no. 16, pp. 4054–59. doi: http://dx.doi.org/10.1021/ac020110j

[53] Fanguy, J.C., and C.S. Henry. 2002. "The Analysis of Uric Acid in Urine Using Microchip Capillary Electrophoresis with Electrochemical Detection." *Electrophoresis* 23, no. 5, pp. 767–73. doi: http://dx.doi.org/10.1002/1522-2683(200203)23:5%3C767::aid-elps767%3E3.3.co;2-#

[54] Hebert, N.E., B. Snyder, R.L. McCreery, W.G. Kuhr, and S.A. Brazill. 2003. "Performance of Pyrolyzed Photoresist Carbon Films in a Microchip Capillary Electrophoresis Device with Sinusoidal Voltammetric Detection." *Analytical Chemistry* 75, no. 16, pp. 4265–71. doi: http://dx.doi.org/10.1021/ac026425g

[55] Larsen, S.T., A. Argyraki, L. Amato, S. Tanzi, S.S. Keller, N. Rozlosnik, and R. Taboryski. 2013. "Pyrolyzed Photoresist Electrodes for Integration in Microfluidic Chips for Transmitter Detection from Biological Cells." *ECS Electrochemistry Letters* 2, no. 5, pp. B5–B7. doi: http://dx.doi.org/10.1149/2.005305eel

[56] Fischer, D.J., M.K. Hulvey, A.R. Regel, and S.M. Lunte. 2009. "Amperometric Detection in Microchip Electrophoresis Devices: Effect of Electrode Material and Alignment on Analytical Performance." *Electrophoresis* 30, no. 19, pp. 3324–33. doi: http://dx.doi.org/10.1002/elps.200900317

[57] Martin, R.S., A.J. Gawron, S.M. Lunte, and C.S. Henry. 2000. "Dual-Electrode Electrochemical Detection for Poly(Dimethylsiloxane)-Fabricated Capillary Electrophoresis Microchips." *Analytical Chemistry* 72, no. 14, pp. 3196–202. doi: http://dx.doi.org/10.1021/ac000160t

[58] Keeley, G.P., A. O'Neill, N. McEvoy, N. Peltekis, J.N. Coleman, and G.S. Duesberg. 2010. "Electrochemical Ascorbic Acid Sensor Based on DMF-Exfoliated Graphene." *Journal of Materials Chemistry* 20, no. 36, pp. 7864–69. doi: http://dx.doi.org/10.1039/c0jm01527j

[59] Xiao, X., T.E. Beechem, M.T. Brumbach, T.N. Lambert, D.J. Davis, J.R. Michael, C.M. Washburn, J. Wang, S.M. Brozik, D.R. Wheeler, D. Bruce Burckel, and R. Polsky. 2012. "Lithographically Defined Three-Dimensional Graphene Structures." *ACS Nano* 6, no. 4, pp. 3573–79. doi: http://dx.doi.org/10.1021/nn300655c

[60] Walker, E.K., D.A. Vanden Bout, and K.J. Stevenson. 2012. "Carbon Optically Transparent Electrodes for Electrogenerated Chemiluminescence." *Langmuir* 28, no. 2, pp. 1604–10. doi: http://dx.doi.org/10.1021/la2042394

CHAPTER 7

C-MEMS-Based 3D Interdigitated Electrode Arrays for Redox Amplification

Victor H. Perez-Gonzalez, Jose M. Rodriguez-Delgado, and Sergio O. Martinez-Chapa

School of Engineering and Sciences, Sensors and Devices Research Group, Tecnologico de Monterrey, Mexico

7.1 INTRODUCTION

Atoms, molecules, ions, and compounds are present everywhere at different concentrations, partial pressures, activities, and so on. These quantities are commonly regarded as chemical information and exist in the solid, liquid, or gas phase. Chemical sensors are devices that transform chemical information into a continuous analytically useful signal (e.g., an electrical signal). The chemical sensors research field continues to grow rapidly. From its early contributions in the 1880s to its current state of the art, chemical sensor technology has found a wide range of applications including biomedical engineering, industrial engineering, food safety, environmental monitoring, and water and air quality control, among others. These sensors can be broadly classified into six major categories based on their physical and chemical principles of operation (see Table 7.1) [1–4].

According to [5], the most dominant category of chemical sensors is the electrochemical, representing 55 percent of the complete chemical sensor market worldwide. This clear dominance has been attributed to

Table 7.1. Types of chemical sensors

Category	Examples
Optical	Absorbance, reflectance, luminescence, fluorescence, refractive index, optothermal effect, and light scattering sensors
Electrochemical	Potentiometric, conductometric, and amperometric sensors
Electrical	Metal oxide semiconductor, organic semiconductor, electrolytic conductivity, and electric permittivity sensors
Mass sensitive	Piezoelectric and surface acoustic wave sensors
Magnetic	Gas sensors, magnetic resonance imaging sensors
Thermometric	Catalytic and optothermal sensors
Others	X-, β-, or Γ-radiation-based sensors

the many advantages electrochemical sensors have over other types of chemical sensors. For instance, electrochemical sensors feature a better dynamic range, they can operate in turbid solutions and in highly resistive environments, their production is less expensive because of the less-sophisticated electronic instrumentation, and enhanced mass transport (because of convection) can be incorporated to increase signal strength for certain applications [6, 7]. Furthermore, electrochemical sensors, in contrast to optical sensors, benefit from miniaturization, for example, smaller electrodes have a better lower limit of detection (LOD) and produce faster response times. For miniaturization of electrochemical sensors, one can readily take advantage of advanced fabrication methods from the integrated circuit (IC) or microelectromechanical systems (MEMS) industry [8]. Electrochemical sensors have been successfully used for the detection of nitric oxide, pesticides, glucose, hydrogen sulfide, hydrogen peroxide, and even biological macromolecules such as enzymes and other proteins, among many other molecules of interest [9].

Electrodes constitute the sensing elements in an electrochemical cell. They can be classified as working electrodes (WEs), reference electrodes (REs), and counter electrodes (CEs). WEs are made from an electrically conductive, chemically inert material (e.g., gold, platinum, silver, or carbon). Such materials are not prone to oxidize or reduce when an electric current flows through them. In an electrochemical cell, the WE is the electrode at which the reaction of interest occurs. As a result of such reaction, the potential of the WE changes during an electrochemical experiment. In order to accurately and consistently measure the

potential of the WE, an RE is used as benchmark. Standard REs include the saturated calomel electrode, silver or silver chloride, copper or copper sulfate, and normal hydrogen electrode. REs are stable electrodes, whose potential, ideally, do not vary during the time course of an electrochemical experiment. Nonetheless, if a large current flows through an RE, its potential might change, impacting the measurement of the WE potential negatively. CEs are used to overcome this limitation. The role of a CE is to provide, along with the WE, an electric circuit for current to flow through (i.e., acting as a source or sink of electrons). In this way, no current will flow through the RE, whose potential will therefore remain constant. In the CE, reactions *counter* to those occurring at the WE take place. CEs are fabricated from the same materials used in the fabrication of WEs.

As previously listed, there are three main subcategories for electrochemical sensors, that is, potentiometric, conductometric, and amperometric [10]. In potentiometric sensors, a potential difference obtained at equilibrium (when no current is flowing through the electric circuit) between the WE and the RE provides quantitative information about the chemical species of interest. Conductometric sensors, on the other hand, monitor the change in sample conductance as a function of an excitation signal (DC or AC). Finally, an amperometric sensor measures the faradaic current at the WE upon the application of a suitable voltage between the WE and the RE. In amperometric sensors, the measured current is in direct proportion to the concentration of the target analyte.

There are three different setups that can be used to implement an electrochemical sensor. These are the two-electrode setup (WE and RE), the three-electrode setup (WE, CE, and RE), and the four-electrode setup (WE1 [generator], WE2 [collector], CE, and RE). The selection of electrode setup depends on the requirements of the particular sensing application. The two-electrode setup is commonly used to measure whole-cell voltages (e.g., in batteries). The three-electrode setup is most commonly used in electrochemistry and enables one to study the potential change at the WE separately (i.e., half-cell). Finally, the four-electrode setup is used when the absolute highest level of sensitivity is required. The latter two setups are mostly used in the amperometric mode, in which a voltage is applied between the WE and the RE to produce an oxidation or a reduction of the analyte of interest. This chapter focuses on the implementation of a four-electrode-based amperometric sensor in which the generator and collector electrode are interdigitated arrays (IDAs).

In Section 7.2, we describe the theoretical background required to understand the role of miniaturization in amperometric sensing and redox amplification. In Section 7.3, we present two different approaches to the

fabrication of interdigitated electrode arrays (IDEAs), that is, metal based versus carbon based. In Section 7.4, we introduce a survey on the state of the art of carbon microelectromechanical systems (C-MEMS)-based IDEAs for redox amplification applications. Finally, in Section 7.5, we present our concluding remarks.

7.2 BACKGROUND

7.2.1 MICROELECTRODES IN AMPEROMETRIC SENSORS

The miniaturization of electrodes has unlocked many new possibilities in electrochemical sensing. For instance, highly sensitive sensing becomes possible with microelectrodes (with at least one of their dimensions in the sub-25 μm range) even in low conductivity solutions or in nonpolar solvents.

Let's explore how microelectrodes positively impact the sensitivity of electrochemical measurements. Consider a three-electrode setup to analyze an analyte solution with bulk concentration C. Before applying a potential to the WE, no diffusion layer exists at the electrode–solution interface, but as soon as an oxidation (or a reduction) potential is applied, electroactive species deplete at the interface, creating a concentration gradient. This concentration gradient, whose thickness is a function of time, is the diffusion layer. Initially, the thickness of that diffusion layer is smaller than the characteristic surface dimension of the (macro- or micro-) WE, giving rise to planar diffusion [6]. Even at longer times, although the thickness of the diffusion layer increases, it remains smaller than the characteristic surface dimension of a macro-WE, and therefore, the diffusion profile remains planar. In contrast, for a micro-WE, the thickness of the diffusion layer becomes larger than its characteristic surface dimension, causing the diffusion to shift from a planar regime to a hemispherical one. This shift causes enhanced mass transport so that very high current densities and very low currents (e.g., in the nanoampere or picoampere range), resulting in improved lower LOD, are obtained. Microelectrodes can also be used to study very fast electrode processes (either homogeneous or heterogeneous) because of the negligible iR effects at very high scan rates [11].

A microelectrode attains a stable current signal for a given analyte concentration significantly faster than a macroelectrode, which generally requires experimental time scales in the order of seconds [12, 13]. The limiting steady-state current obtained with a microelectrode can be written as [5]

$$i = \frac{nFA\sqrt{DC}}{\sqrt{\pi t}} + \frac{nFADC}{r} \tag{7.1}$$

where n represents the number of electrons transferred in a reaction; F is the Faraday constant; D and C represent the diffusivity and bulk concentration of the species, respectively; t is time of the experiment; r is the radius of the electrode; and A represents the area of the electrode.

Equation 7.1 consists of two terms, a Cottrell term and a geometrical term. From this equation, it is clear that there are two ways to achieve a steady-state current: (1) increase the time of the experiment and (2) reduce the size of the electrode. As the time of the experiment increases, the Cottrell term becomes negligible and a steady-state current can be obtained with either macro- or microelectrodes. On the other hand, as the radius of the electrode decreases, the geometrical term dominates, the measurement is no longer a function of time, and one may obtain steady currents even at high-potential sweep rates.

7.2.2 REDOX AMPLIFICATION WITH INTERDIGITATED ELECTRODE ARRAYS

IDEAs are a special kind of microelectrodes with two working electrodes (microelectrode arrays) arranged in an interdigitated manner. IDEAs are also referred to by other names, such as IDAs or comb microelectrode arrays. IDEAs have been successfully used for a wide variety of applications including electrical stimulation of tissues, dielectrophoretic separation of particles, and the implementation of highly sensitive electrochemical sensors, among others [14–18].

IDEAs for amperometric sensing applications require extremely small gap spacing between the digits. With small enough electrode gaps, the diffusion layers of consecutive digits overlap upon application of a specific potential. Theoretically, with such IDEAs, when two adjacent electrodes are biased at different potentials (dual mode) against an RE, redox species undergo oxidation at the electrode with the higher potential (generator), while the oxidized species undergo reduction at the electrode with the lower potential (collector), before diffusing out into the bulk solution. As the redox species is cycled between the two electrodes multiple times, the generator current is amplified (in comparison to the current obtained in single mode, with the generator electrode biased at a certain potential and the collector electrode kept at an open potential).

This phenomenon is known as redox amplification (see Figure 7.1) and results in a significantly lowered LOD [19]. In order to obtain a significant amplification factor with an IDEA, the gap spacing between digits must be in the submicrometer range. The redox amplified current, i_r (measured from the generator or collector electrode), for IDEAs is defined as [20]

$$i_r = mbnFCD\left[0.637\ln\left(2.55/x\right) - 0.19x^2\right] \tag{7.2}$$

where m is the number of digits in the array and b is the length of each electrode. In Equation 7.2, $x = g/(w + g)$ with w representing the width of a digit and g representing the gap spacing between individual digits. Equation 7.2 was verified experimentally by different groups and clearly shows the dependence of the limiting current on electrode geometry [21–24]. The redox amplification factor is defined as

$$RA = i_{g,r}/i_g \tag{7.3}$$

where $i_{g,r}$ represents the generator current in dual mode and i_g represents the generator current in single mode. Another metric of performance evaluation in redox-amplification-based sensing is the collection efficiency (*Ceff*). *Ceff* is defined as $i_{c,r}/i_{g,r}$, where $i_{c,r}$ represents the collector current in dual mode. As a matter of fact, the redox amplification factor can also be approximated from the collection efficiency as

$$RA = 1/\left(1 - Ceff^2\right) \tag{7.4}$$

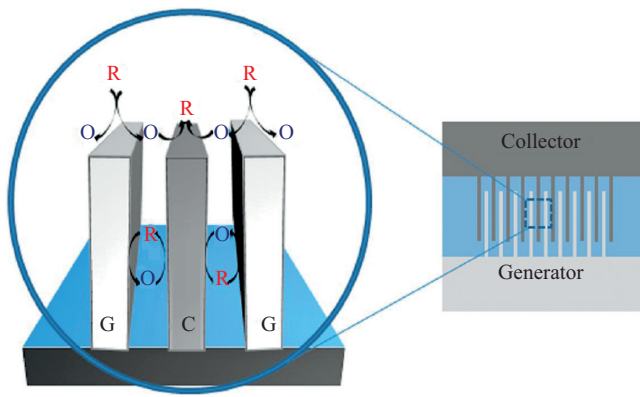

Figure 7.1. Schematic representation of the redox amplification phenomenon in IDEAs. O: Oxidized species, R: Reduced Species, G: Generator, C: Collector.

Ideally, in order to gain the maximum benefit from an IDEA, *Ceff* must be equal to 1 ($RA = \infty$). In such a case, the collector electrode will reduce all the species oxidized by the generator electrode and vice versa. A parameter that significantly contributes to the improvement of the *Ceff* is the gap spacing between the digits. Interdigit gaps of 10 μm were proved to produce weak redox amplification effects. With smaller gaps, stronger amplification factors have been reported. Notwithstanding, simulations predict that interdigit gaps smaller than 100 nm do not further improve the performance of IDEA-based redox amplification sensors [25].

7.3 METHODS TO IDEAS FABRICATION

7.3.1 METALLIC IDEAS

Conventional IDEAs used in redox amplification are made from noble metals using complex multistep fabrication techniques. Deep-UV projection lithography and electron beam lithography are two of the often used lithography techniques in this process. These lithographic methods have important drawbacks. For instance, deep-UV projection lithography suffers limitations in resolution because of diffraction and requires the use of an excimer laser. On the other hand, electron beam lithography provides much higher resolution; nonetheless, it requires high vacuum conditions for its operation, which makes it an even more expensive serial process (only one IDEA can be patterned at a time). In addition, metal deposition is carried out using costly physical or chemical vapor deposition methods. Moreover, noble metals such as Au or Pt (which are popular choices for the fabrication of IDEAs) require an adhesion layer (e.g., Cr or Ti), as they exhibit weak adhesion to glass or Si substrates. Deposition of metals is followed by a lift-off step, which is likely to leave metal residues randomly dispersed on the substrate surface. Furthermore, in spite of their excellent electrical conductivity, noble metals present unwanted electrochemical side reactions, even at low potentials. Moreover, bilayers such as Cr–Au or Ti–Au create a galvanic couple when in contact with an electrolyte, thus leading to corrosion. Finally, for 3D IDEAs (height ≥ 200 nm), the cost and complexity of the fabrication process rises significantly because of additional fabrication steps such as an additional photolithography step to define photoresist wells atop the planar IDEAs and electroless or electroplating to make the tall metal electrode structures.

However, in spite of these drawbacks, IDEAs made from noble metals have achieved very high amplification factors. For instance, in [26], an amplification factor of ~70 was reported for the $K_4[Fe(CN)_6]$ molecule

with 3D metal IDEAs. Also, in [25], an even higher amplification factor of ~110 was attained for the detection of paracetamol (200 μM concentration) with metallic IDEAs.

7.3.2 C-MEMS-BASED 3D IDEAS

The use of carbon as a working material in technological applications has a long and rich history. In the 19th century, Edison used carbonized rayon fibers as filaments in electric light bulbs [27]. The system of carbon allotropes spans a wider range of physical and chemical properties than those of silicon and noble metals commonly used in the IC industry. In addition, the fabrication of carbon-based micro- or nanostructures is, in general, less expensive than the fabrication of their metallic and semiconductive counterparts. Moreover, carbon is chemically inert, has a wider electrochemical stability window than noble metals, and presents excellent biocompatibility [28]. Because of these very attractive features, carbon-based micro- or nanostructures have found applications in fields as diverse as biomedical and environmental engineering, food safety, and clean energy generation, among others, many of which are thoroughly covered in this book.

Although carbon is difficult to machine, polymers are not. Some polymers with low oxygen content can be transformed into carbon through a pyrolysis step. The C-MEMS process includes a series of fabrication steps that allow for patterning of photosensitive materials and transformation of the resulting structure into carbon. Polyfurfuryl alcohol, polyacrylonitrile, and SU-8 photoresist are examples of commonly used carbon precursor materials used in the C-MEMS process [29].

The conventional C-MEMS process has been described in Chapter 1of Volume 1 and in several other chapters of this book. Nonetheless, the fabrication of 3D carbon IDEAs with submicrometer resolution requires modifying some of the C-MEMS processing steps. Therefore, to avoid confusion, the complete fabrication process for 3D carbon IDEAs is shown in Figure 7.2 and is detailed next.

7.3.2.1 Oxide Growth

Because of their high melting point (over 1,400°C), silicon wafers are preferred as substrate material in the C-MEMS process. Such high melting point is critical because of the high temperature experienced

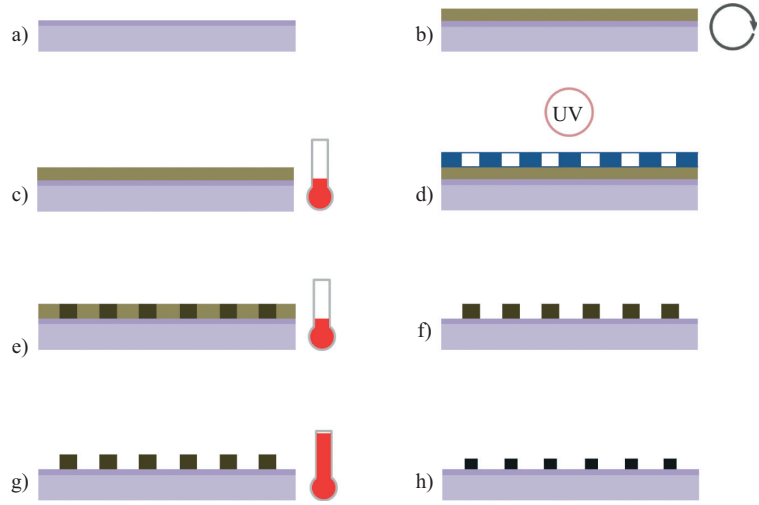

Figure 7.2. Steps for C-MEMS process: (a) oxide grow over Si wafer, (b) spin coating of photoresist, (c) soft baking, (d) exposure to UV light, (e) postexposure bake, (f) development, (g) pyrolysis, (h) final structure.

during the final pyrolysis step (~900°C or above). Nonetheless, the resistivity of silicon is not high enough to avoid leakage currents. Therefore, a thin oxide layer is required to electrically insulate the conducting structures in multielectrode systems. A 50-nm-thick oxide layer is grown over the silicon substrate through a thermal oxidation process (Figure 7.2a).

7.3.2.2 Spin Coat

A thin film of low-viscosity SU-8 (2000.5, 2002, or 2005) is then spin coated over the silicon wafer (Figure 7.2b). With low-viscosity SU-8, to ensure that the wafer will be uniformly coated, it is essential to dispense the photoresist over the complete wafer surface manually before spinning. The selection of low-viscosity photoresists is critical in order to achieve submicrometer patterning resolution.

7.3.2.3 Soft Bake

The photoresist layer must be soft baked in order to increase its adhesion to the SiO_2 layer through solvent evaporation (Figure 7.2c). Soft baking is

carried out at a temperature of 95°C for 1 min. on a hot plate. A convection oven is not recommended for this processing step, as it seals the photoresist film, avoiding solvent evaporation. This step is critical to ensure flatness of the film, which is essential for the next step.

7.3.2.4 UV Exposure

In order to pattern the photoresist film, it is exposed to UV light (365 nm) through a photomask (see Figure 7.2d). Use of a hard-contact mask aligner is recommended, as it reduces significantly the diffraction of light between the mask and the film. Sometimes, exposure doses recommended by the SU-8 manufacturer do not lead to an acceptable resolution for the fabrication of 3D IDEAs. In such cases, the dose needs to be lowered. When SU-8 is exposed to UV light, a strong acid is generated, which diffuses to the SU-8 monomers and initiates cationic polymerization, leading to cross-linking [30]. Therefore, a lower dose of UV light will generate a lesser amount of acid in the SU-8 film, preventing its diffusion across the IDEAs gaps.

7.3.2.5 Post Exposure Bake

In contrast with the soft-bake processing step, the postexposure bake (PEB) is carried out in a convection oven to uniformly heat the photoresist layer (Figure 7.2e). The PEB catalyzes the cross-linking process started during UV exposure of the SU-8. PEB parameters were also optimized to improve patterning resolution. First, the SU-8-coated wafer is baked at 95°C for 2 mins., then at 70°C for another 2 mins., and finally, at 50°C for 4 mins.

7.3.2.6 Development

After the PEB, the processed wafer is immersed in a glass dish filled with developer solution, which dissolves unexposed photoresist regions (Figure 7.2f). As the film used herein is very thin, the development step should not exceed 2 mins. and it requires no agitation. Then, the structures are rinsed first with fresh developer solution for 10 secs. and then with IPA for another 10 secs. Finally, the wafer is dried using compressed N_2.

7.3.2.7 Pyrolysis

For pyrolysis, the wafer is placed in a pyrolysis furnace (Figure 7.2g) and heated up to 900°C under an inert atmosphere (either vacuum [$< 10^{-6}$mbar] or flow of ultrapure N_2 [2000 sccm]). This step transforms the SU-8 patterns into carbon. The pyrolysis process is initiated in a precarbonization step from 25°C to 300°C (ramp rate of 4.5°C/min) with a dwell time of 60 mins. at 300°C. Then the temperature is increased to 900°C (ramp rate of 10°C/min) with a dwell time of 60 mins. at 900°C. Finally, the furnace chamber is cooled down to 25°C (ramp rate of −3.25°C/min). The final structure (Figure 7.2.h) is a high-quality glassy carbon electrode with a mass lower than that of the original SU-8 structure.

7.4 STATE OF THE ART IN C-MEMS-BASED IDEAS FOR REDOX AMPLIFICATION APPLICATIONS

Recently, C-MEMS-based IDEAs were successfully used as amperometric sensors. Different electrode designs were found to produce redox amplification and studies were carried out to assess their performances [19, 31]. Such studies provided important insights on the impact of several design parameters on the LOD of the sensor. Also, in [32], carbon IDEAs were used to detect dopamine in the presence of ascorbic acid. This section summarizes those findings and highlights the advantages of using C-MEMS-based IDEAs, over conventional metallic IDEAs, for redox amplification applications.

7.4.1 CARBON IDEAS FOR ELECTROCHEMICAL SENSING

In [31], the first implementation of C-MEMS for redox-amplification-based sensors was presented. In this work, Heo et al. studied the impact of electrode gap and thickness of the IDEA on the *RA* factor. Two different IDEA designs were fabricated. Before pyrolysis, IDAs in this study featured an interdigit gap of 1 μm, and each digit had a width of 1 μm with a thickness of 1 or 2.95 μm. The pyrolysis step transformed such microstructures into electrodes with a larger interdigit gap of 1.6 μm, and a digit width of 300 nm with a thickness of 80 or 340 nm (see Figure 7.3, which shows the thick electrode design only).

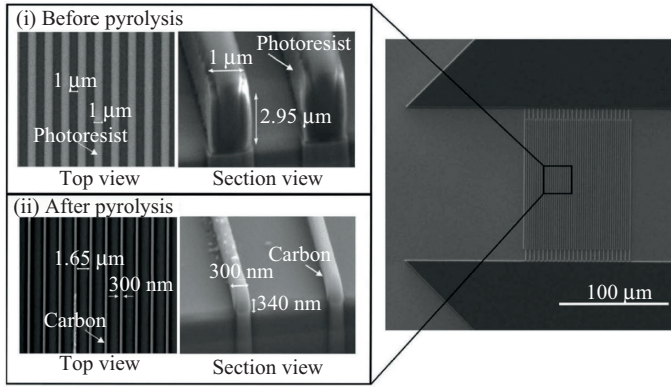

Figure 7.3. Scanning electron microscope (SEM) images of IDEAs before and after pyrolysis [31].

An aqueous solution of 10 mM $K_4Fe(CN)_6$ and 500 mM KCl was prepared to study the redox cycling on these carbon IDEAs. Cyclic voltammetry (CV) measurements in single (where only the generator electrode is biased) and dual (where the generator and collector electrodes are biased at different potentials) modes were used to estimate the *RA* factor. For single-mode operation, the generator electrode was swept from 0 to 600 mV at a potential scan rate of 50 mV/s against an Ag–AgCl RE, while the CE was kept at open potential. In dual mode, the generator electrode was swept at the same rate in the same potential window, while the CE was kept at a reduction potential of −0.3 V.

Dual-mode CV measurements demonstrate that for both electrode designs (thin electrodes [80 nm] and thick electrodes [300 nm]), the generator currents increase with an increment in film thickness and a reduction in electrode gap. Even though the surface area of the thick carbon electrodes is only 2.1 times higher than that of the thin electrodes, its generator current is 5.4 times higher than that measured from the thin electrodes at an oxidation potential of 0.6 V. Linear diffusion between the walls of the digits is responsible for this behavior, as its contribution is larger than that obtained from an increase in surface area only. Additionally, it was demonstrated that in dual-mode operation, both electrode designs exhibit an almost linear current–voltage regime. Such linearity is due to the low conductivity of carbon electrodes when compared to that of electrodes made from noble metals such as Pt or Au. The lower conductivity of carbon increases the effect of the IR drop, reducing the potential at the electrode.

The effect of interdigit gap and electrode thickness on the *Ceff* and *RA* factors were also characterized. For these experiments, electrode arrays

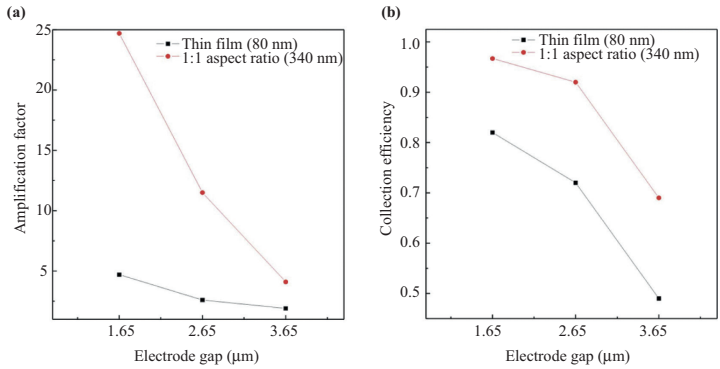

Figure 7.4. Redox cycling behavior of carbon IDEAs as a function of film thickness and interdigit gap, (a) amplification factor and (b) collection efficiency [31].

with gaps of 1.65, 2.65, and 3.65 μm were fabricated, each featuring thicknesses of 80 and 340 nm. Results clearly show that smaller electrode gaps produce higher collection efficiencies and amplification factors. Experiments conducted using the 340-nm-thick carbon IDEAs result in an amplification factor of ~25 for the smallest interdigit gap (i.e., 1.65 μm) as shown in Figure 7.4a. As the electrode gap is increased to 3.65 μm, the amplification factor is reduced to a value close to 5. Smaller gaps increase the probability of a molecule being cycled several times between the two working electrodes (before diffusing out into the bulk solution). Moreover, with thick electrodes, the gap region acts as a trench, which improves further this redox cycling probability. This is also supported by *Ceff* measurements reaching values close to 1 for closely spaced thick carbon IDEAS (see Figure 7.4b).

7.4.2 3D CARBON IDEAS FOR REDOX AMPLIFICATION

Kamath and Madou [19] improved and significantly expanded the work presented in [31]. They characterized the performance of 3D carbon IDEAs as a function of electrode height, width-to-gap ratio, potential sweep rate, and sample flow rate. Moreover, with an optimized fabrication process (see Section 7.3.2), they reported an amplification factor of 37, the highest reported yet for carbon IDEAs fabricated using conventional UV photolithography.

Table 7.2 summarizes the dimensions of four designs that were experimented with. Dimensions were measured using SEM and profilometry. The CE and RE were fabricated at a distance of 500 μm

Table 7.2. IDEAs dimensions before pyrolysis (bp) and after pyrolysis (ap)*

Height	Width	Gap	Width/gap (avg)
$H_{bp} = 0.6$, $H_{ap} = 0.22$	$W_b = 2.72$	$G_b = 1.08$	1.66
	$W_t = 2.02$	$G_t = 1.78$	
$H_{bp} = 2.1$, $H_{ap} = 0.59$	$W_b = 2.72$	$G_b = 1.08$	1.63
	$W_t = 1.99$	$G_t = 1.81$	
$H_{bp} = 3.6$, $H_{ap} = 0.86$	$W_b = 2.7$	$G_b = 1.1$	1.59
	$W_t = 1.96$	$G_t = 1.84$	
$H_{bp} = 5.1$, $H_{ap} = 1.1$	$W_b = 2.7$	$G_b = 1.1$	1.58
	$W_t = 1.95$	$G_t = 1.85$	

* *W_b: width at the base of the electrode, W_t: width at the top of the electrode. All dimensions are measured in micrometers*

on either side of the IDEA. The carbon electrode intended as the RE was coated with a droplet of Ag–AgCl ink and dried in a convection oven for one hour at 60°C to make a pseudo-reference electrode. Additionally, a 1.5-mm-wide and 100-µm-high polydimethylsiloxane channel was fabricated and sealed onto the IDEA substrate to prevent sample evaporation during the experiments.

CV and chronoamperometry (CA) techniques were used to study redox amplification on these 3D carbon IDEAs. CVs were carried out in a 500 mM KCl solution containing 1 mM $K_4Fe(CN)_6$ at two different potential sweep rates (50 and 5 mV/s). CVs were performed in single and dual modes. In single-mode operation, the collector electrode was kept at an open potential while the generator electrode was swept between −200 and 600 mV. In dual mode, the collector electrode was held constant at −250 mV while the generator potential was swept versus the pseudo-reference electrode. CA measurements were also carried out in single and dual modes. First, dual-mode measurements were performed with the generator electrode kept at an oxidation potential of 400 mV and the collector electrode kept at a reduction potential of −250 mV. After approximately 30 secs. of operation, the collector electrode was disconnected and kept at open circuit to measure the single-mode current. Also, for experiments under flow conditions, the flow rate was kept at 500 nL/s. Finally, in order to avoid air bubbles in the channel, the solution was flown for several seconds before starting the CV and CA experiments.

In Figure 7.5a, we show the amplification factor and the collection efficiency measurements as a function of electrode height and potential

sweep rate. These data were obtained from IDEAs with a width-to-gap ratio of 1.6. From the graph, it can be observed that at 5 mV/s, the *Ceff* increases from 0.97 to 0.985 and the *RA* factor increases from 9 to 37, as the electrode height increases from 0.2 to 1.1 µm. This is expected, as the tall electrode walls act as a trench that allows for more efficient redox cycling. Both *Ceff* and *RA* are negatively affected by faster potential sweep rates. This is attributed to the time available for redox cycling, which is significantly longer at low potential sweep rates. Additionally, Figure 7.5b reveals that *Ceff* and *RA* factors improve with increments in the width-to-gap ratio. This is explained by the fact that an increase in electrode width has a different effect when working in single mode than it does when operating in dual mode. With IDEAs working in single mode, an increase in electrode width produces an increase in diffusion layer overlap, causing a decrease in the generator current. In dual mode, the opposite occurs, with larger overlaps in the diffusion layer increasing the measured generator current because of redox cycling. Additionally, CA measurements were used to characterize the effect of sample flow rate on the *RA* factor. Results are summarized in Figure 7.6, showing that the generator current is positively impacted by flow when working in single mode, while it is negatively affected when operating in dual mode. In single mode, mass transport is improved with fluid flow, increasing the amount of species oxidized or reduced at the electrode surface. Nonetheless, in dual mode, efficient elliptical diffusion is impeded by flow as half of the species must diffuse upstream during redox cycling. This adverse effect decreases with increments in electrode height, where linear diffusion dominates.

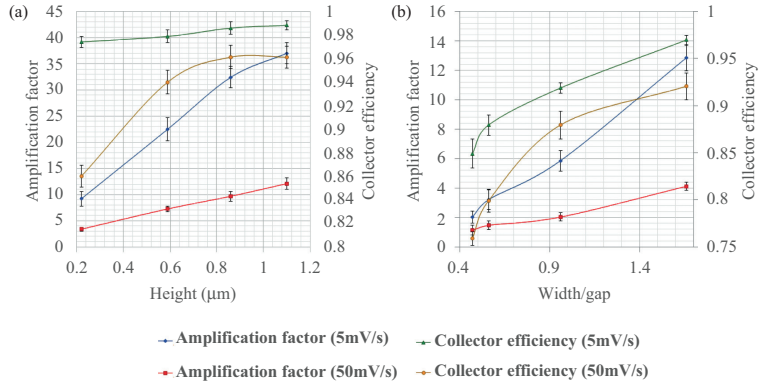

Figure 7.5. Amplification factor and collection efficiency as function of potential sweep rate and (a) electrode height, or (b) width-to-gap ratio.

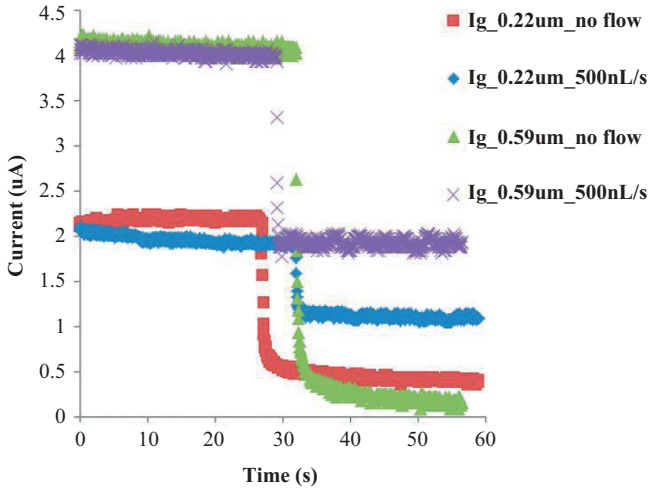

Figure 7.6. Effect of sample flow in redox cycling [19].

7.4.3 DOPAMINE DETECTION WITH 3D CARBON IDEAS

Dopamine is an essential neurotransmitter for a variety of biological and chemical processes in the mammalian central nervous system [33, 34]. This neurotransmitter plays a significant role in motor control, neurorecognition, and reward-motivated behavior [35, 36]. Imbalance of dopamine in the basal ganglia region of the brain is associated with neurological disorders such as Parkinson's disease [37], Huntington's disease [38], Tourette's syndrome [39], schizophrenia [40], and—attention deficit hyperactivity disorder [41]. Some studies have shown that dopamine may also play a direct role in damaging cellular macromolecules [42]. Therefore, detecting dopamine concentrations accurately in the extracellular fluid (ECF) is essential for pathological research as well as a diagnostic tool.

In the ECF, dopamine coexists with other constituents that have similar redox potentials, for example, ascorbic acid. Thus, the main challenge in electrochemically measuring dopamine concentrations is to separate the dopamine signal contribution from the ascorbic acid interfering signal [43]. The sensing problem is even more challenging by considering the fact that dopamine concentration in the ECF (0.01 to 10 μM) is much lower than that of ascorbic acid (100 to 500 μM) [44]. As dopamine is electrochemically reversible, redox cycling with IDEAs is possible. This is accomplished through the application of the required potentials to oxidize and reduce the targeted species to the generator and collector electrodes, respectively. On the generator electrode, the dopamine

undergoes oxidation to form dopamine-quinone. Then, dopamine-quinone diffuses to the collector electrode where it is converted back to dopamine. Nonetheless, the excess ascorbic acid present in the sample can reduce dopamine-quinone before it reaches the collector electrode, significantly reducing the collection efficiency of the sensor.

Kamath and Madou [32] reported the use of three-dimensional carbon IDEAs for dopamine detection in the presence of ascorbic acid. The carbon electrode arrays used for the experiments feature 70 pairs of digits with the following dimensions: the digit width is 1 μm at the top and 1.7 μm at the base, the interdigit space is 1.8 μm at the top and 1.1 μm at the base, the digit height is 0.6 μm, and the digit length is 2 mm. RE and CE were fabricated as described in Section 7.4.2.

In this study, CV, linear sweep voltammetry, and CA techniques were used to evaluate the performance of C-MEMS-based 3D IDEAs as amperometric detectors of dopamine. Samples used for experimentation emulated the physiological concentrations of dopamine (0.02 mM) and ascorbic acid (0.1 mM), as well as the pH (7.4) of the ECF. As both species, dopamine and ascorbic acid, have similar redox potentials, sodium dodecyl sulfate (SDS) in a 4 mM concentration was used to mask the interference signal of ascorbic acid.

Through linear sweep voltammetry (LSV), it was found that the ascorbic acid oxidation potential shifts 280 mV to more positive values in the presence of SDS (i.e., the oxidation peak shifts from 250 to 530 mV). However, the redox potential of dopamine is almost unaffected. Therefore,

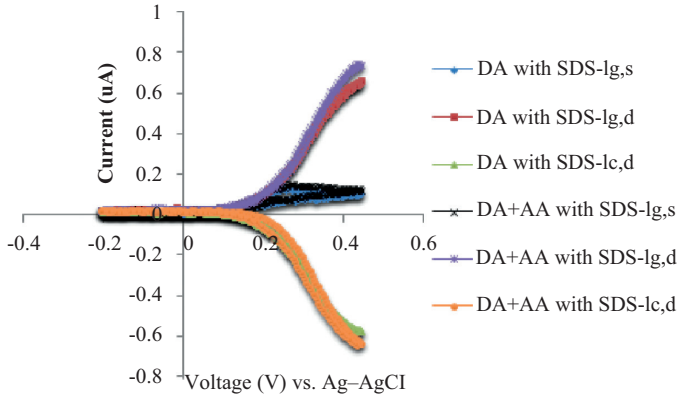

Figure 7.7. Cyclic voltammograms of 0.02 mM dopamine (DA) in the presence and absence of ascorbic acid (AA) in 1 × PBS (7.4 pH). The solution contained 4 mM SDS. Ig: Generator current, Ic: Collector current, s: Single mode, d: Dual mode. Reproduced from [32].

CVs (dual mode) were recorded with the collector electrode held at −250 mV and the generator electrode cycling between −200 and 450 mV to avoid the ascorbic acid interference. For single-mode CVs, the collector electrode was kept at an open potential. In Figure 7.7, we show that the generator current for dopamine in dual mode features an *RA* factor of 10 when compared to the current in single mode. Moreover, the generator current in the presence and absence of ascorbic acid is almost identical, and with this negligible background current, an LOD for dopamine of 1.5 μM was reached. Finally, CAs performed at different dopamine concentrations revealed a linear range from 5 to 500 μM. These results demonstrate that 3D carbon IDEAs are a viable (and less expensive) alternative to conventional metallic IDEAs for the detection of dopamine in the presence of ascorbic acid at physiological concentrations and pH.

7.5 CONCLUDING REMARKS

In this chapter, we have shown that the C-MEMS process constitutes an attractive approach for the fabrication of 3D IDEAs. Advantages of carbon (in comparison to noble metals commonly used in the fabrication of electrodes) were highlighted and include its chemical inertness, wider electrochemical stability window, and excellent biocompatibility. Moreover, carbon polymerizes better than Si, is available in a wide variety of allotropes, has low cost, is easy to derivatize, and is nature's building block for living things (more details in Chapters 1 and 2 of Volume 1 of this book). Furthermore, in the C-MEMS process, the use of complex multistep fabrication techniques such as deep-UV projection lithography and electron beam lithography is not required, making it much less expensive and less time consuming than conventional metal-based fabrication methods. Additionally, the formation of galvanic couples, produced by metal bilayers such as Cr–Au or Ti–Au in contact with an electrolyte, is avoided with C-MEMS-based electrodes.

The performance of C-MEMS-based 3D IDEAs as amperometric sensors was reported in terms of several design parameters (interdigit gap, electrode thickness, width-to-gap ratio, potential sweep rate, and flow rate). It was shown that the redox amplification factor increases with ever smaller interdigit gaps and with thicker electrodes. This is due to trenches formed in the interdigit gap region, which prevent the species from diffusing out into the bulk solution, therefore improving the cycling efficiency. It was also shown that an increase in the width-to-gap ratio of C-MEMS-based 3D IDEAs leads to an enhanced redox amplification

factor. In addition, fast potential sweep rates were demonstrated to negatively affect the IDEAs performance, as the time available for redox cycling is significantly smaller than that at low potential sweep rates. Flow rate also had a negative effect in the redox amplification factor (efficient elliptical diffusion atop the electrodes is impeded by flow). However, thicker electrodes were able to mitigate this effect significantly. For the experiments, a standard probe ($K_4Fe(CN)_6$) and a biological probe (dopamine) were used. Redox amplification factors as high as 37 were attained with carbon IDEAs. Moreover, dopamine was detected in the presence of excess ascorbic acid, requiring no chemical modification of the electrode surface.

REFERENCES

[1] Göpel, W., and K.-D. Schierbaum. 1995. "Definitions and Typical Examples." In *Sensors Set: A Comprehensive Survey*, ed. Weinheim, 1–27. Germany: Wiley-VCH Verlag GmbH.

[2] Göpel, W., T.A. Jones†, W. Göpel, J. N. Zemel, and T. Seiyama. 1995. "Historical Remarks." In *Sensors Set: A Comprehensive Survey*, ed. Weinheim, 29–59. Weinheim, Germany: Wiley-VCH Verlag GmbH.

[3] Seiyama, T. 1988. "Chemical Sensors—Current State and Future Outlook." In *Chemical Sensor Technology*, ed. T. Seiyama, 1–13. Amsterdam, Netherlands: Elsevier.

[4] Hulanicki, A., S. Glab, and F. Ingman. 1991. "Chemical Sensors: Definitions and Classification." *Pure and Applied Chemistry* 63, no. 9, pp. 1247–50. doi: http://dx.doi.org/10.1351/pac199163091247

[5] Janata, J. 2009. *Principles of Chemical Sensors*. New York, NY: Springer US.

[6] Bard, A.J., and L.R. Faulkner. 1980. *Electrochemical Methods: Fundamentals and Applications*. New York, NY: Wiley.

[7] Wang, J. 2006. *Analytical Electrochemistry*. Hoboken, NJ: John Wiley & Sons.

[8] Madou, M.J. 2002. *Fundamentals of Microfabrication: The Science of Miniaturization*. Boca Raton, FL: CRC press.

[9] Zhang, X., H. Ju, and J. Wang. 2008. *Electrochemical Sensors, Biosensors and Their Biomedical Applications*. San Diego, CA: Academic Press.

[10] Kappes, T., B. Galliker, M.A. Schwarz, and P.C. Hauser. 2001. "Portable Capillary Electrophoresis Instrument with Amperometric, Potentiometric and Conductometric Detection." *TrAC Trends in Analytical Chemistry* 20, no. 3, pp. 133–39. doi: http://dx.doi.org/10.1016/s0165-9936(00)00088-1

[11] Heinze, J. 1993. "Ultramicroelectrodes in Electrochemistry." *Angewandte Chemie International Edition in English* 32, no. 9, pp. 1268–88. doi: http://dx.doi.org/10.1002/anie.199312681

[12] Compton, R.G., A.C. Fisher, R.G. Wellington, P.J. Dobson, and P.A. Leigh. 1993. "Hydrodynamic Voltammetry with Microelectrodes: Channel Microband Electrodes; Theory and Experiment." *The Journal of Physical Chemistry* 97, no. 40, pp. 10410–15. doi: http://dx.doi.org/10.1021/j100142a024

[13] Strutwolf, J., and W.W. Schoeller. 1996. "Linear and Cyclic Sweep Voltammetry at a Rotating Disk Electrode. A Digital Simulation." *Electroanalysis* 8, no. 11, pp. 1034–39. doi: http://dx.doi.org/10.1002/elan.1140081111

[14] Bratov, A., J. Ramón-Azcón, N. Abramova, A. Merlos, J. Adrian, F. Sánchez-Baeza, M.-P. Marco, and C. Domínguez. 2008. "Three-Dimensional Interdigitated Electrode Array as a Transducer for Label-Free Biosensors." *Biosensors and Bioelectronics* 24, no. 4, pp. 729–35. doi: http://dx.doi.org/10.1016/j.bios.2008.06.057

[15] Bratov, A., N. Abramova, M.P. Marco, and F. Sanchez Baeza. 2012. "Three-Dimensional Interdigitated Electrode Array as a Tool for Surface Reactions Registration." *Electroanalysis* 24, no. 1, pp. 69–75. doi: http://dx.doi.org/10.1002/elan.201100392

[16] Sheppard, N.F., Jr., R.C. Tucker, and C. Wu. 1993. "Electrical Conductivity Measurements Using Microfabricated Interdigitated Electrodes." *Analytical Chemistry* 65, no. 9, pp. 1199–02. doi: http://dx.doi.org/10.1021/ac00057a016

[17] Ahadian, S., J. Ramón-Azcón, S. Ostrovidov, G. Camci-Unal, V. Hosseini, H. Kaji, K. Ino, H. Shiku, A. Khademhosseini, and T. Matsue. 2012. "Interdigitated Array of Pt Electrodes for Electrical Stimulation and Engineering of Aligned Muscle Tissue." *Lab on a Chip* 12, no. 18, pp. 3491–03. doi: http://dx.doi.org/10.1039/c2lc40479f

[18] Sun, T., H. Morgan, and N.G. Green. 2007. "Analytical Solutions of AC Electrokinetics in Interdigitated Electrode Arrays: Electric Field, Dielectrophoretic and Traveling-Wave Dielectrophoretic Forces." *Physical Review E* 76, no. 4, pp. 046610. doi: http://dx.doi.org/10.1103/physreve.76.046610

[19] Kamath, R.R., and M.J. Madou. 2014. "Three-Dimensional Carbon Interdigitated Electrode Arrays for Redox-Amplification." *Analytical chemistry* 86, no. 6, pp. 2963–71. doi: http://dx.doi.org/10.1021/ac4033356

[20] Aoki, K. 1990. "Approximate Models of Interdigitated Array Electrodes for Evaluating Steady-State Currents." *Journal of Electroanalytical Chemistry* 284, no. 1, pp. 35–42. doi: http://dx.doi.org/10.1016/0022-0728(90)87060-w

[21] Iwasaki, Y., and M. Morita. 1995. "Electrochemical Measurements with Interdigitated Array Microelectrodes." *Current Separations* 14, no. 1, pp. 2–8. http://www.currentseparations.com/issues/14-1/cs14-1a.pdf

[22] Niwa, O., M. Morita, and H. Tabei. 1991. "Highly Sensitive and Selective Voltammetric Detection of Dopamine with Vertically Separated Interdigitated Array Electrodes." *Electroanalysis* 3, no. 3, pp. 163–68. doi: http://dx.doi.org/10.1002/elan.1140030305

[23] Niwa, O., M. Morita, and H. Tabei. 1990. "Electrochemical Behavior of Reversible Redox Species at Interdigitated Array Electrodes with Different Geometries: Consideration of Redox Cycling and Collection Efficiency." *Analytical Chemistry* 62, no. 5, pp. 447–52. doi: http://dx.doi.org/10.1021/ac00204a006

[24] Niwa, O. 1995. "Electroanalysis with Interdigitated Array Microelectrodes." *Electroanalysis* 7, no. 7, pp. 606–13. doi: http://dx.doi.org/10.1002/elan.1140070702

[25] Goluch, E.D., B. Wolfrum, P.S. Singh, M.A. Zevenbergen, and S.G. Lemay. 2009. "Redox Cycling in Nanofluidic Channels Using Interdigitated Electrodes." *Analytical and Bioanalytical Chemistry* 394, no. 2, pp. 447–56. doi: http://dx.doi.org/10.1007/s00216-008-2575-x

[26] Dam, V.A.T., W. Olthuis, and A. van den Berg. 2007. "Redox Cycling with Facing Interdigitated Array Electrodes as a Method for Selective Detection of Redox Species." *Analyst* 132, no. 4, pp. 365–70.doi: http://dx.doi.org/10.1039/b616667a

[27] Marsh, H. 1989. *Introduction to Carbon Science*. London, England: Butterworth-Heinemann.

[28] Singh, A., J. Jayaram, M. Madou, and S. Akbar. 2002. "Pyrolysis of Negative Photoresists to Fabricate Carbon Structures for Microelectromechanical Systems and Electrochemical Applications." *Journal of the Electrochemical Society* 149, no. 3, pp. E78–83. doi: http://dx.doi.org/10.1149/1.1436085

[29] Wang, C., and M. Madou. 2005. "From MEMS to NEMS with Carbon." *Biosensors and Bioelectronics* 20, no. 10, pp. 2181–87. doi: http://dx.doi.org/10.1016/j.bios.2004.09.034

[30] Keller, S., G. Blagoi, M. Lillemose, D. Haefliger, and A. Boisen. 2008. "Processing of Thin SU-8 Films." *Journal of Micromechanics and Microengineering* 18, no. 12, p. 125020. doi: http://dx.doi.org/10.1088/0960-1317/18/12/125020

[31] Heo, J., D. Shim, G.T. Teixidor, S. Oh, M. Madou, and H. Shin. 2011. "Carbon Interdigitated Array Nanoelectrodes for Electrochemical Applications." *Journal of Electrochemical Society* 158, no. 3, pp. J76–80. doi: http://dx.doi.org/10.1149/1.3531952

[32] Kamath, R., and M.J. Madou. 2014. "Selective Detection of Dopamine Against Ascorbic Acid Interference Using 3D Carbon Interdigitated Electrode Arrays." *ECS Transactions* 61, no. 7, pp. 65–73. doi: http://dx.doi.org/10.1149/06107.0065ecst

[33] Damier, P., E. Hirsch, Y. Agid, and A. Graybiel. 1999. "The Substantia Nigra of the Human Brain: II. Patterns of Loss of Dopamine-Containing Neurons in Parkinson's Disease." *Brain* 122, no. 8, pp. 1437–48. doi: http://dx.doi.org/10.1093/brain/122.8.1437

[34] Castellano, C., S. Cabib, and S. Puglisi-Allegra. 1996. "Psychopharmacology of Memory Modulation: Evidence for Multiple Interaction Among Neurotransmitters and Hormones." *Behavioural Brain Research* 77, no. 1–2, pp. 1–21. doi: http://dx.doi.org/10.1016/0166-4328(96)00200-8

[35] Berridge, K.C., and T.E. Robinson. 1998. "What Is the Role of Dopamine in Reward: Hedonic Impact, Reward Learning, or Incentive Salience?" *Brain Research Reviews* 28, no. 3, pp. 309–69. doi: http://dx.doi.org/10.1016/s0165-0173(98)00019-8

[36] Wise, R.A. 1998. "Drug-Activation of Brain Reward Pathways." *Drug and Alcohol Dependence* 51, no. 1–2, pp. 13–22. doi: http://dx.doi.org/10.1016/s0376-8716(98)00063-5

[37] Wightman, R.M., L.J. May, and A.C. Michael. 1988. "Detection of Dopamine Dynamics in the Brain." *Analytical Chemistry* 60, no. 13, pp. 769A–793A. doi: http://dx.doi.org/10.1021/ac00164a718

[38] Bibb, J.A., Z. Yan, P. Svenningsson, G.L. Snyder, V.A. Pieribone, A. Horiuchi, A.C. Nairn, A. Messer, and P. Greengard. 2000. "Severe Deficiencies in Dopamine Signaling in Presymptomatic Huntington's Disease Mice." In *Proceedings of the National Academy of Sciences* 97, pp. 6809–14. doi: http://dx.doi.org/10.1073/pnas.120166397

[39] Mink, J.W. 2001. "Basal Ganglia Dysfunction in Tourette's Syndrome: A New Hypothesis." *Pediatric Neurology* 25, no. 3, pp. 190–98. doi: http://dx.doi.org/10.1016/s0887-8994(01)00262-4

[40] Grace, A. 1991. "Phasic Versus Tonic Dopamine Release and the Modulation of Dopamine System Responsivity: A Hypothesis for the Etiology of Schizophrenia." *Neuroscience* 41, no. 1, pp. 1–24. doi: http://dx.doi.org/10.1016/0306-4522(91)90196-u

[41] Phillips, P.E., G.D. Stuber, M.L. Heien, R.M. Wightman, and R.M. Carelli. 2003. "Subsecond Dopamine Release Promotes Cocaine Seeking." *Nature* 422, no. 6932, pp. 614–18. doi: http://dx.doi.org/10.1038/nature01476

[42] Stokes, A.H., T.G. Hastings, and K.E. Vrana. 1999. "Cytotoxic and Genotoxic Potential of Dopamine." *Journal of Neuroscience Research* 55, no. 6, pp. 659–65. doi: http://dx.doi.org/10.1002/(sici)1097-4547(19990315)55:6%3C659::aid-jnr1%3E3.0.co;2-c

[43] O'Neill, R.D. 1994. "Microvoltammetric Techniques and Sensors for Monitoring Neurochemical Dynamics in Vivo. A Review." *The Analyst* 119, no. 5, pp. 767–79. doi: http://dx.doi.org/10.1039/an9941900767

[44] Chitravathi, S., B.K. Swamy, G. Mamatha, and B. Sherigara. 2011. "Simultaneous Electrochemical Determination of Dopamine and Ascorbic Acid Using Poly (l-serine) Modified Carbon Paste Electrode." *Journal of Molecular Liquids* 160, no. 3, pp. 193–99. doi: http://dx.doi.org/10.1016/j.molliq.2011.03.019

INDEX

Carbon: The Next Silicon?

Book 2 – Applications

Marc J. Madou • Victor H. Perez-Gonzalez • Bidhan Pramanick

Nuclear Magnetic Resonance (NMR) and Electron Spin Resonance (ESR) spectroscopies are well-known characterization techniques that reveal the molecular details of a sample non-invasively. The authors discuss how NMR can provide useful information on the microstructure of carbon and its surface properties and explain how C-MEMS/C-NEMS technology can be explored for building improved NMR microdevices.

The authors highlight the manipulation of fluids and particles by dielectrophoresis and the use of carbon electrodes for dielectrophoresis in Lab-on-a-Chip. The use of these electrodes in sample preparation through electrical polarization of a sample for identification, manipulation, and lysis of bioparticles is also discussed and they introduce a new generation of neural prosthetics based on glassy carbon micromachined electrode arrays. The tuning of the electrical, electrochemical and mechanical properties of these patternable electrodes for applications in bio-electrical signal recording and stimulation, and results from in-vivo testing of these glassy carbon microelectrode arrays is reported, demonstrating a quantifiable superior performance compared to metal electrodes.

Dr. Marc J. Madou is the chancellor's professor in mechanical and aerospace engineering (MEA) as the University of California Irvine. Dr. Madou is the author of several books, including *Fundamentals of Microfabrication*. Some of Dr. Madou's current research work involves a compact disc-based fluidic platform and carbon MEMS. Learn more about those recent research projects, visit www.biomems.net.

Dr. Victor H. Perez-Gonzalez, received the BS degree from *Universidad Autonoma de Nuevo Leon*, Mexico; and his MS and PhD from *Tecnologico de Monterrey*, Mexico, where he is now a research associate. He is a member of the National System of Researchers, Mexico. Dr. Perez-Gonzalez's research interests are focused in the field of miniaturization science, where he has published several papers.

Dr. Bidhan Pramanick received his PhD from Indian Institute of Technology Kharagpur, India. He was assistant professor in the Indian Institute of Space Science and Technology before joining Tec de Monterrey, Mexico (and UCI, CA) as postdoctoral research investigator. He has authored and co-authored several papers in international journals and conference proceedings and one book.

MOMENTUM PRESS
ENGINEERING

ISBN: 978-1-60650-883-1
90000
9 781606 508831